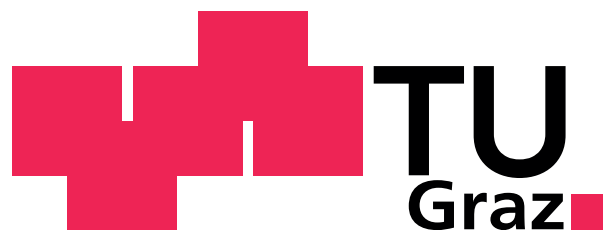


Stefan Kirnstötter

**Electron Beam Induced Current
Investigations of Proton Implanted
Silicon and Power Semiconductor
Devices**

DOCTORAL THESIS

For obtaining the academic degree of
Doktor der technischen Wissenschaften
Doctoral Programme of Technical Physics



Graz University of Technology

Supervisor:

Univ.-Prof. Peter Hadley Ph.D.
Institute of Solid State Physics

Graz, Februar 2015

EIDESSTÄTTLICHE ERKLÄRUNG

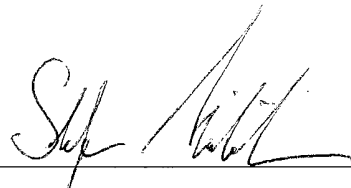
AFFIDAVIT

Ich erkläre an Eides statt, dass ich die vorliegende Arbeit selbstständig verfasst, andere als die angegebenen Quellen/Hilfsmittel nicht benutzt, und die den benutzten Quellen wörtlich und inhaltlich entnommenen Stellen als solche kenntlich gemacht habe. Das in TUGRAZonline hochgeladene Textdokument ist mit der vorliegenden Masterarbeit/Diplomarbeit/Dissertation identisch.

I declare that I have authored this thesis independently, that I have not used other than the declared sources/resources, and that I have explicitly indicated all material which has been quoted either literally or by content from the sources used. The text document uploaded to TUGRAZonline is identical to the present master's thesis/diploma thesis/doctoral dissertation.

Feb 10th 2015

Datum / Date

A handwritten signature in black ink, appearing to be 'Steph. ...', written over a horizontal line.

Unterschrift / Signature

Acknowledgments

During the last years I got a lot of support from different persons in my live that made it possible for me to do the research presented in this PhD thesis. It is a pleasure for me now to thank all of them that were somehow involved in my work.

First of all I would like to thank Univ.-Prof. Peter Hadley Ph.D. for guiding me through this thesis. Your passion for science and research is contagious and exiting, also your positive attitude of life made it a pleasure to work with you.

I want to thank my supervisors from Infineon Technologies AG, Dr. Werner Schustereder and Dr. Johannes G. Laven for providing me with specimen material and their broad knowledge about implantation physics. I also want to thank my manager Dr. Markus Harfmann for supporting me financially. A big thank you goes to Dr. Hans-Joachim Schulze for his supervision and helpful suggestions during our meetings the last couple of years. At this point I also want to thank Prof. Reinhart Job for his great input during our meetings.

Moreover I want to thank Dipl. Ing. Martin Faccinelli, my college and friend, without you the whole time in the lab would have been half the fun it was!

Thanks to Dipl. Ing. Gernot Gruber and Dipl. Ing. Moriz Jelinek for the fruitful discussions and cooperation, but even more for the fun we had together during our conference stays and beside our common projects.

I want to thank Prof. Roland Resel and Prof. Robert Schennach for letting me use their scientific equipment and for the the scientific support. Thanks to Elisabeth Stern for her cheerful personality. I also want to acknowledge the very interesting and pleasant cooperation with Dr. Christian Gspan and Prof. Werner Grogger from the research institute of electron microscopy (FELMI).

I want to thank the whole team of Infineon Technologies in Villach and Munich. Special thanks go to Dr. Holger Schulze, Tobias Bianga, Dipl. Ing. Christoph Weiss, Irmgard Glawar-Barth supporting me during my thesis in different tasks.

Nevertheless, I want to appreciate the great time that I had in Graz with my good friends Michael Mayrhofer-Reinharhuber, Immanuel Mayrhuber, Alex Vormayr, Christoph Sigl and the rest of the Nerds08 football team (Mothe, Fiz, Max, Phil, Michi D., Michi H., Christiano, Humsi).

Of course I also want to thank my parents and my sister for their support during the whole time of my studies.

Finally, I want to thank my significant other Stephanie "Steffi" Hocheneder for her love and patience during the last years. Without your support in difficult times I would not have finished this thesis.

Contents

1	Introduction	2
2	Background, fundamentals and reflection of field of research	4
2.1	Silicon - from quartz sand to semiconductor power devices	4
2.1.1	Czochralsky process (Cz)	5
2.1.2	Zone melting refinement process- Float zone silicon (Fz)	6
2.1.3	Neutron/nuclear transmutation doping	7
2.1.4	Epitaxial silicon	7
2.1.5	Processing: from the wafer to the packaged chip	8
2.2	Physical and electrical properties of silicon and semiconductors	9
2.2.1	Crystal structure of silicon	9
2.2.2	Electrical properties - band diagram	10
2.2.3	Band structure of silicon - dispersion relationship $E(\vec{k})$	11
2.2.4	Analytical description	13
2.2.5	Important material properties of semiconductors	14
2.3	Defects	17
2.3.1	Point defects	17
2.3.2	Line defects - dislocations	18
2.3.3	Planar defects - plane defects	18
2.3.4	Volume defects	18
2.3.5	Intrinsic defects in silicon	18
2.4	Acceptor and donor levels in silicon	19
2.5	Hydrogen implantation process	21
2.5.1	Hydrogen implantation process	21
2.5.2	Analytical analysis of proton implantation process	22
2.5.3	Implantation damage	23
2.5.4	The annealing process - defect migration and formation	23
2.5.5	Reaction-diffusion equations	25
2.5.6	Defect evolution	26
2.6	Oxygen related thermal donors (OTD) in silicon	27
2.7	Hydrogen related thermal donors in Silicon	33
2.8	Hydrogen defect complexes	34
2.9	H ⁺ -implantation dose variation	36
2.9.1	Low implantation doses	36
2.9.2	Medium implantation doses	36
2.9.3	High implantation doses	37

2.10	Charge carrier concentration (doping) profile due to H^+ -implantations into silicon	38
2.10.1	Qualitative description of H^+ -implantation profile in Fz silicon	38
2.10.2	Qualitative description of H-implantation profile in Cz/m:Cz silicon	40
2.11	PN-junction and Schottky junctions	42
2.11.1	PN-junction	42
2.11.2	Zero external bias	42
2.11.3	Forward bias	42
2.11.4	Reverse bias	43
2.11.5	Schottky junction	44
3	Analytical methods	46
3.1	Scanning electron microscope (SEM)	46
3.1.1	Secondary electron detector	48
3.1.2	Backscattered electron detector	50
3.2	Electron beam induced current (EBIC)	52
3.2.1	Interaction of the electron beam with the semiconducting material	52
3.2.2	Charge carrier separation - analytical description	52
3.2.3	EBIC measurement techniques	54
3.2.4	Schottky-EBIC measurements	57
3.2.5	EBIC Lock-In Measurements	58
3.2.6	Measurement setup: sample holder, current circuit, beam-chopping experiments	59
3.2.7	Extraction of the minority charge carrier diffusion length L_D	59
3.2.8	Biased Schottky EBIC measurement	61
3.2.9	EBIC investigations of III/V semiconductors	64
3.3	Optical beam induced current (OBIC)	68
3.4	Transmission electron microscopy (TEM)	69
3.4.1	TEM investigation of H^+ -implanted silicon	69
3.4.2	Electron diffraction investigations	71
3.4.3	Advanced electron diffraction investigations	74
3.5	Spreading resistance profiling (SRP)	81
3.6	Scanning spreading resistance measurements (SSRM)	83
3.7	Four point measurements	84
3.7.1	Four point measurements on a thin film	86
3.8	Stopping and range of ions in matter (SRIM/TRIM) simulations	87
4	Publications	90
5	Conclusions and outlook	138
5.1	Reflection of work and state of knowledge	138
5.1.1	H^+ -implantation into silicon - point defects in semiconductors	138
5.1.2	EBIC measurement techniques	140
5.2	Promising future studies	141
5.3	Summary	145

6	Appendix	148
6.1	Analytical analysis of SRP measurements	148
6.2	Measurement equipment and materials	154
6.2.1	Measurement equipment	154
6.2.2	Specimen materials	155

Abstract

One major part of this thesis is about the investigation of hydrogen ion (H^+) implantation induced defects in silicon. The second part covers the development and improvement of the measurement method Electron Beam Induced Current (EBIC), that was used to investigate semiconductor material parameters and power semiconductor devices. Due to the implantation of high energetic hydrogen ions (protons) into silicon, radiation damage and defect complexes are generated in the crystal lattice. Depending on implantation parameters, and the incorporated thermal budget due to the subsequent annealing step, different defect complexes are formed and electrically activated. Hydrogen related thermal donor complexes are of special interest in this work. They consist of radiation induced defect complexes that are decorated by diffusing hydrogen during the annealing process, leading to the formation of donor complexes. The exact microscopic structure of these defects is still under investigation. Depending on the oxygen concentration of the silicon substrate material, the charge carrier concentration profiles after the proton implantations vary a lot. The activation and evolution of the hydrogen implantation induced doping profiles was investigated using Spreading Resistance Profiling (SRP). Effective diffusion coefficients and the activation energy for the hydrogen diffusion were determined. Using high resolution Transmission Electron Microscopy (TEM) the microscopic structure of the formed defect complexes was investigated. The variation of the implantation dose results in the formation of different defect complexes. Additionally, significant differences in the crystal row distances were detected. During this work the measurement method EBIC was used intensively. The focus was on the development and improvement of the method to investigate semiconductor material parameters and power semiconductor devices. The micro-manipulator working place inside the scanning electron microscope enabled controlled electrical measurements on a low magnification. By forming Schottky contacts between the micro-manipulator metal tip (diameter > 100 nm) and the semiconductor material it was possible to locally determine the doping type as well as the minority charge carrier diffusion length. In the special case of proton implantation induced doping profiles, when there is a doping type conversion due to the activation of defect complexes, EBIC-Schottky measurements are a very sensitive method to determine the doping type. Further on, the position of the pn -junction can be determined very accurately. It also proved to be a very useful method in the investigation process of power semiconductor devices. The expansion of space charge regions during the reverse biased mode of a device was displayed in-situ until the device depleted completely.

Kurzfassung

Diese Arbeit befasst sich zu großen Teilen mit der Untersuchung von Defekten, erzeugt durch Protonen (H^+) Implantationen in Silizium, und mit der Weiterentwicklung der Untersuchungsmethode "Electron Beam Induced Current" (EBIC). Durch Protonenimplantation in Silizium erzeugte Defektkomplexe, die durch die Implantation und einen nachfolgenden Temperprozess entstehen, können sich, je nach Implantations- und Temperparameter, sehr stark voneinander unterscheiden. Von speziellem Interesse für diese Arbeit ist die Defektfamilie der thermische Donatoren. Diese Defekte bestehen aus durch Implantationsschäden erzeugte Defektkomplexen, die dann während der Temperung, von dem zur Diffusion angeregten Wasserstoff, dekoriert werden und elektrisch aktive Donatoren bilden. Die exakte mikroskopische Struktur dieser Defekte ist noch nicht geklärt. Je nach Materialeigenschaften des Siliziumausgangsmaterials, im speziellen die unterschiedlich hohe Sauerstoff- und Kohlenstoffkonzentration, unterscheiden sich die im Silizium aktivierten Dotierprofile sehr stark. Die Untersuchungen der durch die Protonenimplantation erzeugten Dotierprofile wurde mittels Ausbreitungswiderstandsmessungen (SRP) durchgeführt. Es wurden effektive Diffusionskoeffizienten des implantierten Wasserstoffs und die Aktivierungsenergie zur Diffusion des Wasserstoffs in Silizium bestimmt. Die mikroskopischen Strukturen der erzeugten Defektkomplexe wurde mit transmissionselektronenmikroskopischen (TEM) Messungen untersucht. Die Variation der Implantationsdosis führt zur Erzeugung unterschiedlicher Defektkomplexe. Des Weiteren zeigten sich signifikante Unterschiede in den Kristallebenenabständen in der Implantationstiefe des Wasserstoffs. Während dieser Arbeit wurde die Untersuchungsmethode "Electron Beam Induced Current" (EBIC) besonders intensiv genutzt. Der Fokus lag hierbei auf der Weiterentwicklung der Messmethode zur Untersuchung von Halbleitermaterialeigenschaften im Besonderen von Leistungshalbleiterbauelementen. Mit einem Mikromanipulatormessspitzenplatz im Rasterelektronenmikroskop (REM) konnten elektrische Messungen hoch aufgelöst durchgeführt werden. Durch die Bildung von Schottky Kontakten zwischen den Messspitzen (Spitzendurchmesser rund 100 nm) und dem zu untersuchenden Halbleitermaterial, konnten lokal der Dotiertyp sowie die Minoritätsladungsträger-Diffusionslänge bestimmt werden. Im speziellen Fall, der durch Protonenimplantation erzeugten Dotierprofile, war es durch EBIC Untersuchungen möglich sehr kleine Änderungen der Konzentration von elektrisch aktiven Defektkomplexen, e.g. Aktivierung von Donatoren/Akzeptoren während der Temperung die zu einer Dotiertypkonversion führten, darzustellen. Des Weiteren war eine sehr genaue Untersuchung der Position der erzeugten *pn*-Übergänge möglich. Es konnte gezeigt werden, dass EBIC eine sehr gut geeignete Methode ist, um Leistungshalbleiterbauelemente zu untersuchen. Die Verarmung eines Bauteils bzw. die Ausbreitung der Raumladungszonen in den Bauelementen im Sperrbetrieb konnte bis zur kompletten Verarmung dargestellt werden.

Initiatory statement regarding the structure of this thesis

This work is a so called cumulative Ph.D. thesis, structured according to the rules suggested by the Doctoral School of Physics at Graz University of Technology. That means the thesis is based on peer-reviewed scientific articles to which the author of this thesis has significantly contributed. The thesis begins with an introduction, an overview about the field of research and the description of the analytical methods used during this thesis. Then the scientific publications are enclosed in the middle of the thesis, in the as in the journals published form. After the already accepted and published work, a reflection of the state of knowledge, promising future studies and finally a pointed conclusion of the most important findings of this thesis are presented.

List of publications

This is a list of the peer-reviewed publications published/submitted until September 2014 associated with the scientific work during the three and a half years of my Ph.D. studies

S. Kirnstoetter, M. Faccinelli, M. Jelinek, W. Schustereder, J. G. Laven, H.-J. Schulze and P. Hadley, *H⁺ Implantation Profile Formation in m:Cz and Fz silicon*, 20th International Conference on Ion Implantation Technology (IIT)(pp. 1-4) IEEE (2014) <http://ieeexplore.ieee.org/xpls>

S. Kirnstoetter, M. Faccinelli, M. Jelinek, W. Schustereder, J. G. Laven, H.-J. Schulze and P. Hadley, *High Dose Proton Implantations into Silicon: A Combined EBIC, SRP and TEM Study*, *physica status solidi (c)*, 1610-1642 (2014), doi:10.1002/pssc.201400051

S. Kirnstoetter, M. Faccinelli, M. Jelinek, W. Schustereder, J. G. Laven, H.-J. Schulze and P. Hadley, *Depletion Behavior of Superjunction Power MOSFETs Visualized by Electron Beam Induced Current and Voltage Contrast Measurements*, *physica status solidi (c)* 1610-1642 (2014), doi:10.1002/pssc.201400050

M. Faccinelli, S. Kirnstoetter, W. Schustereder and P. Hadley, *An EBIC and SRP Study of High Temperature Thermal Donors in Proton Implanted p-type Magnetic Czochralski Silicon*, *physica status solidi (c)*, 1610-1642 (2014) doi:10.1002/pssc.201400045

G. Gruber, P. Hadley, M. Koch, T. Aichinger, S. Kirnstötter, H. Schulze and W. Schustereder, *Electrically detected magnetic resonance study on defects in Si pn-junctions created by proton implantation* *physica status solidi (c)*, 1610-1642 (2014) doi:10.1002/pssc.201400053

A. Kraxner, F. Roger, B. Loeffler, M. Faccinelli, S. Kirnstoetter, R. Minixhofer and P. Hadley, *Investigations on CMOS photodiodes using scanning electron microscopy with electron beam induced current measurements* Proc. SPIE 9236, Scanning Microscopies (2014), 923607 doi:10.1117/12.2066124

M. Jelinek, W. Schustereder, J. G. Laven, S. Kirnstoetter, M. Rommel, and L. Frey, *MeV-proton channeling in crystalline silicon*, 20th International Conference on Ion Implantation Technology (IIT)(pp. 1-4) IEEE (2014) <http://ieeexplore.ieee.org/xpls>

M. Jelinek, J. G. Laven, S. Kirnstoetter, W. Schustereder, H.-J. Schulze, M. Rommel and L. Frey, *A DLTS Study of Hydrogen Doped Czochralski-grown Silicon*, to be published in Nuclear Instruments and Methods B: Beam Interactions with Materials and Atoms

S. Kirnstoetter, M. Faccinelli, W. Schustereder, J. G. Laven, H.-J. Schulze and P. Hadley, *Hydrogen Decoration of Radiation Damage Induced Defect Structures* AIP Conference Proceedings, Vol. 1583 (51), doi:10.1063/1.4865603

S. Kirnstoetter, M. Faccinelli, M. Jelinek, W. Schustereder, J. G. Laven, H.-J. Schulze and P. Hadley, *Multiple proton implantations into silicon: A combined EBIC and SRP study*, *Solid State Phenomena* Vol. 205-206 (2014) doi:10.4028/www.scientific.net/SSP.205-206.311

S. Kirnstoetter, M. Faccinelli, P. Hadley, R. Job, W. Schustereder, J. G. Laven and H.-J.Schulze,
*Investigation of Doping Type Conversion and Diffusion Length Extraction of Proton Implanted Silicon
by EBIC* ECS Transactions, 50, 115-120 (2012) doi:10.1149/05005.0115ecst

S. Kirnstoetter, M. Faccinelli, P. Hadley, R. Job, W. Schustereder, J. G. Laven and H.-J.Schulze
Imaging Superjunctions in CoolMOS Devices using Electron Beam Induced Current ECS Transactions,
49, 475-481 (2012) doi:10.1149/04901.0475ecst

List of conference presentations

This is a list of talks and posters that were presented of the scientific work during my Ph.D. studies. The presenting author is underlined.

Talks

S.Kirnstoetter, M. Faccinelli, M. Jelinek, W. Schustereder, J. G. Laven, H.-J. Schulze and P. Hadley, *High Dose Proton Implantations into Silicon: A Combined EBIC, SRP and TEM Study*, European Material Research Society Meeting (EMRS), Lille, France (2014)

S.Kirnstoetter, M. Faccinelli, P. Hadley, *Investigation of Semiconductor Material Properties using Electron Beam Induced Current Measurements*, Kleindiek User Meeting, Reutlingen, Germany (2013)

S.Kirnstoetter, *Investigation of Semiconductor Material Properties and Devices by EBIC*, Innovation meeting Infineon Technologies AG, Munich, Germany (2013)

S.Kirnstoetter, M. Faccinelli, P. Hadley, W. Schustereder, J. G. Laven and H.-J.Schulze, *Electron Beam Induced Current Investigations of Semiconductor Material and Devices*, Physics Doctoral Seminar, Graz, Austria (2013)

S. Kirnstoetter, M. Faccinelli, P. Hadley, R.Job, W. Schustereder, J. G. Laven and H.-J.Schulze, *Investigation of Doping Type Conversion and Diffusion Length Extraction of Proton Implanted Silicon*, Electrochemical Society Meeting PRiME 2012, Honolulu, Hawaii, USA (2012)

S. Kirnstoetter, M. Faccinelli, P. Hadley, R.Job, W. Schustereder, J. G. Laven and H.-J.Schulze, *Imaging Superjunctions in CoolMOS Devices using Electron Beam Induced Current*, Electrochemical Society Meeting PRiME 2012, Honolulu, Hawaii, USA (2012)

Posters

S.Kirnstoetter, M. Faccinelli, M. Jelinek, W. Schustereder, J. G. Laven, H.-J. Schulze and P. Hadley, *Depletion Behavior of Superjunction Power MOSFETs Visualized by Electron Beam Induced Current and Voltage Contrast Measurements*, European Material Research Society Meeting (EMRS), Lille, France (2014)

S.Kirnstoetter, M. Faccinelli, W. Schustereder, J. G. Laven, H.-J. Schulze and P. Hadley, *Hydrogen Decoration of Radiation Damage Induced Defect Structures*, International Conference on Defects in Semiconductors (ICDS) 27, Bologna, Italy (2013)

S.Kirnstoetter, M. Faccinelli, P. Hadley, R. Job, W. Schustereder, J. G. Laven and H.-J.Schulze, *Electron Beam Induced Current Investigations*, Austrian Physical Society Meeting, Graz, Austria (2013)

S. Kirnstoetter, M. Faccinelli, M. Jelinek, *W.Schustereder*, J. G. Laven, H.-J. Schulze and P. Hadley, *Multiple proton implantations into silicon: A combined EBIC and SRP study*, Gettering and Defect Engineering in Semiconductor Technology (GADEST) 15, Oxford, United Kingdom (2013)

S.Kirnstoetter, M. Faccinelli, M. Jelinek, W. Schustereder, J. G. Laven, H.-J. Schulze and P. Hadley, *Proton implanted silicon wafers investigated by electron beam induced current measurements*, Gettering and Defect Engineering in Semiconductor Technology (GADEST) 14, Loiperdorf, Austria (2011)

Shortcuts and variables

Table 1: **Abbreviations**

AC	Alternating Current
CoolMOS	Super Junction Metal Oxide Semiconductor Field Effect Transistor
Cz-Si	Silicon wafer produced using the Czochalski method
EBIC	Electron Beam Induced Current
EDX	Energy Dispersive X-ray Analysis
EPR	Electron Paramagnetic Resonance
DLTS	Deep Level Transient Spectroscopy
FZ-Si	Silicon wafer produced using the float-zone method
IR	Infra-Red
IV	Current-voltage characteristic
LabVIEW	Laboratory Virtual Instrumentation Engineering Workbench
MOSFET	Metal Oxide Semiconductor Field Effect Transistor
RF	Radio Frequency
SCM	Scanning Capacitance Microscopy
SEM	Scanning Electron Microscope
SRP	Spreading Resistance Profiling
SSRM	Scanning Spreading Resistance Microscopy

Table 2: **Variables**

Variable	Significance	Unit
α	Fitting parameter	
A_{ij}	Arrhenius pre factor for the reaction of P_i and P_j to C_{ij}	
B_m	Magnetic field induction	[T]
C	Capacitance	[F]
c_1, c_2	Integration constants	
$c_{e,p}$	charge carrier concentration	$\frac{1}{\text{cm}^3}$
C_{ij}	Defect complex built up from precursors	P_i and P_j
d	Distance between the two point contacts in an SRP measurement	[m]
D	Diffusion coefficient	$[\frac{\text{m}^2}{\text{s}}]$
$D_{e,h}$	Diffusion coefficient of electrons or holes	$[\frac{\text{m}^2}{\text{s}}]$
E	Electric field	$[\frac{\text{V}}{\text{m}}]$
E_0	Electron beam energy	[keV]
E_c	Conduction band energy	[J]
E_F	Fermi energy	[J]
E_i	Intrinsic energy (mid band gap energy)	[J]
E_v	Valence band energy	[J]
G	Generation term (number of charge carriers generated by the incident electron beam)	
I	Current	[A]
I_{EBIC}	Measured electron beam induced current	[A]
J	Current density	$[\frac{\text{A}}{\text{m}^2}]$
k_B	Boltzmann constant ($1.381 \cdot 10^{-23}$)	$[\frac{\text{J}}{\text{K}}]$
k_{ij}	Reaction rate constant	$[\frac{\text{m}^3}{\text{s}}]$
l	Mean free path of electrons	[m]
L_D	Minority carrier diffusion length	[m]
μ_e	Mobility of electrons	$[\frac{\text{m}^2}{\text{Vs}}]$
μ_p	Mobility of holes	$[\frac{\text{m}^2}{\text{Vs}}]$
n	Number of charge carriers	
n_0	Number of charge carriers at thermal equilibrium	
N_A	Number of acceptors	
N_D	Number of donors	

Variable	Significance	Unit
q	Elementary charge ($1.602 \cdot 10^{-19}$)	[C]
ρ	Resistivity	$[\Omega\text{cm}]$
ρ_m	Mass density	$[\frac{\text{g}}{\text{cm}^3}]$
R	Resistance	Ω
Rec	Recombination term	
R_G	Electron Range	$[\mu\text{m}]$
R_{SRP}	Spreading resistance	$[\Omega]$
T	Temperature	[K]
τ	Minority carrier lifetime	[s]
τ_{surface}	Minority carrier lifetime depending on surface recombination only	[s]
τ_{volume}	Minority carrier lifetime depending on bulk recombination only	[s]
t	Time	[s]
V	Voltage	[V]
V_{bi}	Built in potential across a pn - or a Schottky junction	[V]
v_s	Surface recombination velocity	$[\frac{\text{m}}{\text{s}}]$
Z	Atomic number	
Φ	Electrostatic potential	[V]

Chapter 1

Introduction

This work is about the investigation of hydrogen ion (H^+) implantation induced defects in silicon, and the development and improvement of the measurement method Electron Beam Induced Current (EBIC), that was used to investigate semiconductor material parameters and power semiconductor devices. The defect complexes formed due to H^+ implantation are still a matter of debate. It is of high interest for the semiconductor manufacturing industry to better understand what happens on the atomic scale in this widely used doping method. EBIC measurements are a prominent method to detect built-in electric fields in semiconductors or to detect defects, such as regions of reduced charge carrier lifetime. In this thesis, I show additional applications of this measurement method, like the local determination of the doping type and diffusion length.

Due to their light weight, protons (H^+ or p) can be implanted much deeper into a solid than other dopant's. The depth can range up to hundreds of micrometers. A big advantage, in comparison to regular dopant's, is that without very long diffusion times at high temperatures the protons can be incorporated deep into the semiconductor. In industry, proton implantations are used in power semiconductor devices to introduce recombination centres or to form hydrogen related donor complexes. Proton implantations are also used in the 'smart cut' process to generate defects that can be used to cleave off thin wafers. The doping profiles that are produced are well known from experiment but it is not clear which defect complex is responsible for the observed charge carrier concentration profiles and carrier lifetime reductions. The implantation process itself introduces vacancies, interstitials and hydrogen into the crystal lattice. The maximum concentration of radiation damage and hydrogen is located at the projected implantation depth where most of the implanted protons stop. During the subsequent annealing step, a lot of defect complexes formed during the implantation become decorated by hydrogen that starts to diffuse away from the implantation depth. Defect complexes like VH_4 , V_2H_6 or IH_2 are formed. Additionally the incorporated vacancies, interstitials, and hydrogen can form complexes with dopant atoms (boron, phosphorus, antimony,...) which are already present in silicon before the H^+ implantation. Not all of the formed complexes are electrically active. Some of the defect complexes, however act as donors or acceptors changing the net doping concentration locally. When all implantation and defect formation effects are summarized, H^+ implantation into silicon causes n -type doping but the radiation damage itself can cause p -type doping. The acceptor doping is much stronger in oxygen lean silicon (silicon refined by the float zone process). For a controlled production of doping profiles by H^+ implantation it is

necessary to have a detailed understanding of the defect formation processes at atomic scale.

EBIC is a prominent method to investigate built-in electric fields and defects in semiconductors. Additionally, in this thesis EBIC was used to determine the local doping type and to measure the minority charge carrier diffusion length. The combination of a micro-manipulator setup in a scanning electron microscope made it possible to perform electrical measurements at high resolution. The measurement resolution was limited by the tip diameter that was in the range of about 100 nm and by the electron beam interaction volume. Schottky contacts were formed between the metal tips and the semiconductor specimen surface. These contacts were enough to detect the EBIC signal and to determine the doping type and the minority charge carrier diffusion length in the region around the Schottky contact.

EBIC was also used to investigate H^+ implanted silicon samples. At low doping concentrations, the doping type (n or p) can be determined by defect complexes incorporated by the H^+ implantation. When the doping type changes, the net doping level is very low and can not be determined reliably by measurement methods like Kelvin Probe Force Microscopy (KPFM), Secondary Electron Dopant Contrast (SEDC) or the hot probe method. The EBIC Schottky method can reliably determine the doping type down to $5 \times 10^{12} \frac{1}{\text{cm}^3}$. This is a valuable input parameter during the production process of vertical power devices where often substrate doping levels in the $10^{13} \frac{1}{\text{cm}^3}$ are used. During regular EBIC measurements no external bias voltage is applied during the measurement. To investigate the depletion behaviour of power semiconductor devices, a negative voltage was applied to visualize the behaviour of the device in the reverse bias mode. The expansion of the space charge region of the pn -junctions in the devices was investigated when the reverse bias was increased. This makes it possible to determine charge carrier concentration profiles. Super junction devices, that are conceived on the principle of charge compensation on both sides of the pn -junction, have very symmetrically doping concentration on both sides of the junction. That can be verified when the expansion of the depletion width is monitored, as the device is reverse biased. When the devices are unsymmetrically doped, the expansion of the space charge region is also unsymmetrical (expanding faster/wider in the lower doped region) when it is reverse biased.

Chapter 2

Background, fundamentals and reflection of field of research

2.1 Silicon - from quartz sand to semiconductor power devices

The earth's crust consists to about 15 weight percent of silicon compounds. Silicon is the second most common element after oxygen [1]. Especially sand mainly consists of silicon dioxide SiO_2 .

The production of silicon crystals starts with the mining of silicon dioxide in the form of sand or quartzite. Silicon dioxide is chemically reduced with coal in a melting process producing industrial raw silicon, the so called metallurgical grade silicon (MGS). During this furnace process at about 2200 K, silicon with a purity of about 98.5% can be produced [2].



For the production of poly-crystalline silicon the most popular process is the thermal decomposition of trichlorosilane. This is the so called Siemens Process, with reference to the company that carried out its development. HCl gas at temperatures between 580 and 630 Kelvin is used to form Trichlorosilane [3].



Trichlorosilane is a liquid that can be purified by distillation. After the distillation the resulting impurity concentrations (for example: B, P, Al, Fe, Cu or Au) are less than 1 ppb. Finally the purified $SiHCl_3$ is reacted with hydrogen gas at 1100°C for several hours.



The refined silicon is deposited on hot high purity silicon ingots. The poly-crystalline silicon is deposited with a very slow rate of <1mm/h [4]. With these refining processes a purity of 99.99% can be achieved [3]. Alternatively semiconductor grade silicon/poly-silicon can be

produced using monosilane (SiH_4) and the union carbide process or the ethyl corporation process [5]

For the production of micro- and nanoelectronic devices in the semiconductor device industry, mono-crystalline silicon wafers with even higher purities are required. Therefore two processes with different approaches are used: the Float zone refinement and the Czochralsky process. In reference [6] a historical overview of the silicon crystal pulling development is given. A detailed description of the two approaches is given in the following paragraphs.

2.1.1 Czochralsky process (Cz)

This method is named after J. Czochralsky [7], who determined crystallisation velocities for pulling metals out of a melt. During the Czochralsky process, silicon ingots or poles can be produced by dipping a seed crystal into a crucible of a silicon melt and slowly pulling it upwards while rotating it (as can be seen in figure 2.1). Dopant atoms like phosphorus or boron are added to the melt to adjust the doping type and dopant concentration of the crystal.

Due to the optimization of this process during the last century, nearly perfect silicon crystal wafers with a diameter of twelve inches and impurity concentrations of: oxygen ($5 - 10 \times 10^{17} \text{1/cm}^3$) and carbon ($5 - 50 \times 10^{17} \text{1/cm}^3$) can be produced. The high concentration of oxygen comes from oxygen that dissolves from the quartz crucible into the melt. Although most of the oxygen (99%) vanishes as SiO gas, a small fraction stays in the melt [8]. The high carbon concentration is caused by the fact that not all of it evaporates from the melt as CO . The impurity concentration can be a drawback for semiconductor electronics because of the increased concentration of oxygen precipitates and recombination/gettering centres. On the other hand, the high oxygen concentration results in a higher radiation stability/hardness, which makes Cz silicon a promising candidate for high energy radiation detectors [9], [10].

Magnetic Czochralsky (m:Cz) process

The magnetic Czochralsky process is an upgrade of the regular Cz process, using a strong horizontal (HMCz) or vertical (VMCz) magnetic field to minimize the mixing of the center of the silicon bath with the material close to the edge. That makes it possible to reduce the migration velocity of oxygen in the crystal. This results in a lower and more homogeneous distribution of oxygen [11].

Continuous Czochralsky (CCz) process

This method includes a second crucible, connected to the first one where the Cz silicon ingot is grown. The second crucible works as a reservoir where additional poly-crystalline silicon can be added. That makes it possible to produce longer silicon poles and larger wafer diameters using material with the same resistivity, oxygen concentration and identical thermal history [11].

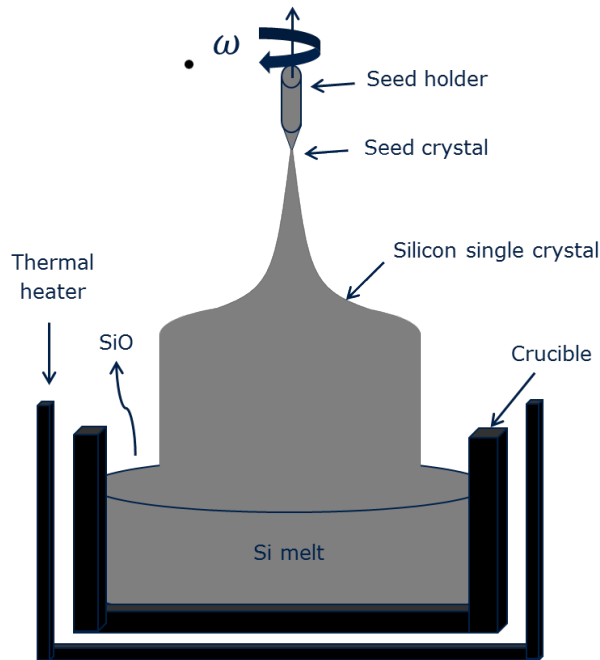


Figure 2.1: Scheme of the Czochralski method to pull single crystalline silicon from melted poly-Si.

2.1.2 Zone melting refinement process- Float zone silicon (Fz)

The zone melting refinement process was invented in 1962 by Theuerer et al. [12]. In this process a mono-crystalline seed crystal is positioned underneath a rod of poly-crystalline silicon. The crystal orientation of the future mono crystalline silicon rod is determined by the orientation of the seed crystal at the base. Keeping the seed crystal in contact with the rod, a narrow region of the rod is melted by a heater in the shape of a ring around the rod. The molten region moves from one side of the rod to the other by slowly pulling the heater ring. Most of the impurities are concentrated in the melt and thus move with the heater (as can be seen in figure 2.2). After pulling over the whole distance, the end of the rod (the region with most of the impurities) can be cut of the rod. This refinement process can be repeated several times. Due to the fact that no crucible is necessary to perform this process, the concentration of oxygen ($[O] < 10^{16}/cm^3$) and carbon ($[C] < 10^{15}/cm^3$) can be kept relatively low in comparison to Cz silicon. The doping is controlled by adding the gases phosphine PH_3 (for n -type doping) or borane B_2H_6 (for p -type doping) to the inert gas atmosphere.

The disadvantage of this method is, that until now it can only be used for a wafer diameter size up to 150 mm (8 inch). For bigger wafer diameters the process is not homogeneous enough. For some readers these differences in the material purities and oxygen or carbon concentrations might seem small. Nevertheless for several technological applications e.g. solar cells made of single-crystalline silicon refined by the Fz process can archive carrier lifetimes

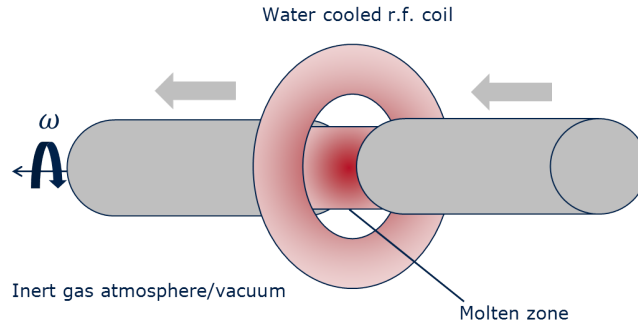


Figure 2.2: Scheme of the zone melting method. Here a molten region moves from one side of the rod to the other by slowly pulling the heater ring.

(average time it takes until a minority charge carrier recombines) up to $1000 \mu\text{s}$. In Cz silicon wafer lifetimes from $20\text{-}200 \mu\text{s}$ and in poly-crystalline silicon $1\text{-}30 \mu\text{s}$ can be archived.

2.1.3 Neutron/nuclear transmutation doping

During the zone refinement process not only impurities but also a fraction of the dopants like substitutional phosphorus or boron are transported out of the silicon ingot. The neutron transmutation provides the possibility of adjusting the n -type doping level via the transmutation of $^{30}_{14}\text{Si}$ isotope to $^{31}_{15}\text{P}$ under the release of a γ quantum



The more stable silicon isotopes (^{28}Si and ^{29}Si) that are present to a much higher percentage 92.23% (^{28}Si) and 4.67% (^{29}Si) are not affected by the neutron transmutation. Within a half-life time of about 2.6 hours and the release of a β quantum,



the silicon transmutes to phosphorus. Because of the deep penetration depth of thermal neutrons into silicon of about 100 cm , this is a very homogeneous doping mechanism. But as a neutron reactor is necessary this process is very expensive and time consuming.

2.1.4 Epitaxial silicon

Several different epitaxy methods for growing silicon on silicon substrate exist, but the most important one in industry is the vapour phase epitaxy [13]. Here for example a wafer acts as a substrate and seed crystal where the silicon is deposited as silicon tetrachloride (SiCl_4), dichlorosilane (SiH_2Cl_2), trichlorosilane (SiHCl_3) or silane (SiH_4). The typical reaction temperature is around 1500 Kelvin . Typical growth rates are in the range of $1 \mu\text{m}/\text{min}$.

2.1.5 Processing: from the wafer to the packaged chip

Semiconductor device fabrication is a process with a lot of steps using photo-lithography, chemical etching and ion implantation to create electric circuits on a wafer. Depending on the device that is produced, different substrate materials are used. For example III/V compound semiconductors like GaN or GaAs are used for novel power devices or the production of high mobility transistors. But even then, mainly sapphire and silicon are used as substrates where the actual substrate material of the future device is deposited on. To go through the whole production line of the manufacturing process until the circuit is packaged and ready to ship takes about 8 weeks. In industry the device processing is separated in two parts: the front and the back end of the production line.

FEOL - front end of line

In the front end of line a number of processes are performed, where the individual electrical devices are patterned in and on the wafer. The most important process steps are the selection and cleaning of the wafer, high temperature annealing processes, photo-lithography, etching, formation of trench structures, ion implantation or in-diffusion of dopants. It generally covers up the processes before the metal deposition [14].

BEOL - back end of line

After the front end processes there are isolated electronic structures on/in the wafer but there are no interconnections between them. In the back end of the line wires, metallic pads and contacts are formed. After the manufacturing process is done, some isolation layers are deposited over the chips and the devices get packaged.

2.2 Physical and electrical properties of silicon and semi-conductors

In this section the most important structural and electrical properties of silicon and semiconductors in general are explained. Especially the concept of the band diagram, the analytical description of intrinsic and extrinsic semiconductors, the Fermi Dirac distribution, important semiconductor properties and several other topics are explained briefly. The explanations are by far not complete, and more detailed explanations can be found in literature of Sze [13] and Kittel [15].

Very generally speaking, a semiconductor is a material with an electrical conductivity between that of an insulator and that of a metal. Their electrical conductivity can be changed by adding dopants or by applying an electric field (like in a transistor where the electrical conductivity is changed in the channel region). Generally semiconductors can consist of one element in the crystal lattice (e.g. Si or Ge) or as compounds (e.g. like GaN, SiC or GaAs).

2.2.1 Crystal structure of silicon

Silicon is a group IV element in the periodic table, it has four valence electrons in the outer electron orbital. The 1s, 2s, 2p and 3s shells are completely filled and in the 3p shell two places are occupied and four places are vacant. As shown in the right part of figure : silicon forms four covalent bonds to its neighbours with an angle of 109.5° between the bonds. This is called the sp^3 hybridisation. The left part of the figure shows silicon as it crystallizes in the diamond structure. It has two atoms in the basis, one at $(0,0,0)$ and the other one at $(\frac{1}{4}, \frac{1}{4}, \frac{1}{4})$. The crystal structure can be constructed when these two atoms are repeated on a face centred cubic Bravais lattice with a lattice constant of 5.43 angstrom.

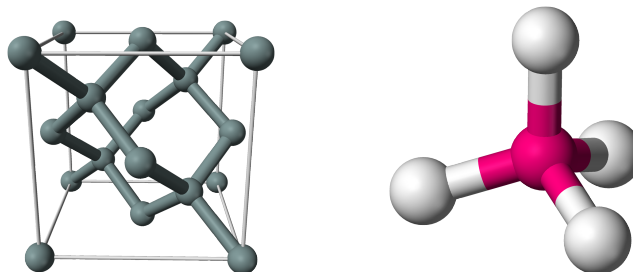


Figure 2.3: (left) Silicon crystallizes in diamond crystal cell. (right) Tetrahedral structure of silicon atoms with four covalent bonds to neighbours. Taken from references [16] and [17]

2.2.2 Electrical properties - band diagram

The electronic band structure describes the ranges of energy an electron in a solid can have in a stable configuration. The electrons are on a discrete set of energy levels called atomic orbitals around the nucleus. When several atoms are brought together to molecules, molecular orbitals are formed with different energy levels. In a solid many atoms are brought together and are interacting with each other. That means a very dense set of molecular orbitals is formed. So the energy levels in the very dense regions can be considered as continuous. These regions are called energy bands. The gaps between the bands should represent energy levels that can not be occupied by electrons at 0K.

The electrical conductivity of a material can be analysed by taking a closer look on the highest filled band of the band diagram. Electrons in delocalized states expand over the crystal lattice and result in a high conductivity. For metals this is represented by a partly filled highest occupied band in the diagram. When a band is fully occupied there is no transport of the electrons, resulting in a barrier between the highest occupied band and lowest not occupied band, the energy gap (or forbidden band). For metals the highest occupied band is partly filled. For semiconductors and isolators the highest occupied band is the valence band (VB) and the lowest not occupied band is the conduction band (CB). The energy gap between them in a semiconductor is about 1 eV. For an isolator the band gap is >3 eV. Some compound semiconductors can have band gaps in the range of isolators. GaN has a band gap of 3.4 eV at room temperature. As illustrated in figure 2.4 the filled bands represent allowed energy levels with electrons occupying them at zero Kelvin.

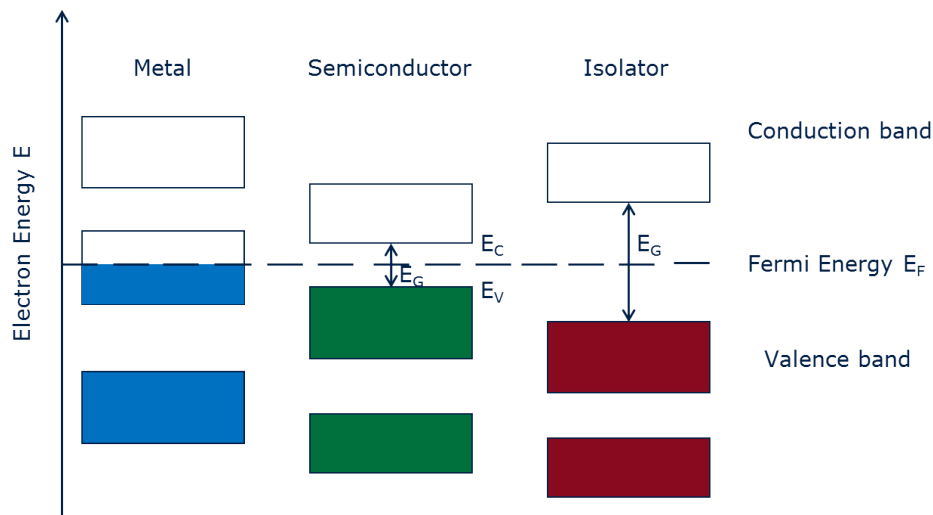


Figure 2.4: Schematic illustration of the band diagrams of metals, semiconductors and isolators.

In metals, even at low temperatures, charge carrier transport is possible because of the partly filled conduction band. For conduction in semiconductors and isolators the barrier of the energy gap has to be overcome. This can be done, e.g., via thermal excitation. For some semiconductors room temperature can be a high enough excitation for a fraction of the elec-

trons to overcome the barrier from the valence band (VB) to the conduction band (CB). The distribution of the occupied electron states depending on the temperature is described via the Fermi-Dirac equation [18], [19].

$$f(E) = \frac{1}{1 + \exp\left(\frac{E - E_F}{k_B T}\right)} \quad (2.6)$$

Here k_B is the Boltzmann constant, T is the temperature and E_F is the Fermi level (the chemical potential at zero Kelvin). At zero Kelvin every energy level underneath E_F is occupied by an electron and every state above is vacant.

2.2.3 Band structure of silicon - dispersion relationship $E(\vec{k})$

In an electron band diagram the energy (in eV) is plotted as a function of the wave vector \vec{k} . The reciprocal lattice is often used in crystallography when the periodicity of the lattice is high. Here the system is assumed to be infinite and homogeneous. The regular space lattice is transformed, via Fourier transformation, into the reciprocal space (also called k-space). E.g., a fcc crystal lattice in real space becomes a bcc crystal lattice in reciprocal space via Fourier transformation. When the energy is plotted as a function of the electron momentum, the motion of the electrons in the different crystal directions can be shown. This is known as the dispersion relationship. Figure 2.5 shows the simulated dispersion relationship of silicon. The simulations were performed by K. Unger (Graz University of Technology) using the simulation software Wien2k [20]. The simulated energy gap is 0.59 eV, but 1.12 eV in reality. The simulations are obviously far off from well known results from literature. Nevertheless the shape of the energy bands and the band splitting has the same shape as the values published in literature [13]. As can be seen, silicon is an indirect semiconductor where the maximum of the VB and the minimum of the CB do not have the same \vec{k} value. An electron cannot be excited from the VB to the CB without changing momentum. That means phonons (lattice vibrations) are necessary to transport an electron from the top of the VB to the bottom of the CB.

G is defined as the maximum of the valence band. To distinguish how easy it is for charge carriers to move through the crystal the dispersion relation is plotted for different crystal directions (e.g. from Γ to L, X). When the curvature of the CB is very high, the effective mass m^* of the electron in one direction is very light and it is easy for the electron to move in this direction. The effective mass is defined as

$$m^* = \frac{\hbar^2}{\frac{d^2 E(\vec{k})}{dk^2}} \quad (2.7)$$

In general the effective mass is used to describe the response of electrons to external forces in the particle picture. Due to the spin-orbit-coupling, the valence band splits into heavy hole, light hole states, and a split off state separated by the spin orbit splitting energy as can be seen in figure 2.5. In the table 2.1 the most important electron band properties, like the longitudinal, transverse, heavy hole, light hole and split off hole band effective masses are listed. The values of silicon are compared to germanium.

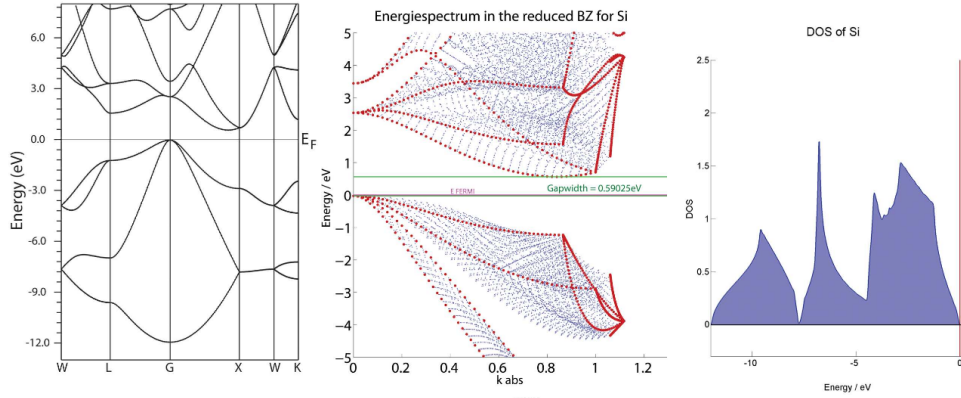


Figure 2.5: Simulated dispersion relationship (left and middle figure) and density of states (right) of silicon. The energy levels of the bands are plotted over the reciprocal space vector k . Taken from reference [21] with permission.

Table 2.1: List of the band gap energies and different effective masses of silicon compared to germanium

Name	Symbol	Silicon	Germanium
Band gap energy	E_g [eV]	1.12	0.66
Longitudinal effective mass	$m_{e,l}^*/m_0$	0.98	1.64
Transverse effective mass	$m_{e,t}^*/m_0$	0.19	0.082
Longitudinal direction		(100)	(111)
Heavy hole band effective mass			
Effective mass	m_{hh}^*/m_0	0.49	0.28
Light hole valence band maximum at $k = 0$			
Effective mass	m_{lh}^*/m_0	0.16	0.044
Split-off hole valence band maximum at $k = 0$			
Effective mass	$m_{h,so}^*/m_0$	0.29	0.084

Here $m_0 = 9.11 \times 10^{-31}$ kg is the free electron rest mass. The higher slope of the light hole band compared to the heavy hole band results in a lower effective mass of the holes in the light hole band. This results in a faster/stronger response to a potentially applied electric field. Due to the wave particle dualism it should be stated that electrons move like waves but exchanges energy and momentum like particles [15]. Due to the fact that silicon is an indirect semiconductor, always also phonon's have to participate to realize charge transport over the minimum band gap.

2.2.4 Analytical description

Intrinsic semiconductors

A very important factor for the description of semiconductors is the free charge carrier concentration. The free charge carriers contribute to the charge transport and thus define the conductivity of the semiconductor. The probability that an energy level is occupied is given by the Fermi-Dirac distribution function (equation 2.6). The probability that an energy state at the Fermi level (E_F) is occupied is exactly 50% in thermal equilibrium. The concentration p of free holes in the valence band and the concentration n of free electrons in the conduction band can be calculated via:

$$n = \int_{E_C}^{\infty} dE \cdot D_C(E) \cdot \frac{1}{1 + \exp\left(\frac{E - E_F}{k_B T}\right)} \quad (2.8)$$

$$p = \int_0^{E_V} dE \cdot D_V(E) \cdot \frac{1}{1 + \exp\left(\frac{E_F - E}{k_B T}\right)} \quad (2.9)$$

here $D(E)$ is the density of states in the respective bands. E_C and E_V are the band edge energies of the conduction and the valence band, respectively, the density of states can be calculated by

$$N(E) = \frac{\pi}{2} \cdot \left(\frac{2m^* L^2}{\hbar^2 \pi}\right)^{3/2} \cdot \sqrt{E - E_C} \quad (2.10)$$

here L is the length of the area. The effective density of states in the VB and in the CB are

$$N_C = 2 \cdot \left(\frac{m_e^* k_B T}{2\pi \hbar^2}\right)^{3/2}, \quad (2.11)$$

$$N_V = 2 \cdot \left(\frac{m_h^* k_B T}{2\pi \hbar^2}\right)^{3/2}. \quad (2.12)$$

For intrinsic semiconductors the law of mass action can be derived by the multiplication of the concentration p of free holes in the VB and the concentration n of free electrons in the CB:

$$np = N_C \exp\left(\frac{E_F - E_C}{k_B T}\right) N_V \exp\left(\frac{E_V - E_F}{k_B T}\right). \quad (2.13)$$

The values of the conduction band energy and valence band energy cancel out giving

$$np = N_C N_V \exp\left(\frac{-E_g}{k_B T}\right). \quad (2.14)$$

The law of mass action as it is commonly known:

$$n = p = n_i = \sqrt{N_C N_V} \exp\left(\frac{-E_g}{2k_B T}\right) \quad (2.15)$$

where n_i symbolises the intrinsic charge carrier concentration. Using the formulas for the effective density of states, the Fermi-Dirac distribution, and the law of mass action the intrinsic Fermi level $E_{F(intr)}$ can be calculated:

$$E_{F,intr} = \frac{E_C + E_V}{2} + \frac{k_B T}{2} \ln\left(\frac{N_V}{N_C}\right). \quad (2.16)$$

This formula shows the temperature dependency of the Fermi energy for intrinsic semiconductors.

Extrinsic semiconductors

When impurities are introduced into the semiconductor to change the electric conductivity also the formulas to calculate the values of n , p or E_F change. These formulas and their derivations can be looked up in literature (e.g. Sze et al. [13]) For intrinsic semiconductors n equals p and the conductivity is strongly temperature dependent. For extrinsic semiconductors n is not equal to p and the conductivity is nearly temperature independent. This is true at least in the operation temperature range of semiconductor devices. With increasing temperature at some point in a semiconductor the intrinsic free charge carriers become dominant again. The number of ionized impurities can be calculated by the following formulas

$$N_D^+ = \frac{N_D}{1 + 2 \exp\left(\frac{E_F - E_D}{k_B T}\right)} \quad \text{and} \quad N_A^- = \frac{N_A}{1 + 4 \exp\left(\frac{E_A - E_F}{k_B T}\right)}. \quad (2.17)$$

whereby N_D is the donor density, N_A the acceptor density brought into the semiconductor, N_D^+ is the ionized donor density and N_A^- is the ionized acceptor density. The factor 2 or 4 in the denominator depends whether materials with light holes or heavy holes are used. Due to the controlled activation of the incorporated impurities $N_D^+ = N_D$ and $N_A^- = N_A$ (nearly all donors/acceptors are ionized). And after all the charge neutrality condition has always to be fulfilled

$$n + N_A^- = p + N_D^+. \quad (2.18)$$

2.2.5 Important material properties of semiconductors

In this subsection the most important semiconductor properties should be explained briefly. These parameters are important for the production of semiconductor devices from substrate materials. Depending on the purpose of the device material properties are more important than others.

Resistivity ρ and Conductance σ

The electrical resistivity ρ is also known as the specific electrical resistance of a material and quantifies the amount of current flowing through an area A of a material with a electrical resistance R with a length l via

$$\rho = R \cdot \frac{A}{l} \quad \text{in} \quad [\Omega \text{ cm}] \quad (2.19)$$

The conductance σ is the inverse of the resistivity

$$\sigma = \frac{1}{\rho} \quad \text{in} \quad [(\Omega \text{ cm})^{-1}] \quad (2.20)$$

During the manufacturing step of mono crystalline silicon the resistivity can be modulated via the doping process. High concentrations of dopants result in a low resistance and resistivity of the semiconductor material.

Minority charge carrier diffusion length L and charge carrier lifetime τ

The minority charge carrier diffusion length L is the length that e.g. a generated excess charge carrier can move in the semiconductor material until it recombines or reacts somewhere else. In crystalline semiconductors the diffusion length can be very high, e.g., 100-300 μm in single crystalline silicon. It can be reduced dramatically by the incorporation of defects/recombination centres.

The charge carrier lifetime τ is the time period it takes until a generated excess charge carrier recombines. It is closely related to the diffusion length via the diffusivity constant D [cm^2s^{-1}]:

$$L = \sqrt{D\tau} \quad \text{in } [\mu\text{m}]. \quad (2.21)$$

Electron/hole mobility μ

The mobility μ quantifies the value of how fast an charged particle like an electron or holes moves though a semiconductor when an electric field E is applied. The motion of a charged particle due to an electric field is called drift motion. The drift velocity v_d is

$$v_d = \mu \cdot E \quad \text{in } \left[\frac{\text{cm}^2}{\text{Vs}}\right]. \quad (2.22)$$

The conductivity is related to the mobility via the density of electrons n and holes p and the elementary charge e

$$\sigma = e(n\mu_e + p\mu_h) \quad (2.23)$$

here μ_h is the hole mobility, μ_e is the electron mobility.

Einstein relation

The Einstein or Einstein-Smoluchowski relation [22],[23] enables the connection of some of the previously mentioned material properties

$$D = \frac{\mu k_B T}{q} \quad (2.24)$$

where q is the electrical charge of a particle, D is the diffusion constant and μ is the charge carrier mobility. Bringing in the equation for the diffusion length and lifetime

$$L = \sqrt{D\tau} \quad (2.25)$$

by replacing the diffusivity constant by $\frac{L^2}{\tau}$ the most important semiconductor properties discussed in this thesis are combined in one equation.

$$\frac{L^2}{\tau} = \frac{\mu k_B T}{q} \quad (2.26)$$

The charge dopant concentration dependency of the charge carrier mobility is shown in figure 2.6. As can be seen, the mobility of electrons and holes in silicon reduces dramatically for high doping concentrations. For lower doped silicon the electron mobility μ_e becomes constant around 1400 $\frac{\text{cm}^2}{\text{Vs}}$ and the hole mobility at about 400 $\frac{\text{cm}^2}{\text{Vs}}$.

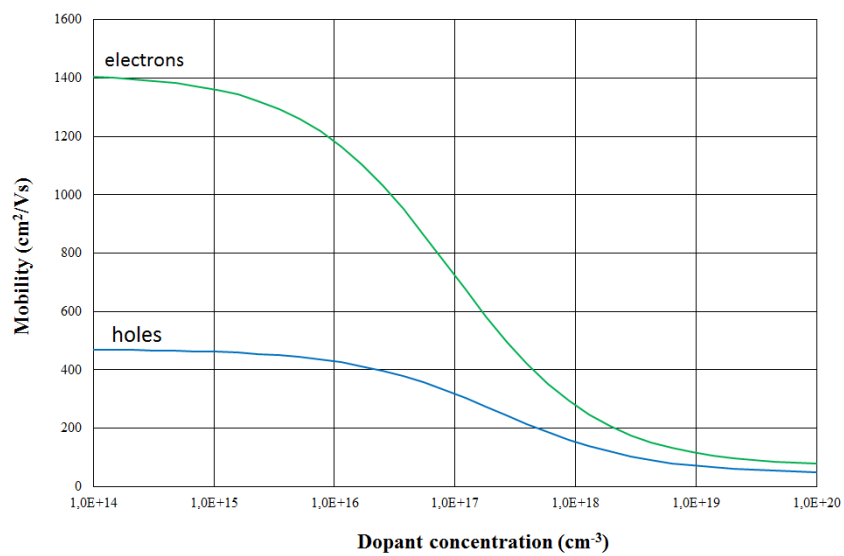


Figure 2.6: Doping concentration dependency of charge carrier mobility. According to Bart Van Zeghbroeck [24].

2.3 Defects

Solids that crystallize in a periodic pattern such as the body centred cubic (bcc), simple cubic (sc), or face centred cubic (fcc) structure, seem to have a perfect structure. In reality every real solid is disturbed in its periodicity by defects or impurities. There are four different types of defect groups: point defects, line defects, planar defects, and volume defects. For instance, small concentrations of defects can have a big influence on the electrical or mechanical properties. Like in the doping process where already small concentrations of boron or phosphorus in silicon can change the electrical conductivity dramatically.

2.3.1 Point defects

Point defects are spacial isolated defects situated on very few lattice sites in the unit cell of the lattice. Point defects can be created due to particle irradiation, deformation and or high temperatures treatments. Furthermore they can be incorporated during the crystal growth or manufacturing process. In general, vacancies, interstitials and substitutional atoms are the most common imperfections. The most prominent point defects are schematically visualized in figure 2.7.

Schottky defect/Vacancy: vacancies are vacant lattice sites which would be occupied in a perfect crystal. A vacancy is created by the transfer of an atom from the lattice to the surface of the crystal.

Interstitial: self interstitials are atoms (of the regular crystal lattice) that occupy a site in the crystal structure at which there is usually no atom. In general, interstitials can also be impurity atoms occupying an interstitial site.

Frenkel pair: a nearby pair of a vacancy and an interstitial is often called a Frenkel defect or Frenkel pair. This is caused when an ion moves into an interstitial site and creates a vacancy.

Antisite defects: occur in an ordered alloy or compound (and are not relevant in silicon or this work). When the atomic structure consisting of atoms A (in the center of the cubic) and B (in the edges of the cubic) is flipped. So one atom A is on a place where normally a B atom sits.

Substitutional impurity atom: is an atom different from the atoms of the bulk material embedded at a lattice site normally occupied by a bulk atom. Often small atoms from the first and second period, especially H,C,N or O constitute substitutional impurities.

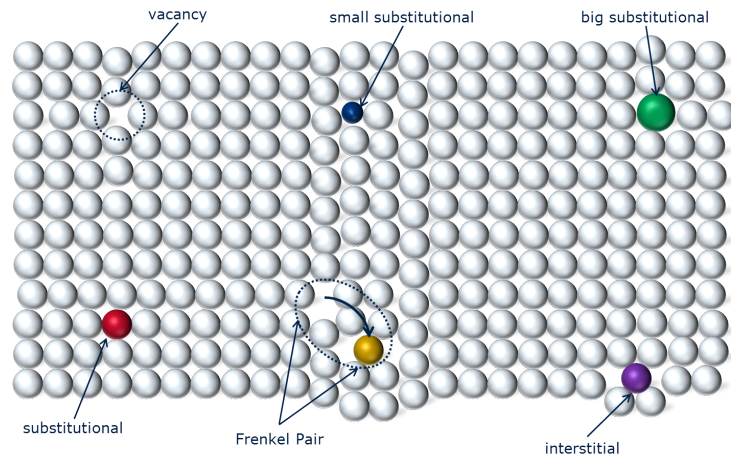


Figure 2.7: Illustration of the most important point defects in solids (vacancy, interstitial, substitutional, Frenkel pair).

2.3.2 Line defects - dislocations

Line defects are typically called dislocations. In general there are two different types: the edge- and the screw dislocation. Dislocations are characterized by the dislocation line \mathbf{v} and the Burgers-vector \mathbf{b} . For an edge dislocation these two vectors are perpendicular to each other, for a screw dislocation they are parallel to each other.

2.3.3 Planar defects - plane defects

Planar defects include all grain boundaries, phase boundaries and stacking faults.

2.3.4 Volume defects

Volume defects, also called voids, form because of the agglomeration of point defects (an agglomeration of vacancies in the case of voids/ gas pockets), or come from dust particles entrapped in the crystal.

2.3.5 Intrinsic defects in silicon

As mentioned above, the manufacturing process of mono-crystalline silicon is highly optimized, nevertheless there are varying concentrations of intrinsic defects present in the nearly perfect crystal lattice. Depending on the manufacturing process and the doping process the concentrations of oxygen, carbon, boron or phosphorus changes by some orders of magnitude.

Simple defects like vacancies (V) and self interstitials (I) can form a range of defect complexes with impurities (e.g. O, C, N) or dopants (e.g. B, P, Sb, As). Prominent complexes that were intensively studied like the A-center [25], [26] which represents an oxygen-vacancy (VO) complex or the E-center (group five element (phosphorus) - vacancy complex [27], [28]) that represents an phosphorus-vacancy complex should be mentioned.

2.4 Acceptor and donor levels in silicon

This section relies on the works of M. Moll [11] and A. Junkes [29]. Electrically active defect complexes in semiconductors can have a strong influence on the material properties of silicon. They can have charge states in the band gap acting as donor or acceptors. In general the complexes can be charged neutral, negative, or positive. Some defects like the thermal double donor (TDD) [30], [31] complex can also be double ionized. In figure 2.8 the energy levels of defect complexes are marked by horizontal lines. The charge state is labelled by minus, plus or \circ signs representing the neutral charge state. Some defect complexes can have several charge states in the band gap, they are called amphoteric. Shallow donors or acceptors are complexes with energy levels close to the conduction band or valence band respectively. Deep levels are the energy levels around the middle of the band gap. At moderate temperatures the very shallow levels have a high probability (according to the Fermi-Dirac distribution) to be ionized and thus contribute to the effective doping concentration of the semiconductor.

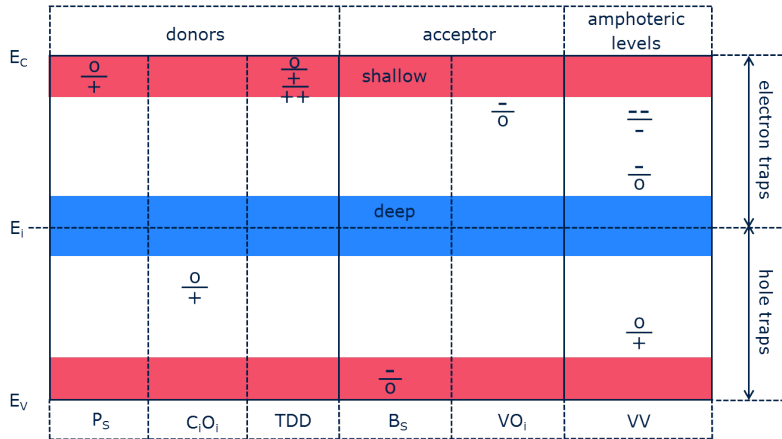


Figure 2.8: Electron Band diagram visualizing deep and shallow traps for electrons and holes. Some prominent acceptor, donor and amphoteric defects in silicon are shown with their levels in the band gap. Figure was generated according to reference [29].

The ionization energy ΔE_i needed to ionize a defect complex i.e., to emit an electron into the conduction band or a hole into the valence band is defined as the difference between the respective band edge and the energy level of the defect (trap level). For donors $\Delta E_t = E_C - E_t$. For acceptors $\Delta E_t = E_t - E_V$. Donors are in general defined as neutral, if filled with an electron and as positive charged when the electron is emitted. An acceptor is charge neutral when empty and negative when filled with an electron. The charge state of a defect depends on the Fermi level (E_F). If the Fermi level is above the defect levels acceptors are charged neutral and donors are positively charged (ionized). If the Fermi level is beneath the energy levels of the complexes, acceptors are negatively charged (ionized) and donors are charged neutral.

2.5 Hydrogen implantation process

This section relies on the works of M. Moll [11] and J. G. Laven [32]. During the semiconductor manufacturing process, impurities are intentionally incorporated into the high purity semiconductor to modulate its electrical properties. A small number of dopant atoms can cause big changes in the electrical properties of the semiconductor. When one dopant atom is added per 100 million silicon atoms the doping is called low or light. When many more dopant atoms (one per ten thousand atoms) are added, the doping is called high or heavy. Silicon is a group IV element and has four valence electrons, by doping pure silicon with group V elements like phosphorus or arsenic an extra unbound valence electron is added to the lattice and results in an *n*-type semiconductor. Doping the silicon lattice with group III elements like boron, that have in comparison to silicon a missing valence electron, creates a *p*-type semiconductor. Due to the incorporation of additional free electrons (*n*-type) or holes (*p*-type) in the silicon lattice the electrical conductivity changes. The electrically activated group V and group III elements are called donors or acceptors respectively.

There are several possibilities to realize the doping process. As mentioned, in the chapter about silicon crystal growth, dopant atoms can be added during the growth process of the ingot to achieve a uniform dopant concentration over the whole ingot. Alternatively to produce small regions of different doping concentration or type they can be injected in selected areas by diffusion or ion implantation. Because of the good controllability the process of ion implantation is very popular. During this process dopant ions are accelerated, by an electric field, and are implanted into a target wafer. This is followed by a thermal annealing step to activate the implanted dopant's and to anneal out the damage that was produced during the implantation. In the following subsection the mechanism of ion and especially hydrogen implantation will be explained.

2.5.1 Hydrogen implantation process

During the ion implantation process, ions of material A, in our case ionized hydrogen (H^+), are accelerated in an electric field and implanted into a target material B (silicon). The whole process causes a lot of damage and structural changes in the target crystal lattice. In this section the proton implantation mechanism will be explained.

Actually, from outside an ion implanter looks like a grey metal box where parameters like the implantation energy, the implantation dose or the implantation current can be adjusted. The schematic structure of a proton implanter is shown in figure 2.9. For proton implantations, the source chamber is filled with H_2 gas. A tungsten cathode serves as an electron source and ionizes the gas molecules. Neutral H atoms and an negatively charged H^- ions are formed. In the pre acceleration system the H^- ions are accelerated towards a tandetron accelerator system. After this acceleration they go into a charge reversal cell (typically filled with N_2 or Ar gas), that changes the polarity of the hydrogen ion from H^- to H^+ . This makes it possible to accelerate the ions a second time in the tandetron accelerator. After full acceleration the ions are focused by an electromagnetic lens system. This deflection system makes it possible to implant the wafer exactly at the desired positions with the required implantation dose. The whole implantation system is under high vacuum with pressures ranging from 10^{-5} to 10^{-7} mbar. The implantation energy of the protons can be varied by the adjustment of the electric field in the tandetron accelerator. The implantation current that determines the implantation

dose can be adjusted by the gas flow and the ionization energy of the electrode that ionizes the gas molecules respectively.

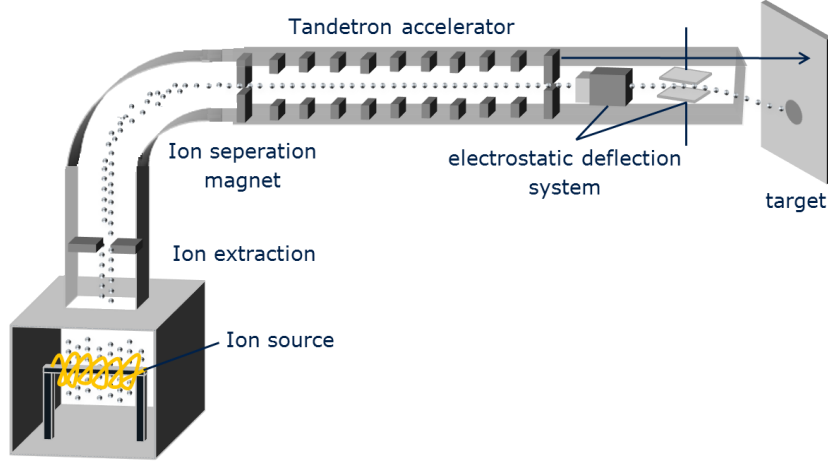


Figure 2.9: Schematic structure of a tandetron proton implanter. Showing all the important components from the ionization, acceleration and implantation. Drawn according to references [33] and [34].

2.5.2 Analytical analysis of proton implantation process

It is important to understand the implantation process properly to be able to predict the resulting implantation profiles that will be discussed in later sections. When the high energetic particles are decelerated in the target material, inelastic and elastic collisions with electrons and nuclei take place. Elastic collisions result in a direct transfer of the kinetic energy. The energy is conserved in an elastic collision. Inelastic collisions take place via ionization or via the emission of Bremsstrahlung (highly energetic photons). There is also an interesting dependency of the energy of the implantation ion and the deceleration mechanism: for very low energies the deceleration due to elastic nuclei interaction S_n dominates slightly. For higher energies up to the high MeV region the inelastic electronic deceleration S_e dominates.

$$S_{e,n} = -\frac{1}{N} \left(\frac{dE}{dx} \right)_{e,n}, \quad (2.27)$$

hereby N is the density of the target material and E is the energy. The total energy loss over the distance is

$$\frac{dE}{dx} = -N [S_n(E) + S_e(E)]. \quad (2.28)$$

The medium depth R (projected implantation depth) an accelerated particle will be implanted into the target material is defined as

$$R = \frac{1}{N} \int_0^{E_0} \frac{dE}{S_n(E) + S_e(E)}, \quad (2.29)$$

here E_0 is defined as the starting energy of the accelerated ion. The ion implantation depth and distribution can be simulated using Monte Carlo simulations as explained in the subsection about SRIM/TRIM. During the implantation channelling can take place. If the implantation direction is parallel to the crystal lattice, the ions can penetrate into the crystal lattice without a lot of collisions with crystal atoms and are mainly electrically decelerated. If the implantation direction is tilted at least a few degrees from the crystal plane direction a lot of random collisions occur.

2.5.3 Implantation damage

During the implantation process, the target material is damaged by the penetrating ions. Depending on the mass and energy of the ions, target material atoms are shifted from their regular position in the crystal lattice. The number N_d of Frenkel pairs generated in the crystal lattice can be estimated using the Kinchin-Pease formula:

$$N_d = \frac{E_0}{2E_d} \quad (2.30)$$

here E_0 is the loss of energy of the accelerated penetrating ion. E_0 can be the total energy of the ion but it can also just be a fraction of it. E_d is the threshold energy necessary to form one Frenkel pair.

Non ionising energy loss (NIEL)

In general the radiation damage created can be differentiated using the Non Ionising Energy Loss (NIEL) hypothesis. This describes the fraction of energy loss of the penetrating ion due to atomic displacements. An important assumption of this theory is that the dissipated energy scales linearly with the amount of generated damage. More details about NIEL can be found in the work of M. Moll [11].

Hardness factor

The NIEL theory defines a specific hardness factor for every material. This makes it possible to compare damages in various materials with the damage resulting of 1 MeV neutrons penetrating into some material. It is not consistent for all sorts of particles or energies but at least it was a benchmark e.g., the concentration of oxygen was found to be a critical factor concerning the hardness of the silicon.

2.5.4 The annealing process - defect migration and formation

The annealing step is a very important step to get rid of radiation damage after the implantation process and to electrically activate the incorporated dopant atoms. When potential dopant atoms are incorporated into the silicon crystal lattice for example via implantation they are oriented somehow in the lattice and might not be electrically active right now. During the anneal the dopant's can move into a silicon lattice position and become electrically active.

There are several possibilities to perform the annealing process. A common method is to put silicon wafers into an oven at high temperatures under inert gas atmosphere. For example to diffuse in a shallow boron implantation deeper into silicon, the wafers are annealed at temperatures around 1000 °C for several hours to diffuse the dopant atoms in and electrically activate them. Alternatively, Rapid Thermal Annealing (RTA) can be used. Here the wafers are illuminated by lamps that make it possible to increase the temperature in the wafer by several hundred Kelvin in a few seconds.

Defect migration, formation, and dissociation

At room temperature the defects in the crystal lattice are nearly immobile and migration takes place very slowly. The annealing process can be used to investigate the accelerated migration of these defects. Due to migration, defects can form complexes with lattice atoms or other impurities when the formation barrier is not too high, e.g., due to the migration of vacancies $V+Si_i \rightarrow Si_s$. Defect complexes might also dissociate at higher temperatures (high energetic phonons). Parts of the former complex might then migrate through the lattice until they get trapped. In Fig. 2.10 the schematic energetic process of migration, defect formation and dissociation are demonstrated.

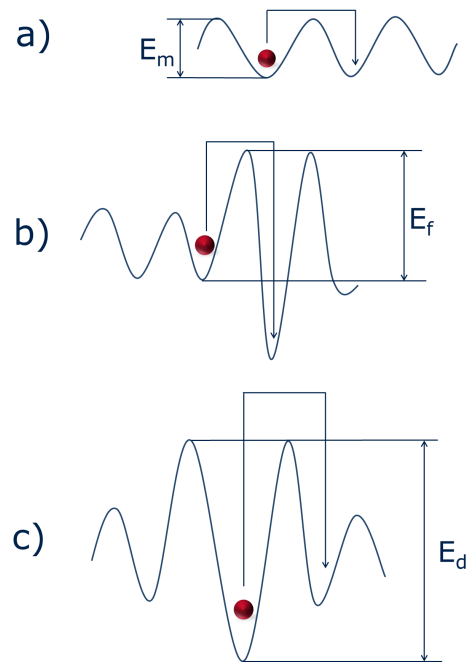


Figure 2.10: Schematic energetic process of migration, defect formation and dissociation. According to reference [11].

It is important to understand that for all these processes it is necessary to overcome some energy barrier: to migrate, to form a complex as well as to dissociate. Fig. 2.10 a) shows that an energy barrier E_m has to be overcome to migrate to the next position. In Fig. 2.10 b) the formation energy E_f has to be overcome to form an energetically more favourable complex. For the dissociation shown in Fig. 2.10 c) the defect complex will overcome a energy barrier E_d .

2.5.5 Reaction-diffusion equations

To understand formation, dissociation and diffusion mechanisms of complexes in semiconductors, a set of reaction-diffusion equations has to be found and solved. The reaction equations provide the reaction rate constants of the relevant defect complexes formed. The diffusion equations yield the diffusion coefficients and activation energies of the different species. Combining these equations it is in principle possible to get the spatially resolved charge carrier concentration due to the formation/diffusion of the electrically active complexes.

The formation and dissociation of a defect complex from two migrating complexes [X] and [Y] during the anneal can be described by



The diffusion equation of the complex X, where [X] stands for a concentration of the respective complex, is

$$D \frac{\delta^2 [X]}{\delta r^2} = \frac{\delta [X]}{\delta t} + G + R, \quad (2.32)$$

where G is the formation term, R is the dissociation term and D is the diffusion coefficient

$$D = D_0 \cdot \exp \frac{-E_m}{k_B T} \quad (2.33)$$

where D_0 is the diffusion prefactor, E_m is the activation energy for the diffusion, k_B is the Boltzmann constant and T is the temperature. The formation term G for the formation of a complex XY is defined as

$$G = \frac{\delta [XY]}{\delta t} = k \cdot [X][Y] \quad (2.34)$$

where [X] and [Y] are the concentrations of the present single elements X and Y, and k is the temperature dependent reaction rate

$$k = k_0 \cdot \exp \frac{-E_F}{k_B T}. \quad (2.35)$$

The dissociation term R of a complex XY into its single elements X and Y is defines as

$$R = \frac{\delta [X]}{\delta t} = k[XY] \text{ and } \frac{\delta [Y]}{\delta t} = k[XY], \quad (2.36)$$

where k is the reaction rate constant for this process. To get all the reaction rates, the reaction equations have to be solved. In general the reaction equation for a complex X_i is

$$\frac{\delta [X_i]}{\delta t} = k_{i,j} [X_j] + k_{i,j,l} [X_j, X_l] + k_{i,j,l,m} [X_j, X_l, X_m] + \text{etc.} \quad (2.37)$$

The rate values $k_{i,j}$ and $k_{i,j,l}$ determine the reaction rates to form X_i complexes from different single elements or smaller complexes. $k_{i,j}$ is the first order reaction rate constant and

$k_{i,j,l}$ is the second order reaction rate constant to form a complex X_i from the elements X_j or X_j and X_l .

The time evolution of the concentrations of the defect complexes can be described by a set of reaction-diffusion equations:

$$\frac{\delta[X_i]}{\delta t} = D_i \nabla^2[X_i] + \sum_j k_{i,j}[X_j] + \sum_{j,l} k_{i,j,l}[X_j, X_l] + \sum_{j,l,m} k_{i,j,l,m}[X_j, X_l, X_m] + \text{etc.} \quad (2.38)$$

The reaction rates during an anneal can be determined when the concentrations of the single complexes before and after an anneal are measured and compared. The diffusivity prefactor D_0 and activation energy E_A can be determined when several anneals are performed at different temperatures (at least three temperatures). The effective diffusion coefficient can be determined from isothermal anneals. The activation energy and the diffusion prefactor can be determined when at least three isothermal annealing series are performed at three different temperatures. When the reaction rate, the value of the diffusivity prefactor D_0 and the activation energy E_A for every single complex are put in the diffusion equation, the equation can be solved resulting in spatially resolved concentration profile of the complex. When this is performed for all, potentially interesting, electrically active defect complexes, their concentrations can be summed up. The resulting effective charge carrier concentration should be comparable with the experimental values for the local charge carrier concentration resulting from SRP.

It should be stated at this point, that the defect complexes formed during the reaction-diffusion processes (like the hydrogen donor complexes) during annealing and cooling down, are typically not in thermodynamic equilibrium. Intrinsic point defects like vacancies might be in thermodynamic equilibrium in some crystal lattices, but for extrinsic defect complexes this is not true in general. At some annealing processes light elements might diffuse out of the sample.

2.5.6 Defect evolution

Some well understood defect evolution mechanisms for carbon, vacancies, and oxygen are explained in this subsection. In carbon rich silicon the reaction of substitutional carbon C_s with interstitial silicon Si_i is an important process to reduce the number of interstitials.



The interstitial carbon C_i is mobile at room temperature and mainly forms $C_i C_s$ and $C_i O_i$ pairs. Vacancies that are not part of a frenkel pair might form di-vacancies



in oxygen rich silicon the creation of vacancy oxygen pairs is also a very probable reaction. The defects are called A-centres.



In phosphorus doped Fz silicon the mobile vacancies may also react to so called E-centres with phosphorus.



2.6 Oxygen related thermal donors (OTD) in silicon

Oxygen related thermal donors are a family of electrically active donor defect complexes containing one or more oxygen atoms. This is a very well investigated scientific topic. For the last 40 years a lot of research has been performed on the investigation of the electrical and structural properties of this special donor family. Most of the investigations were performed on oxygen rich silicon produced by the Cz process. Besides density functional theory (DFT) simulations, mainly Fourier Transform Infra Red Spectroscopy (FTIR), Electron Spin Resonance (ESR) and Deep Level Transient Spectroscopy (DLTS) measurements were performed to analyse the defect structure or the electrical properties of the donor complexes. This section gives an short overview over previous scientific work and the status quo.

The term 'thermal' in thermal donor comes from the fact that this family of donor complexes becomes electrically activated in an annealing step. In general oxygen related thermal donors (so called OTD-complexes) are a family of electrically active (donor) complexes containing one or more oxygen atoms. So they are of special interest in samples with a high oxygen concentration, like in Cz or m:Cz silicon. During the manufacturing process of semiconductor devices, several annealing steps are necessary. During these anneals, the oxygen may combine into complexes that act like donors. If the silicon is lightly doped, such as for example a power transistors or photo-detectors, the thermal donors may contribute significantly to the overall doping. Due to the formation and activation of this donor species at temperatures between 400 and 600 °C the charge carrier concentration of the wafer may change. For low doped *p*-type starting materials, the majority charge carrier type might change due to the formed OTDs.

The first time thermal donors were reported was in 1955 by Fuller et al. [35], performing heat treatment, IR- and resistivity measurements. It was proposed that the thermal donors are SiO₄. Despite extensively criticized from parts of the community from the beginning the structural model was accepted for several years. In the following years numerous models concerning the structure and the formation mechanism of thermal donors annealed in the temperature range around 450°C have been proposed. For example thermal donors were suggested to be substitutional oxygen atoms [36], SiO₂, SiO₃ and SiO₄ [37], or, one substitutional and three interstitial oxygen atoms [38]. In 1964 a study was published that suggested the formation of SiO₂ and SiO₃ acceptors and SiO₄, SiO₅, SiO₆ donors [39]. Further on it was assumed TDs consist of an substitutional oxygen atom and a vacancy [40]. In 1979, for the first time, the assumption was made that there could be single and double donors [41], [42]. In 1981 the existence of two [43] and more oxygen donors was measured [44], [45]. In 1982 the fast diffusion of O₂ molecules was measured and the formation of an O₄ donor complex was assumed [46]. Also the role of carbon, that might reduce the formation of thermal donors was first investigated. With high carbon concentrations the TD formation rate was smaller and the maximum reached concentration was lower [47]. In 1983 nine distinct thermal double donor complexes were reported [48].

In an early work of Suezawa et al. (1984) the nature of thermal donors in silicon was investigated by FTIR measurements [49]. The analysis of formation processes of various kinds of thermal donors brought up the concept that thermal donor complex TD1 to TD6 consist of an increasing number of oxygen atoms. According to this concept, the complex TD1 consists of three oxygen atoms. In the complexes TD2 - TD6, four to eight oxygen atoms are involved. In 1984 Ourmazd et al. proposed that the oxygen related thermal donors are aggregations of oxygen atoms. A new structural and kinetic model was presented in their work, assuming O_xSi

structures of the TD structures [50] that can be attributed to the work in [48]. The formation rate of the TDs was reported to be:

$$\frac{dN}{dt} = k_f \cdot c_O^{4.4} \quad (2.43)$$

where k_f is a formation constant and c_O the initial oxygen concentration of the silicon substrate. Conclusive evidence for the role of oxygen in the thermal donors complexes was given by electron nuclear double resonance (ENDOR) measurements [51]. In 1988, during the anneals at 465 °C the formation of intermediate defect complexes (IDC) parallel to $\langle 110 \rangle$, like the ribbon-like defects (RLD) reported in [52] have been observed. Additional defects form parallel to the 111 plane [53], [54]. In the work of Wagner et al the incorporation of three oxygen atoms in the core of a thermal donor was reported, but no silicon atom in the center of the defect [30]. In this work ground state binding energies from 50-70 meV were reported for the ground state and 114-156 meV for the first ionized state. Additionally the increasing binding energy of the thermal donors indicates an increasing defect size. Due to anneals around 470 °C [55], 500 °C and 600 °C [56] the formation of additional donors was reported. Until then 16 donors were reported. According to theoretical simulation possible core structures of the thermal donors are: V-O₂, V-O₄ or interstitial O₂. The symmetry of all these centres is C_{2v}, what would be consistent with the TD centers. (V-O₂²⁺ seems to be a more stable candidate than the interstitial (O-O)²⁺ complex, but at low annealing temperatures the O-O complex might be the dominant core complex [57]. According to the work of Newman et al. [58] and McQuaid et al. [59] the thermal donor structures TD1-TD16 differ from each other by an oxygen dimer (O₂). That means TD(x) plus an oxygen dimer form TD(x+1).

In the work of D. J. Chadi et al. from 1996 the core structure of thermal donors in Si and Ge as well as the different structures of oxygen atoms to form a core structure for the formation of the thermal donors were simulated. Their conclusion was that in silicon, the core consists of an O₃ complex that shows bi-stability and has a lower total energy than the three isolated oxygen interstitials themselves [60]. In figure 2.11 potential core complexes of thermal donors in silicon according to D. J. Chadi et al are shown.

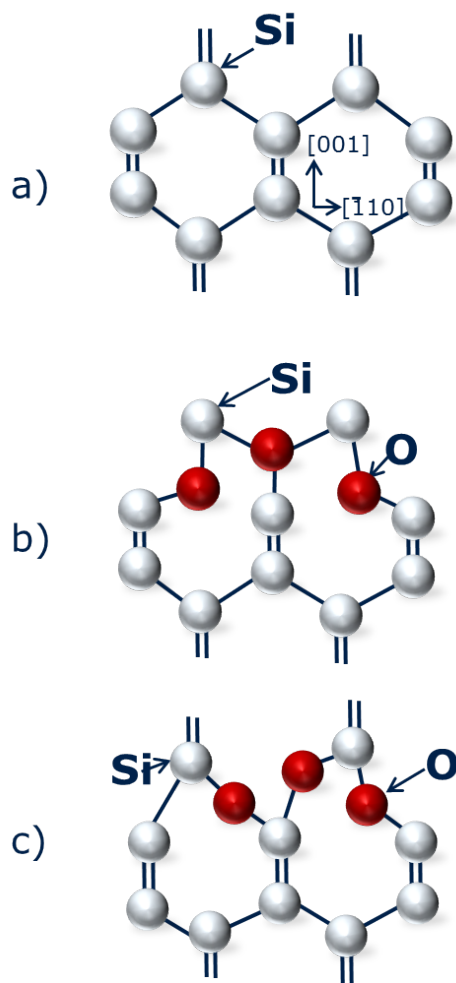


Figure 2.11: a) Projection of silicon lattice on the (110) plane b) O_3 core complex of a thermal donor c) Stable and electrically inactive state of a O_3 complex obtained from atomic rearrangements. According to reference [60]

In the year 2000 M. Pesola et al. published their work about the most likely structures of thermal donors in silicon [61]. They are reporting about thermal double donors (TDD). Their DFT calculations, using the Local Density Approximation (LDA), came to the result that the first three TDDs (TDD0-TDD2) consist of one four member ring with two threefold coordinated oxygen atoms involved, that are responsible for the donor behaviour of the complex. Additionally, one or two adjacent interstitial oxygen atoms are present. So the simplest structure consists of a ring and one adjacent interstitial oxygen atom. The two types of geometries: the R-ring and the Y-structure are compared. Their result was that only for ten oxygen atoms and higher they become energetically comparable. For a lower number of oxygen atoms in-

volved the R-ring structure is more stable.

In a more recent publication of S. Singh et al (2011) a state of the art insight in the formation of thermal donors in silicon was given [62]. Structural models of the formation kinetics are presented for the different donor complexes. According to their results TDD0 and TDD1 consist of three respectively four oxygen atoms arranged in different ways. The TDD0 complex (O_iO_{2r}) acts as a nucleus for the formation of further donors (TDD1 - TDDX). Several donor complexes (e.g. TDD1 and TDD2) might have the same oxygen content, arranged in different structures. Further interactions of oxygen dimers or trimers with one of the complexes might result in the formation of higher order donor complexes. In figure 2.12 some promising candidates for the structures of the TDD1, TDD2 and TDD3 defect are presented.

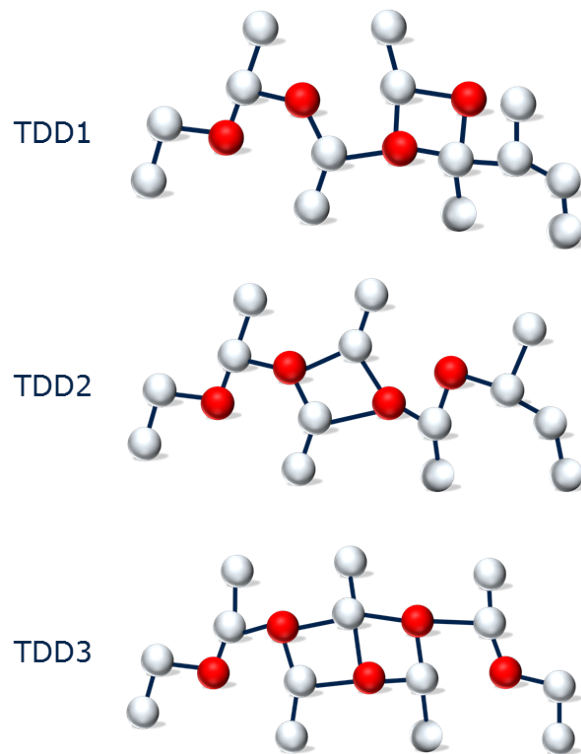


Figure 2.12: Promising candidates for the structures of the TDD1, TDD2 and TDD3 defect according to reference [62]. The red spheres symbolize oxygen atoms and the grey ones silicon lattice atoms.

In the following table 2.2 a list of thermal double donors (TDD) formed in oxygen rich Cz silicon annealed at temperature between 300-550°C is presented. The thermal donor complexes TDD0-TDD16 are listed with their symmetry, local vibrational modes, energy levels in the band gap and proposed structures reported in previous publications. Additional to these values the parameters of the formation energy, the excitation spectrum, diffusion parameters,

reaction rates, the g-tensor would be helpful to understand this complexes in more detail.

Defect	Symmetry	Local vibrational modes	Energy level in bandgap	Potential structure
TDD0	C_{2v} [30]			
TDD1	C_{2v} [30]	exp: 975 cm^{-1} [63], [30] sim: 978 cm^{-1} [64] neutral $v(2p_0)$ 461 cm^{-1} single ionized: 854 cm^{-1} [30]	(0/+) E_C -69.2 meV (+/++) E_C -156.3 meV [30]	$O_{2i} - O_{2r}^{2+}$ [64]
TDD2	C_{2v} [30]	exp: 988 cm^{-1} [63], [30] sim: 992 cm^{-1} [64] neutral: 442 cm^{-1} single ionized: 806 cm^{-1} [30]	(0/+) E_C -66.8 meV (+/++) E_C -149.7 meV [30]	$O_{2i} - O_{2r} - O_i^{2+}$ [64]
TDD3	C_{2v} [30]	exp: 999 cm^{-1} [63], [30] sim: 988 cm^{-1} [64] neutral: 423 cm^{-1} single ionized: 763 cm^{-1} [30]	(0/+) E_C -64.6 meV (+/++) E_C -143.8 meV [30]	$O_{2i} - O_{3r} - O_i^{2+}$ [64]
TDD4	C_{2v} [30]	exp: 1006 cm^{-1} [63], [30] sim: 1000 cm^{-1} [64] neutral: 405 cm^{-1} single ionized: 713 cm^{-1} [30]	(0/+) E_C -62.2 meV (+/++) E_C -138.2 meV [30]	$O_{2i} - O_{4r} - O_i^{2+}$ [64]
TDD5	C_{2v} [30]	exp: 387 cm^{-1} [65], neutral: 388 cm^{-1} single ionized: 678 cm^{-1} [30]	(0/+) E_C -60.1 meV (+/++) E_C -133.0 meV [30]	
TDD6	C_{2v} [30]	exp: 375 cm^{-1} [65] neutral: 372 cm^{-1} single ionized: 645 cm^{-1} [30]	(0/+) E_C -58 meV (+/++) E_C -128.3 meV [30]	
TDD7	C_{2v} [30]	exp: 360 cm^{-1} [65] neutral: 357 cm^{-1} single ionized: 613 cm^{-1} [30]	(0/+) E_C -56.5 meV (+/++) E_C -123.6 meV [30]	
TDD8	C_{2v} [30]	exp: neutral: 343 cm^{-1} single ionized: 585 cm^{-1} [30]	(0/+) E_C -54.5 meV (+/++) E_C -119.3 meV [30]	
TDD9	C_{2v} [30]	neutral: 330 cm^{-1} single ionized: 559 cm^{-1} [30]	(0/+) E_C -53.0 meV (+/++) E_C -116.0 meV [30]	
TDD10	C_{2v} [30]	neutral: 319 cm^{-1} [30]	(0/+) E_C -51.4 meV [30]	
TDD11	C_{2v} [30]	neutral: 307 cm^{-1} [30]	(0/+) E_C -49.9 meV [30]	
TDD12	C_{2v} [30]	$2p_0$ 293 cm^{-1} $5p_{+/-}$ 378 cm^{-1} [66]	(0/+) E_C -48.3 meV [66]	
TDD13	C_{2v} [30]	$2p_0$ 282 cm^{-1} $5p_{+/-}$ 363 cm^{-1} [66]	(0/+) E_C -46.6 meV [66]	
TDD14	C_{2v} [30]	$2p_0$ 270 cm^{-1} $5p_{+/-}$ 350 cm^{-1} [66]	(0/+) E_C -45.0 meV [66]	
TDD15	C_{2v} [30]	$2p_0$ 259 cm^{-1} $5p_{+/-}$ 339 cm^{-1} [66]	(0/+) E_C -43.4 meV [66]	
TDD16	C_{2v} [30]	$2p_0$ 247 cm^{-1} $5p_{+/-}$ 327 cm^{-1} [66]	(0/+) E_C -41.9 meV [66]	

Table 2.2: List of thermal double donor complexes listed in literature. The defect complex symmetry, local vibrational modes, energy levels in bandgap and potential structures are given.

High temperature thermal donors

Thermal donors that are formed at temperatures above 500 °C are called high temperature thermal donors (HTDs). But alternatively also other nomenclatures were defined and they were called "new thermal donors" [67], [68] or "second thermal donors" [69].

Due to short time anneals at temperatures around 550 °C, thermal donors become electrically deactivated, but the complex itself is not destroyed until anneals up to 900 °C [50]. The remaining complexes might grow further by absorbing additional oxygen. But also after anneals at 900 °C donors were reported [70]. The HTDs formation rate also depends on the oxygen concentration in the wafer, but not as strong as it does for TDs. The maximum concentration of formed HTDs ($5 \times 10^{15} \text{cm}^{-3}$) compared to TDs ($2 \times 10^{16} \text{cm}^{-3}$) in oxygen rich Cz silicon ($1.5 \times 10^{18} \text{cm}^{-3}$) is much lower [47]. In this study 770 °C was reported as the optimal formation temperature for HTDs. According to ESR results, the HTDs show crystalline and amorphous precipitates aligning in the $\langle 311 \rangle$ direction [71]. After annealing at moderate temperatures (around 450-500 °C) or after the anneals at higher temperatures 500-1000 °C for shorter durations the regular thermal donors seem to vanish and a new family of oxygen related, so called new donors was discovered. They seem to have shallower levels, smaller generation rates and higher thermal stabilities [72]. In the work of Qian et al TEM and HRTEM investigations of the potential structures of high temperatures thermal donors (HTDs), or new thermal donors are shown [73]. Additionally due to TEM investigations rod-like defects and dislocation loops were found after anneals at 750 °C for 10 and 100 hours respectively [74], [75]. Also amorphous platelets were found due to anneals at 850 °C and 870 °C oriented in $\{100\}$ with 1-4 nm thickness and diameters from 10-50 nm. [76], [77]. The structure of HTDs is assumed to be either a large oxygen silicon complex or SiO₂ particles with electrically active interfaces as reported in [78], [79] and [71].

2.7 Hydrogen related thermal donors in Silicon

In 1970 Schwuttke et al. were the first who reported an decrease of the resistivity in SRP measurements of a silicon wafer upon the irradiation with highly energetic protons (1 MeV , $(3-5) \times 10^{16} \text{ H}^+ / \text{cm}^2$) and thermal annealing [80]. They reported the formation of a donor species that forms at temperatures of $300 \text{ }^\circ\text{C}$ and vanishes above $500 \text{ }^\circ\text{C}$. In 1971, Zohta, Ohmura and Kanazawa used CV-measurements to show that hydrogen implantation in combination with a subsequent annealing step may lead to an increase of the charge carrier concentration in n-doped silicon and for a doping type conversion of *p*-type silicon [81].

The increase of the charge carrier concentration in proton implanted silicon can be related to the formation of a defect complex that is formed after the implantation and annealing. The decoration of this defect with hydrogen electrically activates the complex and produces the often reported shallow donor level complex [80],[81],[82]. The donor levels of the so called shallow donors are in the range of a few 10 meV below the conduction band edge. For the formation of this complex the radiation damage as well as the hydrogen has to be present in the crystal structure. In 1973 Ohmura, Zohta and Kanazawa showed the same donor formation and decoration effect with deuterium and tritium implantation, only shifting the maximum of the implantation peak because of the higher mass of the implanted ions [83]. Gorelkinskii, Sigle and Takibaev investigated the donor formation process upon the implantation of hydrogen, deuterium and tritium into Fz and Cz silicon using Electron Spin Resonance Measurements [82].

As has been shown by Meng et al. in 1995, the radiation damage not necessarily has to come from the proton implantation [84]. Also the neutron radiation of hydrogen rich silicon can be used to increase the electron concentration. Additionally a hydrogen plasma was used to diffuse hydrogen into neutron irradiated silicon [85],[86],[87],[88] (1989-1995). In various studies using different measurement methods the direct participation of hydrogen in the donor complex is shown [89], [90], [91], [92].

In 1994 Stein et al. showed that a small amount of hydrogen increases the formation of donors in the temperature range between 350 and $400 \text{ }^\circ\text{C}$ [93]. This fact was explained by a possible faster co-diffusion of hydrogen and oxygen.

In the work of L. Tsetseris et al. in 2006 the thermal donor formation but also the catalytic role of hydrogen was analysed [94]. Here two different cases were investigated: whether all inactive oxygen chains were present or not. When they are present, the conversion to the three-fold coordinated oxygen ring structure is the most probable thing that happens, with an energy barrier of only 1.15 eV . In the other case, the hydrogen-oxygen co-diffusion is more probable. In that case H binds strongly to the oxygen cluster and transforms into a TD like structure. For temperatures typical for the TD formation the H can be removed and trapped several times from the oxygen complex. So this repeated processes of trapping and release results in a catalysed formation process of thermal donors. As mentioned in the section about oxygen related thermal donors a cluster of three oxygen atoms in a ring configuration was presented as the thermal double donor (TDD) core structure. To better understand the behaviour of H in this system, lots of different binding sites were simulated.

In general the following formation mechanism is described in [94]: (i) H^+ and H^0 transform a staggered chain of oxygen into a single donor (TD) and bind to it strongly. (ii) H^- binds

to the chain and subsequently emits an electron that transforms the complex into a donor (ring structure). (iii) at a typical temperature for the TD formation (350-400 °C) the H-TD complex dissociates. (iv) the released H diffuses in Si again and aids oxygen agglomeration. So they showed that hydrogen can transform electrically non active oxygen chains into active ring structures.

In a publication by E. Simoen et al. (2009), a general review is given about what is known about hydrogen induced thermal donors in silicon [95]. In particular, the impact of hydrogen on OTDs, H-related TDs and their interactions. Against the interpretation of L. Tsetseris et al in reference [94] E. Simoen explains that STDHs are not converting or an early stage of OTDs, but rather become passivated by the attachment of further hydrogen atoms. The role of H is more complex than just acting as a catalyst in the oxygen diffusion. It is shown that at least another STD formation takes place where H is an active participant in the donor formation. However, despite some good points, E. Simoen et al. do not completely rule out that the STDHs convert into OTDs at some point.

In the work of Morris et al. from 2009 about hydrogen as well as nitrogen and oxygen defect complexes in silicon from computational searches an ab initio random structure approach was used to find the lowest energy structures for several defects in silicon [96]. During their search they found a more stable O_{3i} defect than the staggered defect reported in previous literature. Additionally they reproduced the rule that defects with completely saturated bonds have the lowest energy.

The current status on the investigations of the hydrogen related donors is that there is not only one donor complex but a whole group of defects with relatively low ionisation energies. They are strongly sensitive to the annealing procedure, especially the temperature. Anneals between 300 and 500 °C result in the formation of different donor complexes which dissociate above 600 °C.

2.8 Hydrogen defect complexes

This section is based on the work published in the PhD thesis of J. G. Laven. When highly energetic hydrogen is implanted into silicon, the hydrogen is more or less located around the projected implantation depth. As will be explained in more detail in the section about SRIM simulations 3.8 there is also additional radiation damage resulting from the implantation in the region between the penetrating surface and the implantation depth. So hydrogen can easily form a VH pair.



Additionally, hydrogen can decorate already existing point defects like V_2 , VO or V_2O . This is just a small variety of possible defects resulting due to the ion implantation process.



The H-related donors form due to the decoration of already existing defect complexes by the diffusing hydrogen. The hydrogen diffuses and forms these donor complexes at temperatures

from 300-550 °C, at higher temperatures the donor complexes dissociate again. In figure 2.13 a lot of possible reaction paths of vacancies with oxygen and hydrogen with the respective activation energies are displayed.

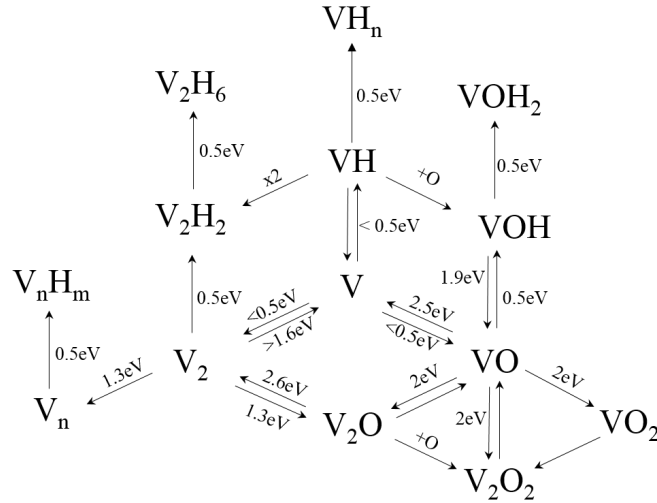


Figure 2.13: Various possible reaction paths for a vacancy with other vacancies (left), oxygen (right) and hydrogen (top) atoms. The figure was generated according to J. G. Laven [32], all references for the activation energies of the reaction paths can be found there.

All reaction paths with oxygen are displayed to the bottom left side. Reaction with hydrogen are visualized to the top and all reactions with additional vacancies to the bottom right side. The probability for the distinct reactions strongly depend on the concentrations of reactants and the temperature. Vacancies for example can already diffuse at very low temperatures. This enables the formation of double vacancy complexes or even bigger V_x complexes especially when there are no other reactants but vacancies around [97],[98]. In the oxygen rich Cz silicon, often V_2O is formed. These complexes are an often reported source for A-centres and vacancies with activation energies in the range of 1.5 eV [99] and 2.2 eV [100]. The dissociation of the V_2O complex into a double vacancy and an oxygen atom is less probable with an activation energy of 2.6 eV [99]. Besides the double vacancy formation, the direct formation of A-centres in oxygen rich silicon is also very probable due to the high diffusivity of vacancies. Interstitial oxygen atoms (2.5 eV [101]) and A-centres (1.8-2.1 eV [102],[101]) have a relatively high activation energy to migrate so they can be treated as localized traps except when higher temperatures are used. The VH_x complexes are thermally unstable and dissociate at temperatures around 250 °C [103], [104]. Only the more complex VH_4 and V_2H_6 complexes seem to have a higher stability [98], [104]. Due to the rather low migration barrier of hydrogen in silicon (actually the precise value is a matter of discussion in the research community) V_2H_x complexes can be formed using rather low thermal budgets. A lot of these complexes have charged states in the band gap of silicon and can act as recombination centres.

2.9 H⁺-implantation dose variation

Defects like vacancies, interstitials, double-vacancies or other small complexes are already formed by low dose implants. For higher doses agglomerations of defect complexes can be formed. The ion implantation into silicon strongly affects the electrical properties like the mobility, carrier lifetime et cetera. The H⁺ implantation process into silicon is used to change several different properties. As listed in the following sub sections, the different applications of this implantation method are distinguished by the implantation doses.

2.9.1 Low implantation doses

Very low dose implantations with doses of $10^9 - 10^{13}$ H⁺/cm² followed by anneals at 200 °C are used to adjust the charge carrier lifetime via the controlled incorporation of recombination centres. Different approaches have been used to adjust the charge carrier lifetime, like the diffusion of gold [105] into silicon that forms, the same as platinum, very effective recombination centres in silicon. The irradiation with particles (in that case electrons) to adjust the switching behaviour of devices was already investigated several decades ago see references [106] and [107]. The implantation of light ions forms a damage profile with a maximum at the implantation depth, that makes it easy to control the lifetime adjustment, as shown by [108] and [109]. At implantation doses of 10^{12} H⁺/cm² the formation of additional donors, as shown in [110] and [111], makes helium, where only damage but no hydrogen related donors are formed, the more suitable choice compared to hydrogen [112].

2.9.2 Medium implantation doses

The H⁺ implantations in the dose range of 10^{13} to 10^{15} H⁺/cm² and anneals in the temperature range from 350 to 550 °C are used to form additional donor complexes. As a doping method the long implantation depth as well as the relatively low thermal budget to activate the donors are definitely an advantage compared to other methods. Drawbacks are the relatively low activation ratio of the implanted protons, which is in the per mille region. Also, at annealing steps above 500 °C the deactivation process of the donor complexes starts. One important example, where the H⁺ doping mechanism can be used, is the field stop in an isolated gate bipolar transistor (IGBT) [110]. At the collector side of an IGBT device normally a *p*-doped region acts as a strong hole emitter in the ON state of the device. In the OFF state the space charge region expands into the lightly doped drift region. To prevent an expansion of the space charge region to the emitter region, followed by a minority charge carrier injection and the loss of the ability of the device to turn off, the drift region (and also the device) has to be very broad. Alternatively to a broadening of the drift region, an increased charge carrier concentration is added between the drift and the emitter region. This field stop region results in a much steeper gradient of the electric field, changing the shape of the electric field over the devices cross section from triangular to nearly trapezoidal. Due to this change in the doping profile, for the same maximal electric field and the same expansion of the space charge region a much higher voltage can be applied without the necessity of broadening the device. Additionally to IGBTs the proton implantation doping mechanism was also used to produce so called super junction (SJ) MOSFETs [113] or for the formation of shallow *pn*-junctions for photovoltaic applications [114], [115].

2.9.3 High implantation doses

Very high implantation doses $\geq 10^{16} \text{H}^+ / \text{cm}^2$ can result in a splitting/breaking of the target material at the implantation depth. Here, high concentrations of damage and hydrogen form so called platelets, that are about 10 nm big crystal defects oriented in parallel to the crystal surface [116], [117]. During the annealing process at temperatures between 400 and 600 °C the platelets grow further resulting in the formation of bubbles. The sample can then be broken at the implantation depth [118]. This is used for so called Smart Cut process [117], [119], [120] to produce very thin wafers by removing the region between the surface and the implantation depth. The implanted hydrogen enables the breaking process of bound regions due to the chemical saturation of the loose silicon bonds [121]. The produced thin layers of silicon are used for silicon on isolator (SOI) applications where the thin layer of silicon is directly removed from the substrate. This is an alternative to buried oxide layers.

2.10 Charge carrier concentration (doping) profile due to H⁺-implantations into silicon

From literature and from our experiments we know that donor and acceptor formations due to the implantation of protons into silicon change the shape of the implantation profile. As mentioned before, the formation processes are strongly dependent on the substrate material (e.g. oxygen and carbon rich or lean) the implantation dose (see section 2.9) and the annealing parameters. In this section, it will be explained why the resulting charge carrier concentration profiles after an H⁺-implantation look the way they do.

2.10.1 Qualitative description of H⁺-implantation profile in Fz silicon

During an H⁺-implantation into Fz silicon (in this example phosphorus doped *n*-type silicon): a hole conducting layer forms in the region between the surface and the projected implantation depth of hydrogen. Also the hydrogen related donors form around the implantation depth where hydrogen and radiation damage are present. During the anneal at 350 °C for five hours the donors are formed/activated and the hydrogen diffuses from the implantation depth forming additional donors. Resulting in the profile shown in figure 2.14.

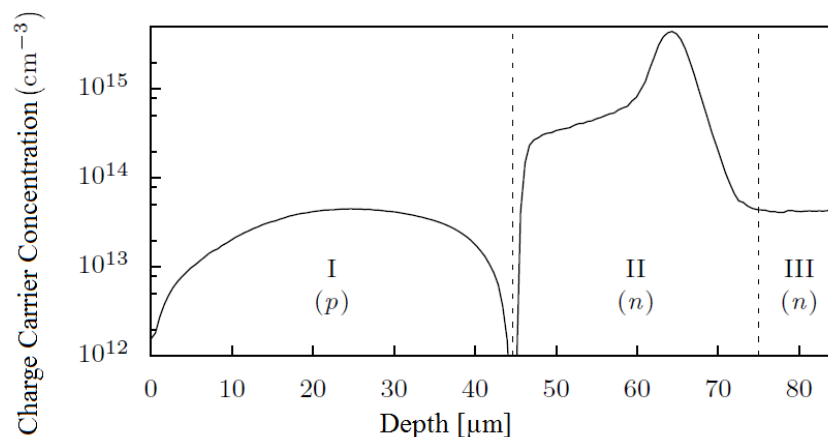


Figure 2.14: Typical Charge Carrier Concentration Profile resulting from a 2.5 MeV H-implantation with $4 \times 10^{14} \text{ H}^+/\text{cm}^2$ annealed at 350 °C for five hours. Figure generated according to reference [32]

I) Hole conducting region

The region labelled with I is the hole conducting region. It starts at the surface (represented by the left edge of the figure) and ends at the minimum of the charge carrier concentration (*pn*-junction) at about 44 μm depth. The implantation damage forms acceptor complexes during

the H^+ -implantation process. The concentration of hydrogen in this region is very low. The acceptors in this region form without any additional thermal treatment besides the implantation process itself.

II) H-related donor region

The layer II starts at the pn -junction and stops at the substrate doping level after the implantation depth ($68 \mu\text{m}$) at approximately $75 \mu\text{m}$ depth. The hydrogen related donor complexes are formed where hydrogen and radiation damage coexist. This results in an expansion of the implantation peak towards the surface during the anneal. In this direction the diffusing hydrogen can decorate radiation induced defect complexes forming HDs/HTDs.

III) Substrate region

The substrate region III starts when the charge carrier concentration after the implantation peak relaxes to the constant substrate value before the implantation process. This region is not affected by the implantation directly. During a post implantation annealing process the formation rate of thermal double donor complexes (OTDs) is low in comparison to oxygen rich Cz silicon.

Figure 2.15 visualizes the depth distribution of the charge carrier concentration profile depending on the diffusing hydrogen. It is shown that when the implanted hydrogen expands during an anneal it decorates radiation damage induced defects (vacancies and other complexes). The resulting pn -junction between the formed HDs and the hole conducting layer shifts to the left as the anneal progresses.

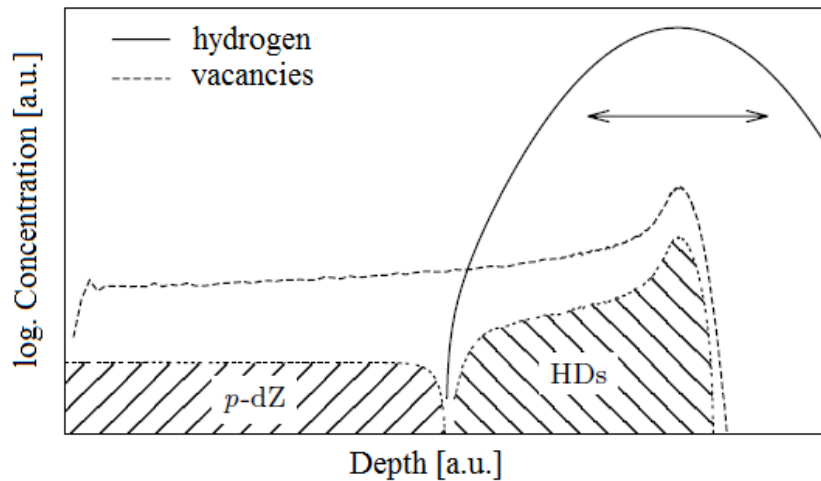


Figure 2.15: Schematic illustration of H-related donor (HD) formation mechanism. Taken and modified from reference [32]

In figure 2.16 the hydrogen concentration after the implantation and the representative shape of the hydrogen distribution after anneals at 400 °C for 1-30 hours are simulated (dotted curves). Additionally the concentrations of acceptors and potentially hydrogen related donors are visualized. The shape and the concentration of these two dopant complexes were simulated using SRIM radiation damage simulation as input parameters and comparing the simulations with experimental results. As can be seen: during the anneal the hydrogen diffuses out from the implantation peak and decorates radiation damage complexes. At the position where the concentration of hydrogen and acceptor complexes is the same, the *pn*-junction forms.

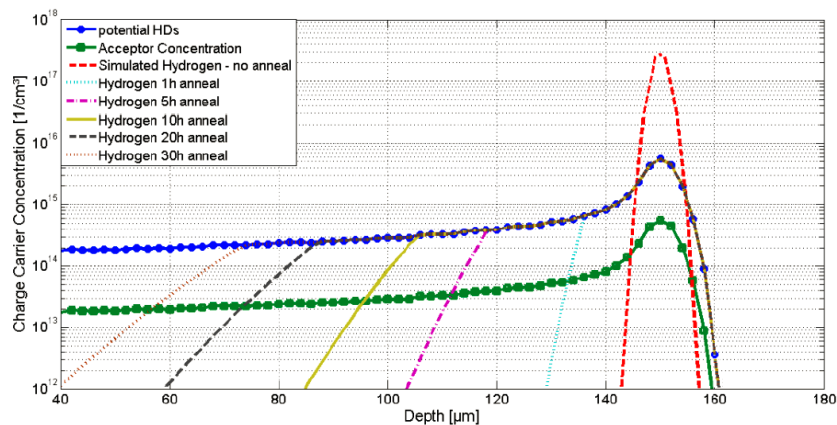


Figure 2.16: Simulation of the H-distribution after implantation and several anneals at 400 °C for 1-30 hours (dotted lines). Simulation of the concentration of acceptors and potentially hydrogen related donors (solid lines with big dots). Taken from reference [122].

More about the diffusion of hydrogen in silicon, in Fz and m:Cz silicon, how to extract the diffusion constant and E_A of hydrogen diffusion can be found in the publication [122].

2.10.2 Qualitative description of H-implantation profile in Cz/m:Cz silicon

In comparison to Fz silicon in Cz/m:Cz silicon four different regions are present after the implantation.

I) Hole conducting region

In comparison to Fz silicon the formation rate and resulting concentration of the acceptors in the hole conducting region is much smaller in Cz silicon. It seems like oxygen or carbon are reducing the acceptor formation.

II) H-related donor region

In Cz silicon the activation energies necessary to form the hydrogen related defects are higher than in Fz silicon (as can be seen in reference [123]). Also the diffusivity of hydrogen is lower in Cz silicon and the shift of the pn -junction towards the surface takes longer for the same temperatures.

III) Shoulder Peak

Region III is located between the implantation peak and the substrate. Donors form in this region directly during the implantation process resulting in a peak that transforms into a shoulder during the annealing process. More information about the shoulder formation process and the possible candidates for that defect are presented in the publication: H^+ Implantation Profile Formation in m:Cz and Fz silicon.

IV) Substrate region

Analogue to Fz silicon, the substrate region retains the doping concentration beyond the region affected by the hydrogen implantation. The only big difference to Fz silicon is that in the oxygen rich Cz silicon thermal double donor complexes may be formed during an anneal at temperatures between 400 and 530 °C. This can be important especially for low doped substrate materials.

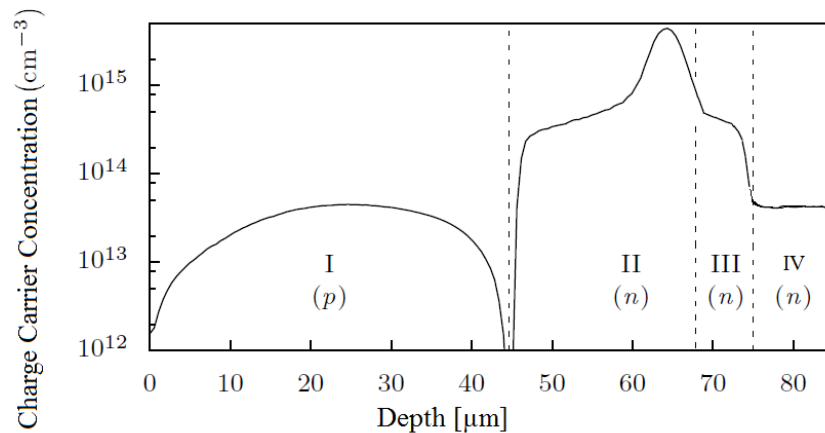


Figure 2.17: Typical Charge Carrier Concentration Profile resulting from a 2.5 MeV H^+ -implantation into Cz or m:Cz silicon

2.11 PN-junction and Schottky junctions

In this section typical electrical structures often used in this thesis should be explained briefly. More information about *pn*-junctions and Schottky contacts/junctions can be found in [13].

2.11.1 PN-junction

A *pn*-junction is a boundary between a *p*-type and *n*-type doped semiconductor region. It does not matter how the single crystalline semiconductor is doped (implantation, diffusion) or produced (from a melt, epitaxial growth). A *pn*-junction is the standard building block for most electronic devices like diodes, solar cells and LEDs, that consist of one *pn*-junction, or transistors and thyristors that consist of more than one *pn*-junction. The region of the *pn*-junction is where the electronic action happens. A *pn*-junction is a diode. In a simplified picture it conducts current in one direction and blocks current in the other direction.

2.11.2 Zero external bias

First of all, the *pn*-junction without any externally applied bias should be explained. By forming the *pn*-junction electrons from the *n*-type region diffuse into the *p*-type region. As they move they leave back positively charged ions, so called donors, in the *n*-type region of the junction. Also holes from the *p*-type region of the junction diffuse into the *n*-type region leaving back negatively charged ions, called acceptors. So the regions close to the junction become charged and form a space charge region resulting in the creation of an electric field that suppresses the diffusion process at some point. So there are two counterbalancing processes going on during the formation of a *pn*-junction. In figure 2.18 the formation of the *pn*-junction is demonstrated. The depleted space charge region with the ionized donors and acceptors forms due to the majority carrier diffusion process resulting in a net charge distribution shown in the top left subfigure. When the equilibrium is reached the charge carrier distribution looks like a step function. The electric field points from the ionized acceptors to the donors.

The formation of the depletion region can be calculated using an abrupt junction approach. This assumption calculates the width of the depletion region, the shape of the electric field for *pn*-junctions with different net doping concentrations in the *n* and *p* regions. When high doping concentrations are used to produce a *pn*-junction they lead to narrower depletion regions with higher electric fields than low doping concentrations.

2.11.3 Forward bias

In forward bias mode the *p*-type region is connected to a positive potential and the *n*-type region to a negative potential (in comparison to the potential applied at the *p*-type region). With the potentials connected that way the electrons are pushed from the *n*-type regions towards the junction and the holes from the *p*-type region towards the junction, resulting in a reduction of the width of the space charge region/depletion region. This lowers the barrier potential and consequently reduces the electrical resistance. So electrons moving towards the junction can penetrate into the *p*-type material, but after some distance (diffusion length) it is energetically

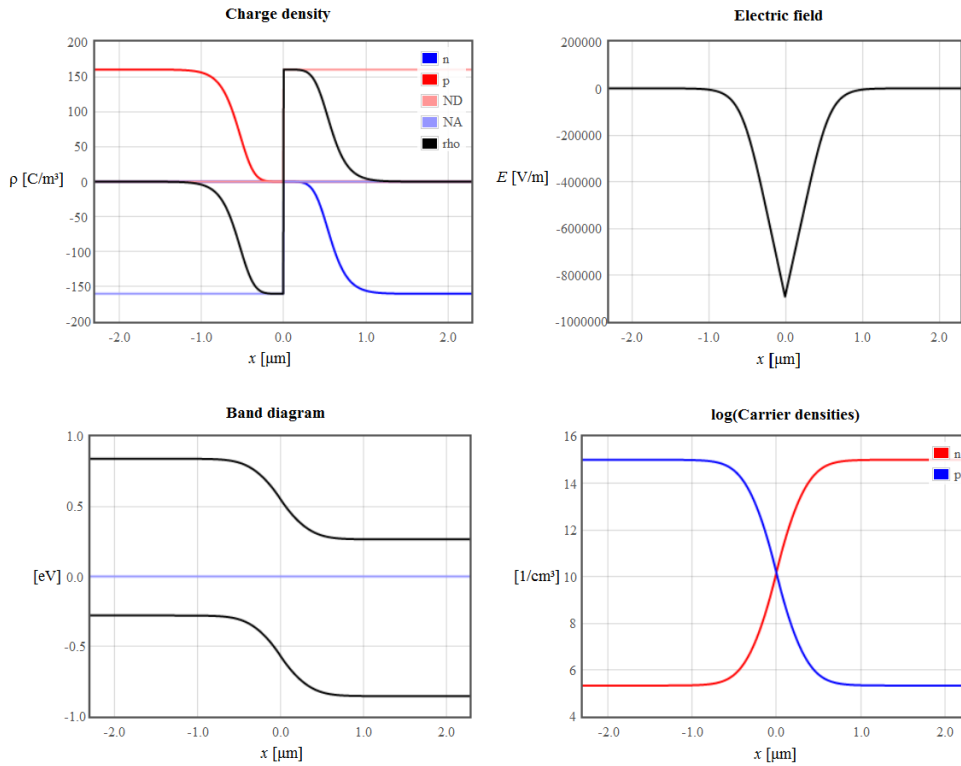


Figure 2.18: Schematic visualization of a pn -junction. The resulting charge carrier concentration, electric field and band diagram and log. charge carrier concentration are plotted

favourable for them to recombine (the same is true for holes in n -type material). Only majority carriers can flow through a semiconductor in macroscopic length scales. So the macroscopic picture of the charge transport in forward bias in a pn -junction is that electrons (from n -type region) and holes (p -type region) are accelerated towards the junction and recombine on the other side of the junction. The net current is the sum of the electron and the hole current across the junction.

2.11.4 Reverse bias

In reverse bias mode the p -type region is connected to a negative potential and the n -type region to a positive potential (in comparison to the potential applied at the p -type region). In both regions the majority charge carriers are pulled away from the pn -junction resulting in the expansion of the depletion region with increasing reverse bias voltage applied. The electric resistance and the electric field increase for increasing reverse bias voltages. Only very small amounts of the charge carriers can pass the junction, which is behaving like an insulator in this mode. If the maximum electric field overcomes the critical electric field (value for silicon), the

diode goes into avalanche breakdown and a high current flows. This can also happen in a more controlled way, like it is done in Zener diodes.

2.11.5 Schottky junction

A Schottky junction, contact or barrier is a metal-semiconductor junction with an energy barrier formed in between. Not all metal-semiconductor contacts form Schottky junctions. It strongly depends on the work functions and band gap energies of the metal and the semiconductor materials whether an ohmic or a Schottky contact forms when they are put together.

When the metal and the semiconductor are put together, the majority charge carriers of the semiconductor diffuse to the metal. In the case of a n -type semiconductor, like it is demonstrated in figure 2.19, electrons are pushed into the metal, leaving back positively charged donors. An electric field is formed, pointing from the positively charged donors towards the metal that pushes back the diffusing majority charge carriers. In the band diagram this is visualized as a bending of the conduction and valence bands. When a Schottky contact is formed between a metal and a p -type semiconductor holes diffuse into the metal, negatively charged acceptors are left back and form an electric field, pointing from the metal towards the p -type semiconductor.

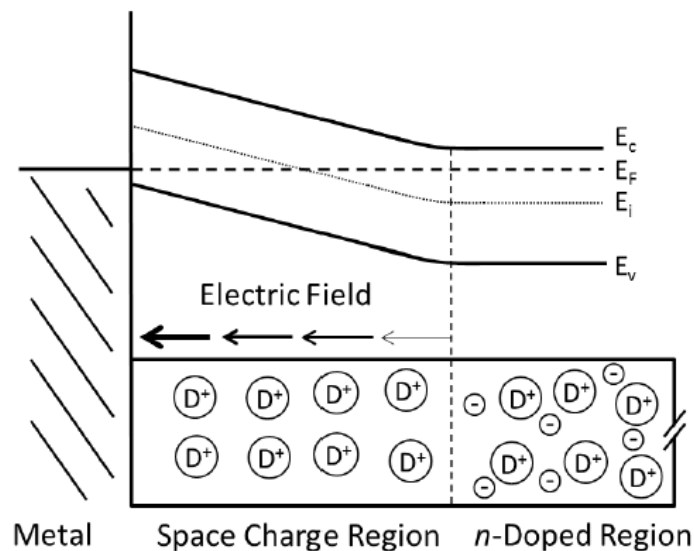


Figure 2.19: (Upper part) Schematic visualization of the formation of a Schottky junction and band bending between a metal and an n -type semiconductor. (Lower part) Schottky contact formation process visualized with charged states of donors and the resulting electric field distribution. Figure taken from [124]

Chapter 3

Analytical methods

3.1 Scanning electron microscope (SEM)

An electron microscope is a measurement tool that makes it possible to display and investigate surface or bulk properties of a specimen by irradiating it with electrons. The wavelength of the electrons can be adjusted by the acceleration energy. In a light microscope the wavelength of the photons is the limiting factor for the resolution of the microscope. The electrons accelerated in an electron microscope have a much shorter wavelength than light waves. But this is not the limiting point in an electron microscope. Here the electron lens aberrations limits the resolution. The maximum resolution of an electron microscope (1 nm) is much better than the resolution of a light microscope (200 nm). In general an electron microscope consists of an electron gun, electromagnetic lenses, a vacuum system and detectors. To understand the data measured with an electron microscope it is very important to understand how the signal was generated. There exist a lot of different electron microscopes with different working principles. In figure 3.1 the schematic components of a scanning electron microscope are shown.

The electron beam, with a diameter of about 10 nm, rasters in periodical patterns over the specimen surface. Due to the interactions of the incoming electron beam with the specimen, electrons with different energies are emitted from the specimen towards some potential detector that makes it possible to generate an image from the detected electrons. In figure 3.2 the interaction mechanisms of the penetrating electrons with a semiconducting material are shown.

The size of the interaction volume of the primary electrons in the sample material strongly depends on the energy of the penetrating electrons and material properties. In early works by Grün [126], Ehrenberg [127] and Cohen [128] the range R_G of the electrons was calculated:

$$R_G = 0.043 \cdot \frac{\mu m}{cm^3} \frac{g}{\rho} \left(\frac{E_B}{1keV} \right)^{1.75} \quad (3.1)$$

where ρ is the density of the specimen material. The exact pre-factor is still a matter of discussion. The value 0.043 is reported in the work of Leamy [129]. Holt et al reported the pre-factor 0.0398 [130]. Friel et al [131] reported a prefactor of 0.064 and an exponent of 1.68. According to

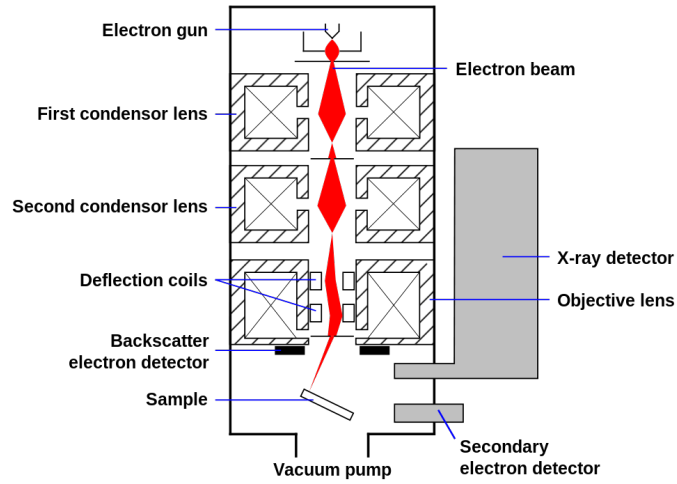


Figure 3.1: Most important components of a Scanning Electron Microscope (SEM). The electron beam path and reduction of the beam diameter is visualized. The figure was taken from [125]

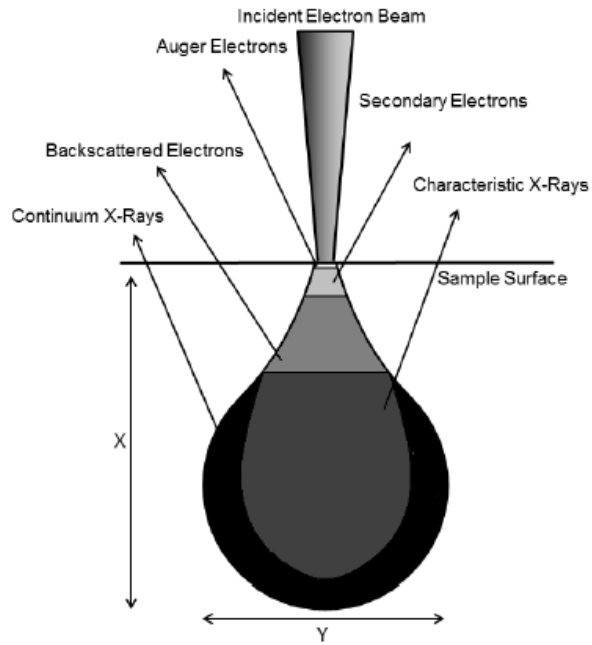


Figure 3.2: Visualisation of the interaction volume and the scattering mechanisms appearing when high energetic electrons penetrate into a semiconductor. Figure taken from [124]

Potts et al [132] the lateral diameter as well as the maximum interaction depth can be calculated as:

$$X = \frac{0.1 \cdot E_0^{1.5}}{\rho} \quad \text{and} \quad Y = \frac{0.077 \cdot E_0^{1.5}}{\rho} \quad (3.2)$$

again ρ is the density of the specimen material and E_0 is the energy of the primary electrons. Our cooperation partners from Austria Micro Systems in Graz are currently using a Pearson IV distribution to simulate the interaction volume.

Casino Simulation is a very useful tool to simulate the interaction volume, the dissipation of energy or the trajectories of the penetrating electrons into the specimen material [133]. In figure 3.3 the trajectories of 20 keV electrons penetrating into silicon are displayed. Additionally the energy dissipation is visualized. The box size is about five by five microns.

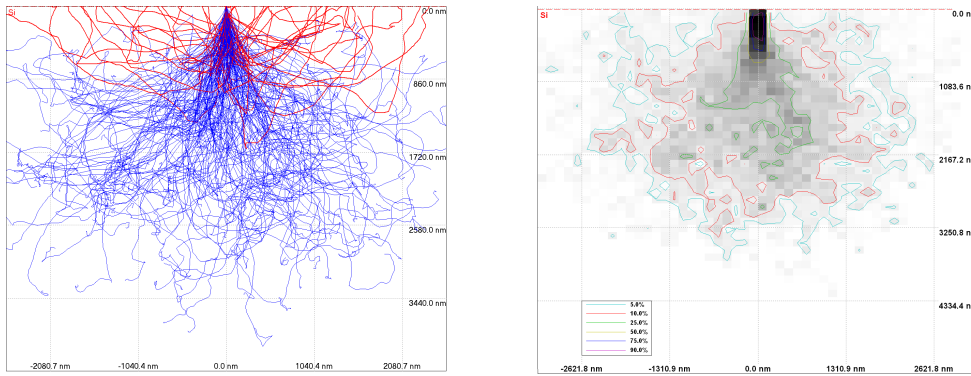


Figure 3.3: Casino Simulations of the penetration paths of 20 keV (left) electrons into silicon. The right image shows the energy dissipation of the electrons in the specimen material. The box size in both figures is about five by five microns.

Sometimes buried junctions or structures are investigated with a scanning electron microscope. In that case it is necessary to know the size of the interaction volume and how deep the electrons can penetrate in the specimen material. During the comparison of recent EBIC simulations and measurement data, it was found out that the use of a broader width of the incident beam (Casino Simulations uses only one or two pixels) leads to a shift of the maximum of the energy dissipation into a region deeper in the sample.

3.1.1 Secondary electron detector

Secondary electrons (SE) are electrons resulting from inelastic scattering events of the primary electron beam in the first few nano-meters of the specimen. They are usually detected using an Everhart Thornley detector or in general scintillator photomultiplier systems. Here the secondary electrons, that are coming from the specimen, are attracted by an electrically biased metal grid. Then the secondary electrons are accelerated until they have enough energy to emit light in the scintillator. The output of the photomultiplier tube is recorded as a function

of the beam position, resulting in a two dimensional secondary electron intensity map. The whole scanning process can be performed in real time mode so the secondary electron intensities can be visualized at video speed. For high resolution scans, secondary electron images are normally the best choice. The resolution strongly depends on the wavelength/energy of the accelerated electrons and further on the size of the interaction volume (the smaller - the higher the resolution). In figure 3.4 the secondary electron detector used in this thesis is shown. This image was recorded using an electron mirror. An electrically isolated sphere is charged in the microscope chamber to deflect the electron beam in the preferred direction. The electron mirror can be a piece of metal or plastic. It is charged by illuminating it with highly energetic (20-30 keV) electrons for several tens of seconds. After the charging the acceleration voltage of the SEM is changed to a low value like 3-5 keV and the incident electrons are deflected by the electron mirror. In our experiments the electron mirror worked stably for several minutes but as the charging of the electron mirror continuously decreased the deflection effect vanished.

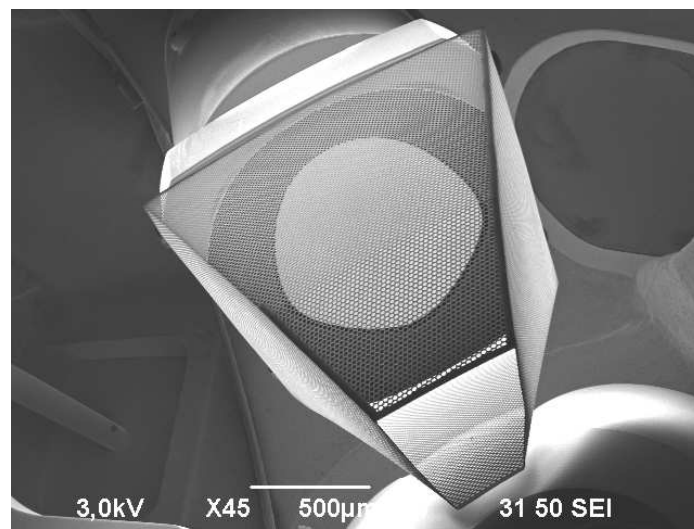


Figure 3.4: Electron mirror image of the Secondary Electron Detector inside the SEM.

3.1.2 Backscattered electron detector

Backscattered electrons (BSE) are high energetic electrons resulting from elastic scattering of the primary electrons with the specimen electrons. Due to the stronger electron backscattering of heavy elements in comparison to light elements, the backscattered electron signal is high for elements with high atomic numbers and low for elements with low atomic numbers. This effect makes it possible to distinguish between regions of different chemical compositions. Biased grid detectors beside the sample, like they are used for secondary electron detectors, are not suitable for BSE detection. Because of the high energy of the backscattered electrons they are not affected by a weak electric field. Backscattered electron detectors are normally mounted above the specimen concentric with the electron beam. In figure 3.5 the backscattered electron detector inside the electron microscope is shown using an electron mirror.

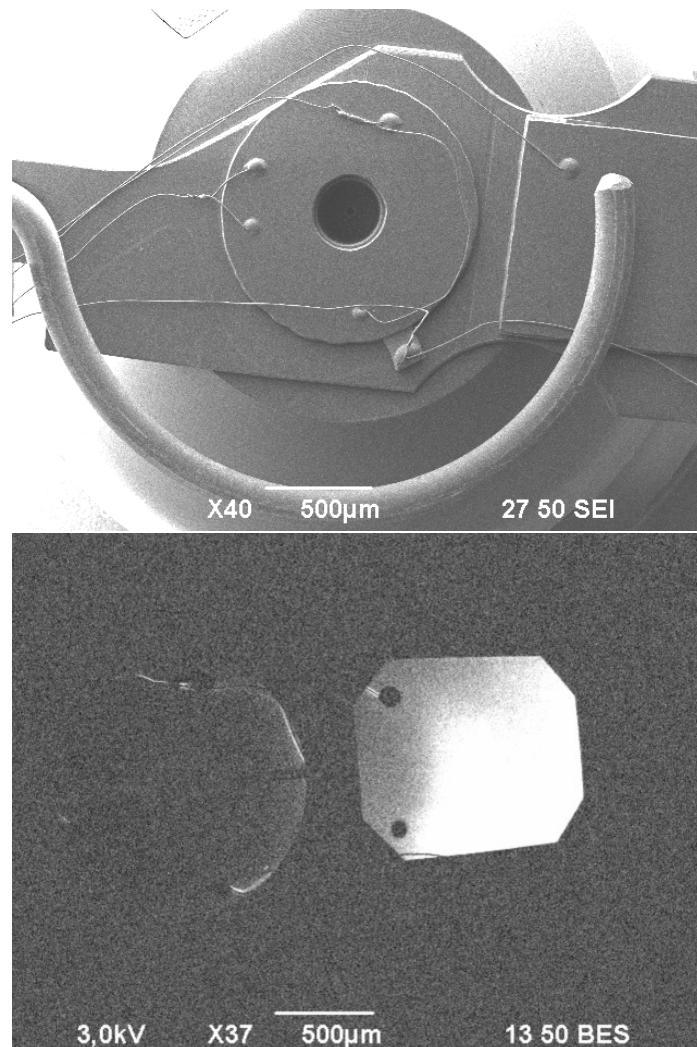


Figure 3.5: (top) Electron mirror image of the backscattered electron detector inside the SEM. The detector around the electron cone is the part of the BSE detector used to image compositional and topological information. The off-axis oriented flat detector area to the right is the BSE shadow detector. It yields a combination of topological and compositional information, while, in contrast to the topological-mode of the detector, the image appears to be illuminated from the side and not from the top. The semicircular metal rod between the detector and the stage, where the electron mirror is positioned on, is a simple safety mechanism that avoids a collision of the stage and the detector. The wires are the contacts of the detector. (bottom) This image was made using the the backscattered electron detector. In this case only the detector itself appears bright.

3.2 Electron beam induced current (EBIC)

Electron beam induced current (EBIC) is a semiconductor analysis technique performed in a scanning electron microscope. It is used to identify buried junctions or defects in semiconductors, or to examine minority charge carrier properties. The electron beam moves over the specimen and electron-hole pairs are generated in the interaction volume of the beam. If the semiconductor sample contains an internal electric field, as it is present in the depletion region of a pn -junction or Schottky junction, the electron-hole (eh) pairs are separated by the built-in electric field. In 1958 Everhart was the first who reported the working mechanism behind EBIC, especially the charge carrier separation and collection mechanism of a pn -junction in a SEM [134]. He noted: "the beam could make a large difference in the back current taken by a pn -junction". In this section the analytical measurement method EBIC is explained in detail. The interaction of the electron beam with the semiconducting material and the behaviour of the generated charge carriers in the semiconductor material are explained. Furthermore, the electron beam induced current generation and detection is analysed. Applications like the determination of the doping type or the minority charge carrier diffusion length are presented. Additionally, the EBIC-chopping measurement is presented. This method makes it possible to image the depletion region of a reverse biased junction.

3.2.1 Interaction of the electron beam with the semiconducting material

Most of the interactions of high-energetic electrons injected into a semiconductor were already explained in section 3.1. Nevertheless the most important facts for the EBIC measurements should be explained in this section. When the high-energetic electrons enter the semiconductor, lots of inelastic scattering events take place and lots of low-energy electron-hole pairs are generated. The generation volume has the shape of a bulb with a high concentration of eh pairs close to the surface. Not all of the initial energy of the incoming electron beam E_B can be converted into eh pairs. So the number of eh pairs generated is smaller than E_B/E_g . Where E_g is the theoretical generation energy for an electron-hole pair. According to Holt et al [130] the formation energy of eh pairs E_{eh} can be calculated with the empirical formula:

$$E_{eh} = 2.1 \cdot E_g + 1.3 \text{ eV}. \quad (3.3)$$

3.2.2 Charge carrier separation - analytical description

Due to the injection of highly energetic electrons, the charge carrier density and the quasi fermi levels of electrons F_e and holes F_h change in the interaction volume. The quasi fermi level describes the population of electrons in the conduction and valence band separately in a non equilibrium distribution. Such a situation can be generated by an applied voltage or by the exposure to light. When the injected concentration of eh pairs (controlled via the electron current of the beam) is small in comparison to the majority charge carrier concentration the situation can be referred to as low injection. In this case the gradient of the quasi fermi levels is not symmetric in the space charge region of a pn -junction as can be seen in figure 3.6. The gradient of F_e is steeper in the direction of the n -type region than in the p -type region. For holes it is exactly the same for F_h into the p -type region. So when the whole process is summed up the electrons flow into the n -type region and the holes into the p -type region.

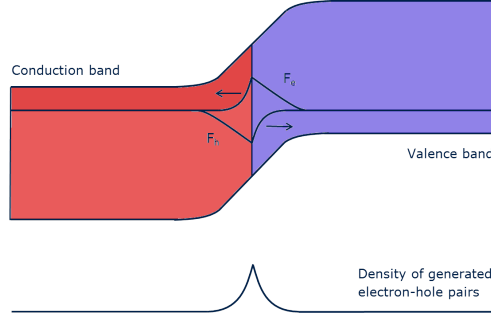


Figure 3.6: Schematic visualization of the quasi Fermi levels of electrons and holes in the space charge region of a pn -junction in the low injection regime. According to [135]

The situation where the injected electron-hole concentration is higher than the majority charge carrier concentration is referred to as high injection. In that case the gradient of F_e and F_h are the same in all directions and no charge carrier separation takes place. For EBIC measurements it is important to stay in the low injection regime.

The starting point for the calculation of the EBIC signal is the continuity equation. For a p -type semiconductor the continuity equation

$$\frac{\delta n}{\delta t} = G_n - R_n + \frac{1}{e} \nabla \cdot J_n, \quad (3.4)$$

shows how the concentration of the minority charge carriers, in this case electrons n behaves over time t with a generation rate G_n , a recombination rate R_n and the migration term. Where e is the elementary charge and J_n the current density of the electrons. The current density J_n consists of a drift and a diffusion component

$$J_n = e\mu_n nE + eD_n \nabla n, \quad (3.5)$$

where μ_n is the electron mobility, E the electric field and D_n the diffusion constant for electrons. The diffusion constant is related to the charge carrier mobility via energy and charge by the Einstein relation

$$D = \frac{\mu k_B T}{e}. \quad (3.6)$$

In the low injection regime the recombination rate can be defined by the lifetime of the excess minority charge carriers,

$$R_n = \frac{n - n_0}{\tau_n} = \frac{\Delta n}{\tau_n}, \quad (3.7)$$

where n_0 is the electron concentration in thermal equilibrium, τ_n is the electron lifetime and Δn is the excess electron concentration. The minority charge carrier lifetime itself can be defined by the surface and bulk lifetime via,

$$\frac{1}{\tau} = \frac{1}{\tau_{bulk}} + \frac{1}{\tau_{surface}}. \quad (3.8)$$

Usually the continuity equation is only solved outside the space charge region, here only the diffusion but not the drift components have to be taken into account. For the space charge

region a charge separation of hundred percent is assumed. The continuity equation for Δn is with a point source at x_1 and a generation rate A is

$$D_n \nabla^2 \Delta n - \frac{\Delta n}{\tau_n} = A \delta(x - x_1) \quad (3.9)$$

v_i is defined as the surface recombination velocity. At the interface to the space charge region Δn is assumed to become zero. Hence the boundary conditions for the surface of the semiconductor is

$$\Delta n = 0 \text{ for } x \in \text{surface of space charge region} \quad (3.10)$$

$$\frac{D \delta n}{\delta x_1} = v_i \Delta n \text{ for } x \in \text{every other interface in the semiconductor} \quad (3.11)$$

where \vec{x}_1 is the normal vector of the relevant surface.

The continuity equation for Δn can be solved with these boundary conditions. Using the solution of this equation a probability $\phi(x_1)$ for an electron generated at a certain position to pass through a surface can be determined. Integrating this function over the whole interaction volume results in the EBIC signal. For a detailed calculations see reference [135]

In general the calculation of the EBIC signal, including the factors of the surface recombination velocity, generation and recombination rates, the diffusion length and additional parameters, is rather complicated. Using simulation software e.g from Synopsis [136], that include EBIC simulation packages, it is possible to simulate the resulting EBIC signal for all kinds of structures.

Donolato et al showed a much easier approach using greens functions to come to a solution for the collection probability function $\phi(x)$ [137].

$$D_n \nabla^2 \phi - \frac{\phi}{\tau_n} = 0 \quad (3.12)$$

using the boundary conditions

$$\phi = 1 \text{ for } x \in \text{surface of space charge region} \quad (3.13)$$

$$D_n \frac{\delta \phi}{\delta x_1} = v_i \phi \text{ for } x \in \text{every other surface} \quad (3.14)$$

resulting in

$$\text{divgrad} \phi - \frac{\phi}{L^2} = 0 \quad (3.15)$$

where L is the diffusion length.

3.2.3 EBIC measurement techniques

EBIC line scan measurements (1D-EBIC)

As demonstrated in figure 3.7, during an EBIC line scan measurement the electron beam remains on every point/position on the line for 20 μs . The measurement signal is summed up and averaged for this time period that corresponds to a full 50 Hz cycle. Without averaging

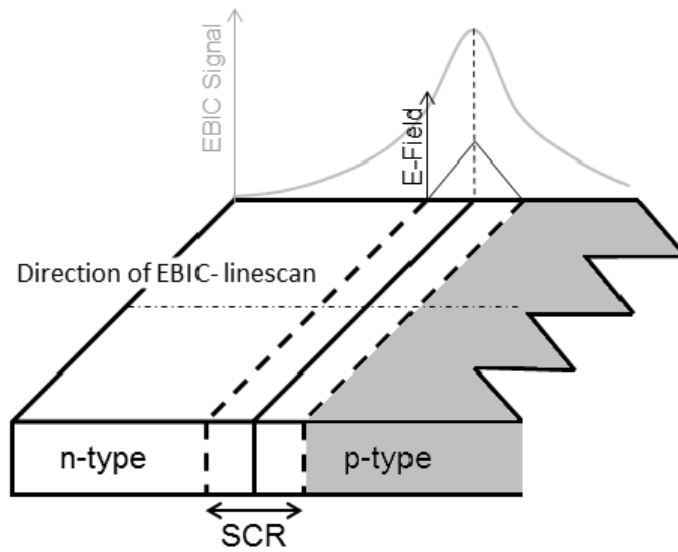


Figure 3.7: EBIC line scan measurement routine over a pn -junction. The direction of the EBIC measurement, over the SCR of the pn -junction, is shown by the dotted line. Figure taken from [124]

over a full 50 Hz cycle a higher influence of outside noise signals was detected.

In figure 3.8 the secondary electron signal and the EBIC signal are combined to one plot, to show the position of maximum electric field on the silicon wafer cross section.

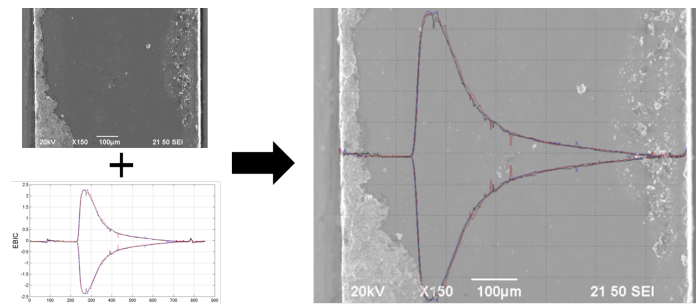


Figure 3.8: Secondary electron image (top left), EBIC linescan signal (bottom left) combined to one plot (right)

Two dimensional EBIC measurements (2D-EBIC)

A two dimensional EBIC measurement is performed by the fusion of a multitude of one dimensional line scans. These are useful to localize the positions of a pn -junctions, to measure diffusion lengths and to visualize defects. Defects appear in several forms, such as inclusions of voids, crystallographic imperfections or extended defects like dislocations or grain boundaries. Defects are often a reason for the reduction of charge carrier lifetime. In a nearly perfect crystal, lattice defects can act as the charge carrier recombination centres. That means the collection rate for the EBIC signal decreases and additional contrast can be seen in the image. In this thesis several different ways are used to present the measured data. The different ways to plot the data are shown in figure 3.9. The regular plot is a grey scale plot where the brightest point is the point of the maximum EBIC signal, representing the position of the maximum electric field. This is the most popular method used in literature, nevertheless it is difficult for the human eye to distinguish all these different levels of grey. Another way is to use a so called contour plot (coloured from red=max to blue=min) that plots contour lines for various signal heights. It is also possible to plot the measured signal three dimensionally. Here, the increase of the signal can be demonstrated more clearly. Additionally it proved to be useful to plot the logarithm of the measured EBIC signal. Especially to visualize very small structures and to visualize changes in of low signal levels.

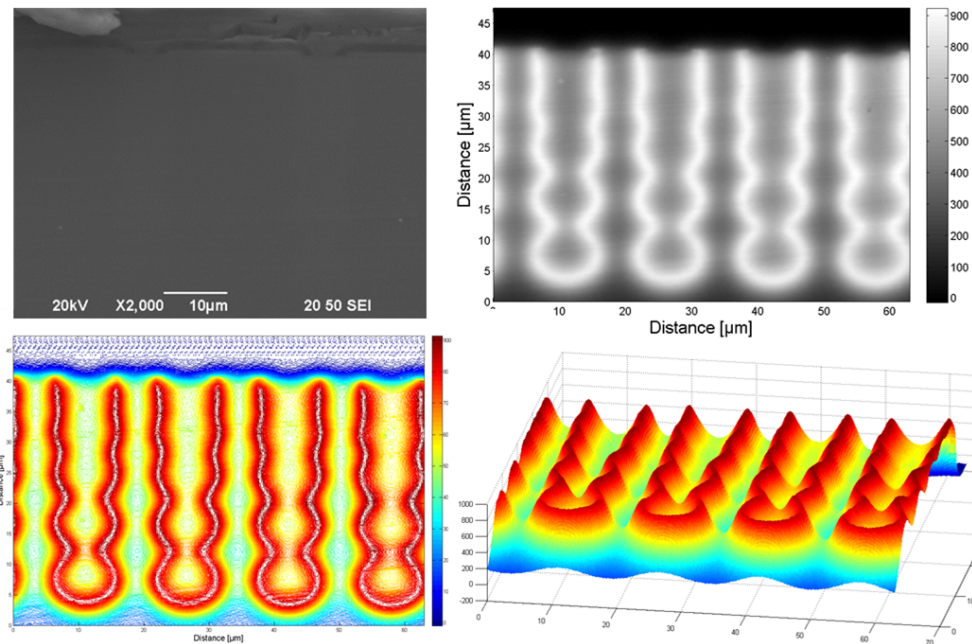


Figure 3.9: EBIC scan over the area shown in the SE image (top left). In the grey scale plot (top right) the bright areas indicate the maximum EBIC signal and the dark areas, regions where no or a low EBIC signal is detected. In the contour plot (bottom left) small changes can be detected more easily. In a three dimensional plot (bottom right) the increase of the signal is demonstrated more clearly, but it is not handy to get an overview over the whole region.

3.2.4 Schottky-EBIC measurements

During a Schottky EBIC measurement, small metal-semiconductor (Schottky) contacts are formed by pressing tungsten needles against silicon. Interface states at the metal-semiconductor interface pin the Fermi energy near the middle of the band gap. The built-in electric field points from metal to semiconductor when the metal is placed on a *p*-type semiconductor and it points from semiconductor to metal when the metal is placed on an *n*-type semiconductor. In figure 3.10 the measurement principle of the Schottky-EBIC measurement method is shown. Performing an EBIC measurement makes it possible to determine the doping type of the semiconductor. Additionally it is possible to determine the minority carrier diffusion length by analysing the decay of the EBIC signal, as the beam is moved away from the Schottky junction. This measurement method is described in detail in section 4. The idea of this measurement method as well as some examples to use the method are presented there.

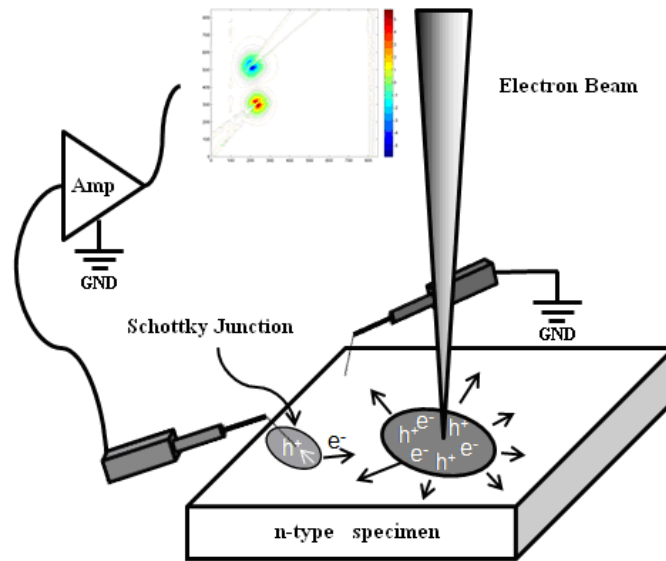


Figure 3.10: Measurement principle of the Schottky-EBIC measurement method to investigate the doping type of a semiconductor and its local minority charge carrier diffusion length. Figure taken from [138]

3.2.5 EBIC Lock-In Measurements

The EBIC lock-in method is a variation of the regular 2D-EBIC measurement where the electron beam is blanked in periodical intervals and the EBIC signal is detected via a lock-in amplifier. This method makes it possible to detect the EBIC signal of biased structures or devices. A schematic of the measurement is shown in figure 3.11

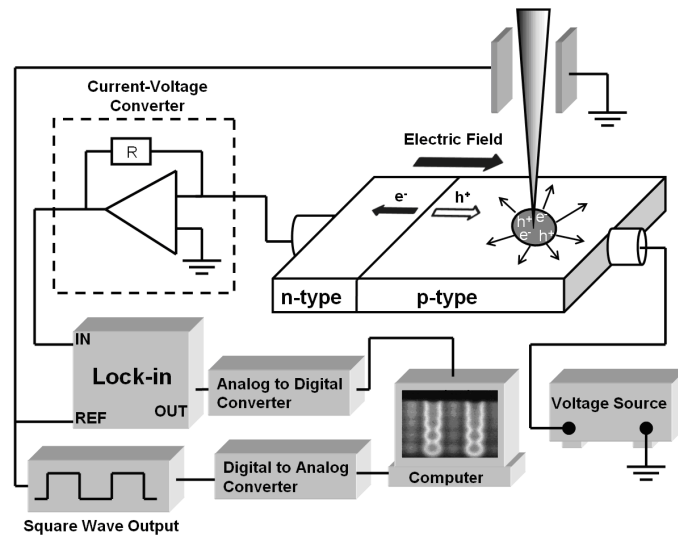


Figure 3.11: Schematic measurement principle of the EBIC Chopping method to investigate reverse biased devices. Figure taken from [139]

3.2.6 Measurement setup: sample holder, current circuit, beam-chopping experiments

In figure 3.12 the typical specimen holders used for EBIC measurements are shown. The cross section specimen holder presses with two copper pieces on the front and backside of the specimen. One of the copper cylinders is in a fixed position and a spring presses the other one with a constant force against it. The electron beam scans over the cross section and the signal is detected. The sample holder has an isolating layer, which separates the electronic connections from the SEM ground contact. The planar view specimen holders are shown in the right part of the figure. They have a very simple geometry without some contacting points. Kleindiek manipulators with sharp metal needles were used to contact the planar structures on these specimen holders.

3.2.7 Extraction of the minority charge carrier diffusion length L_D

When the electron beam hits the semiconductor material, eh pairs are generated in the interaction volume. For extrinsic semiconductors typically used for power electronics/semiconductor diodes, the majority charge carrier concentration is much higher than the minority charge carrier concentration according to the law of mass action. So when charge carriers of both kinds are generated by the e-beam the relative effect on the minority charge carrier concentration is much bigger than on the majority charge carrier concentration. Thus the extracted value of the diffusion length of EBIC measurements is a minority charge carrier property. In literature several different approaches to extract the diffusion length of the minority charge carriers from the EBIC signal decay were published. Mainly one dimensional geometries like in figure 3.7 are used where the electron beam moves perpendicular over the junction under steady state

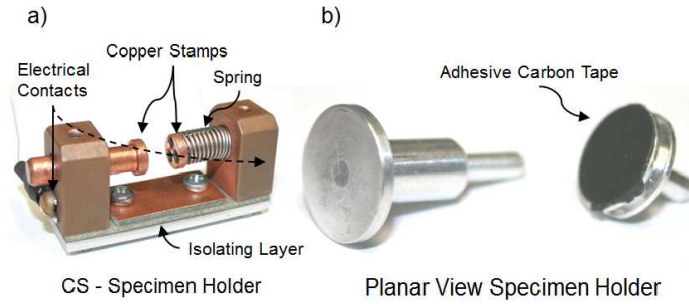


Figure 3.12: Specimen holder for cross sectional (left) and planar (right) EBIC measurements. Figure taken from [124]

conditions. According to the references [140],[141] and [142], the EBIC signal for a surface recombination velocity v_s that is zero, may be written as:

$$I_{EBIC} = k \cdot e^{-\frac{x}{L}}. \quad (3.16)$$

Here x is the distance from the junction, L the diffusion length and k is a constant. By using the natural logarithm of the EBIC signal the diffusion length can be extracted as the inverse slope of the curve.

$$\ln(I_{EBIC}) = -\frac{x}{L} + \ln(k) \quad (3.17)$$

According to the references [141] and [143] the surface recombination velocity can be included in the equation by the variation of the parameter α

$$I_{EBIC} = k \cdot x^\alpha \cdot e^{-\frac{x}{L}} \quad (3.18)$$

The parameter α is zero if the surface recombination velocity is zero, it is $-1/2$ when v_s is infinite. For an alternative measurement geometry like planar structures α is $-1/2$ if v_s is zero and $-3/2$ if v_s is infinite [144], [145],[146]. With this approach only the extreme cases where v_s is zero and infinite are explained, when the value for v_s is somewhere in between there are some ways to extract it from the signal decay as can be seen in [147] and [148]. Another approach is the formation of Schottky junctions with metal tips on a semiconductor. The extraction of the minority charge carrier diffusion length from Schottky EBIC measurements is an important part of the publication "Investigation of Doping Type Conversion and Diffusion Length Extraction of Proton Implanted Silicon by EBIC" in the results section 4 and will not be duplicated in this section.

It should be mentioned that the extraction technique of the minority charge carrier diffusion length is strongly dependent on the offset current measured in regions further away from the EBIC maximum. Depending on the accuracy of the measurement setup and the values for the offset current, very different values for the extracted minority charge carrier diffusion length have been extracted. The analysis of this problem is discussed in the master thesis of M. Faccinelli [124]. Here the offset signal far away from the junction was assumed to be zero. The error implemented by this assumption and some other approaches are explained in this work in detail.

3.2.8 Biased Schottky EBIC measurement

During this so called biased Schottky EBIC experiment a tungsten tip is placed on a lightly doped silicon sample. Additionally, an electric field is applied between both sides of the silicon sample, and the shift of the Schottky EBIC signal is detected. This experiment was designed to extract the local mobility and diffusion constant like in a Haynes Shockley experiment. But from the analysis of the signal shift only the diffusion length which depends on the product of the charge carrier mobility and lifetime can be extracted.

The Schottky contact between the metal and the semiconductor results in a local band bending and the formation of an electric field. Depending on the semiconductor doping type (p - or n -type) an electric field forms, pointing in the direction of the metal or to the semiconductor. In both cases an EBIC signal (positive or negative) can be detected when the electron beam scans over the specimen surface, close to the position where the tip forms the contact. In the left part of figure 3.13 a secondary electron image of the measurement geometry, used for the biased Schottky EBIC measurements is shown. In this geometry the left tungsten tip is used to collect the EBIC signal. The left side of the semiconductor acts as ground potential. The tip positioned at the right acts as one electric contact to apply the electric field. The left side of the sample is metallized and, hence, can be used as a large area, low ohmic contact. In the right part of this figure the region later on investigated with EBIC for several applied electric fields is shown.

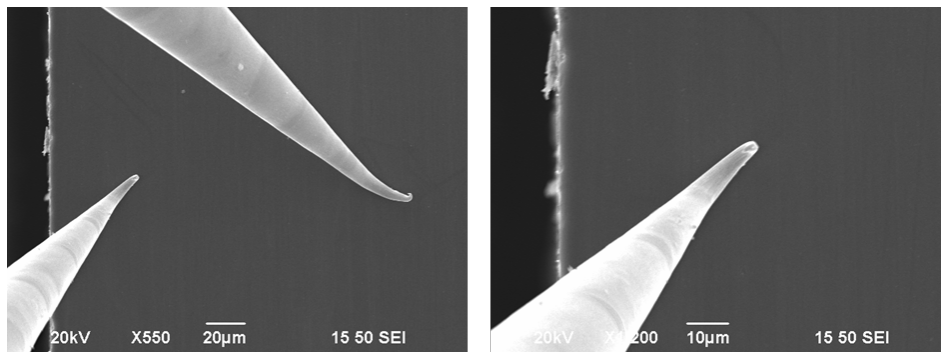


Figure 3.13: (left) Secondary electron image of the measurement geometry used for biased Schottky EBIC experiments. One ohmic contact on the left side of the semiconductor sample and two tungsten tips used as electrical contacts are shown. The left tip (shown in higher resolution in the right image) detects the EBIC signal. (right) Here the chosen region for biased Schottky EBIC measurements is shown.

In the initial measurement geometry the electric field was applied between two tungsten tips, and the EBIC signal was detected by another metal tip. The problem was that one of the tips that applied the electric field had to be reverse biased, resulting in a expansion of the depletion region at the metal-semiconductor junction towards the semiconductor. For higher electric fields this started to affect the initial experiment. To archive a stable measurement results that is not affected by this effect, one ohmic contact was used on the left edge of the specimen.

In figure 3.14 a series of Schottky EBIC measurements with various electric fields applied

between the right tip and the left side of the sample are shown. As can be seen in this contour plot the EBIC Schottky signal is located underneath the tungsten tip where the Schottky contact is formed. In the upper left edge of every single figure the applied electric fields (between the right tip and the left side of the semiconductor sample) can be seen. Already small applied electric fields from 4-48 V/cm shift the EBIC signal to the left. For higher electric fields the maximum of the signal still remains underneath the metal tip but the decay of the signal becomes much wider and shifts with the applied E-field towards the left edge.

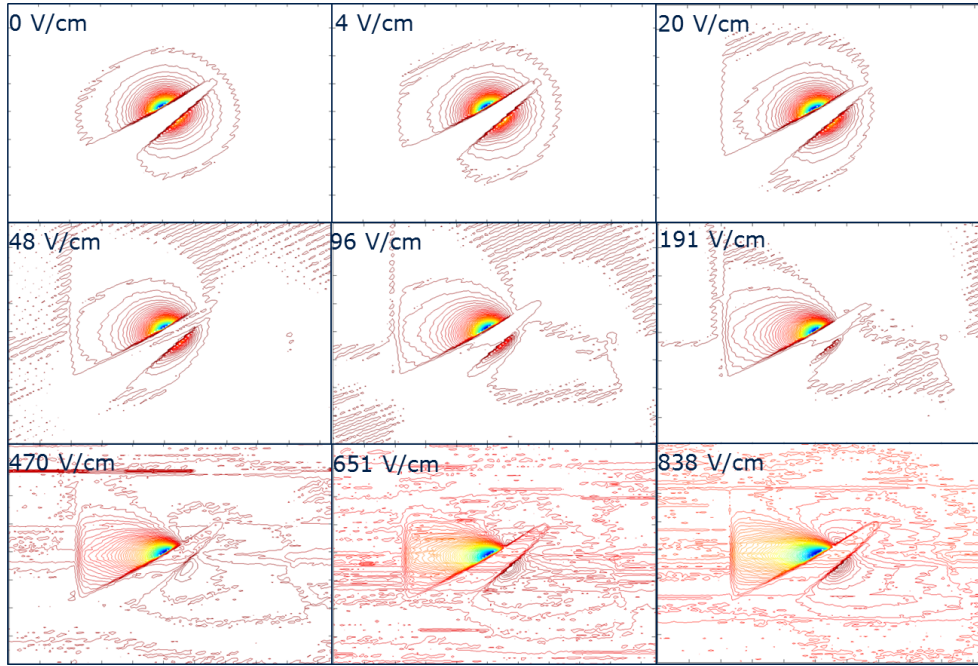


Figure 3.14: A series of biased Schottky EBIC measurements with various electric fields applied. In the upper left edge of every single figure the applied electric field can be seen.

Practically in the experiment, instead of a constant voltage, a constant current was forced to flow. The applied electric field that shifts the EBIC Schottky signal was calculated for our special geometry of a wide ohmic contact to the left and a point contact on the surface to the right using

$$E = \frac{\rho I}{2\pi} \cdot \frac{\vec{r} - \vec{r}_1}{(|\vec{r} - \vec{r}_1|)^3}. \quad (3.19)$$

Here I is the current applied between the tips to build up the electric field, ρ is the resistivity of the substrate material and r is the distance between the tip and the current source. Like in a four point measurement, when a source contact is close to an edge, certain boundary conditions have to be taken into account. One way to achieve this is to add additional image current sources, as shown in the derivation of the four point measurement method in section 3.7. In figure 3.15 EBIC linescans of Schottky EBIC measurements with various electric fields

applied are shown. In the inset top left the electron beam scan direction during the EBIC line scan measurement is indicated. As can be seen there is a clear trend that with increasing electric fields the EBIC Schottky signal shifts to the left respectively becomes higher in the region left from the maxima.

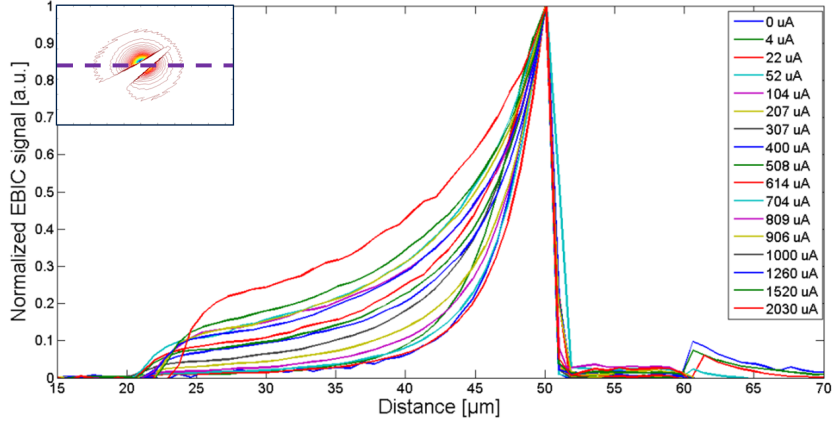


Figure 3.15: EBIC Linescans of Schottky EBIC measurements with various electric fields applied. In the inset top left the electron beam scan direction during the EBIC line scan measurement is indicated.

Due to the fact that minority charge carriers are detected during an EBIC measurement, the distribution of these in the specimen is especially important. When the generation of extra minority charge carriers by an electron beam is approximated with a delta function $G = G_0\delta(\vec{r})$ (e.g. when the electron beam is fixed on a position) their distribution can be calculated by summing up all the delta functions over some period of time.

$$n - n_0 = \frac{G_0}{4\pi r} \exp\left(-\frac{r}{\sqrt{D\tau}}\right) \quad (3.20)$$

where $(n-n_0)$ is the number of excess minority charge carriers, D the diffusivity and r is the distance from the electron beam position. The simulation of the minority charge carrier distribution in the specimen for zero (left) and non zero (middle and right) electric fields applied is demonstrated in figure 3.16. Here delta functions were summed up for $1 \cdot 10^{-7}$ seconds and a diffusion length of $L = 10 \mu\text{m}$.

According to this model of the generation of minority charge carriers and the detection of them during the biased EBIC Schottky measurement in figure 3.17 EBIC Linescans of the biased Schottky EBIC measurements are shown with various electric fields applied and compared to simulated minority charge carrier distributions. For the simulations the minority charge carrier diffusion length of the non biased sample was extracted from EBIC linescans and was used for the simulations.

As can be seen the simulations according to our model and the measurement results do not fit together very well. What makes it difficult to determine exact values for the minority charge

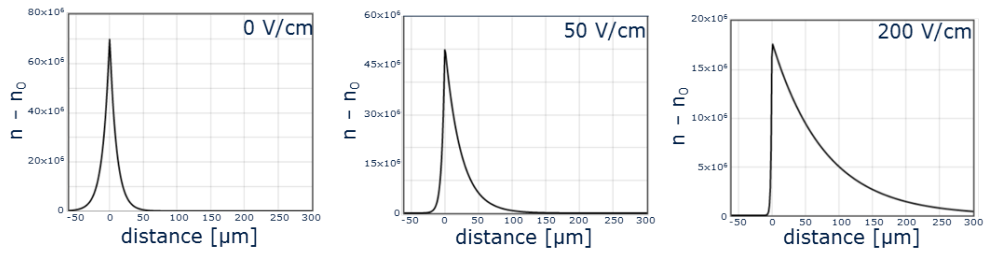


Figure 3.16: Calculated excess minority charge carrier distribution in a specimen for an electric field of 0 V/cm (left), 50 V/cm (middle) and 200 V/cm (right) applied. The generation of the minority charge carriers is assumed as a delta function and localized at the position zero. These simulations were programmed by Peter Hadley

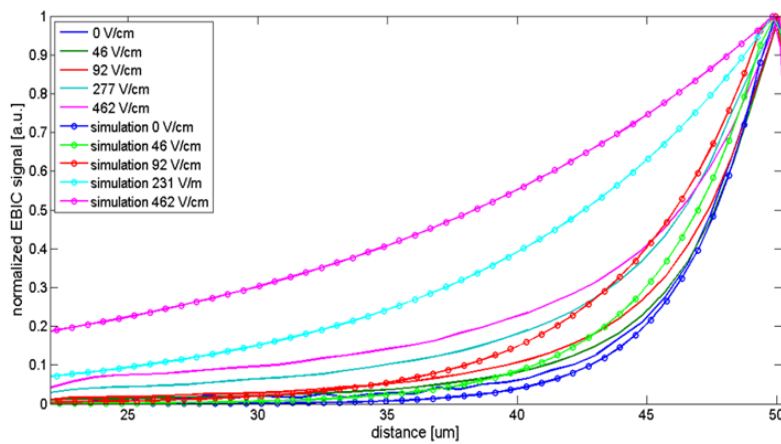


Figure 3.17: Biased Schottky EBIC measurement signals with various electric fields applied (solid lines) compared with simulation results (solid lines + markers)

carrier diffusion length. Nevertheless, this can be a promising approach because by changing the electric field, a lot more data can be collected from a single contact than with an unbiased measurement.

3.2.9 EBIC investigations of III/V semiconductors

In this short subsection the visualization of built in electric fields and defects in III/V semiconductors by EBIC is demonstrated.

EBIC investigation of an epitaxial deposited AlGaIn/GaN hetero junction

First of all GaN/AlGaIn hetero-junction were investigated. These structures are mainly grown by molecule beam epitaxy (MBE) or chemical vapour deposition (CVD). Most grown GaN or AlGaIn layers used in industry are only up to several 100 nm thick. The resolution of the SEM used in this work is not good enough to perform cross sectional investigations on samples of this size. For EBIC investigations the size of the electron beam interaction volume strongly affects the measurement resolution. For a typical acceleration voltage of 20 kV the interaction volume diameter is about 1 μm . Therefore EBIC measurements were performed on a beveled specimen material (comparable to the preparation of SRP samples). Due to this preparation it was possible to investigate the GaN and AlGaIn regions with a thickness of several 100 nm. The electrical contacts necessary to perform the measurement were made by two tungsten tips, contacting both sides of the junction (on the bevel) as can be seen in figure 3.18:

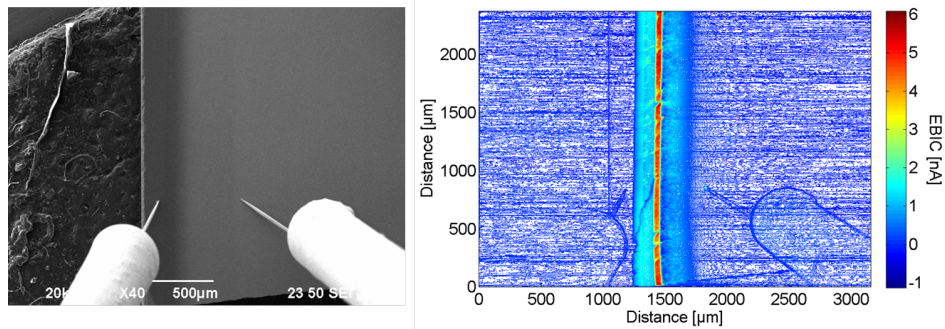


Figure 3.18: (left) SE image of GaN bevel with two tungsten tips pressed on either side of the AlGaIn/GaN hetero-junction. (right) Electron beam induced current measurement, the red region marks the highest EBIC signal and highest built-in electric field.

When the EBIC measurement was performed with a higher magnification, different regions in the specimen material became visible. In figure 3.19 on the left side SE images of the GaN/AlGaIn junction on different positions can be seen. On the right side, EBIC images can be seen. The red region shows the maximum EBIC signal and maximum built-in electric field respectively.

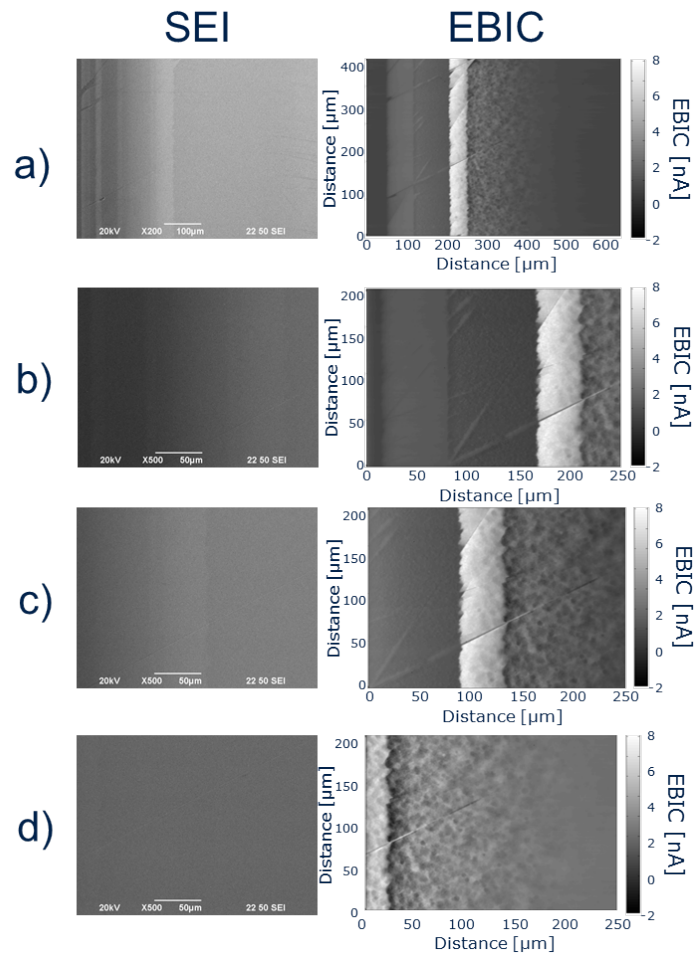


Figure 3.19: SEI (left) and EBIC (right) images of the AlGaIn/GaN heterojunction. In a) an overview shows all regions of the junction. Scan b) shows the region left of the metallurgical junction. c) is oriented directly on the junction. d) shows the region right from the junction.

Depending on the growth conditions, the GaN and AlGaIn layers show varying dislocation densities. As can be seen in the right part of figure 3.20, a much higher concentration of defects can be found in the GaN region right of the junction. In EBIC no real information can be obtained about the microscopic structure of the defects. It can only be seen that there are some recombination centres that collect minority charge carriers on their way to the electric contact.

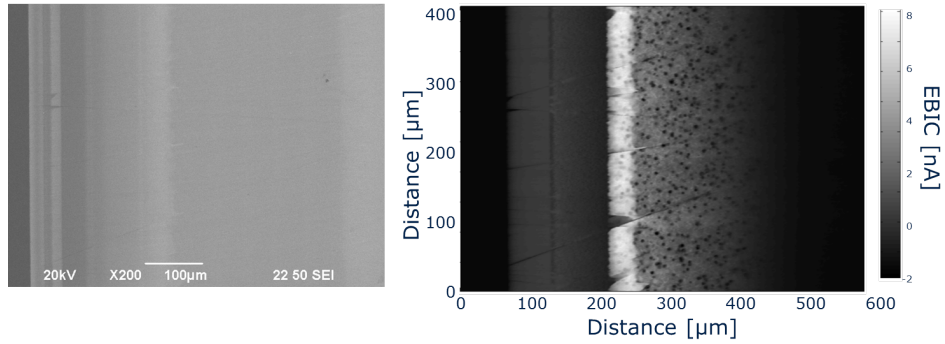


Figure 3.20: (left) SE image and (right) EBIC measurement of AlGaN/GaN hetero junction. The black points in the GaN region to the right of the junction might be due to an increased concentration of crystal defects (e.g. dislocations) in this layer.

FIB cut EBIC scans of AlGaInP devices

This subsection should just be a feasibility study to demonstrate that EBIC measurements can easily be performed in regions cut out by a focused Ion beam (FIB). As can be seen in the following figures, diode structures were investigated and for a TEM analysis a small representative section was cut out using a focus ion beam. In figure 3.21 the EBIC measurement of the FIB cut region is shown. The junction that separates the electron-hole pairs goes parallel to the sample surface in a depth of about $1 \mu\text{m}$ underneath the metal layer.

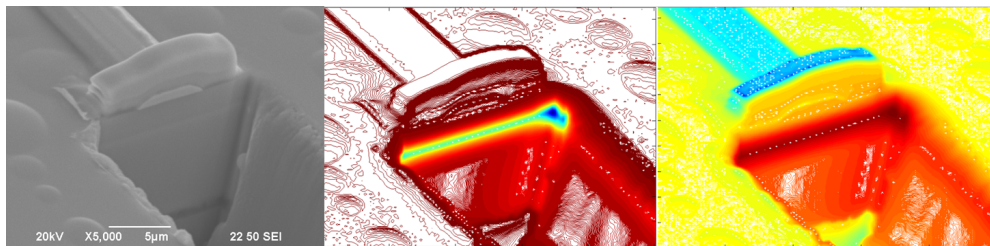


Figure 3.21: (left) SE image of FIB cut region. (middle) EBIC measurement showing the position of the junction in the AlGaInP device. (right) Logarithm of the EBIC signal provides some more structural informations about the device and shows the position of the junction.

3.3 Optical beam induced current (OBIC)

Optical beam induced current or Light Beam Induced Current (LBIC) is a semiconductor analysis technique mainly used to determine sample properties, locate damaged junctions or gate oxide defects and shorts [149], [150]. During the measurement a laser beam scans over the specimen, creating electron-hole pairs that induce a current. During conventional OBIC measurements the laser beam scans over the surface very fast and excites electrons from the valence band to the conduction band due to single photon absorption. Therefore the photon energy has to be higher than the band gap of the investigated semiconductor. In the case of silicon the forbidden (indirect) band gap has an energy of 1.12 eV. Photons with energies less than the direct band gap are not able to push electrons from the valence band to the conduction band. In figure 3.22, SEI, OBIC and EBIC images of planar test structures are shown. The planar test structure is very large and the resolution of the junctions look approximately the same in both scans. Nevertheless, due to the smaller interaction volume of the electrons during an EBIC measurement in comparison to the spot size of the laser beam, EBIC measurements can have a much better spacial resolution when the electron energy is reduced. In this planar geometry, plotting the logarithm of the measured EBIC signal proved to be an useful method to visualize buried structures that might only provide a small signal.

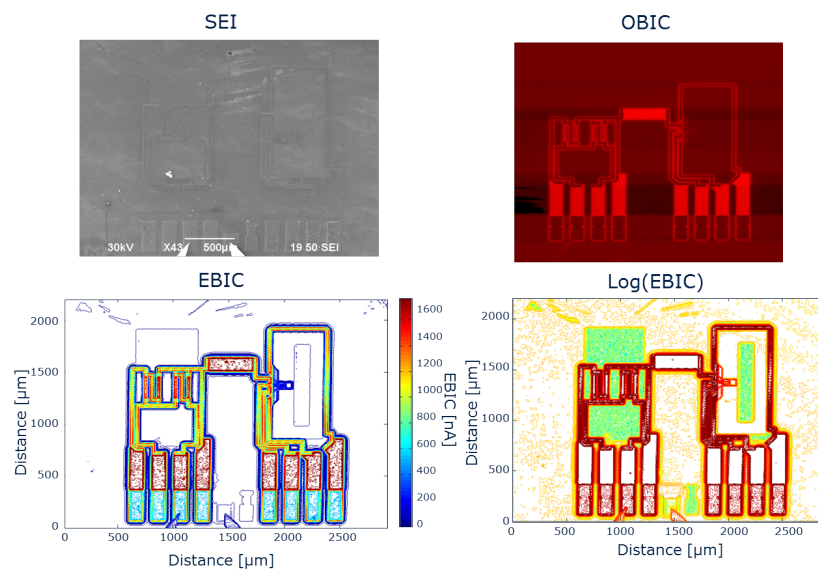


Figure 3.22: (top left) Secondary electron image of a planar sensor teststructure. (top right) OBIC and (bottom left) EBIC measurement signal and (bottom right) logarithm of the measured EBIC signal of the planar test structure. OBIC measurements were performed by Georg Spanring

3.4 Transmission electron microscopy (TEM)

Transmission Electron Microscopy (TEM) is an analytical technique where highly energetic electrons are transmitted through a specimen thinner than 100 nm. By analysing the transmitted electrons, it is possible to produce images with atomic resolution. Depending on the atomic numbers of the elements in the specimen, the thickness of the sample can be between several tens of nano meters and micrometers. Typical acceleration voltages are between 80 keV and 400 keV. A scintillator is used to detect the high energetic electrons. CCD sensors are rather inappropriate to detect the signal directly because the high energy particles would damage the detector. As in other electron microscopes, a high spatial resolution of the measurement can be achieved. Presently the resolution limit of this technique is below 1 Angstrom. The specimen preparation is rather sophisticated. TEM specimens have to be very thin and the preparation method should not introduce additional defects or ions. Typically, the specimens are first cut with a diamond wire saw. Then they are ground on a disc grinder with SiC grinding paper and polished with diamond paste. Afterwards the samples are put into a dimple grinder and ion thinned in a so called Precision Ion Polishing System with 4 keV argon ions. Here ions are accelerated towards the specimen, slowly removing material until some regions close to the dimple hole are especially thin. Only the electron transparent regions can be investigated during the TEM investigations. Alternatively, Focused Ion Beam (FIB) milling is a popular method used to cut out a small specimen volume of interest out of a bulk material. Due to the fact that the highly energetic gallium ions used might influence on the defect complexes in the silicon crystal structure this preparation method was not used. All TEM investigations in this thesis were performed by Dr. Christian Gspan. All specimen preparations to perform TEM measurements were performed by Manuel Paller.

3.4.1 TEM investigation of H⁺-implanted silicon

Parts of the TEM investigations on H⁺-implanted m:Cz silicon were already published and can be found in the paper "High dose proton implantations into silicon: A combined EBIC, SRP and TEM study". In this section TEM and electron diffraction measurements are introduced as a tool to investigate proton implanted Fz silicon. Figure 3.23 shows a TEM image of proton implanted (energy: 400 keV, dose: $1 \times 10^{16} \text{H}^+/\text{cm}^2$) Fz silicon focused at the implantation depth. It can be seen that after high dose implantations platelet-like structures as well as extended defect complexes are formed like in m:Cz silicon.

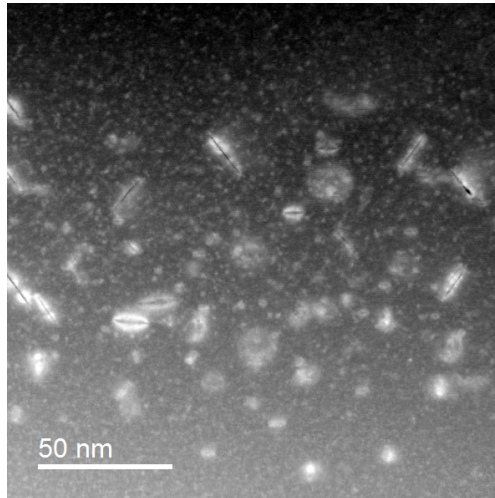


Figure 3.23: TEM overview image of proton implanted ($400\text{ keV } 1 \times 10^{16} \text{H}^+ / \text{cm}^2$) Fz silicon focused in the end of range implantation region.

In figure 3.24 a high resolution TEM image of a platelet defect complex in $[110]$ is shown. As in Cz silicon all of these platelet defect complexes are oriented on 110 planes.

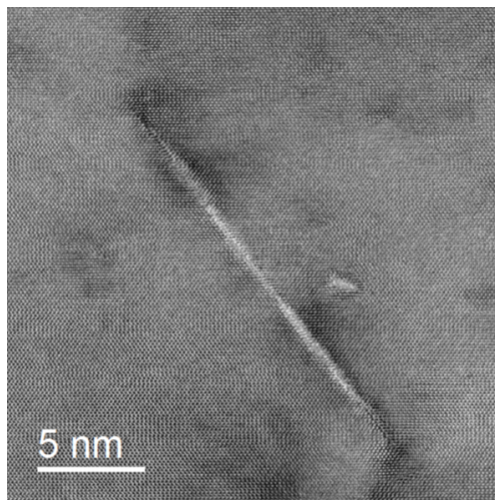


Figure 3.24: High resolution TEM image of a platelet defect complex formed in Fz silicon due to high dose proton implantation (energy: 400 keV , dose: $1 \times 10^{16} \text{H}^+ / \text{cm}^2$).

The TEM investigations in figure 3.25 show that the platelet defect complex looks like a dislocation. An atomic resolution image of indicated area in the left image is shown in the right

image. In the middle of the right image the platelet defect width changes from three atoms to two atom.

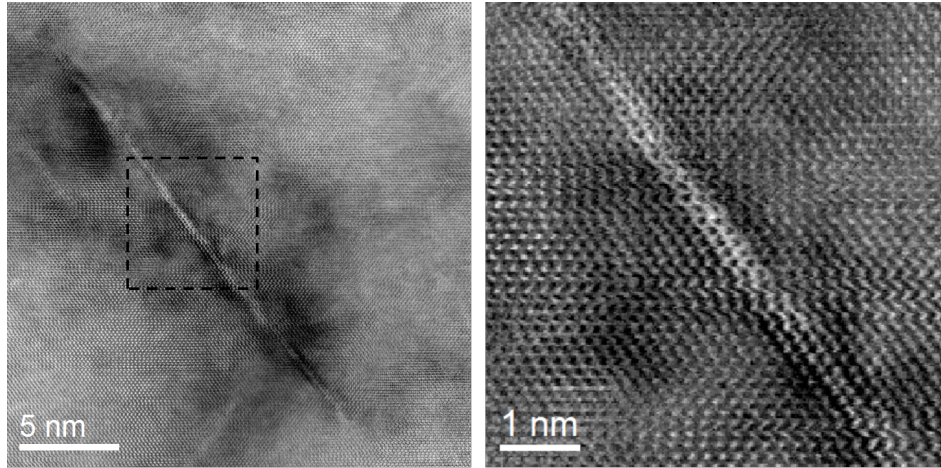


Figure 3.25: (left) High resolution TEM images showing a platelet defect in proton implanted silicon.(right) A dislocation is indicated when the width of the defect complex changes from three to two atom rows.

3.4.2 Electron diffraction investigations

Electron diffraction uses the wave character of electrons and is similar to x-ray or neutron diffraction. Since the wavelength of the electrons is much smaller than the distance between the atoms, the Ewald sphere cuts through those reciprocal lattice points in the plane perpendicular to the beam. This provides information about the crystal structure and the orientation of the crystals. Additionally electron diffraction can be used to study the short range order of amorphous solids. This is used in this thesis when the change of the lattice parameter is investigated near the implantation depth.

In figure 3.26 a TEM image (left) and the fast Fourier transformation (FFT) (right) of a perfect silicon sample are shown. This is how the FFT image looks like for a perfect diamond crystal lattice with nearly no defects nor implantation damage present in this region.

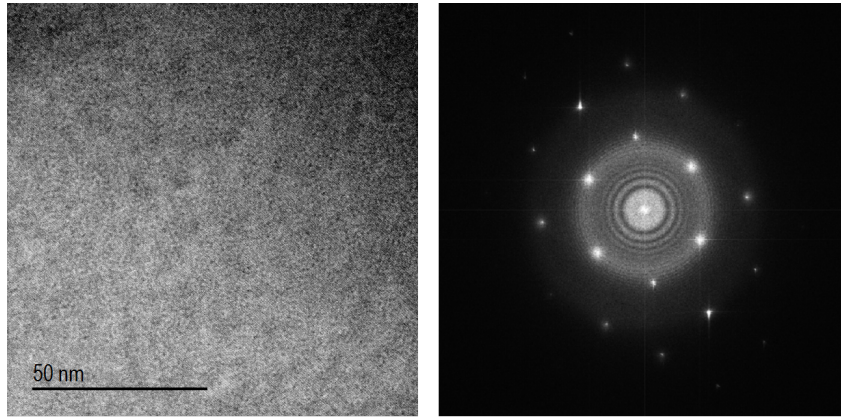


Figure 3.26: (left) TEM image and (right) FFT image of the TEM image of the same area of a perfect silicon sample.

Figure 3.27 shows a TEM image and the FFT of the TEM image of a hydrogen implanted silicon lattice in the area of the implantation depth. There is no clear defect structure visible in the TEM image, there is a lot of damage in the crystal lattice at this depth. In this region the FFT image varies drastically from the initial silicon pattern. Rings formed between some points in the diffraction pattern. This shows that TEM investigations have strong limitations identifying small defect contraction or point defects in general. In comparison to that, the FFT images of the TEM measurements show a clear difference between the two regions, nevertheless they are very difficult to interpret.

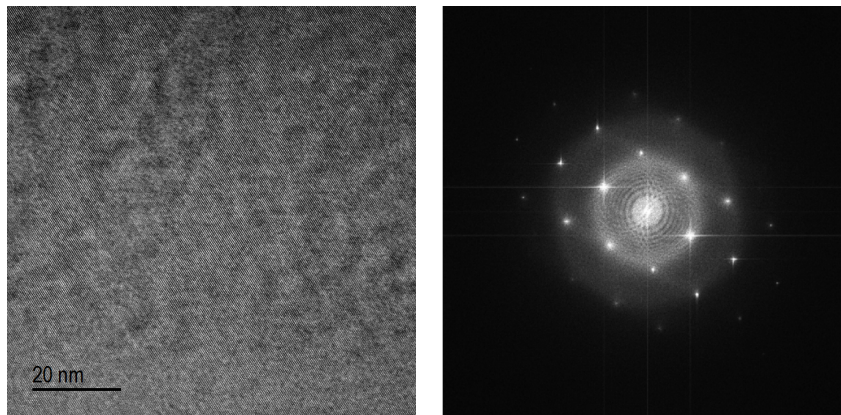


Figure 3.27: (left) TEM image of a hydrogen implanted silicon sample at the implantation depth (implantation energy: 4 MeV, implantation dose: $4 \cdot 10^{14} \text{H}^+ / \text{cm}^2$) annealed at 500 °C for 1 hour (right) FFT image of the same area as the TEM image of this hydrogen implanted silicon sample.

If the detailed structure and orientation of a defect in the crystal lattice is not known it is rather hard to extract this information from the diffraction pattern. In figure 3.28 a comparison between the simulation of an electron diffraction pattern of a regular silicon lattice and a silicon lattice with additional vacancies positioned in periodic patterns in the lattice is shown. It demonstrates that already small defects like vacancies can have a high influence on the electron diffraction pattern, especially when they are present in periodic patterns in the lattice.

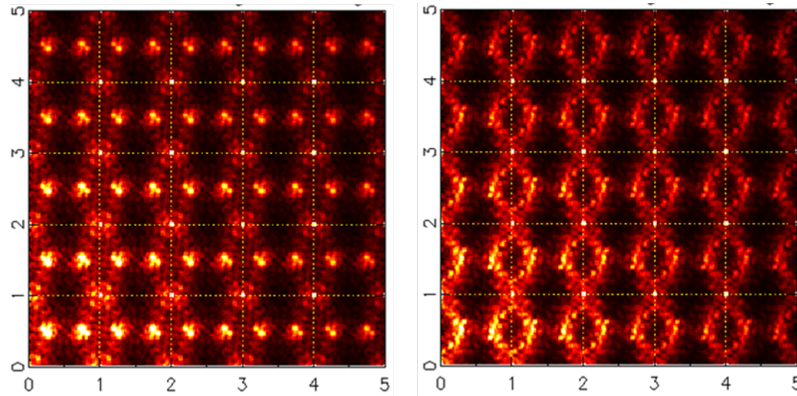


Figure 3.28: (left) Simulation of an electron diffraction pattern of a perfect silicon lattice. (right) Simulation of an electron diffraction pattern of a silicon lattice with additional vacancies in the lattice positioned in periodic patterns in the lattice.

3.4.3 Advanced electron diffraction investigations

The following electron diffraction and electron transmission microscopy investigations should demonstrate what this analytical techniques are capable of and can be used in the future for. All measurements were performed on high dose and low energy proton implanted m:Cz silicon samples (implantation energy: 400 keV, implantation dose: $1 \cdot 10^{16} \text{H}^+ / \text{cm}^2$). Figure 3.29 gives an overview how the end of implantation range defect layer formed due to the proton implantation looks like. The defect layer is located at a depth of about $4.5 \mu\text{m}$ underneath the surface of the silicon wafer. It is about $0.5 \mu\text{m}$ thick and the highest density of the extended defects is clearly concentrated at the projected implantation depth of the protons.

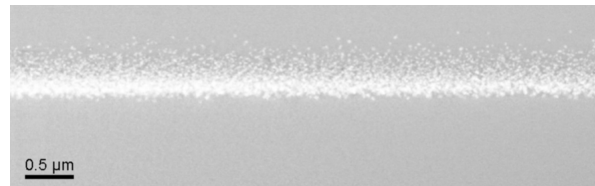


Figure 3.29: TEM overview image of proton implanted damage layer in approx. $4.5 \mu\text{m}$ depth (energy: 400 keV, dose: $1 \cdot 10^{16} \text{H}^+ / \text{cm}^2$). The specimen surface is located underneath the shown area in this image.

In the left part of figure 3.30 an overview TEM image of the formed defect layer is shown. In the computed middle image besides TEM structural informations, every pixel represents electron diffraction measurement informations. The middle image was calculated from the area around the end of range defect layer indicated by the green box in the left image. As shown with the red arrows, convergent beam electron diffraction (CBED) measurements of three different regions are displayed in detail. The lowest electron diffraction image represents the region shallower than the defect layer where the protons were going through without causing too much damage to the crystal lattice. Here the intensities of the central diffraction peaks in the pattern are very high. The middle electron diffraction image from the region directly in the defect layer (end of range implantation depth - where most of the damage is done to the crystal lattice), produces a much broader distribution of electron diffraction peaks. And the highest electron diffraction image from the region shallower than the defect layer, shows very dominant electron diffraction peaks in the center of the pattern again. This region was not harmed at all by penetrating protons.

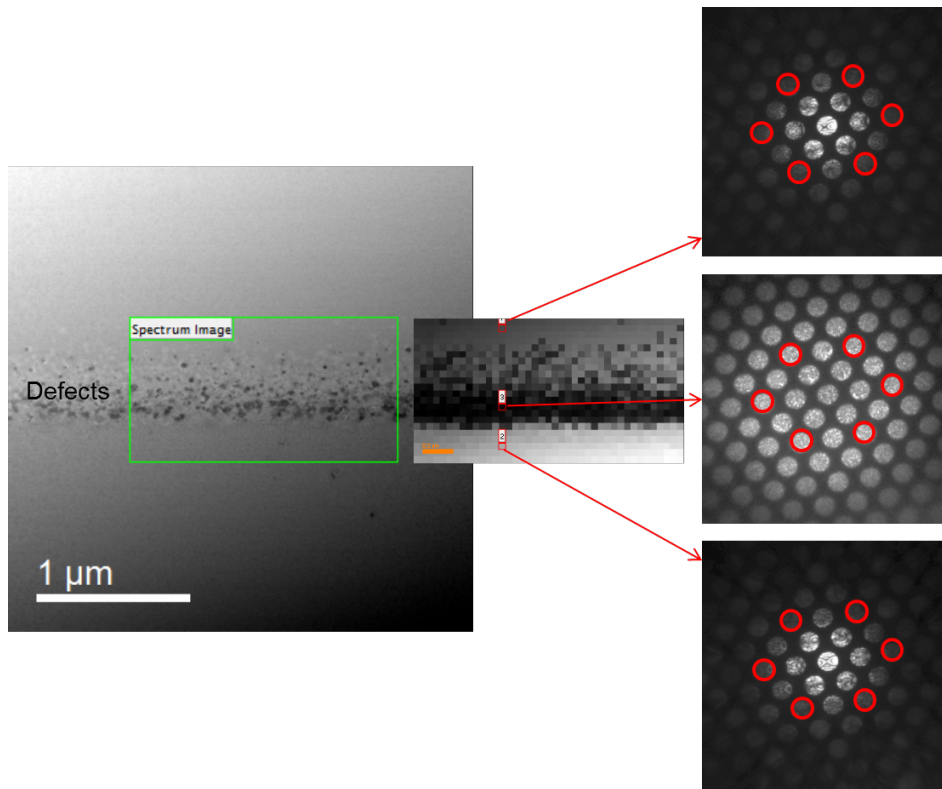


Figure 3.30: (left) TEM image of proton implantation induced defect layer in m:Cz silicon, (middle) electron diffraction measurement map (right) electron diffraction images of prominent positions on the cross section of the silicon wafer (shallower, directly on and deeper than the implantation depth).

As can be seen in figure 3.31 this concept also works the other way round. The electron diffraction patterns can be used to calculate TEM images of the silicon crystal structure and the position/structure of the defect complexes. Only the region of interest can be used to compute the structural image. Computing the right electron diffraction images results into strong dark, bright or dark and bright contrast compared to the grey background. The signal intensity of the defects results from the intensities of the selected reflections in the electron diffractions. A very bright image results from high intensities, a dark signal results from low intensities.

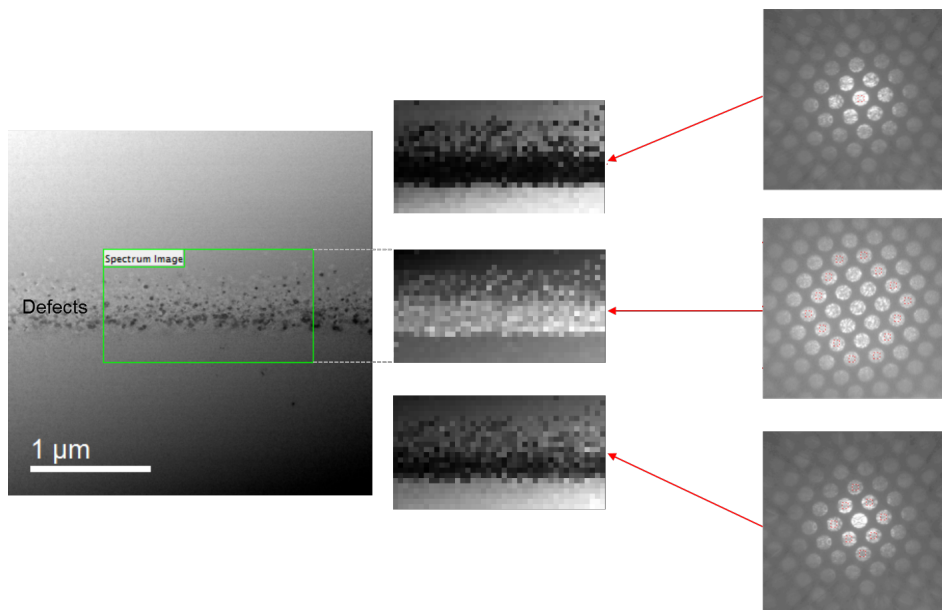


Figure 3.31: (left) TEM image (middle) TEM and electron diffraction map calculated from (right) electron diffraction images of three different regions of interest.

In figure 3.32 the intensity distribution of the electron diffraction peaks is shown in more detail. The line profile of the seven central diffraction peaks used for this investigation are indicated by the light blue box in the top image. In the middle image the electron diffraction intensities of this peaks at different positions are displayed. Again, three different prominent positions were chosen. The implantation was performed from below, so the blue line represents the shallowest position where the defect layer starts. The green line is positioned at the region with maximum implantation damage (implantation depth - end of range peak). The red line represents the position where the damaged layer ends. Obviously the diffraction peak distribution changes a lot. In the maximum damaged region the diffraction peak distribution is homogeneously distributed over the peaks in the pattern. In the more shallow and deeper regions the diffraction peak intensities are concentrated in the center peaks.

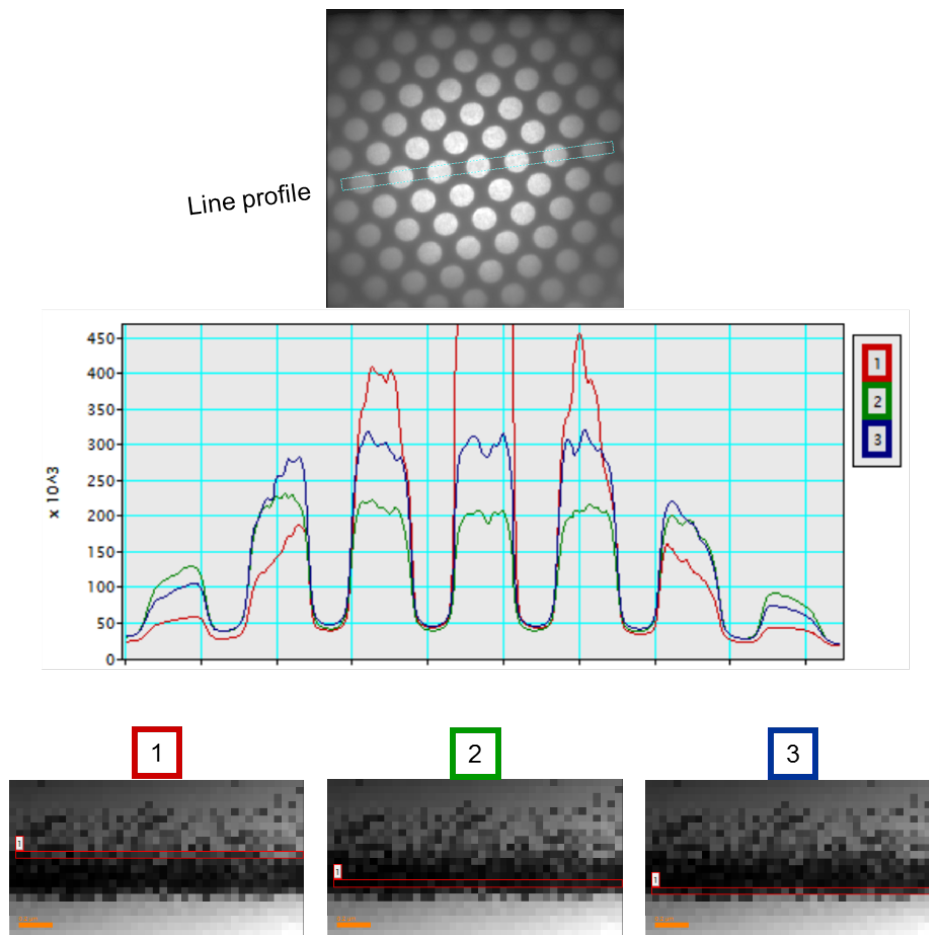


Figure 3.32: (top) Electron diffraction image, (middle) electron diffraction intensity depending on position on damaged layer, (bottom) digitalized TEM images with indicated positions.

Figure 3.33 shows electron diffraction investigations where specific streaks appear in the proton damaged regions. The orientation of this streaks is normal to the formed platelet defect complexes in this region. As was reported the platelets are oriented in the $\langle 110 \rangle$ directions and the streaks form 90 degree to that direction. In the region underneath the implantation depth no diffraction streaks were detected. The orientation and intensity of this streaks can be another input parameter to learn about defect complex orientations.

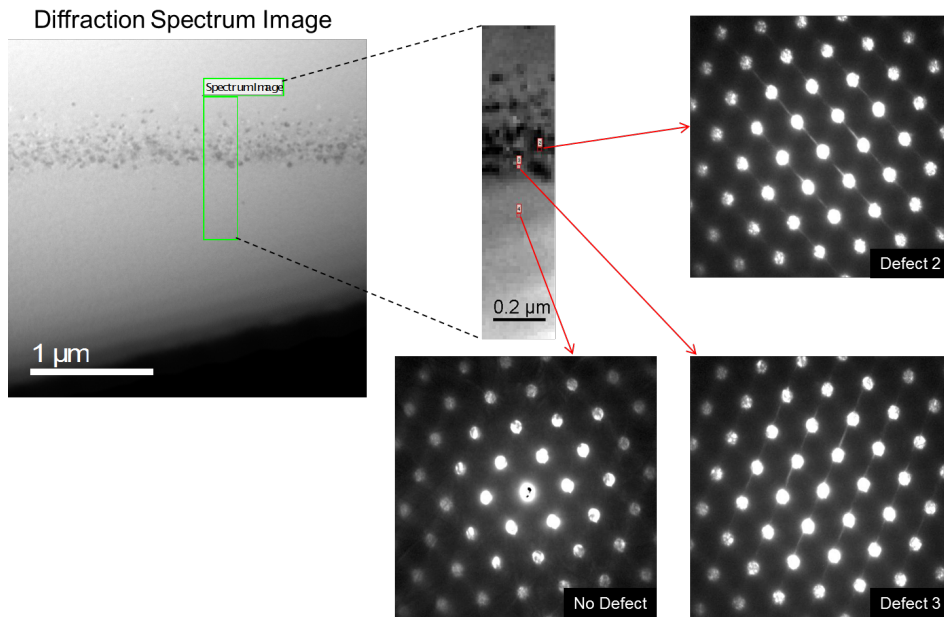


Figure 3.33: (left) TEM image of proton implanted silicon (middle top) Computed TEM and electron diffraction image (right) electron diffraction images of different region around the damaged region formed due to the hydrogen implantation. The red arrows indicate the positions of the electron diffractions.

In figure 3.34, again the capabilities of TEM electron diffraction investigations are demonstrated. For this electron diffraction investigation smaller convergence angles are used. The red arrows in the bottom figures indicate the reconstructed real space defect complexes on the silicon cross section from the electron diffraction images. So again the position, size and orientation of the defects can be determined from the digitalized electron diffraction images.

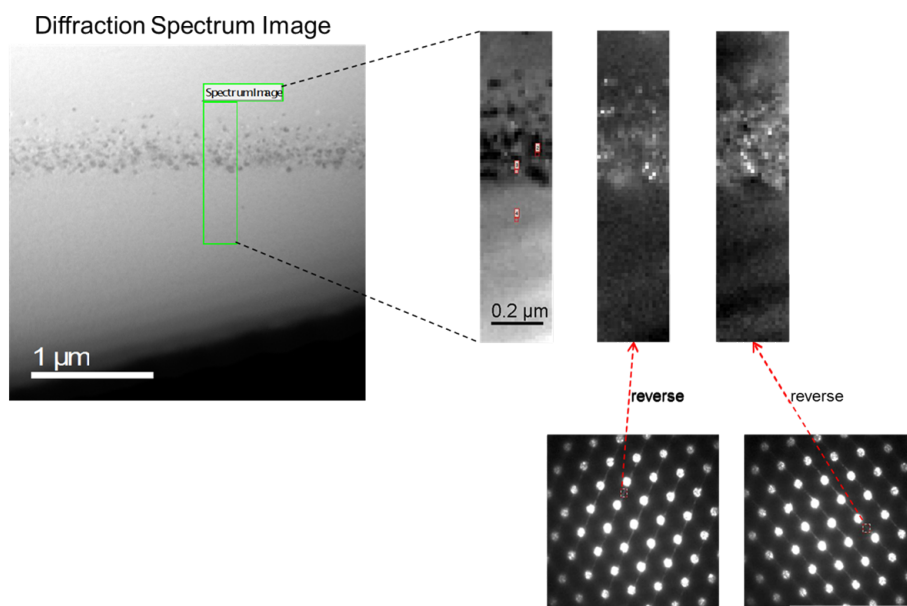


Figure 3.34: (left) TEM image of proton implanted silicon sample, (bottom right) electron diffraction measurements used to calculate the real space structures shown top right

In figure 3.35 it is shown that the inner and outer electron diffraction peaks from measurements (marked by the green and yellow arrows) can be used separately to construct a real space damaged region (range of defects). Obviously the patterns provide different informations. Adding all the informations from the diffraction peaks together, a TEM image containing a fraction of the defect complexes results.

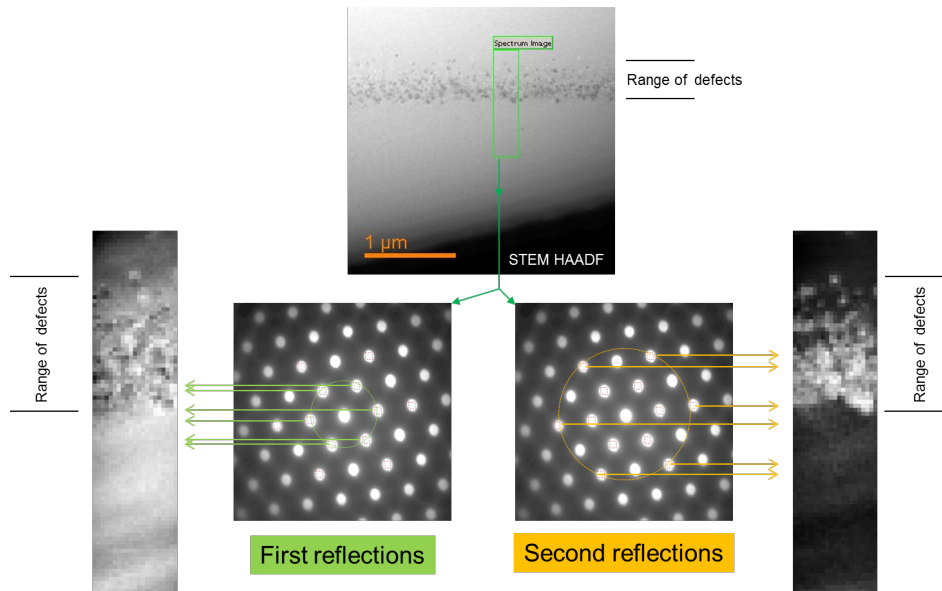


Figure 3.35: (top) TEM image (bottom middle) electron diffraction images (bottom outside) calculated defect complexes in the silicon lattice

To find out more about the influence of the defect structure or the informations the different electron diffraction peaks are delivering, detailed studies of proton implanted silicon samples have to be performed.

3.5 Spreading resistance profiling (SRP)

Spreading Resistance Profiling (SRP) is a measurement technique using two metal tips pressed on a polished specimen surface measuring the resistance profile of a semiconductor sample [151]. Using calibration samples the resistivity and charge carrier concentration profiles can be calculated from the measured resistance. It provides charge carrier concentration profiles over a very broad range from 10^{12} - 10^{19} cm^{-3} .

During the measurement two tungsten probe tips, mounted on manipulators, are pressed on a polished surface in a distance of about 40-50 μm from each other (as can be seen in figure 3.36). The semiconductor sample is ground at an angle and the tips are placed on the bevel during the measurements. This makes it possible to investigate the depth profile more exactly than on the flat cross section surface. However it complicates the interpretation somewhat because the current penetrates the sample to a depth of about the distance between the tips. The probes are pressed on the surface area of about 20 μm^2 with a weight of several grams resulting in a absolute pressure of about 10 GPa. The pressure should be high enough to cause a phase transition of silicon from the diamond crystal structure to the beta-tin phase producing a nearly ohmic contact. But, if the pressure would be that high, the tungsten tips would deform first and the contacting would not be reproducible. In fact the contact consists of several micro-contacts which show more Schottky-like behaviour than ohmic. During the measurement series the tips are lifted up and put down a small distance further on the bevel to investigate the change of the resistance, respectively the charge carrier concentration in this depth. A voltage of 5-20 mV is applied between the tips measuring the current. The measured sum resistance consists of the sample resistance and the contact resistances. There is always some voltage drop across the reversed biased Schottky junctions and the two point measurement geometry in general. To get the correct value for the sample resistance and to make the measurement more reproducible a special preparation of the probing tips and the surface of the sample is necessary [152].

The measured spreading resistance profile can be converted into a resistivity (ρ) profile using the calibration curve. The charge carrier concentration can be calculated using

$$N_{n,p}(x) = \frac{1}{e\rho(x)\mu_{n,p}} \quad (3.21)$$

where $\mu_{n,p}$ is the mobility of the majority charge carriers in the local region. The mobility is influenced by lattice defects, ionized dopants or defects. According to the rule of Mathiessen, the effective mobility is,

$$\mu = \left(\frac{1}{\mu_x} + \frac{1}{\mu_y} + \frac{1}{\mu_z} + \dots \right)^{-1}. \quad (3.22)$$

If there are no high defect concentrations present in the crystal typical values for the mobilities determined by the doping concentration of the sample are used [153], [154].

Due to the fact that SRP measurements are performed on a beveled surface it can have a high spacial resolution. The increment between two measurement points on the beveled surface is 5 μm , in special cases 2.5 μm . This corresponds to a step-size of 43 nm in the resulting profile, if the sample is ground at an angle of 0.5 deg. It is important to keep this in mind when the measurements are analysed. The charge carrier concentration has a minimum at the depletion region of a pn -junction. Depending on the doping concentration this region may spread over several μm . Due to the physical resolution limit of this measurement technique, it is not

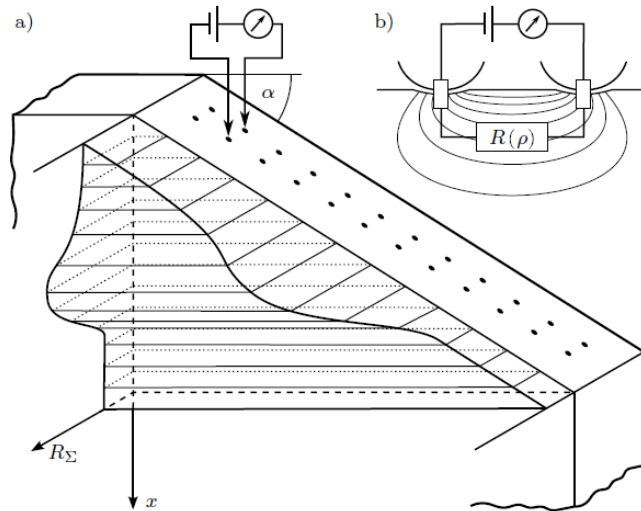


Figure 3.36: a) Measurement principle of Spreading Resistance Profiling (SRP). Two metal tips are pressed against the surface of a semiconductor specimen and the resistance between the tips is measured. b) Representative circuit diagram of the measurement method. Figure has been taken from reference [32]

possible to determine the exact position of the pn -junction. In a measured spreading resistance profile, the junction might be shifted from its actual position. The bevelling of the wafer itself can also have a big influence on the resulting profile. Layers underneath the surface may have higher or lower resistances that can affect the current paths [155],[156]. In every case this can change the measured resistance profile drastically. In the analysis software, several different tools/methods are available to compensate for influences like this [157],[158],[159]. Also several smoothing algorithms are used to correct the signal from measurement noise problems [160],[161]. SRP is not an absolute measurement technique (e.g. like four-point measurements) but it needs calibration samples/curves, and some assumptions (like a constant mobility over the whole region, reproducible contacts,...) to determine the resistivity and charge carrier concentration profile. In this thesis SRP measurements were mainly used to investigate proton implanted silicon wafers. The temperature dependent evolution of the implantation profiles were investigated for different implantation and annealing conditions. Also the activation of donor and acceptor point defects and their dissociation was investigated.

In the appendix an analytical analysis of SRP measurements can be found. A derivation of J. C. Maxwell's result (Maxwell was the first to investigate the electrical properties of point contacts [162]) made by Prof. P. Hadley [163] is shown there. With the help of M. Faccinelli the derivation to calculate the resistance for different measurement geometries was modified.

3.6 Scanning spreading resistance measurements (SSRM)

Scanning Spreading Resistance Measurement (SSRM) is a measurement technique used to map two-dimensional resistance profiles. From the resistance data the local dopant concentration can be calculated. During the scan the change in resistance between a measurement probe (a conductive tip in contact mode - like in an atomic force microscope (AFM)) and the backside of a sample is measured. In comparison to SRP measurements only one measurement tip is used. During the measurement a constant voltage is applied from the tip to the backside of the sample. This current is then amplified by a sensitive current amplifier and saved for every measurement. In figure 3.37 a SSRM measurement of a silicon diode implanted with hydrogen (three implantations with three different implantation energies) is shown.

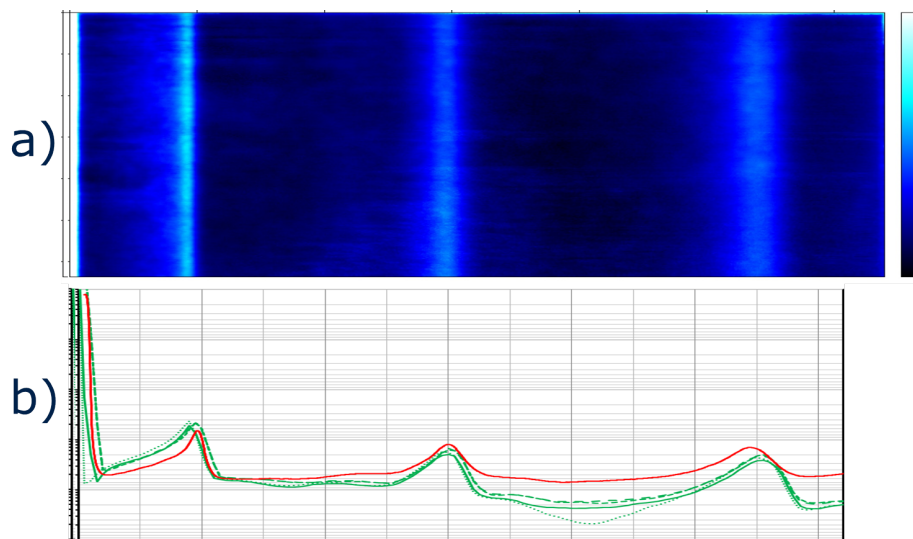


Figure 3.37: SSRM measurement of a test-diode implanted with hydrogen three times with different energies. In figure a) the two dimensional SSRM plot is shown. The bright regions represent higher dopant concentration than the dark regions. In comparison to that in figure b) the one dimensional scan is plotted. This shows the same resolution like all other SRP scans shown in this thesis. SSRM measurements were performed at Infineon Dresden.

Because of the measurement geometry, where the resistance is measured between one tip and the backside of the sample it is complicated to calibrate the setup to obtain absolute and accurate values for the charge carrier concentration. The resulting resolution limit of SSRM measurements is $1 \cdot 10^{14} \text{ cm}^{-3}$. Thus, for the investigation of high resistivity samples, like most samples investigated in this work, it provides no advantage to SRP measurements beside the two dimensional visualization.

3.7 Four point measurements

The resistivity ρ is the quotient of the electric field E and the current density j

$$\rho = \frac{E}{j}. \quad (3.23)$$

where the conductivity is

$$\sigma = \frac{1}{\rho} = n_e e \mu_e \quad (3.24)$$

Here n_e and n_p are the carrier densities, μ_e and μ_p are the charge carrier mobilities and e is the elementary charge. As it was already presented in the section about Spreading Resistance Profiling, the two point measurement performed during a SRP measurement is able to determine the charge carrier concentration. L. B. Valdes [164] analysed very special geometries of metal tips. In this section a more generalized version of this method with a variation of the tip positions is generalized and boundary conditions for the edges of the samples are presented. This is important when the measurements are performed on the cross section of a wafer and when the metal contacts are formed by putting metal tips on the semiconductor.

When an electrical current I is flowing, the current density \vec{j} near a small contact on a flat sample with a uniform resistivity is:

$$\vec{j} = \frac{I}{2\pi r^2} \vec{r} \quad (3.25)$$

when there are two current contacts, and the current is flowing from r_1 to r_2 the current density results in

$$\vec{j} = \frac{I_{12}}{2\pi} \left(\frac{\vec{r} - \vec{r}_1}{|\vec{r} - \vec{r}_1|^3} - \frac{\vec{r} - \vec{r}_2}{|\vec{r} - \vec{r}_2|^3} \right) \quad (3.26)$$

This is only true for a homogeneous, infinitely large sample. If the metal contacts are placed too close to a specimen edge, it is important to ensure that no current flows out of the sample. The condition of zero current perpendicular to the boundary can be achieved by placing two additional image current sources, at the positions \vec{r}_1' and \vec{r}_2' . These positions are mirrored opposite the real current sources in respect to the specimen edge. This results in the following equation,

$$\vec{j} = \frac{I_{12}}{2\pi} \left(\frac{\vec{r} - \vec{r}_1}{|\vec{r} - \vec{r}_1|^3} - \frac{\vec{r} - \vec{r}_2}{|\vec{r} - \vec{r}_2|^3} + \frac{\vec{r} - \vec{r}_1'}{|\vec{r} - \vec{r}_1'|^3} - \frac{\vec{r} - \vec{r}_2'}{|\vec{r} - \vec{r}_2'|^3} \right). \quad (3.27)$$

From this expression the electric field distribution can be calculated by multiplying the current density with the resistivity:

$$\vec{E} = \rho \vec{j} = \frac{\rho I_{12}}{2\pi} \left(\frac{\vec{r} - \vec{r}_1}{|\vec{r} - \vec{r}_1|^3} - \frac{\vec{r} - \vec{r}_2}{|\vec{r} - \vec{r}_2|^3} + \frac{\vec{r} - \vec{r}_1'}{|\vec{r} - \vec{r}_1'|^3} - \frac{\vec{r} - \vec{r}_2'}{|\vec{r} - \vec{r}_2'|^3} \right) \quad (3.28)$$

To perform a four-point measurement, four tips are necessary. A current is biased between the outer tips and the voltage drop is measured between the inner ones. The two additional contacts are placed on the surface (see figure 3.38) at \vec{r}_3 and \vec{r}_4 , the potential difference between these tips V_{34} is,

$$V_{34} = \frac{\rho I_{12}}{2\pi} \int_{r_3}^{r_4} \left(\frac{\vec{r} - \vec{r}_1}{|\vec{r} - \vec{r}_1|^3} - \frac{\vec{r} - \vec{r}_2}{|\vec{r} - \vec{r}_2|^3} + \frac{\vec{r} - \vec{r}_1'}{|\vec{r} - \vec{r}_1'|^3} - \frac{\vec{r} - \vec{r}_2'}{|\vec{r} - \vec{r}_2'|^3} \right) d\vec{r} \quad (3.29)$$

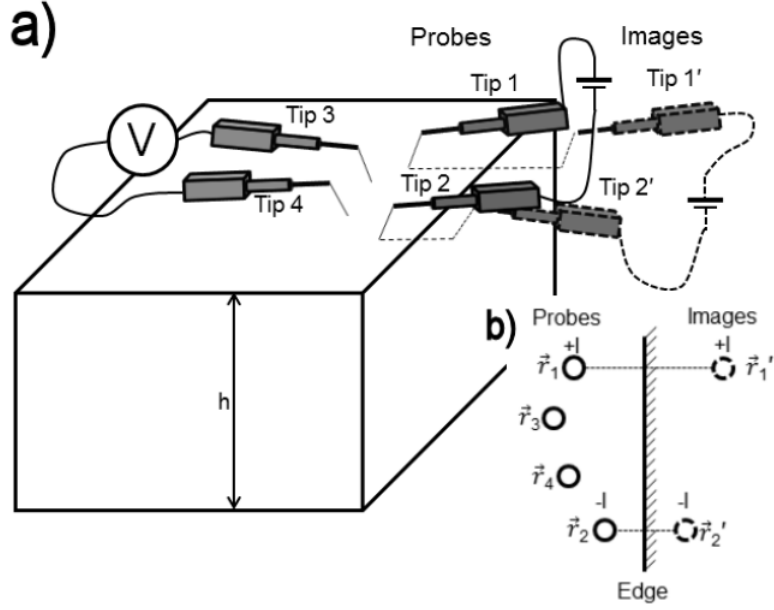


Figure 3.38: a) Schematic illustration of a four-point resistivity measurement, with four micro-manipulator tips contacting on a specimen close to an edge. b) Sketch of the four-point measurement scheme in planar view. Taken from reference [124].

As all contacts are in the $z=0$ plane, the integration only has to be performed for x and y :

$$\begin{aligned}
 V_{34} = & \frac{\rho I_{12}}{2\pi} \int_{x_3}^{x_4} \left(\frac{x - x_1}{[(x - x_1)^2 + (y_3 - y_1)^2]^{3/2}} - \frac{x - x_2}{[(x - x_2)^2 + (y_3 - y_2)^2]^{3/2}} + \right. \\
 & \left. + \frac{x - x'_1}{[(x - x'_1)^2 + (y_3 - y'_1)^2]^{3/2}} - \frac{x - x'_2}{[(x - x'_2)^2 + (y_3 - y'_2)^2]^{3/2}} \right) dx - \\
 & - \frac{\rho I_{12}}{2\pi} \int_{y_3}^{y_4} \left(\frac{y - y_1}{[(x_4 - x_1)^2 + (y - y_1)^2]^{3/2}} - \frac{y - y_2}{[(x_4 - x_2)^2 + (y - y_2)^2]^{3/2}} + \right. \\
 & \left. + \frac{y - y'_1}{[(x_4 - x'_1)^2 + (y - y'_1)^2]^{3/2}} - \frac{y - y'_2}{[(x_4 - x'_2)^2 + (y - y'_2)^2]^{3/2}} \right) dy
 \end{aligned} \quad (3.30)$$

After the integration V_{34} results in

$$V_{34} = \frac{\rho I_{12}}{2\pi} \left(\frac{1}{s_{31}} + \frac{1}{s_{31'}} + \frac{1}{s_{42}} + \frac{1}{s_{42'}} - \frac{1}{s_{41}} - \frac{1}{s_{41'}} + \frac{1}{s_{32}} + \frac{1}{s_{32'}} \right)^{-1}, \quad (3.31)$$

here

$$s_{mn} = \sqrt{(x_m - x_n)^2 + (y_m - y_n)^2} \quad (3.32)$$

For four point measurements with an edge boundary the final equation for the resistivity re-

sults in:

$$\rho = \frac{2\pi V_{34}}{I_{12}} \left(\frac{1}{s_{31}} + \frac{1}{s_{31'}} + \frac{1}{s_{42}} + \frac{1}{s_{42'}} - \frac{1}{s_{41}} - \frac{1}{s_{41'}} - \frac{1}{s_{32}} - \frac{1}{s_{32'}} \right)^{-1}. \quad (3.33)$$

The measurement is performed by sweeping a bias current I_{12} and measuring the voltage drop V_{34} . From this values the resistivity can be calculated.

When the contacts are far from all edges, the following equation can be used for the calculation of ρ :

$$\rho = \frac{2\pi V_{34}}{I_{12}} \left(\frac{1}{s_{31}} + \frac{1}{s_{42}} - \frac{1}{s_{41}} - \frac{1}{s_{32}} \right)^{-1}. \quad (3.34)$$

In this configuration $1/s_{31'}$, $1/s_{32'}$, $1/s_{41'}$ and $1/s_{42'}$ are zero as the edge is very far away from the measured position, compared to the distance between the tips.

3.7.1 Four point measurements on a thin film

When current contacts are placed on a thin film sample with uniform resistivity, the current spreads radially and the current density is

$$\vec{j} = \frac{I}{2\pi t r^2} \vec{r} \quad (3.35)$$

where t is the thickness of the sample as can be seen in figure 3.39. This case was analysed in reference [165]. The expression for the resistivity is

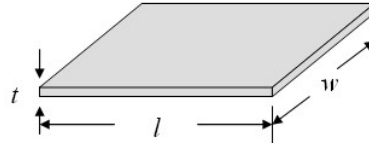


Figure 3.39: Thin film sample investigated with four point measurements. Taken from reference [165] with permission.

$$\rho = \frac{4\pi t V_{43}}{I_{12}} (l_{31} - l_{32} - l_{41} + l_{42})^{-1}. \quad (3.36)$$

V_{43} again is the voltage difference between the inner tips, I_{12} is the current applied between the outer tips and l is

$$l_{mn} = \ln \left((x_m - x_n)^2 + (y_m - y_n)^2 \right). \quad (3.37)$$

from the resistivity the sheet resistance can be calculated. The square resistance is the resistance when $l = w$.

$$R_{square} = \frac{\rho l}{w t} = \frac{\rho}{t} = \frac{4\pi V_{43}}{I_{12} t} (l_{31} - l_{32} - l_{41} + l_{42})^{-1} \quad (3.38)$$

3.8 Stopping and range of ions in matter (SRIM/TRIM) simulations

The ion implantation process (implantation depth, damage and ion-profile) can be simulated using the SRIM software [123]. The online available software package contains simulation packages of the ion implantation mechanism, ion stopping mechanism, implantation ranges and distributions for many ions with a large range of energies in a variety of target materials. Ion implantation energies up to GeV can be simulated using analytical equations for ion-atom collisions. For the interested reader, a detailed description of the working principle of the SRIM simulation package can be found in reference [166]. The software package originally comes from the work of Biersack et al [167] and Ziegler et al [123] and was improved and expanded several times since then. Figure 3.40 shows the simulation results of the implantation of 4 MeV H^+ ions into silicon. The trajectories of the penetrating ions, as well as, the distribution of the ions in the profile are displayed.

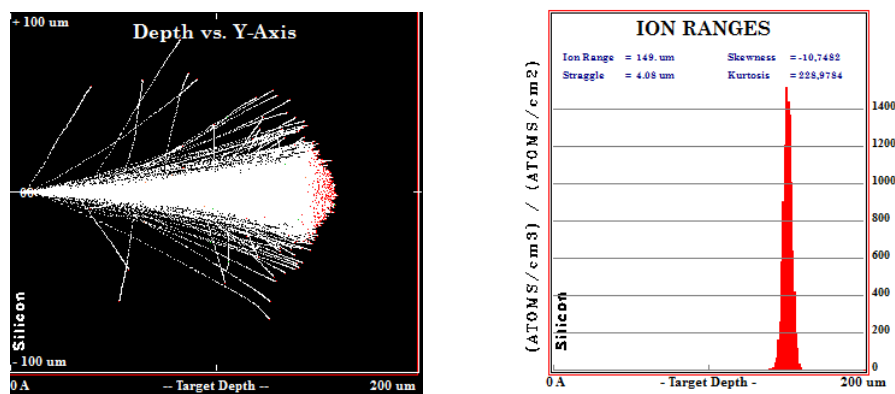


Figure 3.40: The figure on the left shows the implantation with all the trajectories of the penetrating 4 MeV H^+ ions into the silicon lattice. The figure to the right shows the implantation profile distribution(H in Si) for our parameters.

Especially **TR**ansport of Ions in Matter (TRIM) is a very comprehensive set of programs that can calculate the three dimensional distribution of the ions penetrating into the target material including kinetic effects of deceleration and energy loss, implantation damage and ionizations.

In the figures 3.41 and 3.42 the three dimensional distribution and damage profile (displacements and vacancies) of/duo to the implanted ions is shown.

Due to an 2.5 MeV and 1 MeV H^+ implantation into silicon with an implantation dose of $1 \times 10^{14} H^+ cm^{-2}$ the following implantation damage and hydrogen profile calculated using SRIM results can be plotted in the same figure 3.43.

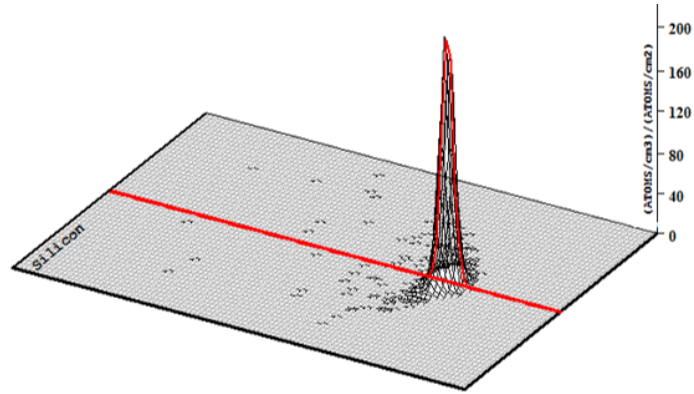


Figure 3.41: Three dimensional 4 MeV H-ion implantation into silicon distribution simulated with SRIM/TRIM

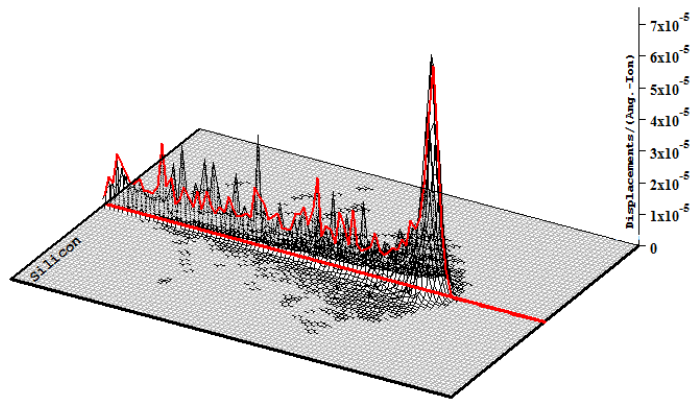


Figure 3.42: The implantation damage (displacements and vacancies) after the implantation of 4 MeV H^+ ions into the silicon lattice

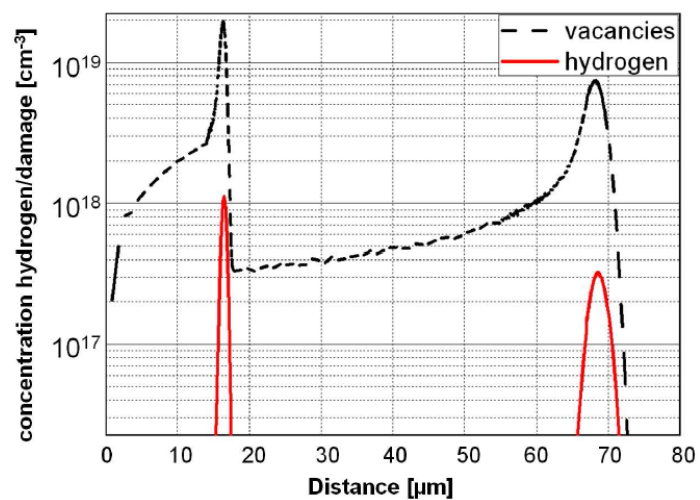


Figure 3.43: (Proton implantations into silicon simulated by SRIM at zero Kelvin. The solid line represents the concentration of hydrogen and the dashed line the vacancy and interstitial concentration of the radiation damage. The H⁺-implantations were performed with 2.5 and 1 MeV and a dose of $1 \times 10^{14} \text{ H}^+ \text{ cm}^{-2}$ [139]

Chapter 4

Publications

Co-Authors

In this short section the co-authors that contributed to the papers published during this PhD thesis are introduced:

Dipl. Ing. Martin Faccinelli was a master student, and is currently employed as a PhD student in the research group of Prof. Peter Hadley at Graz University of Technology. Martin and I have been working as a team on most of the experimental investigations, especially all kind of EBIC studies performed in this research project. He brings in a broad knowledge in chemistry that helps to see/interpret measurement results from a complementary point of view.

Dipl. Ing. Moriz Jelinek started his PhD thesis in 2012 at Infineon Technologies Austria AG in Villach. His research interests concentrate on implantation physics and defects resulting due to proton implantation into silicon. He provides us with proton implanted silicon wafers and helps with the interpretation of implantation studies.

Dr. Johannes G. Laven finished his PhD thesis in 2013 (title: "Protonendotierung von Silizium: Untersuchung und Modellierung protoneninduzierter Dotierungsprofile in Silizium"). He concentrated on SRP and DLTS investigations of proton implanted charge carrier doping profiles due to proton implantations in silicon. Now he is working in the IGBT division at Infineon Technologies in Munich and still actively supports our research group with his know how and ideas.

Dr. Werner Schustereder is an expert on implantation processes at Infineon Technologies Austria AG in Villach. He initiated the project to investigate the properties of defects generated by proton implantation into silicon and he supervises how these processes are presented in journal papers. He consults with us about which implantations should be investigated and he provided us with implanted wafers.

Prof. Reinhart Job is the dean of the department of electrical engineering and informatics at

the Fachhochschule Münster. He is an expert in the field of semiconductor material and device physics and published a variety of papers in this field. He has been in close cooperation with the research and development department of Infineon Technologies for the last two decades. He consults us with his know how about the formation of hydrogen-related defect complexes in silicon.

Dr. Hans-Joachim Schulze is a senior principal researcher at Infineon Technologies AG in Munich Germany. He was one of the leading minds that had the idea to use proton implantations to modify the characteristics of power semiconductor devices which was shown to have a major influence on the device performance of Infineon's semiconductor power devices. He explained the purpose of field stop implantations, super junction devices and doping compensation to us and discussed the interpretation of the results of the publications.

Dr. Christian Gspan is a senior researcher at the institute of electron microscopy at Graz University of Technology. He is an expert in transmission electron microscopy and electron diffraction. He performed all the TEM and electron diffraction measurements shown in this thesis.

Prof. Werner Grogger is the leader of the transmission electron microscopy research group at the institute of electron microscopy at Graz University of Technology. He is an expert in transmission electron microscopy and published a variety of papers in this field. Due to close cooperations with industrial companies, like semiconductor device manufacturers. He gathered a lot of know how about TEM investigations of silicon structures/devices.

Prof. Peter Hadley is leading our research group and the institute of solid state physics at Graz University of Technology. He supports the work in our group with his knowledge and experience when setting up new experimental setups, by programming simulations, interpreting measurement results and he actively takes part at the writing process of manuscripts for journal publications.

Imaging Superjunctions in *CoolMOSTM* Devices using Electron Beam Induced Current

The following corresponds to the publication

S. Kirmstoetter, F. Faccinelli, P. Hadley, R. Job, W. Schustereder, J.G. Laven, H.-J. Schulze, *Electrochemical Society Transactions* Volume 49 (1) 475-481 (2012) The Electrochemical Society

The author of this thesis was responsible for the following points

- EBIC measurements
- measurement analysis and interpretation
- main authorship

The contribution of the other authors of this publication are listed below

- M. Faccinelli: EBIC measurements and measurement analysis
- P. Hadley: authorship, interpretation of measurement results
- R. Job: interpretation of measurement results
- J.G. Laven: authorship
- W. Schustereder: provided test/measurement structures, interpretation of measurement results
- H.-J. Schulze: authorship, interpretation of measurement results

Imaging Superjunctions in CoolMOS Devices using Electron Beam Induced Current

S. Kirnstötter^a, M. Faccinelli^a, P. Hadley^a, R. Job^b, W. Schustereder^c, J.G. Laven^d, and H.J. Schulze^d

^a Institute of Solid State Physics, Graz University of Technology, Graz 8010, Austria

^b Fachbereich Elektrotechnik und Informatik, Fachhochschule Münster, Steinfurt, Münster 48565, Germany

^c Infineon Technology Austria AG, Villach 9500, Austria

^d Infineon Technology AG, Munich 81726, Germany

Electron beam induced current (EBIC) measurements were used to produce cross sectional images of superjunctions in CoolMOS™ power transistors. The positions of the *pn*-junctions were determined by EBIC measurements. Knowing the exact locations of the *pn*-junctions is important for CoolMOS™ since it relies on the principle of charge compensation. For charge compensation, the donors in the *n*-doped regions must be compensated by an equal amount of acceptors in the *p*-doped regions. We show that EBIC can provide valuable input for process tuning and process simulations. This will enable the use of smaller dimensions and higher doping levels resulting in a lower on-state resistance.

Superjunction transistors

Conventional MOSFET (Metal Oxide Semiconductor Field-Effect Transistors) devices exhibit high on-state losses with blocking voltages V_{br} exceeding 100 V. These on-state losses are caused by relatively high on-resistances in conventionally designed MOSFETs with blocking voltages higher than several hundred volts. The contribution of the lightly doped drift region to the on-resistance $R_{DS,on}$ increases superlinearly with V_{br} . So-called superjunction MOSFETs, like Infineon's CoolMOS™, apply the concept of charge compensation, which allows significantly higher substrate doping of the drift region while at the same time maintaining a high breakdown voltage (1,2). In such devices, $R_{DS,on}$ only increases proportionally to $V_{br}^{1.3}$. By this, superjunction devices break the physical limit of the standard Si-MOSFET technology with respect to the area-specific turn-on-resistance value $R_{on} \times A$ (Figure 1). Hence, superjunction transistors are particularly attractive for applications calling for high blocking voltages in the range of 400 V to 1000 V.

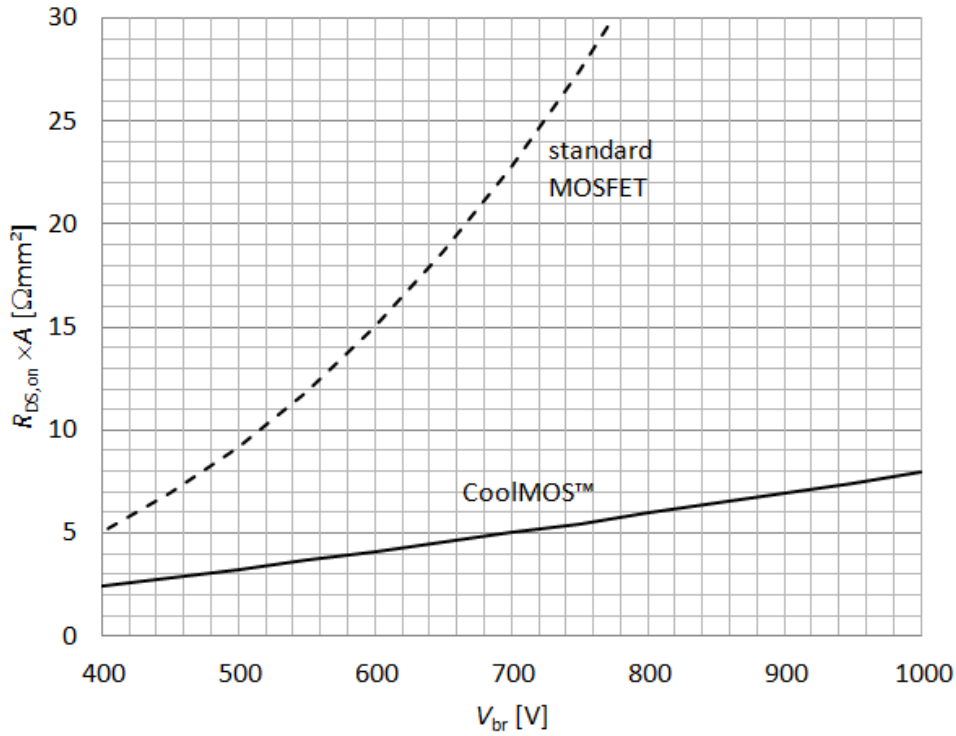


Figure 1: Comparison of $R_{on} \times A$ in a standard high-voltage MOSFET with the CoolMOS™ technology.

Figure 2 (b) depicts a cross-section of a single column in a superjunction MOSFET illustrating the charge compensation principle. The main design difference compared to a conventional high-voltage MOSFET, depicted in Figure 2 (a), are the p -type columns that are placed between the drain and source region. Since the negative ionized acceptor charges in the p -columns compensate for the positive ionized donor charges in the n -columns, the doping concentration in the n -type column can be increased by more than one order of magnitude in a superjunction MOSFET compared to a conventional MOSFET without deterioration of the blocking capability. In the on-state, the n -columns in superjunction MOSFET devices serve as low-resistance paths for the electrical current. The increase in their doping concentration relative to the lightly doped drift region of the classical MOSFET design results in a huge decrease of the on-resistance. However, 50 % of the drift zone area is required for the additional p -type columns. In total, the on-resistance is typically reduced by the factor 5.

The creation of the alternating p -columns and n -columns, and the fact that the acceptor charges in the p -columns must compensate for the donor charges in the n -columns with a very high accuracy poses the main challenge in superjunction MOSFET fabrication. A method to achieve a high accuracy of the charge compensation is based on multiple epitaxial depositions of highly-doped n -type layers and masked acceptor ion implantations in between into each layer in between the depositions. The method is drafted in Figure 2 (c). After depositing all epitaxial layers with the implanted acceptor regions, the implanted acceptor dopants are diffused by a high-temperature annealing step. The p -columns are formed by the broadening of the implanted p -type regions. However, this method leads to a significant deviation from the desired column shape depicted in

Figure 2 (b) which requires careful fine-tuning of the individual implantation doses and annealing parameters. Alternative fabrication methods, e.g., using high-energy proton or helium implantations to implement the n -columns with hydrogen-related donors have also been investigated (3).

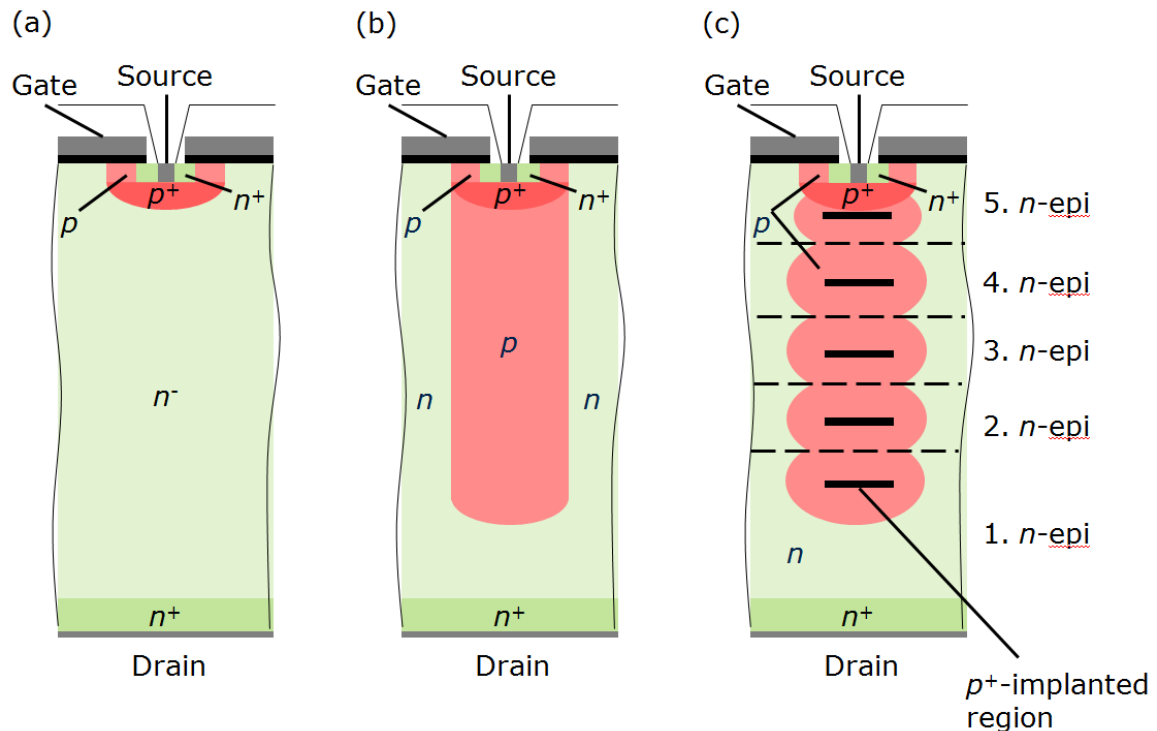


Figure 2: Cross-section of a conventional high-voltage MOSFET (a), a superjunction MOSFET with vertical n -type and p -type columns for charge compensation (b), and an illustration of the fabrication process by multiple epitaxial depositions of n -type layers with masked acceptor ion implantations in between the layers (c).

Electron beam induced current measurements

The Electron Beam Induced Current measurements were performed in a JEOL JSM-6490 LV Scanning Electron Microscope using Stanford Research System SR570 Current Amplifiers. The wafer with the CoolMosTM structures was broken, ground and placed in a specimen holder so that the structures were visible in the SEM for lateral and cross sectional investigations. To perform lateral scans, the superjunctions were exposed by grinding the wafers from the drain side.

EBIC is an analysis method used in a Scanning Electron Microscope (SEM) to investigate buried junctions or defects in semiconductors (4-5). During an EBIC measurement, high-energy electrons from the electron beam enter the silicon and generate electron-hole pairs. If the charge carriers diffuse into a region where there is a built-in electric field, such as a pn -junction, charge separation will occur and a current will flow. This is essentially the same thing that happens in a solar cell except that the electron-hole pairs are generated by light in a solar cell and by high energy electrons in EBIC. The electron beam is scanned across the sample and the current is recorded for

each position of the electron beam. The current contacts are placed on opposite sides of the pn -junction. If the n and p regions have similar dopant concentrations, the maximum EBIC current occurs at the position of the metallurgical junction. This condition is satisfied for the CoolMOS™ superjunctions. The electron beam energies used for these investigations were varied from 5 to 30 kV.

Compared to other methods that were used to investigate the structure of CoolMOS™ superjunctions such as scanning capacitance microscopy or selective etching, (6) EBIC is a relatively fast technique where the surface preparation is not so critical. In EBIC, the high energy electrons penetrate a certain distance below the surface. The region where the electrons lose their energy and generate electron-hole pairs is known as the interaction volume. The EBIC signal arises from the entire interaction volume and is therefore not as surface sensitive as other methods.

Results

The Figures 3-6 show EBIC images of the p -columns of a superjunction. The maximum EBIC current (white in the 2D plots) indicates the positions of the pn -junctions. The image shows that the column width modulates significantly. The wafer was not broken exactly along a row so that columns deeper from the broken surface are visible on the left but not on the right. Thus columns from left to right are imaged at different cross-sectional planes. The modulation of the column widths makes it harder to achieve the desired charge compensation all along the columns. Beside the regular two dimensional image of the EBIC signal also three dimensional images are presented in every figure to provide an idea of the shape of the p -columns.

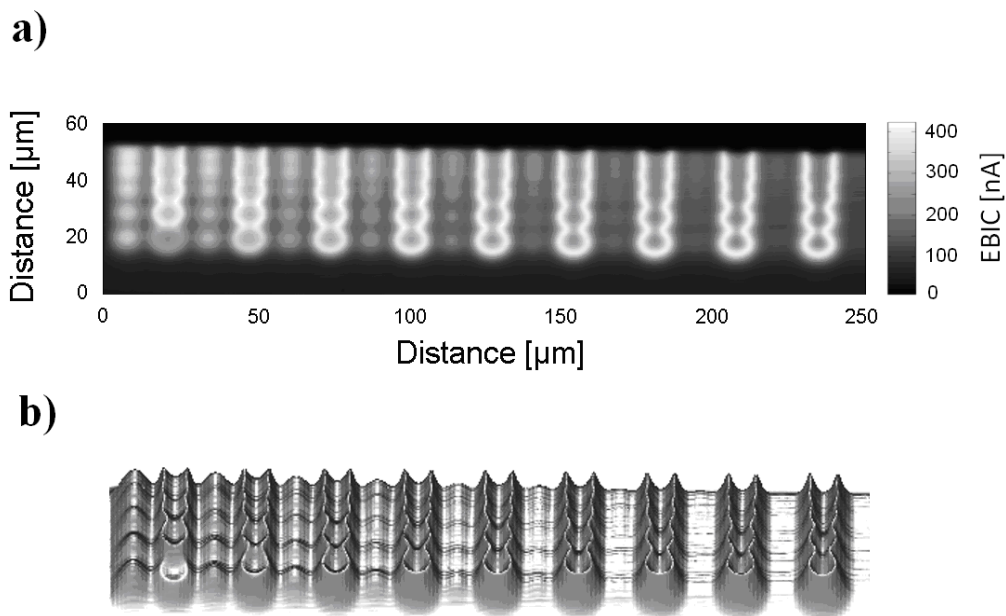


Figure 3: An EBIC image of the p -columns where the EBIC current was measured between the source and drain. The maximum current (white) indicates the positions of the pn -junctions. The image was taken at an acceleration voltage of 20 kV. EBIC measurement of CoolMOS™ structure visualized in a) Grayscale- and b) 3D-Plot.

In Figure 4 an EBIC image taken at an acceleration voltage of 5 kV is presented. Compared to the measurement shown in Fig. 3 where the acceleration voltage was 20 kV, the regions with the strong EBIC signal at the positions of the *pn*-junctions are sharper. This is because the size of the interaction volume is about one order of magnitude smaller for 5 kV as for 20 kV. CASINO Simulations (7) show that the interaction volume is about 0.3 microns at 5 kV and about 3 microns at 20 kV. However, since the image taken at 5 kV collects more information from the part of the sample near the surface, the grinding lines are visible in Fig. 4.

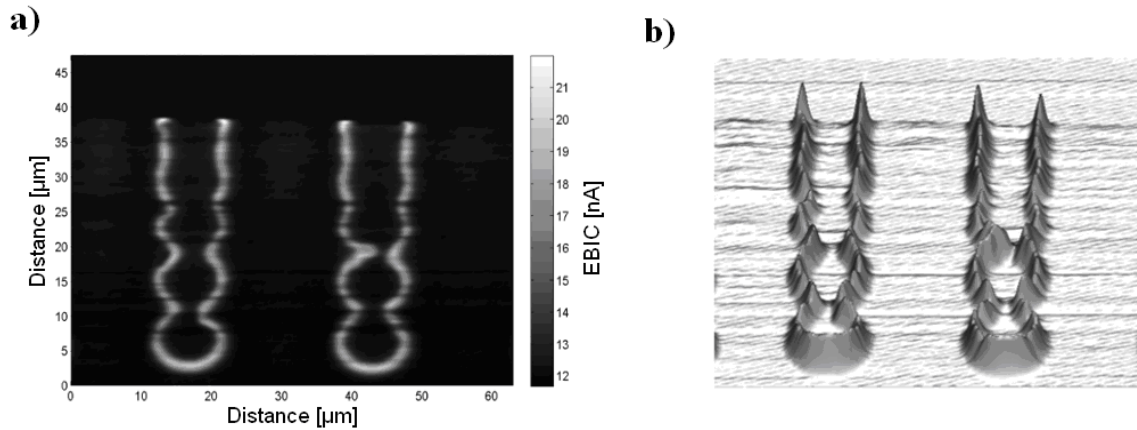


Figure 4: A higher resolution EBIC image taken at an acceleration voltage of 5 kV. EBIC measurement of CoolMOS™ structure visualized in a) Grayscale- and b) 3D-Plot.

Figures 5 and 6 show EBIC images of the superjunctions in a planar view. The sample was ground at an angle to the sample surface so that the top of the image is closer to the sample surface than the bottom.

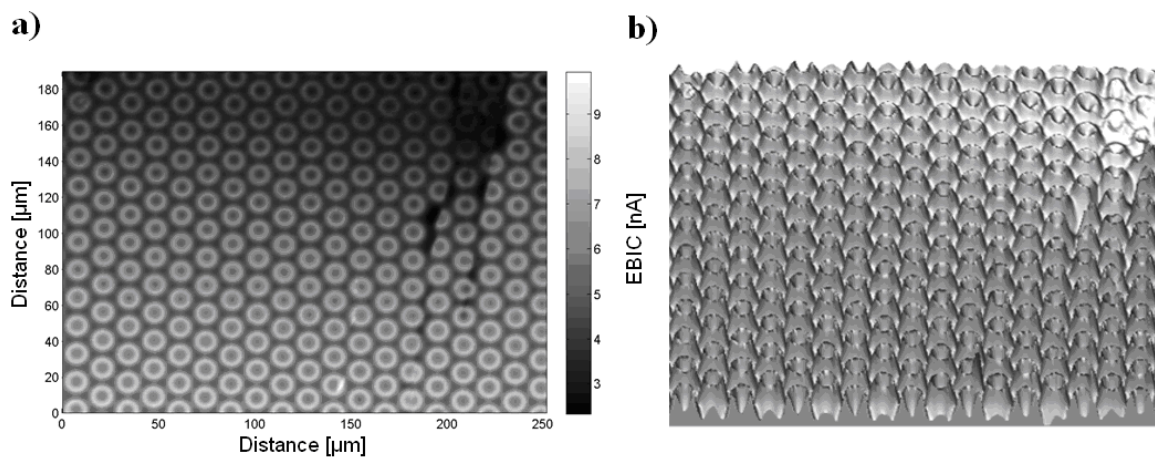


Figure 5: A planar view of the columns. The white circles show the positions of the *pn*-junctions. This image was taken at an acceleration voltage of 20 kV. EBIC measurement of CoolMOS™ structure visualized in a) Grayscale- and b) 3D-Plot.

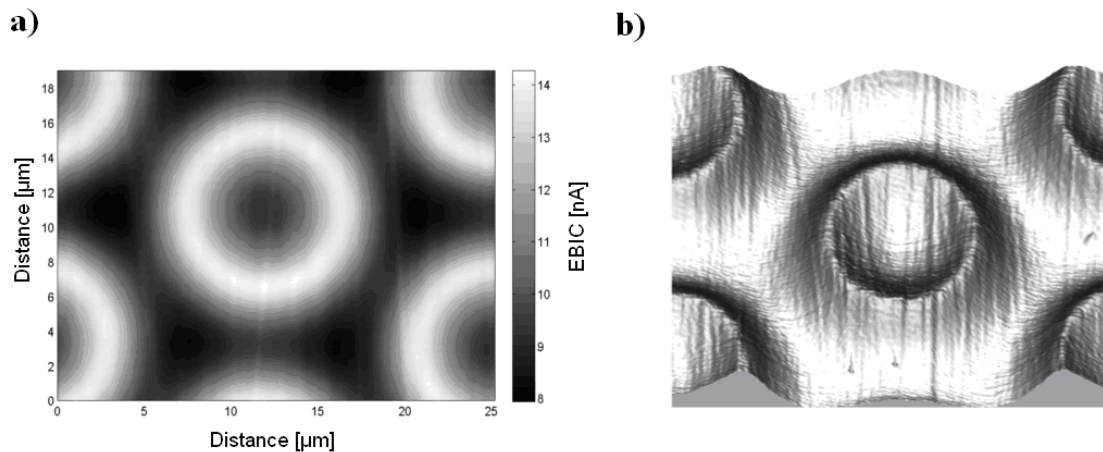


Fig. 6: The columns in a planar view at a higher magnification. This image was taken at an acceleration voltage of 20 kV. EBIC measurement of CoolMOS™ structure visualized in a) Grayscale- and b) 3D-Plot.

Conclusions

EBIC measurements were used to produce experimental images of the pn -junctions in a superjunction transistor. It was possible to make cross sectional images vertically through the wafer or laterally at a depth beneath the wafer surface. Determining the positions of the pn -junctions is useful in devices which depend on charge compensation. The data can be compared to process simulations which are used to tune the process parameters. Better control of the process will allow for higher doping levels and thereby a lower on-state resistance. For the fabrication of superjunction MOSFETs, a trade-off between the processing effort and the deviation of the actual structure from the ideal structure depicted in Fig. 2 (b) must be found. The presented EBIC measurements pose a feasible method to visualize the actual distribution of p - and n -type regions in the device. By this, the impact of process parameter variations (e.g. of the thermal budget for diffusion of the implanted acceptors) on the device can be checked.

References

1. G. Deboy, M. März, J.P. Stengl, H. Strack, J. Tihanyi, and H. Weber, "A new generation of high voltage MOSFETs breaks the limit line of silicon", pp. 983–685, Proc. IEDM (1998).
2. L. Lorenz, G. Deboy, M. März, J.-P. Stengl, and A. Bachofner, "Drastic Reduction of On-Resistance with COOLMOS™", pp. 250–258, PCIM Europe (1998).
3. H.-J. Schulze, M. Buzzo, F.-J. Niedernostheide, M. Rüb, H. Schulze, and R. Job, "Hydrogen-related Donor Formation: Fabrication Techniques, Characterization, and Application to High-voltage Superjunction Transistors", pp. 135–146, ECS Trans. 3 (2006).

4. H. J. Leamy, J. Appl. Phys. 53, R51–R80, (1982)
5. R. F. Egerton, in Physical principles of electron microscopy (Springer, Berlin, 2005)
6. M. Buzzo, M. Ciappa, M. Rüb and W. Fichtner, "Characterization of 2D Dopant Profiles for the Design of Proton Implanted High-Voltage Superjunction", pp. 285-289, IPFA Singapore (2005).
7. Casino Simulations, CASINO - A Fast and Easy-to-use Modeling Tool for Scanning Electron Microscopy and Microanalysis Users

Investigation of Doping Type Conversion and Diffusion Length Extraction of Proton implanted Silicon by EBIC

The following corresponds to the publication

S. Kirnstoetter, F. Faccinelli, P. Hadley, R. Job, W. Schustereder, J.G. Laven, H.-J. Schulze, *Electrochemical Society Transactions* Volume 50 (1) 115-120 (2012) The Electrochemical Society

The author of this thesis was responsible for the following points

- Schottky EBIC measurements
- measurement result analysis and interpretation
- main authorship

The contribution of the other authors of this publication are listed below

- M. Faccinelli: Schottky EBIC measurements, measurement analysis
- P. Hadley: authorship, measurement analysis
- R. Job: interpretation of measurement results
- J.G. Laven: interpretation of measurement results
- W. Schustereder: provided proton implanted sample, interpretation of measurement results
- H.-J. Schulze: interpretation of measurement results

Investigation of Doping Type Conversion and Diffusion Length Extraction of Proton Implanted Silicon by EBIC

S. Kirnstötter^{a,c}, M. Faccinelli^{a,c}, P. Hadley^a, R. Job^b, W. Schustereder^c, J. G. Laven^d, and H.-J. Schulze^d

^a Institute of Solid State Physics, Graz University of Technology, Graz 8010, Austria

^b Department of Electrical Engineering and Computer Science, Muenster University of Applied Sciences, 48565 Steinfurt, Germany

^c Infineon Technologies Austria AG, 9500 Villach, Austria

^d Infineon Technologies AG, 81726 Munich, Germany

Electron beam induced current (EBIC) measurements were used to determine the doping type and to extract the diffusion length in proton implanted silicon wafers. This method makes it possible to distinguish between *n*-type and *p*-type at low carrier concentrations. Because of the defects caused by the implantation, the diffusion length is much smaller in the implanted than in the non-implanted regions.

Introduction

At low doping concentrations, the doping type (*n* or *p*) can be determined by defect complexes. For instance, during a high temperature anneal defect complexes called thermal donors are formed [1]. Sufficient thermal donors can be formed to convert lightly doped *p*-type silicon to *n*-type after annealing [2, 3]. Another way to introduce defects that act as dopants is to irradiate the silicon with high-energy particles such as electrons, neutrons, or protons [4, 5, 6].

During the fabrication of microelectronic circuits, many implantations and annealing steps take place, which can introduce defect complexes that change the doping type. Since it is hard to predict the concentration of the defect complexes, it is sometimes necessary to determine the doping type experimentally. Methods for determining the doping type are Kelvin Probe Force Microscopy (KPFM) [7], Secondary Electron Dopant Contrast (SEDC) [8], and the hot probe method [9]. However, these methods have difficulty distinguishing between *n*-type and *p*-type at low ($<10^{14}$ cm⁻³) carrier concentrations. Here we introduce a method for determining the doping type that works at low concentrations. In this method, sharp needles are used to form Schottky contacts to the silicon and then an Electron Beam Induced Current (EBIC) measurement is performed to determine the doping type.

Electron Beam Induced Current

EBIC is an analysis method used in a Scanning Electron Microscope (SEM) to investigate buried junctions or defects in semiconductors [10, 11]. During an EBIC measurement, high-energy electrons from the electron beam enter the semiconductor and generate electron-hole pairs. If the charge carriers diffuse into a region where there is a

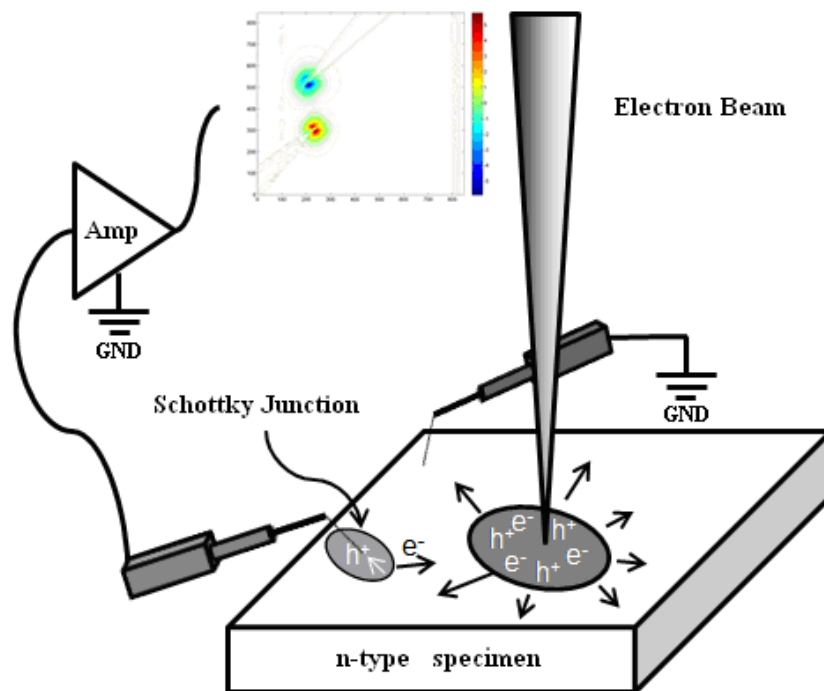


Figure 1. Schematic illustration of an EBIC measurement. The electron beam induces electron-hole pairs (e^-h^+) which diffuse to the metal-semiconductor junction and get separated by the electric field of the Schottky junction. In the case of an n -type semiconductor, the electric field points from the semiconductor to the metal. The minority holes diffuse to the electrical contacts and are detected using a current amplifier. The current amplifier is not biased; it acts like a virtual ground.

built-in electric field, such as a p - n junction or a Schottky contact, charge separation will occur and a current will flow (Figure 1). This is essentially the same thing that happens in a solar cell except that the electron-hole pairs are generated by light in a solar cell and by high-energy electrons in EBIC.

Determination of the Doping Type

For a local measurement of the semiconducting type, the surface was prepared by grinding with SiC 1000 and SiC 4000 grinding paper. The SiC 4000 paper has $6\ \mu\text{m}$ grains. Micromanipulators were used to place tungsten needles on the silicon (Figure 2). These needles formed Schottky contacts with the silicon. For heavy doping, the built-in electric field at the Schottky contact points towards the metal for n -type and away from the metal for p -type. Near an intrinsic doping level, the built-in electric field changes direction. The doping concentration where this occurs depends on the workfunctions of the materials and how the interface states pin the Fermi level. To determine the doping concentration where the electric field changes sign, we calibrated our set-up using measurements on high-resistivity wafers of known doping type (a $600\ \Omega\text{cm}$ n -type wafer and a $1000\ \Omega\text{cm}$ p -type wafer). For the tungsten tips that we used, the built-in electric field at the Schottky contact points towards the metal for n -type and away from the metal for p -type for all wafers with carrier densities above $10^{13}\ \text{cm}^{-3}$.

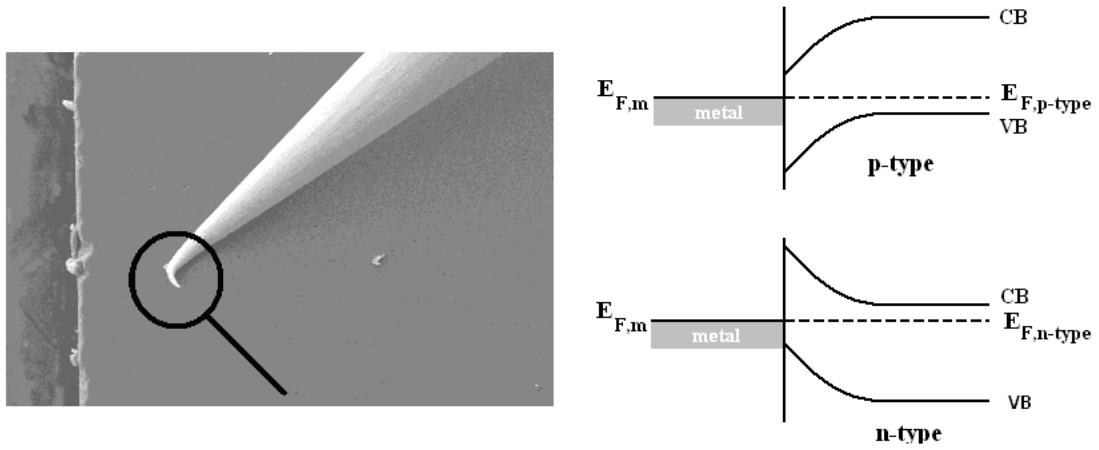


Figure 2. (left) SEM image of a tungsten tip pressed on the cross section of a silicon wafer forming a Schottky contact. The magnifying glass indicates the position of this Schottky contact. (right) Band diagrams indicating the band bending that takes place at a Schottky contact.

Figure 3 shows secondary electron images of the cross section of a lightly ($>1000 \Omega\text{cm}$) p -doped magnetic Cz silicon wafer that has been implanted with hydrogen from the polished side (left side in the SEM image). After the proton implantation (4 MeV, $2 \times 10^{14} \text{ p}^+/\text{cm}^2$), the wafers were annealed at $530 \text{ }^\circ\text{C}$ for 1 h.

The EBIC measurement on the left indicates that the region close to the surface was n -doped. Presumably, this is due to hydrogen-related thermal donors that are induced in the layer between the irradiated surface and projected range ($\sim 140 \mu\text{m}$). The EBIC measurement on the right shows that the unimplanted region has retained its initial p -type doping. The size of the area around the tip where the EBIC current is collected depends on the diffusion length of the charge-carriers induced by the electron beam during the EBIC measurement. In this sample, the diffusion length in the implanted region between the surface and the projected range is much shorter than in the region beyond the penetration depth of the protons.

Extraction of the Diffusion Length

When the high-energy electrons of the electron beam enter the silicon, they generate electron-hole pairs and the minority carrier concentration greatly exceeds the equilibrium minority carrier concentration. These minority carriers diffuse away from their point of generation and eventually recombine on a timescale given by the minority carrier lifetime. The diffusion of the minority carriers is described by the charge continuity equation. In the absence of an electric field this equation is,

$$\frac{dn(\vec{r})}{dt} = D\nabla^2 n(\vec{r}) + G(\vec{r}) - \frac{n(\vec{r}) - n_0}{\tau}. \quad [1]$$

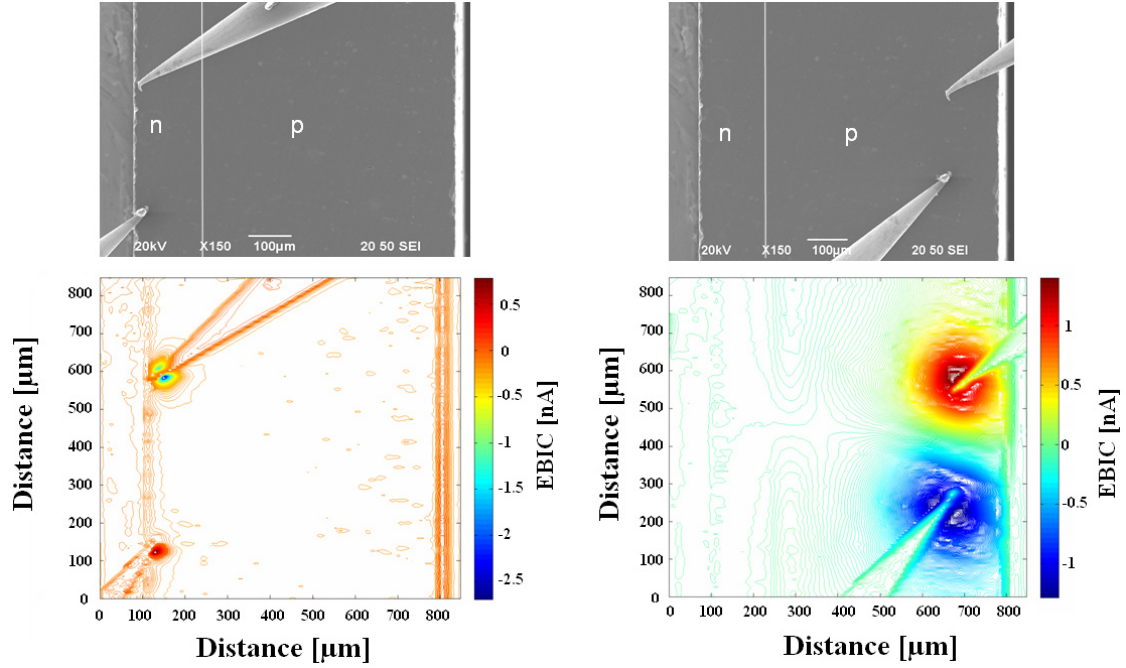


Figure 3. SEM (upper) and EBIC (lower) images of two tungsten needles pressed on the cross section of a proton implanted (4 MeV , $2 \times 10^{14} \text{ p}^+/\text{cm}^2$) and annealed ($530 \text{ }^\circ\text{C}$, 1 h) silicon wafer. The needles are positioned on the proton doped n -type region (left) and on the non implanted p -type region (right). During the EBIC measurement the beam of high energy electrons is scanned over the surface of the sample and the current at the probes is recorded for each point.

Here $n(r)$ is the minority carrier concentration at the position r , D is the diffusion constant, G is the generation coefficient, n_0 is the equilibrium carrier concentration, and τ is the minority carrier lifetime. In steady state, the minority carrier concentration profile does not change in time. If we define the excess minority carrier concentration, $\tilde{n} = n - n_0$, and approximate the generation by the electron beam with a delta function, $G(\vec{r}) = G_0 \delta(\vec{r})$, the continuity equation becomes,

$$D\nabla^2 \tilde{n} + G_0 \delta(\vec{r}) - \frac{\tilde{n}}{\tau} = 0 \quad [2]$$

Due to lattice imperfections of the silicon, the minority carrier lifetime is generally reduced at the surface. We are mostly interested in contribution of the carrier lifetime in the bulk. To reduce the surface recombination, the samples are polished. In the case that the surface recombination is negligible compared to the bulk, the solution to the continuity equation is,

$$\tilde{n} = \frac{G_0}{4\pi r} \exp\left(-\frac{r}{\sqrt{D\tau}}\right). \quad [3]$$

Thus, the minority carrier diffusion length $L = \sqrt{D\tau}$ can be estimated from the EBIC measurement.

In the experiments, there is a regime where the bulk recombination seems to dominate over the surface recombination. Figure 3 shows the EBIC current around two Schottky contacts placed on the surface. On the left the two contacts were placed in the n -doped region between the irradiated surface and the projected range of the protons. On the right, the two contacts were formed on the unimplanted p -region beyond the penetration depth of the protons. Clearly, the minority carriers diffuse further in the unimplanted region than in the implanted region. The surface preparation is the same on both sides of the sample and if surface recombination were dominant, the diffusion length would be the same on both sides. This suggests that the diffusion length measured in the implanted region is dominated by the bulk diffusion length.

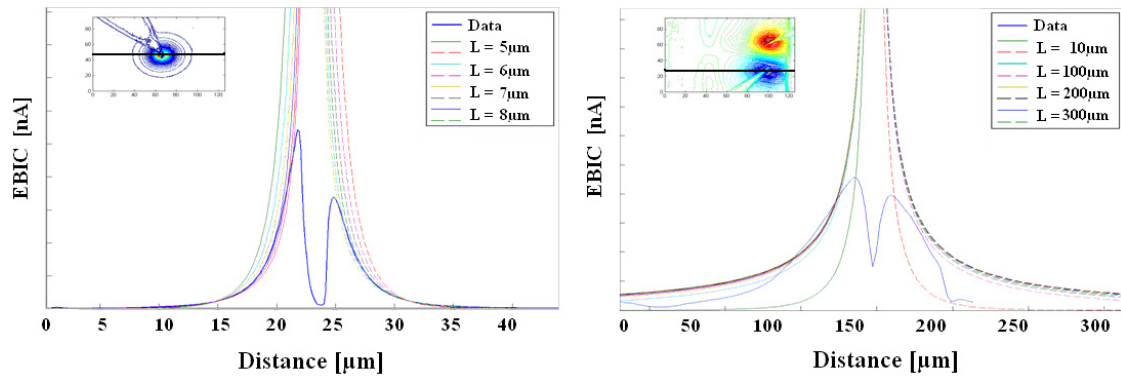


Figure 4. Extraction of the diffusion length from the EBIC signal shape of a Schottky contact formed on a proton implanted (left) and non implanted (right) silicon sample. The line in the inset (upper left) shows the position of the line scan that was extracted from the EBIC signal.

Figure 4 shows line scans of the EBIC signal. The dips in the line scans appear, when the electron beam passes over the tungsten tip and, hence, does not reach the sample. Fits of Eq. 3 to the data in Fig. 4 indicate that the diffusion length is $10 \pm 5 \mu\text{m}$ in the implanted region. A fit of Eq. 3 to the data in the unimplanted region of the sample, depicted in Fig. 4 (right side), gives a diffusion length of $150 \pm 50 \mu\text{m}$. In this case, however, we cannot be certain, that this value is not affected by surface recombination. The smaller diffusion length in the implanted region comes from a lower mobility and a shorter minority carrier lifetime. The diffusion length of the charge-carriers in the implanted region is reduced by a factor of at least 10 relative to the unimplanted bulk.

Conclusion

The formation of Schottky contacts on proton implanted p -type silicon samples in combination with Electron Beam Induced Current measurements were used to distinguish between n -type and p -type regions. The described combination of Schottky contacts with EBIC measurements were shown to be a powerful tool for determining the doping type at very low carrier concentrations. This can be important for devices containing regions

with low doping concentrations like power transistors. The diffusion length can also be estimated from the EBIC data. For the proton implanted sample investigated here, the diffusion length was at least a factor of 10 smaller in the implanted regions compared to the unimplanted regions.

References

1. P. Pichler, *Intrinsic Point Defects, Impurities, and Their Diffusion in Silicon*, Springer Wien, (2004)
2. E. Simoen, Y. L. Huang, Y. Ma, J. Lauwaert, P. Clauws, J. M. Rafi, A. Ulyashin, C. Claeys, *Journal of Electrochemical Society*, **156**, (2009)
3. E. Tuovinen, J. Harkonen, P. Luukka, E. Tuominen, *Material Science in Semiconductor Processing*, **10**, pp. 179-184, (2007)
4. J. Hartung and J. Weber, *Materials Science and Engineering*, B4 pp. 47-50 (1989)
5. A. Junkes, *Influence of radiation defect clusters on silicon particle sensors*, Ph.D. thesis, (2011)
6. M. Moll, *Radiation Damage in Silicon Particle Detectors-microscopic defects and macroscopic properties*, Ph.D. thesis, (1999)
7. M. Nonnenmacher, M. P. O'Boyle, H. K. Wickramasinghe, *Applied Physical Letters*, **58**, pp. 2921-2923, (1991)
8. M. Buzzo, M. Ciappa, M. Stangoni, and W. Fichtner, *Microelectronics Reliability*, **45**, pp. 1499-1504, (2005)
9. G. Golan, A. Axelevitch, B. Gorenstein, V. Manevych, *Microelectronics Journal*, **37**, pp. 910-915, (2006)
10. H. J. Leamy, *J. Appl. Phys.* **53**, R51-R80, (1982)
11. R. F. Egerton, *Physical principles of electron microscopy*, Springer Berlin, (2005)

Hydrogen Decoration of Radiation Damage Induced Defect Structures

The following corresponds to the publication

S. Kirnstoetter, F. Faccinelli, W. Schustereder, J.G. Laven, H.-J. Schulze and P. Hadley, American Institute of Physics (AIP) Conference Proceedings

The author of this thesis was responsible for the following points

- Spreading resistance measurement analysis and interpretation
- main authorship

The contribution of the other authors of this publication are listed below

- M. Faccinelli: measurement analysis and interpretation
- J.G. Laven: measurement analysis and interpretation
- W. Schustereder: provided proton implanted samples, measurement analysis and interpretation
- H.-J. Schulze: measurement analysis and interpretation
- P. Hadley: authorship, measurement analysis and interpretation

Hydrogen Decoration of Radiation Damage Induced Defect Structures

S. Kirnstötter^{a, b}, M. Faccinelli^a, W. Schustereder^b, J. G. Laven^c, H.-J. Schulze^c and P. Hadley^a

^a*Institute of Solid State Physics, Graz University of Technology, 8010 Graz*

^b*Infineon Technologies Austria AG, 9500 Villach, Austria*

^c*Infineon Technologies AG, 81726 Munich, Germany*

Abstract. The defect complexes that are formed when protons with energies in the MeV-range were implanted into high-purity silicon were investigated. After implantation, the samples were annealed at 400 °C or 450 °C for times ranging between 15 minutes and 30 hours. The resistivity of the samples was then analyzed by Spreading Resistance Profiling (SRP). The resistivity shows minima where there is a high carrier concentration and it is possible to extract the carrier concentration from the resistivity data. Initially, there is a large peak in the carrier concentration at the implantation depth where most of the hydrogen is concentrated. For longer anneals, this peak widens as the hydrogen diffuses away from the implantation depth. Following the changes in resistivity as a function of annealing time allows us to characterize the diffusion of hydrogen through these samples. Differences in the diffusion were observed depending on whether the silicon was grown by the magnetic Czochralski (m:Cz) method or the Float zone (Fz) method.

Keywords: Spreading Resistance Profiling (SRP), hydrogen/proton implantation, defects in semiconductors, diffusion in solids, diffusion coefficient, hydrogen diffusion, activation energy

PACS: 61.72.U-, 81.70.Jb, 61.72.uf, 66.30.J-, 66.30.-h

INTRODUCTION

Because of their light weight, protons can be implanted deeply into semiconductor materials. Proton implantations are used for instance in semiconducting power devices where often vertical device structures are used. Three distinct layers are formed by an implantation. From the surface until the implantation depth the radiation damage results in the formation of acceptor-like defect structures. [1] The protons mostly pass through this layer and accumulate near the implantation depth x_0 . Near the implantation depth, both hydrogen and radiation damage are present. This results in the formation of a high concentration of hydrogen related donor complexes (HDs). [2, 3] Deeper than the implantation depth, no implantation damage occurs. During the annealing process, hydrogen diffuses away from the implantation depth. Hydrogen donors are formed in the region where radiation damage exists, i.e., closer to the surface than the implantation depth. This is observed by a change in the resistivity. Although hydrogen also diffuses into the region deeper than the implantation depth, no HDs are formed, as no radiation damage is present. Thus, the substrate doping beyond the implantation depth remains about constant.

A pn -junction is formed between the surface layer that is doped p -type due to the acceptors that are induced by the radiation damage and the layer near the implantation depth that is doped n -type due to the HDs. This pn -junction causes a clear dip in the carrier concentration. This dip moves towards the surface for longer anneals as the hydrogen diffuses away from the implantation depth. At the pn -junction, the concentration of hydrogen donors equals the concentration of acceptors, $C_{HD}(x_{pn}) = C_A(x_{pn})$. The hydrogen concentration is presumed to diffuse following a Gaussian profile,

$$C_H(x, t) = \frac{\phi}{\sqrt{4\pi D_H t}} \exp\left(-\frac{(x - x_0)^2}{4D_H t}\right),$$

where C_H is the concentration of hydrogen, D_H is the diffusion constant of hydrogen, and ϕ is the proton dose in protons/m². The integral of C_H over all x for any time is the proton dose ϕ . The profile of radiation-induced defects $C_R(x)$ was calculated using the simulation tool SRIM. [4] This simulation calculates the spatial distribution of vacancies and interstitials created during implantation. More complex defect complexes are responsible for the doping. We assume that the concentration of radiation induced acceptors $C_A(x)$ and the radiation induced defects that

become hydrogen donors when they are decorated by hydrogen $C_{HD}^*(x)$ are both proportional to $C_R(x)$. The proportionality constants can be extracted from the SRP data. Since both hydrogen and radiation damage must be present to form hydrogen donors, we model the hydrogen donor concentration as $C_{HD}(x) = \min[\alpha C_H^*(x,t), C_{HD}^*(x)]$ where α is a constant that describes the fraction of the hydrogen that participates in hydrogen donor formation. By setting $C_{HD} = C_A$, the position of the pn -junction can be calculated to be,

$$x_{pn} = x_0 - \sqrt{4D_H t \ln \left(\frac{\alpha \phi}{C_A(x) \sqrt{4\pi D_H t}} \right)}.$$

Figure 1 shows the simulated radiation damage profiles superposed with the hydrogen concentration profiles for different times. The pn -junction forms at the intersection of the hydrogen and the acceptor concentrations where $C_{HD} = C_A$.

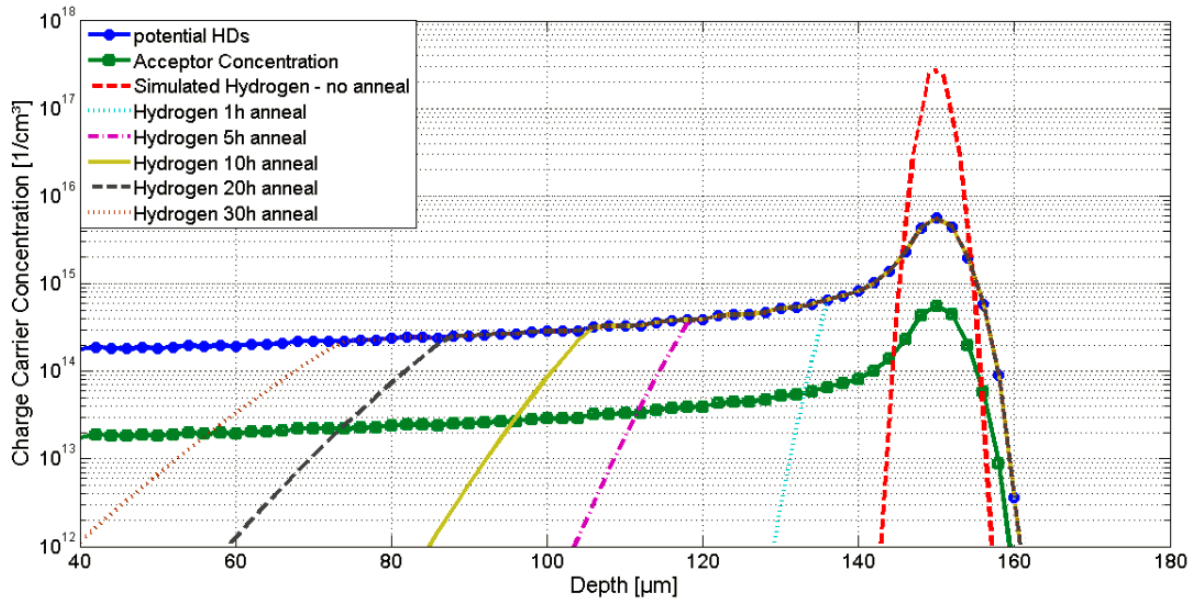


FIGURE 1. Simulation of the diffusion of hydrogen in radiation damaged crystalline silicon. The starting concentration of hydrogen-induced, radiation damage (potential HDs) was simulated with SRIM. The acceptor concentration is expected to be proportional to the simulated damage distribution. The implanted hydrogen diffuses towards the surface when the sample is annealed. The radiation damage is assumed to remain the same during an anneal.

RESULTS AND DISCUSSION

In this work, commercially available FZ and m:Cz boron doped $\langle 100 \rangle$ silicon wafers were implanted at room temperature with a dose of $1 \times 10^{14} \text{ cm}^{-2}$ protons with an energy of 4 MeV. The samples were annealed at 400 °C or 450 °C under nitrogen flow for durations between 15 minutes and 30 hours. The evolution of the doping profiles was measured by Spreading Resistance Profiling (SRP). [5] Figure 2 shows the spreading resistance profile of a proton implanted FZ silicon wafer annealed at 400 °C. The peak at around 150 μm depth marks the implantation depth of the hydrogen. Already during the implantation process, hydrogen related donors are formed there. The sharp minimas to the left of the implantation peak represent the pn -junction between the generated HDs (n -type) and the p -type acceptor complexes formed during the implantation process. The diffusion of the hydrogen from the implantation depth and the decoration of the radiation damage complexes can be seen as the pn -junction moves further towards the surface the longer the sample is annealed. Before the implantation, the samples are regularly boron doped (p -type). Also right of the peak at about 160 μm a minima appears, representing a pn -junction between the n -type implantation region and the p -type boron doped substrate. The hydrogen also diffused to the right but

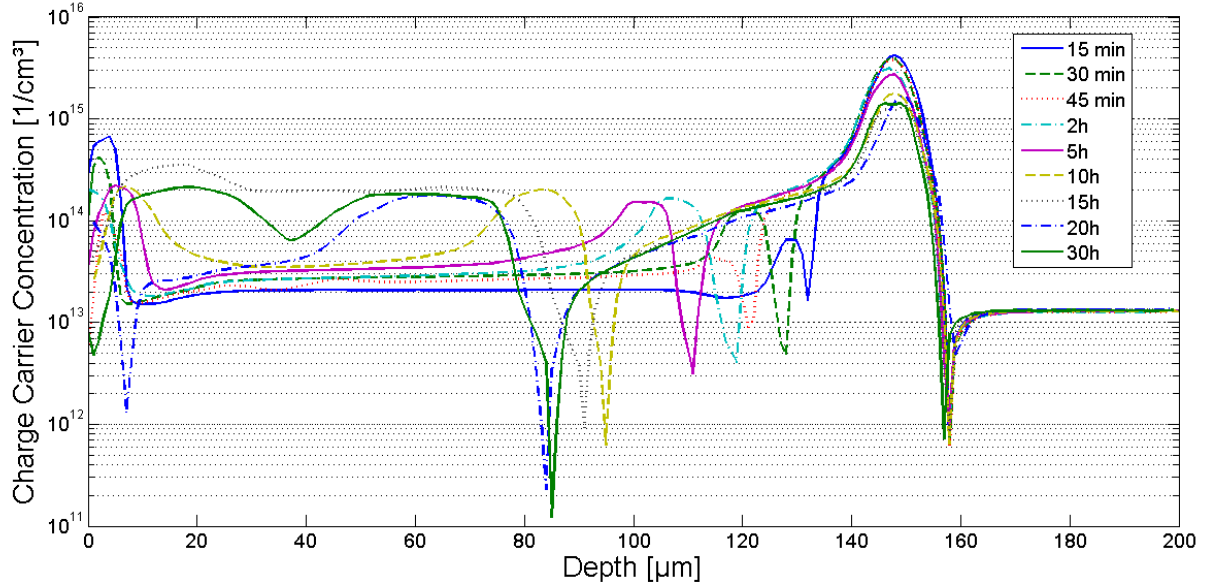


FIGURE 2. Spreading Resistance Profile of a proton implanted FZ silicon wafer annealed at 400 °C for durations from 15 minutes to 30 hours.

there is no radiation damage present to form HDs. For increasing annealing times, the charge carrier concentration of the peak at 150 μm decreases. For long annealing times, the concentration of hydrogen at the position of the implantation depth becomes less than the radiation damage. However, this decrease in the carrier concentration is due to the thermal decomposition of the hydrogen donors. [6]

Figure 3 shows the Spreading Resistance Profile of a proton implanted m:Cz silicon wafer annealed at 450 °C for durations from 30 minutes to 15 hours. The m:Cz data is more difficult to interpret because of the thermal donors that form during the anneal. Thermal donors are oxygen related defect complexes that form when there is oxygen present in silicon that is annealed at temperatures between 350 °C and 500 °C. [7] The m:Cz samples have a much higher concentration of oxygen than the FZ samples. Consequently, the carrier concentration in the region that was not implanted (on the right in Fig. 3) varies significantly with annealing time. Compare this to the same region of the Fz sample shown in Fig. 1 where the carrier concentration is constant in the unimplanted region for all anneals. It is not clear how the thermal donor concentration depends on radiation damage. Nevertheless the dips in the carrier concentration are clear signatures of the pn-junctions that are formed. We used the positions of the pn-junctions to estimate the diffusion of hydrogen in the m:Cz samples.

In Fig. 4, the position of the *pn*-junctions of proton implanted FZ and m:Cz silicon samples annealed at 400 °C and 450 °C is plotted versus the square root of the annealing time. The lines all cross at 140 μm, the position of the *pn*-junction of before annealing. The data was fit to a form,

$$x_{pn} = x_0 - \sqrt{4D_{HD}t},$$

where D_{HD} is the effective diffusion constant for hydrogen donors.

The effective diffusion constant is temperature dependent for both the Fz and m:Cz samples. We assume that the diffusion is thermally activated and the temperature dependence of the diffusion constant is $D_{HD}(T) = D_0 \exp(-E_A/k_B T)$, where E_A is the activation energy. In Fig. 5 an Arrhenius plot of the logarithm of the effective diffusion coefficients is shown. The red squares are the diffusion coefficients of the FZ samples and the blue circles the diffusion coefficients of the m:Cz material. The slope of the lines yield the activation energies and the intercepts yield the prefactors D_0 . To increase the reliability of the extracted activation energy and prefactors D_0 , additional data points were added from a very recent study from Laven et al. [6]

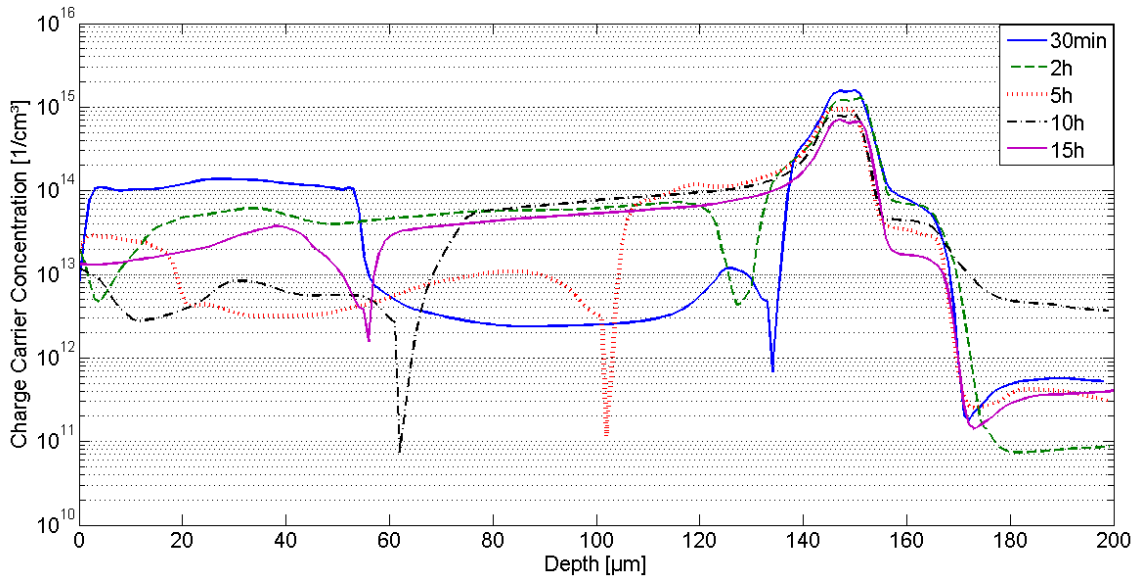


FIGURE 3. Spreading Resistance Profile of a proton implanted m:Cz silicon wafer annealed at 450 °C for durations from 30 minutes to 15 hours.

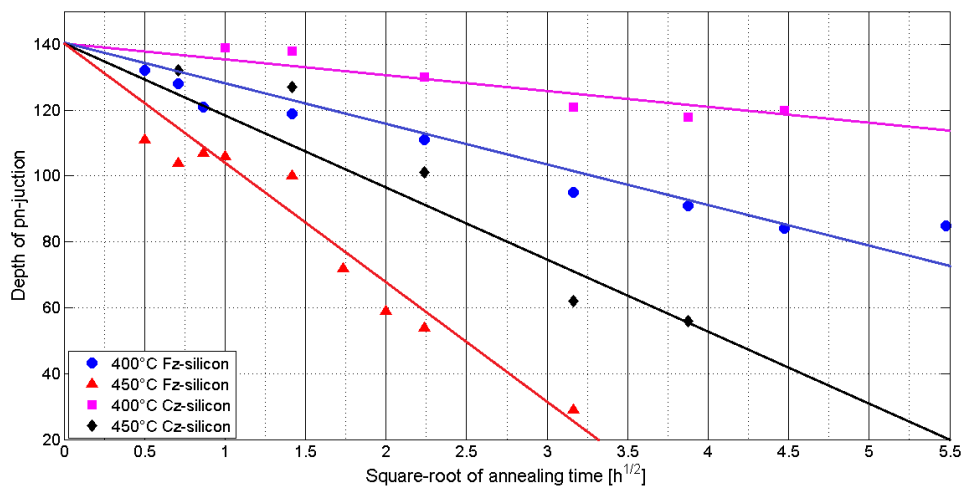


FIGURE 4. Depth of *pn*-junctions of proton implanted FZ and m:Cz silicon samples annealed at 400 °C and 450 °C for various durations plotted over the square root of the annealing/diffusion time.

In literature, the reported diffusion coefficients of hydrogen in silicon vary over several orders of magnitude from 10^{-5} to 10^{-13} cm^2s^{-1} . Activation energies of hydrogen in silicon, extracted by experimental measurements, are reported from 0.48 eV [8] to 1.2 eV [9-11]. For the temperature range the authors are interested in this publication, diffusion coefficient from 10^{-7} to 10^{-12} cm^2s^{-1} were reported.

These big differences result from the quality of the used silicon, the concentration of hydrogen and the way the hydrogen was implanted or brought in by a plasma source. Santos and Jackson [12] for example report a change in the activation energy of hydrogen from 1.2 -1.5 eV to 0.5 eV, when the hydrogen is supplied by a plasma source or diffusing from a saturated layer of hydrogen.

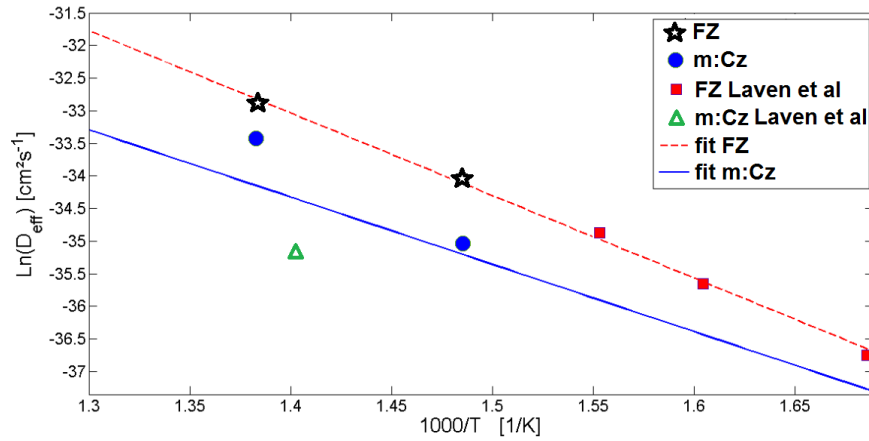


FIGURE 5. Arrhenius plot of the logarithm of the effective diffusion coefficients over $1/T$ to determine the activation energy of the hydrogen through the radiation damaged layer.

Table 1 gives an overview over the extracted values of the effective diffusion coefficients and activation energies.

TABLE (1). Summary of extracted diffusion coefficients, activation energies and diffusion prefactors of implanted hydrogen diffusion through a radiation damaged layer in Fz and m:Cz silicon

Substrate	Annealing Temperature [°C]	Effective Diffusion Coefficient [cm^2s^{-1}]	Activation Energy [eV]	Diffusion prefactor D_0 [cm^2s^{-1}]
Fz	400	$(1.6 \pm 0.1) \times 10^{-11}$	1.1 ± 0.1	$(2.1 \pm 0.1) \times 10^{-3}$
Fz	450	$(5.0 \pm 0.1) \times 10^{-11}$	1.1 ± 0.1	$(2.1 \pm 0.1) \times 10^{-3}$
Cz	400	$(6.1 \pm 0.1) \times 10^{-12}$	1.5 ± 0.1	$(2.3 \pm 0.1) \times 10^{-5}$
Cz	450	$(3.0 \pm 0.1) \times 10^{-11}$	1.5 ± 0.1	$(2.3 \pm 0.1) \times 10^{-5}$

CONCLUSION

The long time annealing series of proton implanted Fz and m:Cz silicon wafers presented in this work showed that the differences in the oxygen and carbon concentration can cause large variations in the doping profile and the diffusion of hydrogen in the crystal lattice. The activation energy of hydrogen is higher in m:Cz silicon. A reason for that could be the enhanced concentration of trapping centers, e.g., oxygen and carbon in m:Cz silicon. The diffusion coefficients reported in this work are rather low in comparison to other investigations reported in literature. This might be because of the radiation induced damage in the layer that the hydrogen was diffusing through.

REFERENCES

1. I. Pintilie, E. Fretwurst, G. Lindström, J. Stahl, *Appl. Phys. Lett.*, 82, 13 (2003) 2169-2171.
2. Y. Zohta, Y. Ohmura, and M. Kanazawa, *Jpn. J. Appl. Phys.*, 10, 4 (1971) 532-533.
3. Yu. V. Gorelkinskii, V. O. Sigle, and Zh. S. Takibaev, *Phys. Status Solidi A*, 22, (1974) K55-K57.
4. J. F. Ziegler, *Proc. of Conf. on Ion Beam Analysis*, 219-220 (2004) 1027-1036.
5. M. Pawlik, *Journal Vacuum Science and Technology B*, 10, 1 (1992) 388-396.
6. J. G. Laven, R. Job, H.-J. Schulze, F.-J. Niedernostheide, W. Schustereder, L. Frey, *ECS J. Solid State Sci. Technol.*, 2(9), (2013) P389-P394.
7. E. Simoen, Y. L. Huang, Y. Ma, J. Lauwaert, P. Clauws, J. M. Raff, A. Ulyashin, and C. Claeys, *J. Electrochem. Soc.*, 156(6) (2009) H434-H442.
8. A. van Wieringen and N. Warmoltz, *Physica*, 22, 849 (1956).
9. Y. L. Huang, Y. Ma, R. Job, and A. G. Ulyashin, *J. Appl. Phys.*, 96(12), 7080 (2004).
10. R. Rizk, P. de Mierry, D. Ballutaud, M. Aucouturier, and D. Mathiot, *Phys. Rev. B*, 44(12), 6141 (1991).
11. M. Capizzi and A. Mittiga, *Physica B+C*, 146(1-2), 19 (1987).
12. P. V. Santos and W. B. Jackson, *Phys. Rev. B*, 46(8), 4595 (1992).

Multiple proton implantations into silicon: A combined EBIC and SRP study

The following corresponds to the publication

S. Kirnstoetter, F. Faccinelli, M. Jelinek, W. Schustereder, J.G. Laven, H.-J. Schulze and P. Hadley, *Solid State Phenomena Vols. 205-206* (2014) pp 311-316

The author of this thesis was responsible for the following points

- Spreading resistance measurement analysis and interpretation
- Electron beam induced current measurements and interpretation
- SRIM(Stopping and Range of Ions in Matter) simulations
- main authorship

The contribution of the other authors of this publication are listed below

- M. Faccinelli: measurement result analysis and interpretation
- M.Jelinek: performed proton implantation and provided specimen structures, measurement result analysis and interpretation
- W. Schustereder: performed proton implantation and provided specimen structures, measurement result analysis and interpretation
- J.G. Laven: measurement result analysis and interpretation
- H.-J. Schulze: measurement result analysis and interpretation
- P. Hadley: authorship, measurement result analysis and interpretation

Multiple proton implantations into silicon: A combined EBIC and SRP study

S. Kirnstötter^{1, 2, a}, M. Faccinelli¹, M. Jelinek², W. Schustereder², J. G. Laven³,
H.-J. Schulze³ and P. Hadley^{1, b}

¹Institute of Solid State Physics, Graz University of Technology, 8010 Graz, Austria

²Infineon Technologies Austria AG, 9500 Villach, Austria

³Infineon Technologies AG, 81726 Munich, Germany

^astefan.kirnstoetter@tugraz.at, ^bp.hadley@tugraz.at

Keywords: Electron Beam Induced Current (EBIC), Spreading Resistance Profiling (SRP), hydrogen/proton implantation, defects in semiconductors, doping type, diffusion

Abstract. Protons with energies of 1 MeV and 2.5 MeV were implanted into a *p*-doped silicon wafer and then the wafer was annealed at 350 °C for one hour. This resulted in two *n*-doped layers in the otherwise *p*-doped sample. The carrier concentration was measured using spreading resistance profiling while the positions of the four *pn*-junctions were measured using electron beam induced current measurements. The carrier concentration is not limited by the available hydrogen but by the concentration of suitable radiation induced defects.

Introduction

In the semiconductor industry, proton implantation is used both to dope and to introduce defects that reduce the minority carrier lifetime. An advantage of protons is that they can be implanted much deeper than other dopants, up to hundreds of microns. The doping profiles that can be achieved are known from experience but it is not clear which defects are responsible for the observed doping and minority carrier lifetime reduction. Implanting protons into silicon introduces vacancies, self-interstitials, and hydrogen into the crystal. The highest concentration of these defects is at the implantation depth where most of the protons stop. During a subsequent anneal, defect complexes like VH_4 , V_2H_6 , or IH_2 are formed. Vacancies, interstitials, and hydrogen can also form complexes with the dopants already introduced in the crystal (typically boron or phosphorous). Some of these defect complexes are electrically active and dope the semiconductor. The net result is that the proton implantation causes *n*-doping at the implantation depth. Here we investigate oxygen-poor float-zone silicon that has been implanted with protons at energies of 1 MeV and 2.5 MeV and investigated by Spreading Resistance Profiling (SRP) and Electron Beam Induced Current (EBIC) measurements.

There are two competing effects that take place during proton doping. Radiation damage from energetic particles (protons, neutrons, electrons, gammas) is known to introduce acceptor-like defects [1]. When hydrogen is added to a region where there is radiation damage, and subsequently annealed, donor-like defects occur [2, 3]. Right after the implantation, the hydrogen is mostly concentrated at the implantation depth which is a function of the implantation energy. The radiation damage is spread out over a larger region and is asymmetrically distributed mostly above the implantation depth.

Experimental results

The starting wafer was oxygen-poor float-zone silicon that had been boron doped at $2 \times 10^{13} \text{ cm}^{-3}$ and then implanted with protons at energies of 1 MeV and 2.5 MeV. The proton implantations resulted in two peaks in the hydrogen concentration. One peak was at a depth of 16 μm and the other was at a depth of 67 μm . After the implantations the sample was annealed under nitrogen atmosphere at 350 °C for one hour. During the anneal, defects diffuse and react with each other. A good part of the interstitials and vacancies annihilate each other while various defect complexes

involving hydrogen, boron, and the remaining vacancies and interstitials are created. At the conclusion of the anneal, there are still concentration gradients and the sample was not in thermal equilibrium. A longer anneal would result in a different defect concentration profile. The resulting carrier concentration profile was measured by Spreading Resistance Profiling (SRP) [4]. Briefly, this involves pressing two sharp tungsten carbide needles against the sample and measuring the resistance. From the resistance, it is possible to calculate the resistivity and the charge carrier density.

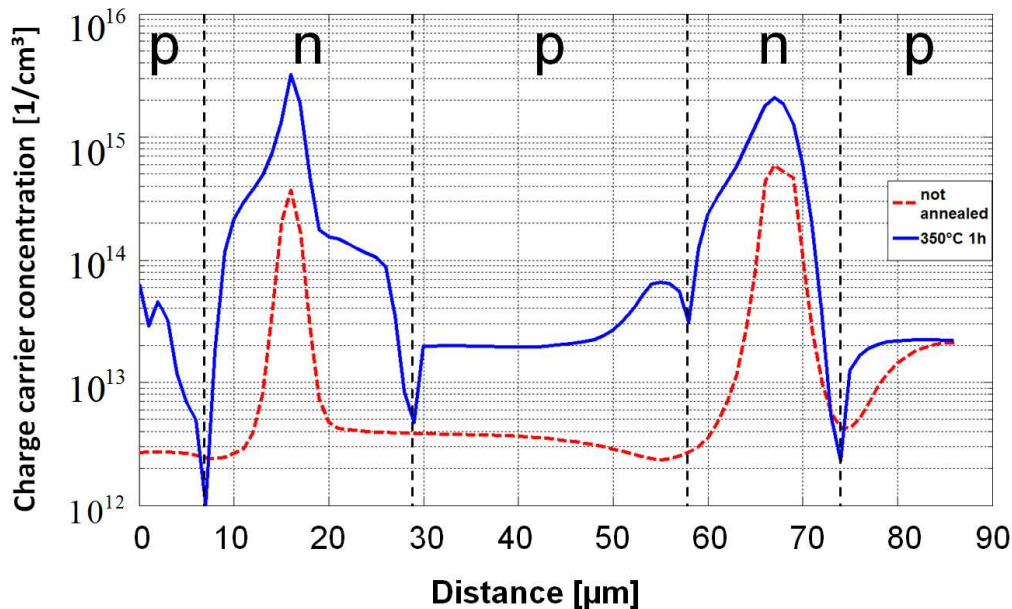


Figure. 1 The carrier concentration calculated from an SRP measurement using the assumption that the mobility is not affected by the implantation. The dotted line indicates the charge-carrier concentration before the anneal and the solid line is the carrier concentration after an anneal at 350 °C for one hour. The *p* and *n* labelling represents the local majority carrier type in the annealed sample.

Figure 1 shows the charge carrier density calculated from an SRP measurements taken before and after the anneal. The protons were implanted from the left and the sample surface was at a depth of zero. For depths greater than 80 μm , the original substrate doping of $2 \times 10^{13} \text{ cm}^{-3}$ is observed. Before annealing, two peaks in the carrier concentration are observed at 16 μm and 67 μm where the hydrogen is concentrated. There is a dip in the carrier concentration of the unannealed sample at about 73 μm . This is caused by the depletion layer of a *pn*-junction between the *n*-type doping induced by the implantation and the *p*-type substrate at that position. No other *pn*-junctions are clearly visible in the unannealed data. For the annealed sample, at depths between 58 μm and 73 μm , there is a large peak in the carrier concentration which reaches a factor of 100 higher than the substrate doping. This is an *n*-type region created by hydrogen donors from the 2.5 MeV implantation. At 73 μm , there is a dip in the carrier concentration due to the *pn*-junction that was also observed in the unannealed measurement. There is another dip in the carrier concentration due to the depletion region of a *pn*-junction at 58 μm . Just to the left of this dip there is a peak in the carrier concentration that is three times higher than the substrate carrier concentration. This *p*-doping comes from acceptor like defects which are produced by radiation damage and where there is a low concentration of hydrogen [5]. There is a large peak in the carrier concentration at 16 μm where the hydrogen from the 1 MeV implantation is concentrated. To the right of this peak there is a plateau in the carrier concentration between 20 μm and 26 μm . In this region, hydrogen from the 1 MeV implantation combined with radiation damage from the 2.5 MeV implantation creates hydrogen donors. This plateau in the carrier concentration ends at 29 μm where the dip in the carrier concentration indicates a *pn*-junction. Notice that the *pn*-junctions are symmetrically

arranged around the peak at 16 μm but asymmetrically arranged around the peak at 67 μm . The hydrogen implanted to 16 μm had radiation damage on both sides. The radiation damage to the left it was from the 1 MeV implantation and to the right it was from the 2.5 MeV implantation. However, near the hydrogen peak at 67 μm , the radiation damage was mostly to the left from the 2.5 MeV implantation. This makes it clear that the hydrogen donors only form where there is both radiation damage and hydrogen [6]. Figure 2 shows radiation damage and hydrogen profile after the two hydrogen implantations at zero Kelvin simulated by the program SRIM [7]. For room temperature implantations only about one percent of the radiation damage remains and the hydrogen peaks broaden. Therefore they reach much lower values than in the simulation.

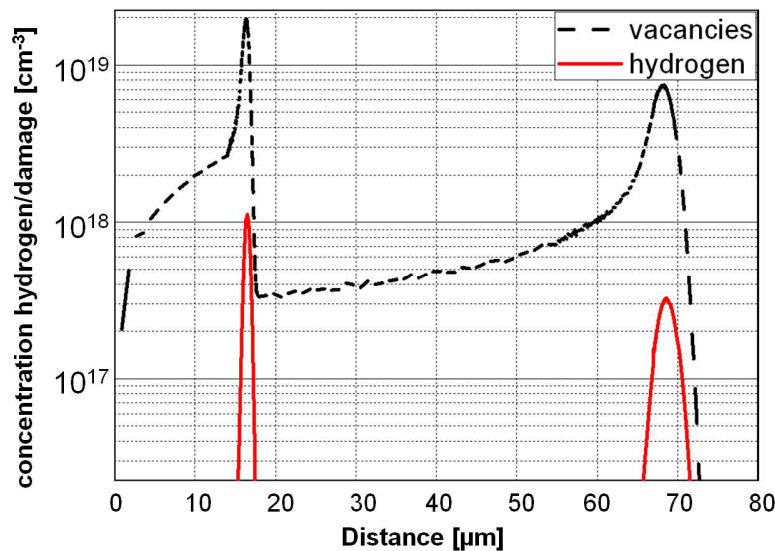


Figure 2. Hydrogen implantations into silicon simulated by SRIM at zero Kelvin. The solid line represents the concentration of hydrogen and the dashed line the vacancy and interstitial concentration of the radiation damage. The H-implantations were performed with 2.5 and 1 MeV and a dose of $1 \times 10^{14} \text{ cm}^{-2}$.

The proton dose for each implantation was $1 \times 10^{14} \text{ cm}^{-2}$. Before the anneal, the hydrogen is localized to a layer about 10 μm thick resulting in a hydrogen concentration of $1 \times 10^{17} \text{ cm}^{-3}$. This is about 1000 times higher than the observed carrier concentration. After the anneal, the hydrogen spreads to a layer that is about 20 μm thick corresponding to concentration of $5 \times 10^{16} \text{ cm}^{-3}$. The measured carrier concentration after the anneal never exceeds $3 \times 10^{15} \text{ cm}^{-3}$. There is a much higher concentration of hydrogen than there is of carriers, implying that the carrier density is limited by the availability of suitable radiation induced defects. The carrier density of the annealed sample in the range 10 μm to 30 μm has a form that reflects the radiation damage, as can be seen in Fig. 2. There is a peak due to the 1 MeV implantation and a constant background due to the 2.5 MeV implantation. The concentration of hydrogen would be expected to be more uniform than the carrier density profile. This also suggests that the carrier density is not limited by the concentration of hydrogen.

Electron Beam Induced Current Measurements (EBIC) support the interpretation of the SRP results. The principle of EBIC is similar to that of a solar cell except charge carriers are generated by a focused electron beam in EBIC measurements while they are generated by light in a solar cell. If charge carriers are generated near a *pn*-junction, the positive and negative charge carriers are separated like in a solar cell and a current flows [8]. The direction of the current indicates the orientation of the *pn*-junction. Figure 3 shows the current from EBIC measurements where the electron beam was scanned across a cross section of the wafer. The current was measured that flows from the front side to the back side of the wafer. A positive current indicates a *pn*-junction where the *n*-type semiconductor is on the left and a negative current indicates a *pn*-junction where the *p*-

type semiconductor is on the left. The EBIC signal of the not annealed sample shows one clear *pn*-junction between the deepest implantation and the substrate. The EBIC signal of the annealed sample shows four *pn*-junctions in the same positions as they were measured by SRP.

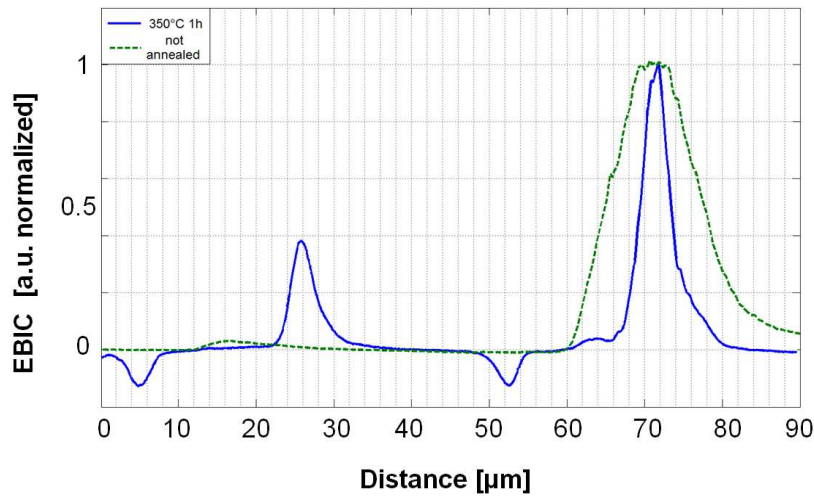


Figure 3. Electron beam induced current measurement of the cross section of a proton implanted (energies: 2.5 and 1 MeV, doses: $1 \times 10^{14} \text{ cm}^{-2}$) Fz silicon wafer annealed with 350°C for one hour.

In Fig. 3 the EBIC measurement signals were normalized to be able to compare them with each other. It should be mentioned that the measured current is smaller in the annealed sample because there are more *pn*-junctions in series and at least one is reverse biased. Two EBIC measurements are shown in Fig. 4. In this case, sharp tungsten needles were used to make contact to the wafer cross section. On the left is a secondary electron image and an EBIC image where the needles were placed on the substrate (far away from the implantations). The current between these two tips was measured as the electron beam was scanned over the surface. On the right, a needle was placed on the *p*-type region between the two implantations of the annealed sample. The current was measured between the needle and the front side (left) of the wafer. The sign of the detected EBIC signal provides information about the local doping type [9]. The direction of the current in the EBIC measurements indicated that the needles were in contact to a *p*-type region in both measurements. Also there are bright vertical lines at the positions of the *pn*-junctions indicating that a current is pushed towards the needle in these locations. This is consistent with the SRP measurements.

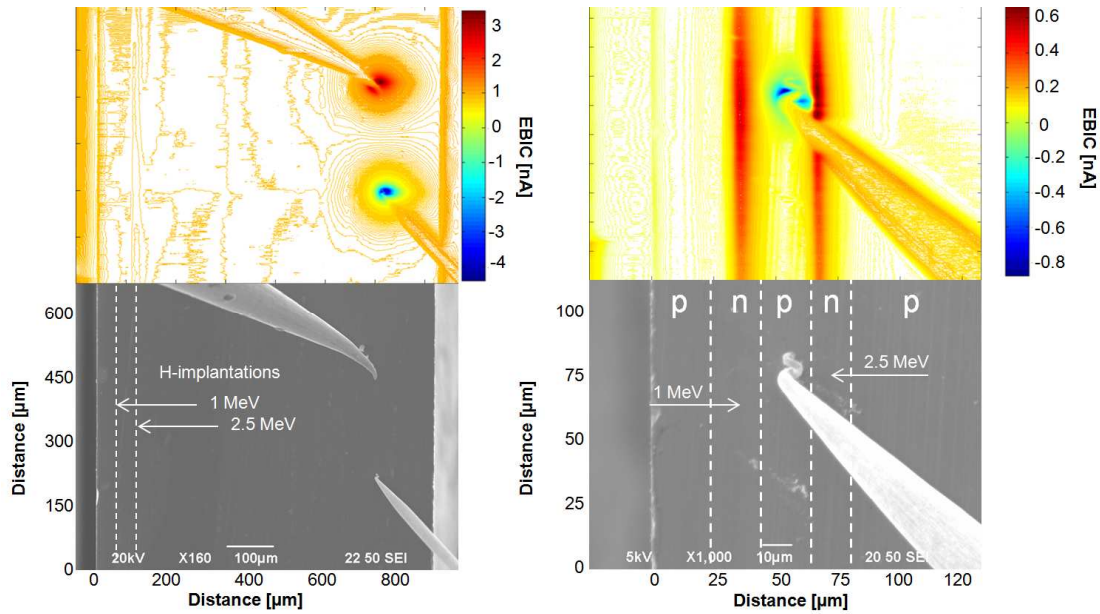


Figure 4. (bottom) Secondary electron image of the cross-section of a proton implanted (energy: 2.5 and 1 MeV, dose: $1 \times 10^{14} \text{ cm}^{-2}$) Fz silicon wafer annealed at 350°C for one hour. Schottky contacts are formed by placing tungsten tips on the cross-section. (top) Electron beam induced current images where the EBIC signal was collected by the metal tips.

Figure 5 shows an EBIC measurement that was used to extract the minority carrier diffusion length L_D [7]. The electron beam was scanned along the black line shown in the inset. Charge carriers were generated along this line in the p -type region of the sample. The minority carriers decay like $\exp(-L_D r)/r$ where r is the distance from the generation point. The current collected at the Schottky contact were the needle presses on the silicon is proportional to the minority carrier concentration. The diffusion length was measured to be $5 \pm 1 \mu\text{m}$ in the p -type region. A similar measurement in the n -type region near the implantation depth yielded a diffusion length of $8 \pm 2 \mu\text{m}$ and a measurement in the substrate far from the implantations yielded a diffusion length of $25 \pm 5 \mu\text{m}$. The diffusion length is related to the diffusion constant D and the minority carrier lifetime τ , $L_D = \sqrt{D\tau}$. The diffusion constant is related to the mobility μ by the Einstein relation, $eD = \mu k_B T$. Here e is the electron charge, k_B is Boltzmann's constant and T is the absolute temperature. The defects introduced by the implantations influences both the minority carrier lifetime and the mobility resulting in a shorter diffusion length in the implanted regions.

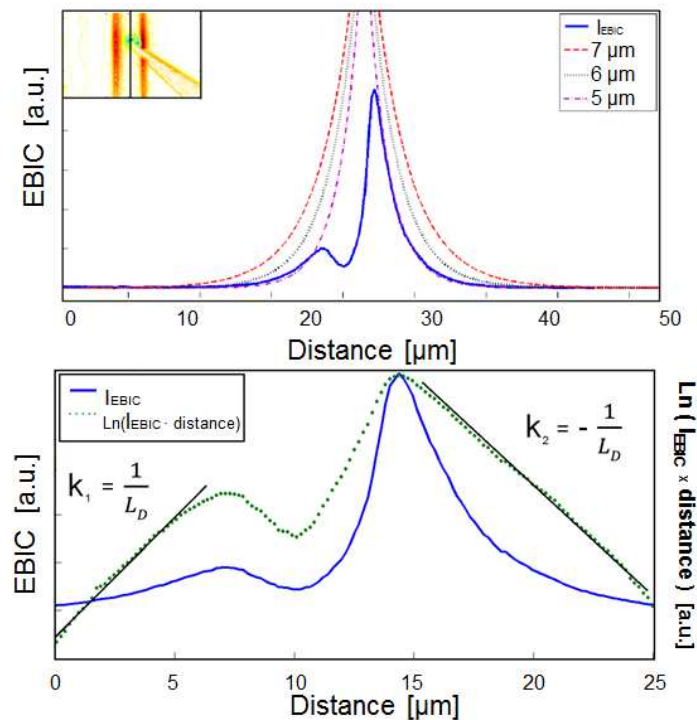


Figure 5. Determination of the diffusion length of the minority charge carriers L_D in the p -type doped region by the investigation of the measured EBIC signal decay. (bottom) L_D is inversely proportional the slope of the logarithm of the EBIC signal times the distance. The decay of the EBIC signal was simulated for different L_D . (top)

Conclusions

Proton doped silicon was examined by SRP and EBIC. The measurements show that n -doped regions were formed at the implantation depth of the hydrogen. During an anneal the hydrogen diffuses and hydrogen donors are formed in radiation damaged regions. The resulting carrier concentration profile is proportional to the concentration of radiation induced defects not to the concentration of hydrogen. The measurements of the minority carrier diffusion length show that it is much shorter in the implanted regions.

References

- [1] I. Pintlilie, E. Fretwurst, G. Lindström, J. Stahl, Appl. Phys. Lett., 82, 13 (2003) 2169-2171
- [2] Y. Zohta, Y. Ohmura, and M. Kanazawa, Jpn. J. Appl. Phys., 10, 4 (1971) 532-533
- [3] Yu. V. Gorelkinskii, V. O. Sigle, and Zh. S. Takibaev, Phys. Status Solidi A, 22, (1974) K55-K57
- [4] M. Pawlik, Journal Vacuum Science and Technology B, 10, 1 (1992) 388-396
- [5] R. Job, J. G. Laven, F.-J. Niedernostheide, H.-J. Schulze, H. Schulze, W. Schustereder, physica status solidi (a) 209, 10 (2012) 1940-1949
- [6] J. G. Laven, H.-J. Schulze, F.-J. Niedernostheide, W. Schustereder and L. Frey, ECS Trans. 50, 5 (2013) 161-175
- [7] J. F. Ziegler, Proc. of Conf. on Ion Beam Analysis, 219-220 (2004) 1027-1036
- [8] H. J. Leamy, J. Appl. Phys. 53 (1982) R51-R80
- [9] S. Kirnstötter, M. Faccinelli, P. Hadley, R. Job, W. Schustereder, J. G. Laven, H.-J. Schulze, ECS Trans. 50, 5 (2013) 115-120

Depletion of Superjunction Power MOSFETs Visualized by Electron Beam Induced Current Measurements

The following corresponds to the publication by

S. Kirnstoetter, M. Faccinelli, M. Jelinek, W. Schustereder, J.G. Laven, H.-J. Schulze and P. Hadley, *Depletion Behavior of Superjunction Power MOSFETs Visualized by Electron Beam Induced Current and Voltage Contrast Measurements*, *physica status solidi (c)* 1610-1642 (2014), doi:10.1002/pssc.201400050

The author of this thesis was responsible for the following points

- Electron Beam Induced Current measurements
- measurement result analysis and interpretation
- main authorship

The contribution of the other authors of this publication are listed below

- M. Faccinelli: Electron Beam Induced Current measurements, measurement result analysis and interpretation
- M.Jelinek: measurement result analysis and interpretation
- W. Schustereder: measurement result analysis and interpretation
- J.G. Laven: measurement result analysis and interpretation
- H.-J. Schulze: measurement result analysis and interpretation
- P. Hadley: authorship, measurement result analysis and interpretation

Depletion of superjunction power MOSFETs visualized by electron beam induced current and voltage contrast measurements

Stefan Kirnstoetter^{**1,2}, Martin Faccinelli¹, Moriz Jelinek², Werner Schustereder², Johannes G. Laven³, Hans-Joachim Schulze³, and Peter Hadley^{*1}

¹ Institute of Solid State Physics, Graz University of Technology, Graz 8010, Austria

² Infineon Technologies Austria AG, Villach 9500, Austria

³ Infineon Technologies AG, 81726 Munich, Germany

Received 29 April 2014, revised 25 May 2014, accepted 26 May 2014

Published online 13 August 2014

Keywords EBIC, voltage contrast, power devices, MOSFET, depletion

* Corresponding author: e-mail p.hadley@tugraz.at, Phone: +43 316 873 8967, Fax: +43 873 108 967

** e-mail stefan_kirnstoetter@gmx.at, Phone: +43 664 1433596

Electron Beam Induced Current (EBIC) measurements were used to produce cross sectional images of superjunction power transistors. These images show how the depletion width expands under reverse bias. Superjunctions are alternating p- and n-type doped vertical columns placed between drain and source in a power transistor (Deboy et al., in: Proc. IEDM, 983-685 (1998); Lorenz et al., in: Proc. PCIM Europe, 250-258 (1998)). These columns allow a higher substrate doping of the drift region, resulting in a lower on-state resistance while still maintaining a high breakdown voltage. When the

device is reverse biased, the space charge region of the superjunction should expand symmetrically due to the homogeneous doping (in the n and p region) until the complete device depletes. The depletion process was also visualized using voltage contrast (VC) measurements. Here the secondary electron signal was detected when the device was reverse biased. We show that EBIC and VC measurements can provide valuable input for process tuning and process simulations, enabling the use of smaller dimensions and higher doping levels.

© 2014 WILEY-VCH Verlag GmbH & Co. KGaA, Weinheim

1 Introduction In comparison to regular vertical power MOSFET devices, superjunction MOSFET devices have a very high breakdown voltage V_{br} and a relatively low on-state resistance $R_{DS,on}$ [3]. Regular MOSFET devices designed for blocking voltages above 100 V show a strong increase of the on-state resistance ($\sim V_{br}^2$). In a superjunction MOSFET $R_{DS,on}$ increases proportional to $V_{br}^{1.3}$. These devices apply the concept of charge compensation that allows a higher substrate doping of the drift region while still maintaining a high breakdown voltage [1, 2]. In a superjunction MOSFET alternating p- and n-type doped columns are placed between the drain and the source contact. Due to the mutual compensation of the positively charged donors in the n-type columns and the negatively charged acceptors in the p-type columns, the overall doping concentration in the area of the columns can be increased by more than an order of magnitude without the loss of any blocking capability. In the on-state the current

flow goes through the n-type doped columns. In the off-state when the superjunction device is reverse biased, the depletion region between the p- and the n-type regions expands until the whole device depletes. To allow for good charge compensation, the doping concentration in the n- and p-type columns has to have accurately the same level. The columns are created by several epitaxial depositions of phosphorous doped silicon layers each followed by a boron implantation to form the p-type columns. Alternative fabrication methods have been tested, where the formation of n-type columns was realized via the implantation of hydrogen ions [4, 5]. Although the formation of deep doping profiles due to the implantation of hydrogen [6] is a very useful method, this process is not used because the formation/dissociation [7] and diffusion processes [8] of the hydrogen-related thermal donors are still not well understood and may lead to reliability issues.

2 Experimental To make cross sectional images of the transistors, the (100) wafers were cleaved by hand to expose a (010) surface. To perform investigations in planar view the front side of the wafer was polished using SiC grinding paper to expose a (100) plane. Electrical contacts were made to the source and drain contacts and the devices were mounted in a JEOL JSM-6490 LV Scanning Electron Microscope. For the EBIC measurement, Stanford Research System SR570 current amplifiers were used. In this study the collection of the electron beam induced current at the cross section of superjunction MOSFET devices was performed under reverse bias conditions. For this, a reverse bias from -2.5 V to -50 V was applied using a Keithley 2636A source meter electrically coupled to the drain and source electrodes of the device. To eliminate the DC leakage current that appeared due to the biasing, the electron beam was blanked periodically using an AdWin Pro II digital-to-analog converter and the EBIC signal was collected using a lock-in amplifier (Stanford Research Systems Mode SR830). A schematic of the pulsed beam EBIC measurement is shown in Fig. 1 [14, 15]. A complementary measurement to EBIC is a voltage contrast measurement [18]. For this latter, the superjunction was reverse biased while images were made using the secondary electron detector.

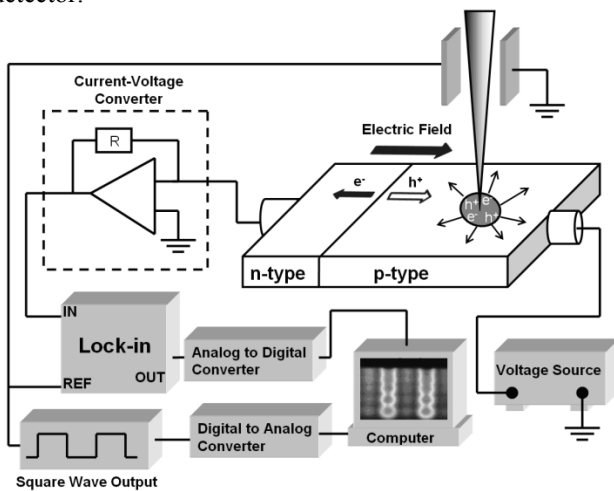


Figure 1 A schematic of the EBIC measurement setup to investigate devices under reverse bias. The electron beam is blanked periodically and the EBIC signal is collected using a lock-in amplifier.

3 Electron beam induced current investigations EBIC is an analytical technique used in a SEM to investigate junctions, built-in electric fields or defects in semiconductors [9, 10]. Material properties like the effective minority charge carrier diffusion length [11] or the surface recombination velocity [12] can be extracted with this method. During an EBIC measurement, an electron beam is scanned over the sample and generates electron hole (eh) pairs in the semiconducting material. These eh-pairs diffuse around until they get separated by a built-in

electric field at a pn-junction or a Schottky contact. When the eh-pairs are generated close to such a built-in electric field, some excess charge carriers will diffuse there and an EBIC signal can be detected. If the eh pairs are generated far from a junction, the excess charge carriers recombine and no EBIC signal is detected. The maximum EBIC signal is located at the maximum electric field, which is at the position of the metallurgical pn-junction. Because of the high doping concentrations of the n- and p-regions in a superjunction device, a high EBIC signal can be detected directly at the superjunction [13].

In the left part of Fig. 2 a schematic cross section of a superjunction MOSFET with vertical p-type and n-type columns for charge compensation is shown. The different epitaxial layers are indicated by the dotted lines. Due to the annealing process after the deposition and implantation the acceptors diffuse around and thus bubbles form. In the right part of Fig. 2 a series of normalized pulsed beam EBIC measurements of a superjunction device under different reverse bias voltages applied is shown. The red region represents the maximum EBIC signal. The blue regions indicate a low EBIC signal. As the reverse bias voltage is increased, the peak in the EBIC signal near the pn-junction broadens. This broadening comes from the expansion of the depletion region [16]. Between the red columns in the figure there are p-type columns buried deeper under the specimen surface that give a weaker EBIC signal (as can be seen in Fig. 3).

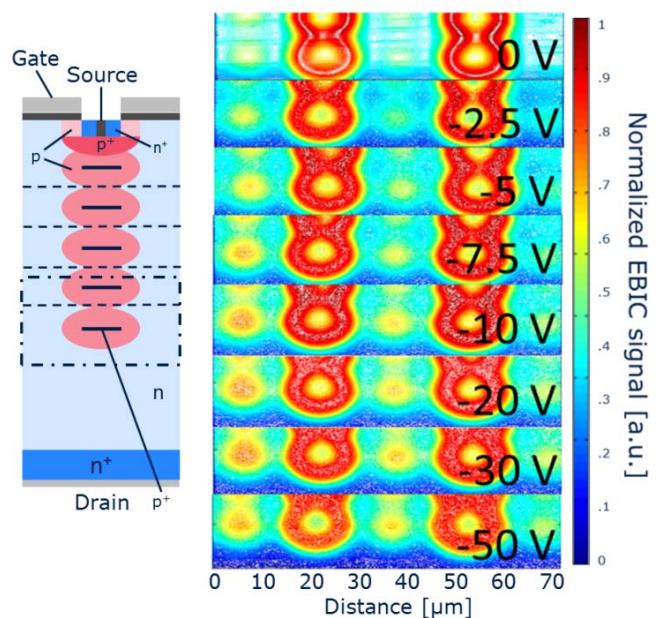


Figure 2 (left) Schematic cross section of a superjunction MOSFET with vertical p-type and n-type columns for charge compensation. The dash-dotted square indicates the investigated region in the EBIC measurement to the right. (right) Normalized pulsed beam EBIC measurements of the cross section of a reverse-biased superjunction device. Reverse bias voltages up to -50 V were applied. The acceleration voltage was 20 keV.

With increasing e-beam energy the electron penetration depth and interaction volume increases and more charge carriers can be collected. The shape and size of the interaction volume of an electron beam in various materials can be simulated using Casino Simulations [17]. Figure 3 shows EBIC images of the pn-junctions in a planar view.

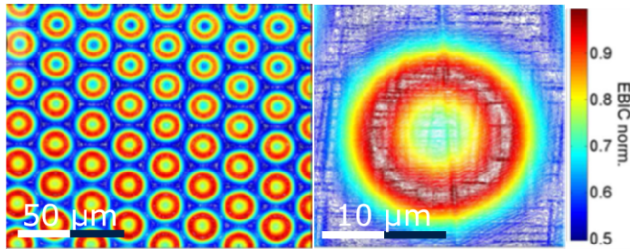


Figure 3 Planar view EBIC images of the superjunction columns. The electron beam acceleration voltage was 20 keV.

Figure 4 shows line scans of the EBIC signal for different bias voltages. The scans have been recorded along the white line indicated in the inset of the figure. Each subsequent curve is offset by 1 nA from the previous curve where the curve for 0 V bias has no offset. For low bias voltages, the peaks in the EBIC signals indicate the positions of the pn-junctions. The EBIC signal is high when the beam strikes a depleted region where the minority carrier lifetime is long and becomes lower when the beam strikes a region that is not depleted and the minority carrier lifetime is short. For low reverse bias voltages, there are dips in the EBIC signal at about 20 and 50 μm. This is due to recombination in the undepleted regions of the p-columns. As the reverse bias voltage increases, the whole p-columns deplete and the dips disappear. The measurements show which regions are depleted under which bias conditions.

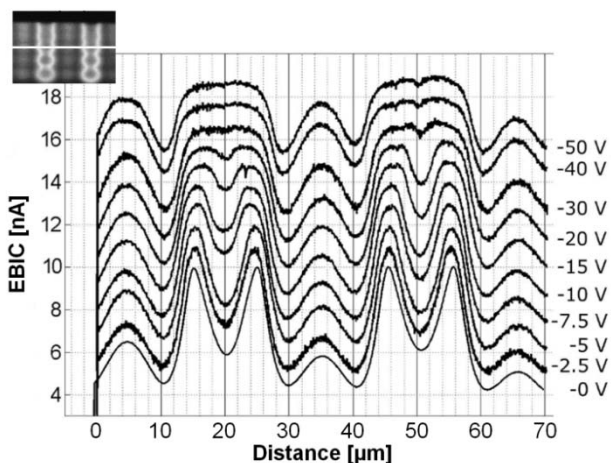


Figure 4 Waterfall plot of EBIC measurements of biased superjunctions. The specimen was mounted in the specimen holder and reverse bias voltages from 0 to -50 V were applied. In the top left image the position on the columns is shown where the line scans were performed. There is no offset in the curve with zero bias voltage. Each subsequent curve is offset by 1 nA from the previous curve.

4 Voltage contrast measurements Figure 5 shows the voltage contrast images. The regions with the highest negative potential appear brighter in the images. This is due to the fact that these regions have the lowest work function. The work function describes the barrier the electrons must overcome to escape from the specimen surface. At zero bias voltage, the columns cannot be distinguished from the bulk material. However, when -2.5 V are applied, the p-type columns can clearly be seen. The maximum contrast was observed at -7.5 V. For larger reverse bias voltages, the apparent width of the p-type columns as well as the contrast decreases. The voltage contrast becomes very weak for reverse bias voltages of more than -50 V. The concrete mechanism that causes the voltage contrast is not clearly understood [19, 20] and it is not known why the contrast decreases for large reverse bias voltage.

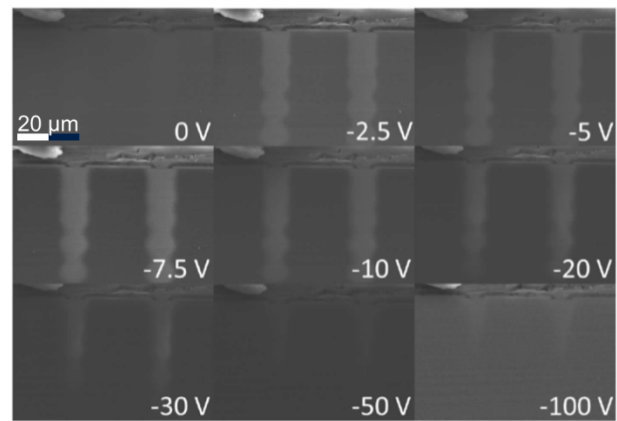


Figure 5 Voltage contrast measurements at the cross section of a superjunction device. A bias from -2.5 V to -100 V was applied between the source and drain contact and the secondary electron signal was measured.

While both voltage contrast and EBIC measurements can show the p-type columns at low voltages, the EBIC signal better resolves their exact position, since the maximum EBIC signal is generated in the depletion layer at the pn-junctions. The EBIC signal also remains visible at much higher reverse bias voltages so it is more suitable for investigating how the depletion region broadens.

5 Conclusions EBIC measurements were used to visualize pn-junctions in a superjunction transistor. It was possible to make cross sectional images vertically through the wafer. Determining the positions of the pn-junctions is useful in devices which depend on charge compensation. The EBIC and Voltage Contrast measurements under reverse bias illustrate how the depletion occurs within a superjunction. These measurements can be compared to process flow simulations which are used to tune the physical process parameters. Better control of the process will allow for higher doping levels and thereby a lower on-state resis-

tance. For the fabrication of superjunction MOSFETs, a trade-off between the processing effort and the deviation of the actual structure from the ideal structure must be found. The EBIC measurements presented here provide a feasible method to visualize the actual distribution of p- and n-type regions in the device. They provide a valuable input for the adjustment of the doping concentrations to reach a better charge compensation. Additionally the impact of process parameter variations (e.g. of the thermal budget for diffusion of the implanted acceptors) on the electrical properties of the device can be checked.

Acknowledgements The work has been performed in the project EPPL, co-funded by grants from Austria, Germany, The Netherlands, Italy, France, Portugal- ENIAC member States and the ENIAC Joint Undertaking. This project is co-funded within the programme "Forschung, Innovation und Technologie für Informationstechnologie" by the Austrian Ministry for Transport, Innovation and Technology.

References

- [1] G. Deboy, M. März, J. P. Stengl, H. Strack, J. Tihanyi, and H. Weber, in: Proc. IEDM, 983-685 (1998).
- [2] L. Lorenz, G. Deboy, M. März, J.-P. Stengl, and A. Bachofner, in: Proc. PCIM Europe, 250-258 (1998).
- [3] T. Fujihira, Jpn. J. Appl. Phys. **36**(part 1), 6254-6262 (1997).
- [4] H.-J. Schulze, M. Buzzo, F.-J. Niedernostheide, M. Rüb, H. Schulze, and R. Job, ECS Trans. **3**, 135-146 (2006).
- [5] M. Buzzo, M. Ciappa, M. Rüb, and W. Fichtner, in: Proc. IPFA Singapore, 285-289 (2005).
- [6] G. H. Schwuttke, K. Brack, E. F. Gorey, A. Kahan, and L. F. Lowe, Radiat. Eff. Defects Solids E **6**, 103-106 (1970).
- [7] J. G. Laven, R. Job, H.-J. Schulze, F. J. Niedernostheide, W. Schustereder, and L. Frey, ECS J. Solid State Sci. Technol. **2**, 389-394 (2013).
- [8] S. Kirmstötter, M. Faccinelli, W. Schustereder, J. G. Laven, H. J. Schulze, and P. Hadley, AIP Conf. Proc. **1583**, 51-55 (2014).
- [9] T. E. Everhart, K. C. A. Smith, and O. C. W. Oatley, in: Proc. 4th Int. Conf. on Electron Microscopy Physics, Vol. 1, pp. 269-273 (1958).
- [10] H. J. Leamy, J. Appl. Phys. **53**, R51-R80 (1982).
- [11] D. E. Ioannou and C. A. Dimitriadis, IEEE Trans. Electron Devices **29**, 445-450 (1982).
- [12] V. K. S. Ong, J. C. H. Phang, and D. S. H. Chan, J. Solid State Electron. **37**, 1-7 (1994).
- [13] S. Kirmstötter, F. Faccinelli, P. Hadley, R. Job, W. Schustereder, J.G. Laven, and H.-J. Schulze, in: ECS Trans. **49**, 475-481 (2012).
- [14] T. Sekiguchi and K. Sumino, Rev. Sci. Instrum. **66**, 4277-4282 (1995).
- [15] A. Pugatschow, T. Geinzer, R. Heiderhoff, F.-J. Niedernostheide, H.-J. Schulze, B. Wiedenhorst, and L. Balk, in: Proc. ISPSD, IEEE International Symposium on Power Semiconductor Devices and IC's, pp. 1-4 (2006).
- [16] N. C. MacDonald and T. E. Everhart, Appl. Phys. Lett. **7**, 267-269 (1965).
- [17] H. Demers, N. Poirier-Demers, A. R. Couture, D. Joly, M. Guilmain, N. de Jonge, and D. Drouin, Scanning **33**, 135-146 (2011).
- [18] R. F. Egerton, in: Physical Principles of Electron Microscopy (Springer, Berlin, 2005).
- [19] D. D. Perovic, M. R. Castell, A. Howie, C. Lavoie, T. Tiedje, and J. S. W. Cole, Ultramicroscopy **58**, 104-113 (1995).
- [20] R. Turan, D. D. Perovic, and D. C. Houghton, Appl. Phys. Lett. **69**, 1593-1595 (1996).

High Dose Proton Implantation into Silicon: A Combined EBIC, SRP and TEM Study

The following corresponds to the publication

S. Kirnstoetter, F. Faccinelli, C. Gspan, W. Grogger, M. Jelinek, W. Schustereder, J.G. Laven, H.-J. Schulze, *High Dose Proton Implantations into Silicon: A Combined EBIC, SRP and TEM Study*, physica status solidi (c), 1610-1642 (2014), doi:10.1002/pssc.201400051

The author of this thesis was responsible for the following points

- EBIC and SRP measurements
- EBIC and SRP measurement results analysis and interpretation
- main authorship

The contribution of the other authors of this publication are listed below

- M. Faccinelli: EBIC measurements, measurement result analysis and interpretation
- C. Gspan: transmission electron microscopy (TEM) and electron diffraction measurement and interpretation
- W. Grogger: transmission electron microscopy (TEM) and electron diffraction measurement results interpretation
- J.G. Laven: measurement result analysis and interpretation
- W. Schustereder: measurement result analysis and interpretation
- H.-J. Schulze: measurement result analysis and interpretation
- P. Hadley: authorship, measurement result analysis and interpretation

High dose proton implantations into silicon: a combined EBIC, SRP and TEM study

Stefan Kirnstoetter^{*,1,3}, Martin Faccinelli¹, Christian Gspan², Werner Grogger², Moriz Jelínek³, Werner Schustereder³, Johannes G. Laven⁴, Hans-Joachim Schulze⁴, and Peter Hadley^{*,1}

¹Institute of Solid State Physics, Graz University of Technology, 8010 Graz, Austria

²Institute for Electron Microscopy and Nanoanalysis (FELMI), Graz University of Technology, 8010 Graz, Austria

³Infineon Technologies Austria AG, 9500 Villach, Austria

⁴Infineon Technologies AG, 81726 Munich, Germany

Received 29 April 2014, revised 25 May 2014, accepted 27 May 2014

Published online 13 August 2014

Keywords hydrogen implantation, silicon, TEM, EBIC, spreading resistance profiling

* Corresponding author: e-mail p.hadley@tugraz.at, Phone: +43 316 873 8967, Fax: +43 873 108967

** e-mail stefan_kirnstoetter@gmx.at, Phone: +43 664 1433596

Proton (H^+) implantations are used in power semiconductor devices to introduce recombination centers (Hazdra et al., *Microelectron. J.* **32**(5), 449-456 (2001)) or to form hydrogen related donor complexes (Zohta et al., *Jpn. J. Appl. Phys.* **10**, 532-533 (1991)). Proton implantations are also used in the 'smart cut' process to generate defects that can be used to cleave thin wafers (Romani and Evans, *Nucl. Instrum. Methods Phys. Res. B* **44**, 313-317 (1990)). However, the implantation damage resulting from H^+ implantations is not completely understood. In this study, protons with energies from 400 keV up to 4 MeV and doses up to $10^{16} H^+/cm^2$ were implanted into highly ohmic boron doped m:Cz silicon (100). Electron Beam Induced Current (EBIC) measurements were performed to locally determine the minority charge carrier dif-

fusion length. The diffusion length decreases with increasing implantation dose and incorporated damage. Spreading Resistance Profiling (SRP) measurements were performed to analyze the charge carrier concentration profiles for different annealing procedures. The electrical activation and growth of the defect complexes varies strongly with the annealing parameters. Transmission Electron Microscopy measurements were made to investigate the microscopic structures formed by the high dose implantation processes. Due to the high local damage density resulting from low energy and high dose H^+ implants, platelet structures are formed. During high-energy high-dose H^+ implantations, the implanted hydrogen generates strain in the crystal lattice resulting in changes in the distances between atomic planes.

© 2014 WILEY-VCH Verlag GmbH & Co. KGaA, Weinheim

1 Introduction Because protons (H^+) are so light, they can be implanted deep into silicon. The implantation depth can be adjusted by changing the implantation energy of the ions. There are various useful ways proton implantations are used in the manufacturing process of semiconductor devices. Very low doses, 10^{11} - $10^{13} H^+/cm^2$, followed by anneals at temperatures around 200°C are used to adjust the charge carrier lifetime via the controlled incorporation of recombination centers. Alternative approaches have been used to adjust the charge carrier lifetime like the diffusion of gold [4] or platinum [5] but lifetime control via the implantation of light particles is a rather simple approach where a damage profile with a maximum at the

implantation depth is formed [6, 7]. This works very well up to implantation doses of $10^{12} H^+/cm^2$, because of the formation of additional H-related thermal donor complexes [8, 9]. This makes helium in comparison to hydrogen, where only damage but no donors form, a more suitable candidate for charge carrier lifetime control [10]. A second application of H^+ implantations is to create regions of n -type doping. H^+ implantations in the dose range of 10^{13} - $10^{15} H^+/cm^2$ and anneals in the temperature range from 350 °C to 550 °C are used to form H-related thermal donor complexes [2, 11]. The concentration and type of these thermal donors strongly depend on the annealing temperature and annealing time [12-16]. The structure as well as

the formation and dissociation process of these donor complexes was investigated in various studies using deep level transient spectroscopy [17], infra-red spectroscopy [18], electron paramagnetic resonance [19] and spreading resistance profiling [20]. One important application of H^+ implantation doping is as a field stop of an Isolated Gate Bipolar Transistor (IGBT) [8]. A third application of hydrogen implantations is to cleave the top layer of a wafer off in the so called Smart Cut process [21, 22]. Very high implantation doses, larger than $10^{16} H^+/cm^2$, can result in a splitting/breaking of the target material at the implantation depth. Here, high concentrations of the incorporated damage and hydrogen form platelet crystal defects about 10 nm in size [21, 23]. These platelets grow during an annealing step between 400 °C and 600 °C after the implantation. When the implantation dose is high enough, the implanted semiconductor can be splitted at the implantation depth [24]. The implanted hydrogen promotes the splitting process due to a chemical saturation of the dangling silicon bonds created during the implantation [25].

2 Experimental In this work commercially available highly-ohmic ($\geq 1000 \Omega cm$) m:Cz silicon wafers were implanted with protons with implantation energies from 400 keV up to 4 MeV. Proton doses in the range of 4×10^{14} - $1 \times 10^{16} H^+/cm^2$ were implanted at room temperature. To perform EBIC measurements on the cross section of the H^+ -implanted wafers, the wafers were broken by hand and polished using SiC grinding paper. Schottky contacts were made on various positions on the cross section using thin tungsten metal tips mounted in Kleindiek micromanipulators. The EBIC measurements were performed in a JEOL JSM-6490 LV Scanning Electron Microscope using Stanford Research System SR570 Current Amplifiers and an AdWin Pro II analog-to-digital converter. For SRP measurements, the sample surface was ground at an angle and the metal tips were placed on the bevel during the measurements. To prepare samples for TEM measurements, small pieces were cut out with a diamond wire saw. Then they were ground on a disc grinder with SiC grinding paper and polished with diamond paste. Then the samples were put into a dimple grinder and finally ion thinned in a precession ion polishing system with 4 keV argon ions. The electron transparent regions were investigated later during the TEM investigations. To investigate point or line defects with TEM, the Focused Ion Beam (FIB) could not be used to cut out a small piece from the specimen material because the damage produced by the FIB could not easily be distinguished from the defect structures originally present.

3 Electron beam induced current (EBIC) investigations EBIC is an analysis technique used in a Scanning Electron Microscope (SEM) to investigate buried junctions, like pn-junctions, Schottky contacts, or defects in semiconductors. It can also be used to determine electrical

properties of semiconductors like the doping type or the minority charge carrier diffusion length L_D [25, 27, 28] as demonstrated in Fig. 1.

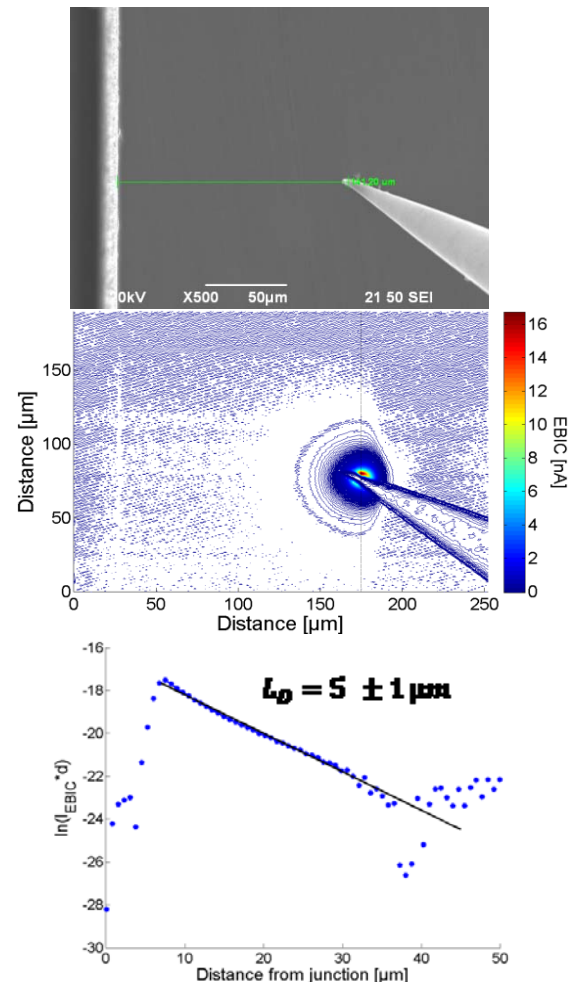


Figure 1 (top) Secondary Electron Image of a metal tip making contact to the cross section of a silicon wafer (middle) EBIC image of this configuration (bottom) extraction of the diffusion length from the decay of the EBIC signal from the metal semiconductor contact.

During an EBIC measurement, an electron beam scans over the specimen and generates electron hole pairs in the semiconductor. These excess charge carriers are separated by a built-in electric field when the interaction volume is close enough to such a built-in electric field so that the charge carrier can diffuse to it before they recombine. Then an electron beam induced current can be measured between the electrical contacts. The measurement geometry used in Fig. 1 was used to locally determine the doping type and the minority charge carrier diffusion length at every position of the H^+ implantation profile. When such a metal tip forms a Schottky contact, depending on the semiconductor doping type a built-in electric field forms point-

ing towards (p) or away (n) from the semiconductor resulting in a negative (p-type) or positive (n-type) EBIC signal detected from the metal tip. From the exponential decay of this measurement signal, the diffusion length can be extracted as explained in reference [26]. As can be seen in the middle part of Fig. 1, the decay of the EBIC signal is strongly affected by the implanted hydrogen on the right of the Schottky contact so the diffusion length can only be extracted from the decay in *y*-direction. In Fig. 2 and 3, the resulting charge carrier concentration (CCC) profiles of H⁺ implanted silicon wafers are plotted together with the local *L_D* values. Fig. 2 shows the SRP and *L_D* profiles of a silicon wafer implanted with 2.5 MeV, 5 × 10¹⁵ H⁺/cm² and 1 × 10¹⁶ H⁺/cm² annealed at 500 °C for 5 hours. In Fig. 3, the profiles of wafers implanted with 4 MeV 1 × 10¹⁵ H⁺/cm² and 4 × 10¹⁴ H⁺/cm² annealed at 500 °C for 5 hours are shown. The solid lines represent the CCCs calculated from spreading resistance measurements. As expected, the CCC increases with increasing implantation dose as can be seen in both Figs. 2 and 3. The red and blue dotted lines represent the measured minority charge carrier diffusion lengths. The *L_D* values are given on the right *y*-axis. In Figs. 2 and 3 it can be seen that the *L_D* profiles are approximately the inverse of the CCC profiles obtained from SRP measurements. At the position of the CCC maximum the *L_D* profile has its minimum and it strongly increases into the bulk region of the silicon wafer. Also it can be seen that when the implantation dose is increased, *L_D* decreases. In the region between the surface (left edge) and the implantation depth this decrease can be explained with a higher number of incorporated recombination centers and defect complexes reducing the diffusion length. This can be seen more clearly in Fig. 2.

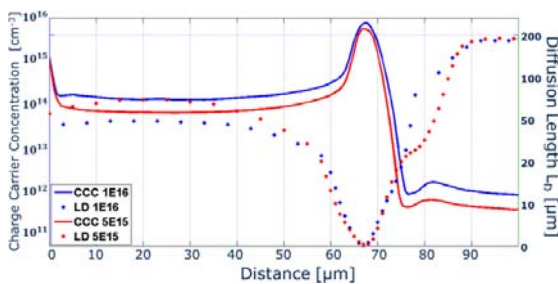


Figure 2 (left *y*-axis) The solid lines represent the charge carrier concentration calculated from Spreading Resistance Profiling measurements of H⁺ implanted and annealed silicon wafers (implantation energy: 2.5 MeV, implantation dose: 5 × 10¹⁵ H⁺/cm² and 1 × 10¹⁶ H⁺/cm², anneal: 500 °C for 5 hours). (right *y*-axis) The dotted lines represent the minority charge carrier diffusion length *L_D*. The red line represents *L_D* for the 5 × 10¹⁵ H⁺/cm² implantation dose and the blue line stands for the 1 × 10¹⁶ H⁺/cm² implantation dose.

In the region beyond the implantation peak, the increase of the CCC with increasing H⁺ implantation dose can be explained by the role of hydrogen as a catalyst during the oxygen diffusion process and the oxygen thermal

donor (OTD) formation process in oxygen rich silicon [29]. The oxygen concentration in the m:Cz silicon wafers investigated in this study was approximately 4 × 10¹⁷ cm⁻³ according to the wafer manufacturer. It should be mentioned that the extraction of the charge carrier diffusion length using EBIC can only be used to qualitatively measure changes of *L_D* when no concrete values for the surface recombination velocity *v_s* are taken into account. The measured diffusion length *L_{D,eff}* can be described as having a surface component and a bulk component

$$L_{D,eff} = \frac{1}{\frac{1}{L_{D,surface}} + \frac{1}{L_{D,bulk}}} \quad (1)$$

The diffusion lengths in the plots are the bulk diffusion lengths calculated using this formula where the measured values are used for *L_{D,eff}* and the surface contribution is assumed to be the same everywhere. The value of the surface contribution is determined in the substrate region where there is no implantation damage and the bulk diffusion length is known to be around 200 μm. The extracted *L_D* values for n-type doped semiconductors are typically lower than the values for p-type semiconductors. This is because the mobility of holes is lower than that of electrons and during the measurement the surface gets negatively charged which pulls the holes towards the surface where they recombine [30,31].

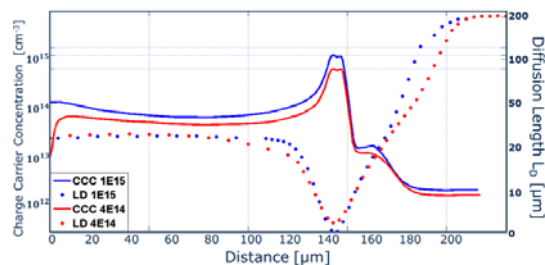


Figure 3 (left *y*-axis) The solid lines represent the charge carrier concentration calculated from Spreading Resistance Profiling measurements on H⁺ implanted and annealed silicon wafers (implantation energy: 4 MeV, implantation dose: 4 × 10¹⁴ H⁺/cm² and 1 × 10¹⁵ H⁺/cm², anneal: 500 °C for 5 hours). (right *y*-axis) The dotted lines represent the minority charge carrier diffusion length *L_D*. The red line represents *L_D* for the 4 × 10¹⁴ H⁺/cm² implantation dose and the blue line for the 1 × 10¹⁵ H⁺/cm² dose.

4 Transmission electron microscopy (TEM)

TEM measurements were used to investigate defect structures resulting from high dose hydrogen ion implantations in silicon. The crystal defects incorporated due to the implantation have been investigated before and after an anneal. The focus of this study is the comparison of high dose H⁺ implants with low energies (400 keV) and high energies (4 MeV). As was reported in various studies [22–24] the implantation of high doses of low energy (≤ 400 keV) protons into silicon results in the formation of platelet structures. Figure 4 shows a TEM image of silicon im-

planted with 400 keV protons at the projected implantation depth. A dose of $1 \times 10^{16} \text{ H}^+/\text{cm}^2$ was implanted and the specimen was subsequently annealed at $500 \text{ }^\circ\text{C}$ under N_2 atmosphere for one hour. The image shows an $200 \times 200 \text{ nm}^2$ area directly at the H^+ implantation depth.

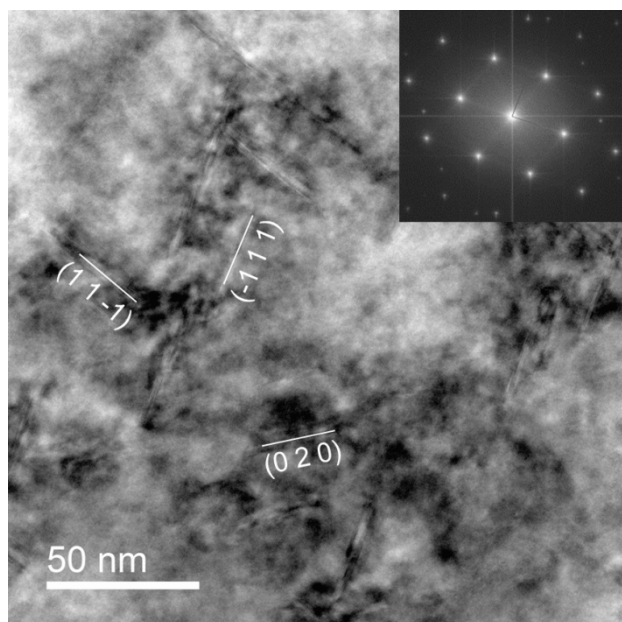


Figure 4 Transmission Electron Microscopy image of H^+ implanted silicon (implantation energy: 400 keV, implantation dose: $1 \times 10^{16} \text{ H}^+/\text{cm}^2$ annealing parameters: $500 \text{ }^\circ\text{C}$ under N_2 atmosphere for one hour). (Inset) FFT image of the TEM image.

As can be seen the platelet structures are formed in the $\{111\}$ and $\{100\}$ planes as reported in literature for (100) grown silicon wafers implanted with high doses of hydrogen ions [21-24]. In the Fast Fourier Transformation (FFT) image, thin lines can be seen between the main peaks originating from the orientations of the formed defect structures. In Fig. 5 a TEM image of hydrogen implanted silicon implanted with a much higher energy and lower dose is shown (implantation dose: $4 \times 10^{14} \text{ H}^+/\text{cm}^2$ implantation energy: 4 MeV). The image was taken of an $50 \times 50 \text{ nm}^2$ area directly at the implantation depth. In the implantation depth, about 5 nm thick layers with differing lattice constants, oriented from the top left edge to the bottom right edge, are formed. These layers/regions can be identified more clearly in the lower plot of Fig. 5. Here a special low pass filter was used to visualize the different regions formed due to the H^+ implantation. These regions, or the defects formed in this regions also form in the $\{111\}$ planes. To check for the formation of amorphous regions due to the implantation, FFT's are shown for the two regions marked in the figure. These clearly show that the sample is crystalline.

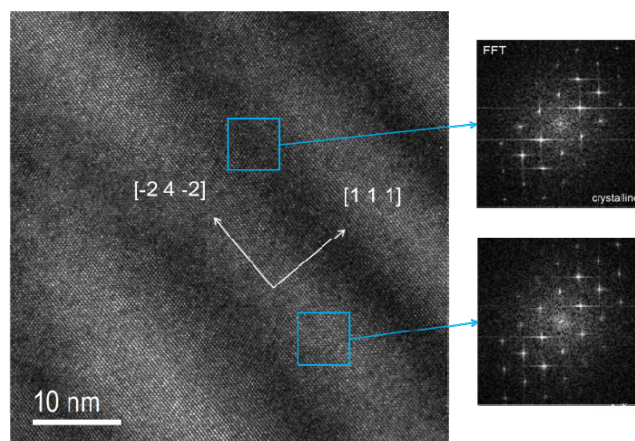


Figure 5 (left) Transmission Electron Microscopy image of hydrogen implanted silicon (implantation energy: 4 MeV, implantation dose: $4 \times 10^{14} \text{ H}^+/\text{cm}^2$). To better visualize the structures formed due to the H^+ implantation a low pass filter was used. (right) FFT images of the areas indicated by the small blue boxes.

Due to continuative investigations of these layer structures changes in the crystal lattice spacing due to the implantation of hydrogen were recognized (as can be seen in Fig. 6). It was found that the lattice constant over 5 atoms rows (2.5 nm) changed by a distance of 0.1 nm between the nearby regions indicated in Fig. 6. This modulation of the lattice constant may be the precursor to the formation of the platelets.

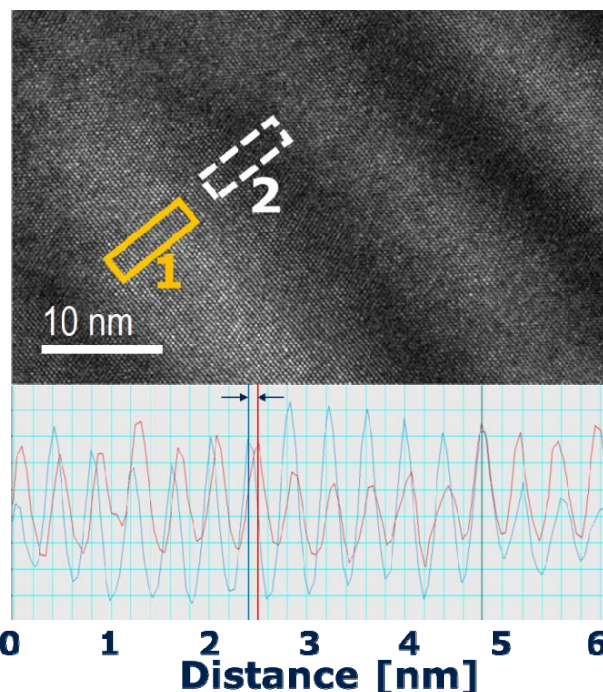


Figure 6 (top) Transmission Electron Microscopy image of hydrogen implanted silicon with a yellow solid and a white dotted line indicating the areas where the lattice spacing was measured. (bottom) Measurement of the lattice spacing in the blue and red area.

During these investigations the main goal was the investigation of point/line defects structures formed due to H^+ implantations with high and low energies into silicon. In the past such high dose implantations were mainly performed with very low implantation energies below 100 keV. Due to high local concentration of damage and hydrogen the formation of blisters, platelet structures or bubbles were reported. Due to the high energy implantation for the same doses, the distribution of H in the implantation depth is much broader for high energy implants as shown in Fig. 7 using SRIM/TRIM simulations [32].

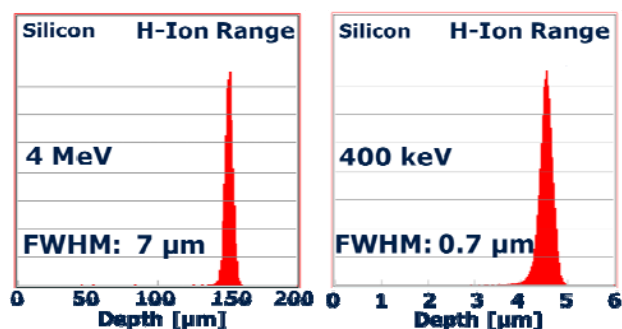


Figure 7 (left) TRIM simulation of a 4 MeV H-implantation into silicon. (right) TRIM simulation of a 400 keV H-implantation into silicon.

Due to this broader distribution of hydrogen at the implantation depth only precursor structures of the platelet structures reported in literature can be formed. At least it seems that the implanted hydrogen or the defects formed due to this implantation and the subsequent anneal also form in the $\{111\}$ planes like platelet formations were reported in literature [33].

5 Electron diffraction The diffraction of electrons utilizes the wave character of electrons and can be used similarly to X-ray or neutron diffraction. Since the wavelength of the electrons is much smaller than the distance between the atoms, the Ewald sphere cuts through those reciprocal lattice points in the plane perpendicular to the beam. This provides information about the crystal structure and the orientation of the crystals. In this study the short range order of point defects is investigated at the implantation depth. In Fig. 8 an electron diffraction image of a perfect silicon sample is shown.

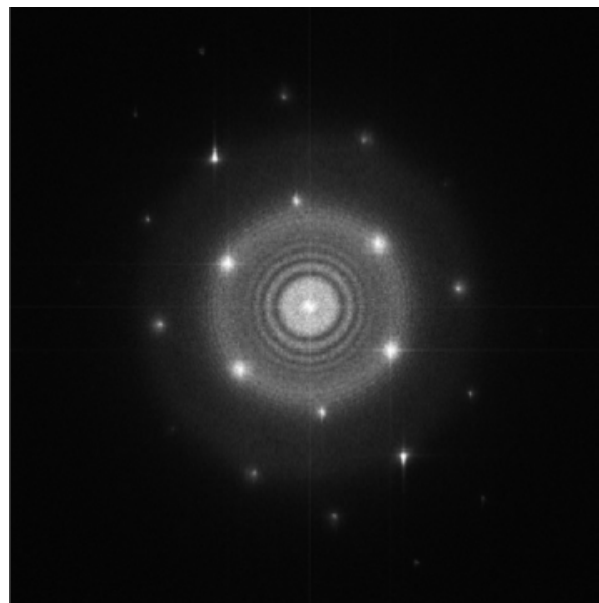


Figure 8 Electron diffraction image of a perfect silicon sample.

Figure 9 shows an electron diffraction pattern of a hydrogen implanted silicon lattice in the area of the projected implantation depth. Even if there is no clear defect structure visible in the TEM images, there is a lot of damage in the crystal lattice in this depth. In this region the electron diffraction images differ from the crystalline silicon pattern. Instead of the concentric rings observed for the crystalline silicon, a more complex interference pattern is observed for the implanted region.

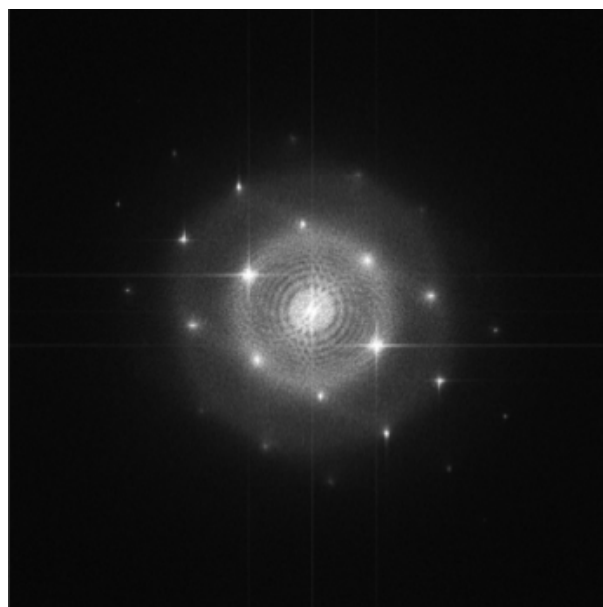


Figure 9 Electron diffraction image of hydrogen implanted silicon sample at implantation depth (implantation energy: 4 MeV, implantation dose: $4 \times 10^{14} H^+/cm^2$ annealed at 500 °C for one hour).

6 Conclusions The local measurement of the minority charge carrier diffusion length L_D along an electrically activated implantation profile using EBIC analysis techniques provides qualitative information about this electrical property. To determine quantitative values for L_D the influence of the surface recombination velocity as well as the doping type influence on the measurement method has to be investigated in more detail. TEM investigations showed that high dose low energy proton implantations in silicon result in the formation of extended defect structures called platelets oriented in $\{111\}$ and $\{100\}$ planes. High-energy high-dose implants result in the formation of electrically active donor complexes that orient, like precursor structures of these platelets also in the $\{111\}$ plane. Electron diffraction investigations only showed us differences between the distorted implantation regions and the perfect crystal. Obviously there is a lot of strain in the crystal lattice at the implantation depth.

Acknowledgements The work has been performed in the project EPPL, co-funded by grants from Austria, Germany, The Netherlands, Italy, France, Portugal- ENIAC member States and the ENIAC Joint Undertaking. This project is co-funded within the programme “Forschung, Innovation und Technologie für Informationstechnologie” by the Austrian Ministry for Transport, Innovation and Technology.

References

- [1] P. Hazdra, K. Brand, J. Rubeš, and J. Vobecký, *Microelectron. J.* **32**(5), 449-456 (2001).
- [2] Y. Zohta, Y. Ohmura, and M. Kanazawa, *Jpn. J. Appl. Phys.* **10**(4), 532-533 (1991).
- [3] S. Romani and J. H. Evans, *Nucl. Instrum. Methods Phys. Res. B* **44**(3), 313-317 (1990).
- [4] K. Sixtus and W. Gerlach, German Patent Schutzrecht DE1 564 251: Steuerbarer Halbleitergleichrichter (1966).
- [5] M. D. Miller, H. Schade, and C. J. Nuese, *J. Appl. Phys.* **47**(6) 2569-2578 (2008).
- [6] Yu. V. Bulgakov, T. I. Kolomenskaya, N. V. Kuznetsov, V. I. Shulga, and V. A. Zaritskaya, *Radiat. Eff. Lett.* **54**, 129-134 (1991).
- [7] N. Q. Khanh, Cs. Kovacsics, T. Mohacsy, M. Adam, and J. Gyulai, *Nucl. Instrum. Methods Phys. Res. B* **147**, 111-115 (1999).
- [8] W. Wondrak and D. Silber, *Physica B* **129**, 322-326 (1985).
- [9] W. Wondrak, PhD thesis, Frankfurt am Main, Johann-Wolfgang-Goethe-Universität (1985).
- [10] W. Wondrak and A. Boos, in: *Proc. ESSDERC*, Vol. 1, pp. 649-652 (1987).
- [11] S. Kirmstötter, M. Faccinelli, W. Schustereder, L. G. Laven, H.-J. Schulze, and P. Hadley, *AIP Conf. Proc.* **1583**, 51 (2014).
- [12] C. S. Fuller, J. A. Ditzenberger, N. B. Hannay, and E. Buehler, *Phys. Rev.* **96**, 833 (1955).
- [13] E. Simoen, Y. L. Huang, Y. Ma, J. Lauwaert, P. Clauws, J. M. Rafi, A. Ulyashin, and C. Claeys, *J. Electrochem. Soc.* **156**, H434 (2009).
- [14] W. Kaiser, H. L. Frisch, and H. Reiss, *Phys. Rev.* **112**, 1546 (1958).
- [15] H. Navarro, J. Griffin, J. Weber, and L. Genze, *Solid State Commun.* **58**, 151 (1986).
- [16] Y. Kamiura, F. Hashimoto, and M. Yoneta, *J. Appl. Phys.* **65**, 600 (1989).
- [17] D. V. Lang, *J. Appl. Phys.* **45**, 3023 (1974).
- [18] W. Kaiser, P. H. Keck, and C. F. Lange, *Phys. Rev.* **101**, 1264 (1955).
- [19] S. H. Muller, M. Sprenger, E. G. Sieverts, and A. A. J. Ammerlaan, *Solid State Commun.* **25**, 987 (1978).
- [20] J. G. Laven, R. Job, H.-J. Schulze, F. J. Niedernostheide, W. Schustereder, and L. Frey, *ECS J. Solid State Sci. Technol.* **2**(9), 389-394 (2013).
- [21] B. Aspar, M. Bruel, H. Moriceau, C. Maleville, T. Poumeyrol, A. M. Papon, and A. Claverie, *Microelectron. Eng.* **36**(1-4), 233-240 (1997).
- [22] M. Bruel, Process for the production of thin semiconductor material films, Patentschutzrecht FR2 681 472, US 5 374 5641993.
- [23] K. A. Reinhardt and W. Kern, in: *Handbook of Silicon Wafer Cleaning Technology*, 2nd ed., edited by W. Andrew, (Noyes Publications, New Jersey, 2008).
- [24] W. K. Chu, R. H. Kastl, R. F. Lever, S. Mader, and B. J. Masters, *Phys. Rev. B* **16**(9), 3851-3859 (1977).
- [25] A. Agarwal, T. E. Haynes, V. C. Venezia, O. W. Holland, and D. J. Eaglesham, *Appl. Phys. Lett.* **72**, 1086-1088 (1998).
- [26] S. Kirmstoetter, F. Faccinelli, P. Hadley, R. Job, W. Schustereder, J.G. Laven, and H.-J. Schulze, *ECS Trans.* **50**(1), 115-120 (2012).
- [27] V. K. S. Ong, J. C. H. Phang, and D. S. H. Chan, *Solid-State Electron.* **37**(1), 1-7 (1994).
- [28] L. Chernyak, A. Osinsky, H. Temkin, J. W. Yang, Q. Chen, and M. Asif Khan, *Appl. Phys. Lett.* **69**(17), 2531-2533 (1996).
- [29] R. C. Newman, J. H. Tucker, A. R. Brown, and S. A. McQuaid, *J. Appl. Phys.* **70**(6), 3061-3070 (1991).
- [30] M. S. Tyagi, *Solid-State Electron.* **26**, 577 (1983).
- [31] J. A. del Alamo and R. M. Swanson, *Solid-State Electron.* **30**, 1127 (1987).
- [32] J. F. Ziegler, in: *Proc. Conf. on Ion Beam Analysis*, Vol. 219-220, 1027-1036 (2004).
- [33] T. Höchbauer, A. Misra, M. Nastasi, and J. W. Mayer, *J. Appl. Phys.* **89**, 5960 (2001).

H^+ Implantation Profile Formation in m:Cz and Fz silicon

The following corresponds to the publication

S. Kirnstoetter, M. Faccinelli, M. Jelinek, W. Schustereder, J. G. Laven, H.-J. Schulze and P. Hadley, accepted for publication in IEEE

The author of this thesis was responsible for the following points

- EBIC and SRP investigations
- measurement result analysis and interpretation
- main authorship

The contribution of the other authors of this publication are listed below

- M. Faccinelli: EBIC measurements, measurement result analysis and interpretation
- M. Jelinek: provided proton implanted specimen structures, measurement result analysis and interpretation
- W. Schustereder: provided proton implanted specimen structures, measurement result analysis and interpretation
- J. G. Laven: measurement result analysis and interpretation
- H. Schulze: measurement result analysis and interpretation
- P. Hadley: authorship, measurement result analysis and interpretation

H⁺ Implantation Profile Formation in m:Cz and Fz Silicon

S. Kirnstoetter, M. Faccinelli and P. Hadley

Institute of Solid State Physics
Graz University of Technology
Graz, Austria
p.hadley@tugraz.at

M. Jelinek, W. Schustereder
Infineon Technologies Austria AG
Villach, Austria
werner.schustereder@infineon.com

J. G. Laven and H.-J. Schulze

Infineon Technologies AG
Munich, Germany
johannes.laven@infineon.com

Abstract— Implanting hydrogen ions (H⁺) into silicon creates defects that can act as donors. The microscopic structure of these defects is not entirely clear. There is a difference in the resulting doping profiles if the silicon is produced by the float zone (Fz) process or the magnetic Czochralski (m:Cz) process. Silicon produced by the m:Cz process has higher concentrations of oxygen and carbon than silicon produced by the Fz process. The presence of the oxygen and carbon affects the formation of defects and thereby the doping profile. We implanted high resistivity *p*-type m:Cz and Fz wafers with protons. Due to the *n*-type doping from the H⁺ implantation, a *pn*-junction was generated in the sample. Simulations indicate that the H⁺ implantation depth is 148 μm. Spreading Resistance Profiling (SRP) measurements of just implanted and not annealed samples show a donor peak at 148 μm in the Fz samples but the peak is at about 160 μm depth in m:Cz samples. After a low temperature anneal of the m:Cz samples at temperatures between 150 and 250 °C for at least 30 minutes, the expected end of range (EOR) donor peak (at about 148 μm) appears. For higher annealing temperatures, the hydrogen related donor complexes (HTD's) become activated and the EOR peak becomes dominant in the implantation profile. In an SRP study we show the evolution of the doping profile of hydrogen implanted m:Cz and Fz wafers as a function of the annealing temperature. To monitor the depth of the formed *pn*-junction and the effective local diffusion length in the proton radiation damaged region, Electron Beam Induced Current (EBIC) measurements were performed.

Keywords—proton implantation, silicon, donors, defects, SRP, EBIC, charge carrier diffusion length

I. INTRODUCTION

The implantation of H⁺ (protons) into silicon is a widely used technique in the manufacturing process of semiconductor devices. Because of their low weight and due to the controlled incorporation process, using conventional ion implanters, the complexes generated due to the ion implantation are used to form recombination centers to adjust the carrier lifetime [1], to form deep donor profiles [2], or to cleave off thin wafers in the

so called “Smart Cut” Process [3]. To dope the silicon by introducing HTD's, H⁺ implantations in the dose range from 10¹³ to 10¹⁵ H⁺/cm² and a subsequent annealing step, at a temperature between 350 °C up to 550 °C, are performed[4-9]. The formation/dissociation and the microscopic structure of the formed donor complexes has been investigated with IR-spectroscopy [10], deep level transient spectroscopy (DLTS) [11], electron paramagnetic resonance (EPR) [12], spreading resistance profiling (SRP) [13], and photo thermal ionization spectroscopy (PTIS) [6]. Nevertheless the microscopic structure of the different donor complexes formed is still a matter of debate. The float zone refinement process [14] cannot be applied reliably to silicon ingots with diameters beyond 8 inch. Therefore most 12 inch wafers available on the market are produced via the Czochralski growth process [15] or the magnetic Czochralski process [16]. This means that the only wafers available have high oxygen and nitrogen concentrations. This is especially important for vertical device structures, such as power semiconductor devices. In this study, we investigate charge carrier concentration (CCC) profiles formed in Fz and m:Cz silicon wafers due to H⁺ implantations. Of special interest is a donor peak formed beyond the end of range peak in oxygen rich m:Cz silicon. This peak does not form in Fz silicon after an H⁺ implantation. Due to this extra donor peak, the position the *pn*-junction is deeper in m:Cz silicon than in Fz silicon after the same implantation and annealing process.

II. EXPERIMENTAL

Two types of commercially available silicon wafers were used. The Fz wafers were phosphorous doped with a resistivity of 120 Ωcm, had an oxygen concentration [O] ~ 1×10¹⁷ cm⁻³ and a carbon concentration [C] of 2×10¹⁶ cm⁻³. The m:Cz wafers were boron doped with a resistivity greater than 1000 Ωcm, and had an oxygen concentration [O] ~ 4×10¹⁷ cm⁻³. All of this information was taken from the manufacturer specification sheets.

The high resistivity silicon wafers were implanted with high energetic (2.5 or 4 MeV) protons with an implantation dose of $1-4 \times 10^{14} \text{ cm}^{-2}$ and were subsequently annealed under N_2 atmosphere. The H^+ implantations were performed at room temperature and the implantation temperature in/on the wafer was measured using a pyrometer. Depending on the implantation current, the implantation temperature was held constant at temperatures between 70 and 180 °C. Before the EBIC measurements the wafers were broken into samples and the edges were ground with SiC grinding paper to archive reproducible surface for all EBIC investigations. The measurements were performed in a JEOL JSM-6490 LV Scanning Electron Microscope (SEM) using Stanford Research SR570 current amplifiers and an Adwin Pro II AD-converter. To locally determine electrical properties, Schottky contacts were made on the cross section of the specimen using thin tungsten needles mounted in Kleindiek micromanipulators [17]. To perform SRP measurements the samples were ground on a bevel angle of 11.537 °. During the SRP measurements two metal tips were placed on the bevel about 40 μm apart and the current was measured while a voltage of 5 mV was applied. Measuring the current all along the bevel results in a spreading resistance profile. Using the assumption of a constant mobility over the whole sample and calibration samples, it is possible to calculate resistivity and charge carrier concentration profiles from the spreading resistance profiles.

III. RESULTS

A. Spreading Resistance Profiling

SRP measurements were performed to visualize the doping profile formation in H^+ implanted (energy: 2.5 or 4 MeV, dose: $4 \times 10^{14} \text{ H}^+ \text{ cm}^{-2}$) and annealed silicon wafers produced via the Fz or the m:Cz process. The H^+ implantation was performed at room temperature and the wafer surface temperature was measured with a pyrometer. The end of range implantation peak for 4 MeV H^+ ions into silicon is 148.5 μm according to STIM/TRIM simulations [18]. This was confirmed by recent experiments. In Fig. 1, an isochronal annealing series (annealing time: one hour) of H^+ implanted m:Cz silicon is shown. In oxygen rich m:Cz silicon, the highest donor peak is at about 160 μm directly after the implantation (solid blue curve, in the top part of Fig. 1). Unexpectedly, this is 12 μm deeper than where the bulk of the hydrogen was deposited at the EOR (148.5 μm). The peak position remains at 160 μm for all anneals below 250 °C. When the specimen was annealed at higher temperatures, a donor peak appears at the EOR position and eventually becomes the dominant peak while the original peak at 160 μm appears as a shoulder.

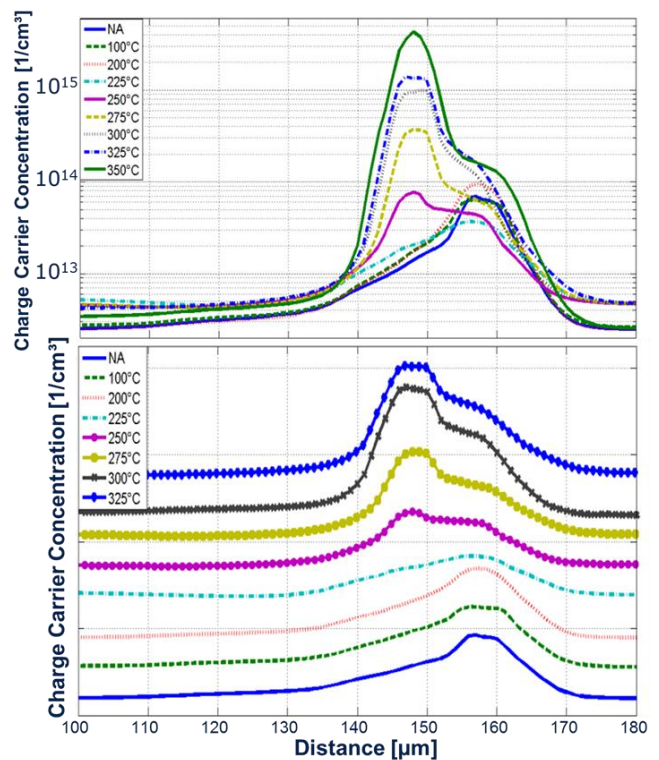


Fig. 1:(top) Absolute values of the charge carrier concentration profiles obtained from SRP measurements of m:Cz silicon implanted with high energetic H^+ (energy: 4 MeV, dose: $4 \times 10^{14} \text{ H}^+ \text{ cm}^{-2}$) and annealed at various temperatures for one hour; (bottom) waterfall plot of the same annealing series to better visualize the profile formation process.

In contrast to the m:Cz wafers, no donor peak forms beyond the EOR in oxygen-lean Fz silicon wafers which were H^+ implanted and subsequently annealed., H^+ implantations were performed with various energies and the shape of the donor profile never changed. The only thing that changes with increasing energy is the implantation depth. In Fig. 2, the HTD peak at the EOR in Fz silicon can be seen for various annealing temperatures. The simulated EOR in 2.5 MeV H^+ implanted silicon is 68.5 μm .

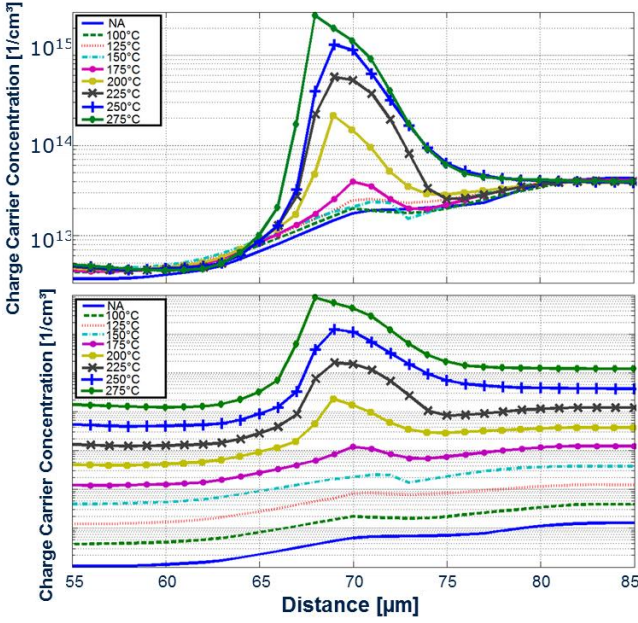


Fig. 2: (top) Absolute values of the charge carrier concentration profiles obtained from SRP measurements of Fz silicon implanted with high energetic H^+ (energy: 2.5 MeV, dose: $4 \times 10^{14} H^+/cm^2$) and annealed at temperatures between room temperature and 400 °C for 30 minutes; (bottom) waterfall plot of the same annealing series to better visualize the profile formation process.

Fig. 3 shows the doping profile measured by SRP for different H^+ implantation temperatures. The temperature of the surface of the wafer was measured during the implantation with a pyrometer. Because of the good thermal conductivity of silicon, it has been assumed that the temperature at the surface would be the same as the temperature at the implantation depth. However, the data in Fig. 3 shows that the EOR peak in m:Cz silicon is already present after implantations at 130 °C without additional annealing step. The profile shape and the peak height is comparable with at 70 °C H^+ implanted and subsequently at 300 °C for one hour annealed charge carrier concentration profile. This suggests that the temperature at the EOR during the implantation is higher than the surface temperature for these samples. SRP measurements were used to determine the positions of the peaks. The decrease in the concentration at higher temperature implies that the donor complexes dissociate at higher temperatures. The donors that form the deeper peak dissociate at a lower temperature than the donors that form the EOR peak as can be seen in Fig. 4.

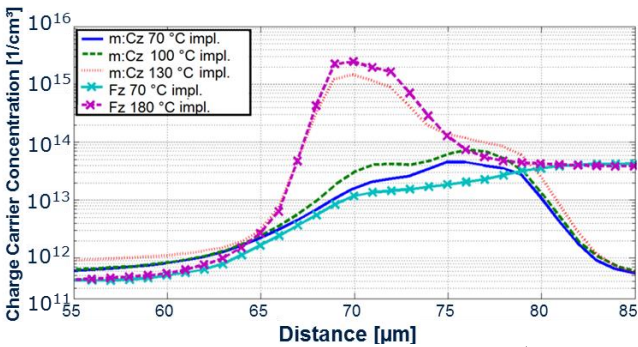


Fig. 3: Charge carrier concentration profile resulting due to H^+ implantations at different implantation temperatures in m:Cz and Fz silicon.

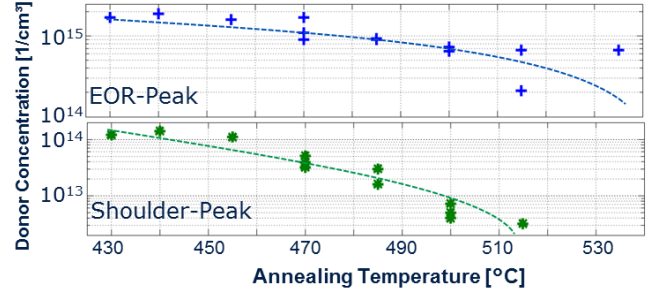


Fig. 4: Charge carrier concentration in the EOR- and in the deeper shoulder peak in 2.5 MeV H^+ implanted m:Cz silicon after anneals at temperatures between 430 and 535 °C for five hours.

B. Diffusion Length - Electron Beam Induced Current Investigations

The minority carrier diffusion length depends on the concentration of defects. It may have a different spatial dependence than the donor profile because not all defects act as donors. The diffusion length was measured by Electron Beam Induced Current (EBIC) measurements. This is a semiconductor analysis technique used in a scanning electron microscope. When an electron beam scans over the semiconductor sample, electron hole (eh) pairs are generated in an interaction volume where the beam strikes the sample. The excess minority charge carriers diffuse around until they become separated by a built-in electric field and an EBIC current can be detected at the electrodes. When the excess charge carriers don't reach a built-in field, they recombine at some crystal imperfection. To create a built-in field, micromanipulators were used to place thin tungsten needles on the silicon. The resulting Schottky contacts were used to collect the charge carriers that were generated by the electron beam. By observing how the current decreased as the electron beam moved away from the Schottky contact, the effective minority charge carrier diffusion length $L_{D,eff}$ can be determined at the position of the Schottky contact.[17, 19-20]. The tungsten needle was moved across the sample surface to determine the diffusion length as a function of position. As shown in equation (1) we modeled the measured effective diffusion length as having a bulk component and a surface component.

$$L_{D,eff} = \frac{1}{\frac{1}{L_{D,surface}} + \frac{1}{L_{D,bulk}}} \quad (1)$$

The surface component describes the recombination that takes place at defects at the surface and it is assumed to be constant everywhere on the sample. The value of the surface contribution is determined in the substrate region where there is no implantation damage and the bulk diffusion length is known to be around 200 μm . Fig. 5 shows the calculated bulk diffusion length in H^+ implanted m:Cz wafers after various annealing steps. The L_D profiles are compared to the SRP profiles obtained from these samples. The calculated bulk charge carrier diffusion lengths are plotted on the right y-axis.

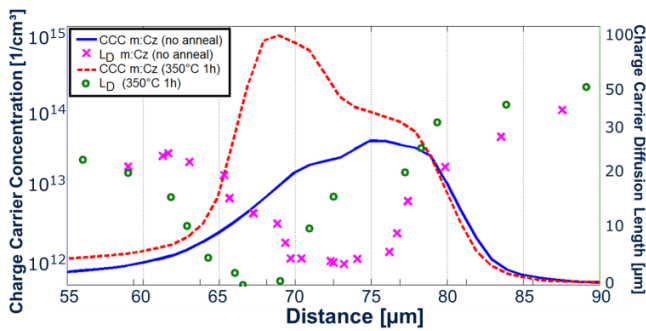


Fig. 5: Charge carrier concentration (CCC) and calculated bulk diffusion length (L_D) profile of 2.5 MeV H^+ implanted m:Cz, just implanted and not annealed (solid blue curve and pink crosses) and implanted and annealed at 350 °C for one hour (dotted red line and green circles).

The diffusion lengths reflect the changes in the donor profiles indicating that the same defects that cause the doping are also the ones decreasing the diffusion length.

IV. CONCLUSION

Spreading resistance profiling studies were used to monitor the formation process of the donor complexes due to H^+ implantations into silicon as a function of the annealing temperature. For Fz samples the donor peak appears at the EOR where the bulk of the hydrogen is deposited. Curiously, for m:Cz samples, a donor peak is initially observed deeper than the EOR. After annealing the implanted m:Cz samples, a dominant donor peak appears at the EOR but a shoulder in the doping concentration is still observed deeper than the EOR. The microscopic structure of defects responsible for the shoulder is not known. Diffusion length measurements indicate that the defects that cause a reduction of the diffusion length are created by the implantation and the concentration of these defects changes during the annealing process. Dips in the diffusion length appear where there are peaks in the donor concentration suggesting that the defects that act as donors are also those primarily responsible for the reduction in the diffusion length.

ACKNOWLEDGMENT

Part of this work has been performed in the project EPPL, co-funded by grants from Austria, Germany, The Netherlands, Italy, France, Portugal- ENIAC member States and the ENIAC Joint Undertaking. This project is co-funded within the programme "Forschung, Innovation und Technologie für Informationstechnologie" by the Austrian Ministry for Transport, Innovation and Technology.

REFERENCES

[1] P. Hazdra, K. Brand, J. Rubeš and J. Vobecký, "Local lifetime control by light ion irradiation: impact on blocking capability of power P-i-N diode", *Microelectr. J.* vol 32 (5), pp. 449-456, 2001.

[2] Y. Zohta, O. Yamichi and M. Kanazawa. "Shallow Donor State Produced by Proton Bombardment of Silicon." *Jap. jour. appl. phys.* Vol. 10.4 pp. 532-533, 1971.

[3] S. Romani and J. H. Evans, "Platelet defects in hydrogen implanted silicon", *Nuclear Instruments and Methods in Physics Research Section B: Beam Interactions with Materials and Atoms* vol. 44(3), pp. 313-317 1990.

[4] S. Kimstötter, M. Faccinelli, W. Schustereder, L. G. Laven, H.-J. Schulze, P. Hadley, "Hydrogen decoration of radiation damage induced defect structures", *AIP Conf. Proc.* vol. 1583, pp. 51-55, 2014.

[5] C. S. Fuller, J. A. Ditzenberger, N. B. Hannay, and E. Buehler, "Resistivity changes in silicon single crystals induced by heat treatment", *Phys. Rev.* vol. 96, pp. 833, 1955.

[6] E. Simoen, Y. L. Huang, Y. Ma, J. Lauwaert, P. Clauws, J. M. Rafi, A. Ulyashin, and C. Claeys, "What do we know about hydrogen-induced thermal donors in silicon?", *J. Electrochem. Soc.* vol. 156, pp. H434, 2009.

[7] W. Kaiser, H. L. Frisch, and H. Reiss, "Mechanism of the formation of donor states in heat-treated silicon", *Phys. Rev.* vol. 112, pp. 1546, 1958.

[8] H. Navarro, J. Griffin, J. Weber, and L. Genze, "New oxygen related shallow thermal donor centres in Czochralski-grown silicon", *Solid State Commun.* vol. 58, pp. 151, 1986.

[9] Y. Kamiura, F. Hashimoto, and M. Yoneta, "A new family of thermal donors generated around 450 °C in phosphorus-doped Czochralski silicon", *J. App. Phys.* vol. 65, pp. 600, 1989.

[10] W. Kaiser, P. H. Keck and C. F. Lange, "Infrared absorption and oxygen content in silicon and germanium. *Physical Review*, vol. 101(4), pp. 1264, 1956.

[11] B. Holm, K. Bonde Nielsen and B. Bech Nielsen, "Deep state of hydrogen in crystalline silicon: Evidence for metastability", *Phys. Rev. Lett.* vol. 66, pp. 2360, May 1991

[12] S. H. Muller, M. Sprenger, E. G. Sieverts, and A. A. J. Ammerlaan, "EPR spectra of heat-treatment centers in oxygen-rich silicon," *Solid State Commun.* vol. 25, pp. 987, 1978.

[13] J. G. Laven, R. Job, H.-J. Schulze, F. J. Niedernostheide, W. Schustereder and L. Frey, "Activation and Dissociation of Proton-Induced Donor Profiles in Silicon", *ECS j. solid state sci. technol.* vol. 2 (9), pp 389-394, 2013.

[14] W. G. Pfann, "Principles of Zone Melting", *Transactions of the American Institute of Mining and Metallurgical Engineers*, vol. 194, pp. 747-753, 1952.

[15] J. Czochralski, Ein neues Verfahren zur Messung der Kristallisationsgeschwindigkeit der Metalle. In: *jour. of. phys. chem.* vol.. 92, pp. 219-221, 1918.

[16] V. Savolainen, J. Heikonen, J. Ruokolainen, O. Anttila, M. Laakso, and J. Paloheimo, "Simulation of large-scale silicon melt flow in magnetic Czochralski growth". *Journal of crystal growth*, vol. 243(2), pp. 243-260, 2002

[17] S. Kimstötter, M. Faccinelli, P. Hadley, R. Job, W. Schustereder, J. G. Laven, H.-J. Schulze, "Investigation of Doping Type Conversion of Hydrogen Implanted Cz-Silicon by EBIC", *ECS Transactions* vol. 50 (1) pp. 115-120, 2012.

[18] J. F. Ziegler, "SRIM-2003" in *Proc. of Conf. on Ion Beam Analysis* vol. 219-220, pp. 1027-1036, 2004.

[19] V. K. S. Ong, J. C. H. Phang, and D. S. H. Chan. "A direct and accurate method for the extraction of diffusion length and surface recombination velocity from an EBIC line scan", *Solid-State Electronics* vol. 37 (1), pp. 1-7, 1994.

[20] L. Chernyak, A. Osinsky, H. Temkin, J. W. Yang, Q. Chem, and M. Asif Khan, "Electron beam induced current measurements of minority carrier diffusion length in gallium nitride", *Appl. Phys. Lett.* vol. 69 (17), pp. 2531-2533, 1996.

Chapter 5

Conclusions and outlook

The conclusions and outlook section of this thesis is separated in three parts. In the first part, a reflection of the scientific work performed during this thesis is given. In the second part, promising studies that should be performed in the near future are discussed. In the last part, a pointed summary is given where the most important discoveries and investigations during this work are pointed out.

5.1 Reflection of work and state of knowledge

In this section the author tries to give a reflection of the scientific work performed during this PhD thesis on the fields of H⁺-implantation into silicon and EBIC measurement techniques.

5.1.1 H⁺-implantation into silicon - point defects in semiconductors

In this work the measurement methods Infrared Spectroscopy, Raman Spectroscopy, Micro Raman Spectroscopy, Photo Luminescence, Deep Level Transient Spectroscopy, Electron Spin resonance, X-ray diffraction, Electrically detected spin resonance, Electron Beam Induced Current, Electron Channeling Contrast Imaging, Transmission Electron Microscopy and Electron Diffraction have been used to investigate H⁺ implanted silicon samples¹. The dedicated mission of all these investigations was the identification of the microscopic structure of the hydrogen related donor (HTDs) complexes and the thermal double donor (TDD) complexes in silicon. Obviously, some measurement methods are able to provide only indirect information about the formed donor complexes because of the limited spacial resolution or nature of measurement data generated.

During a lot of the measurements, the overall defect concentration in the silicon was too low, to get information about the H-related defect complexes. The implantation of hydrogen creates a very localized profile in the silicon wafers and does not result in a very high homogeneous defect concentration over the whole silicon sample/wafer. This property of implanta-

¹some of these investigations were performed by external partners/colleagues from other institutes

tions can not be solved by multiple implantations, because when the overall concentration of defects becomes too high in the crystal lattice, as a result of high dose implantations the structure of the defect complexes changes.

For measurement methods that use transmitting photons, like transmission IR-Spectroscopy, there is only a very small overall concentration of the point defects of interest in the whole specimen. Some way to increase the overall point defect concentration could be to perform a shallow H^+ -implantations and remove the rest of the wafer using a controlled grinding or ion milling process. To perform measurements in a reasonable resolution, it would also be important to work at low temperatures. Very high resolution measurements can only be performed at liquid helium (or at least liquid nitrogen) temperature. During IR-spectroscopy measurements performed in reflectance mode, when the photon beam is only interacting with the highest layers of the specimen, a lot of information gets lost because of the bulk doping character of the H^+ implantation method - at least with the setup used during this thesis, implantations shallower than 4 microns were not possible. Also, additional surface effects occurring during the implantation and annealing process have to be taken into account. From X-ray diffraction measurements the distortions in the otherwise nearly perfect crystal lattice can be detected and tension in the lattice is displayed, but no structural information about the defects is obtained. Deep Level Transient Spectroscopy measurements provide the energy level of ionized donors, but can deliver no information about their microscopic structure. Due to different thermal treatments and implantation parameter variations additional information about the variety of formed donors can be collected. Nevertheless, to tell which donor complexes are present, the energy values, obtained by DLTS, can only be compared to literature values and comparable studies performed with other measurement methods. The measurement methods ESR and EDMR directly provide structural informations about point defects. But this information is very hard to interpret. Especially when the defect structure and geometry is difficult and the concentration of them is low, like when a whole family of similarly structured defects are present in a crystal, e.g. the family of HTDs or TDDs in silicon. EDMR measurements can provide structural information about electrically active complexes with an energy level in a region around the middle of the band gap. Shallow donor or acceptor complexes can not be analysed with this method.

From a theoretical point of view, it could be assumed that today's computer power and know how about defect formation mechanisms should be sufficient to simulate the structures and energy levels of possible point defects in the silicon lattice. Starting from very simple point defects, like vacancies or interstitials, one could slowly proceed to more advanced complexes. Including the simulation of the favourable positions of the single components of defect complexes, the alignment of the complete defect complex in the silicon lattice, the possible electrical ionization states of the complete complex and the single components. This would provide informations about the activation and dissociation energy. Additionally the migration and diffusion behaviour of single components and the complete complex would be interesting. Unfortunately it is not that easy. Already very simple defect complexes like a complex of an interstitial and two hydrogen atoms (IH_2) in the silicon lattice can demonstrate the enormity of the problem. First of all the impurity atom H, with the charge states H^+ , H^0 and H^- , can be in several different crystal lattice sites that are energetically favourable. According to Herring et al [168] already single hydrogen atoms have several favourably occupied positions where the atoms could be in the silicon lattice without any additional interstitials involved. So the overall energy level of the defect complex varies when the structure/orientation of the complex as wells as the ionization states of the different components change. This results in a large

number of possible energy levels from simulations to compare them with energy levels detected by measurement methods. Another important parameter is the migration and diffusion behaviour of the defect complexes and their components. During the formation and activation process it is very important to understand which components diffuses faster, to understand the precursor states of the complexes formed and to understand what happens when small parameters, like the oxygen or carbon concentration of silicon vary slightly. For example the presence of hydrogen acts like a catalyst for the diffusion of oxygen in silicon (as explained in more details in the fundamentals section). Finally it can be stated that simulations are of great interest for the point defect community! Unfortunately, only rarely scientists are concentrating on this complicated and non glorious research field.

5.1.2 EBIC measurement techniques

During this work a great number of EBIC investigations have been performed. Most of the studies were done in cross sectional geometry, but also planar studies have been done. Most studies have been performed with silicon but also samples and devices consisting of GaN, AlGaIn and SiC have been examined. Different kind of device structures like diodes, transistors (MOSFET, JFET, HEMT) or thyristors (IGBTs) have been investigated. Micro-manipulators with thin metal needles were used to make contact, or were used to form Schottky contacts on semiconductor specimens. From the sign of EBIC signal at a built-in electric field, it is possible to tell the doping type. Usually the doping type is well known, only in special cases it is unclear. An analytical approach was developed to qualitatively determine the diffusion lengths from Schottky contacts on silicon samples. For quantitative values the surface preparation / surface recombination velocity would have to be taken into account in more detail. In special cases reverse biasing a device structure inside the SEM made it possible to see a voltage contrast in the secondary electron mode. The combination of the regular EBIC measurement setup with a Lock-In amplifier made it possible to visualize the depletion process with EBIC when reverse biasing a diode structure. Using the fact that the depletion process, and the expansion of the depletion process, can be visualized like this the charge carrier concentration profile can be measured like in a CV measurement. Using simulations to calibrate the surface situation of the specimen (surface preparation, surface charge layer) the resulting charge carrier concentration profiles are comparable to SRP and CV results.

5.2 Promising future studies

To the author's opinion, and due to reasons mentioned in the the previous chapters, a combination of TEM-, EDMR/ESR-, DLTS-measurement and point defect simulations seems to be most promising to identify the microscopic structure and energy levels of point defects in semiconductors. Using EBIC, SRP or CV-measurement can be helpful, controlling the production process of specimens and devices. Nevertheless, the information provided can not be correlated exactly to properties of specific point defects. The very powerful, and difficult to interpret, EDMR/ESR investigations need simulations to compare the measurement results to, otherwise it is easy to get lost in the interpretation of the data. It has to be mentioned that also high resolution TEM investigations reach their limit, when trying to resolve point defect complexes consisting of mainly light elements.

A promising strategy could be to start out with extended defect structures that are generated after implantations with H^+ energies of 400 keV and doses of $1 \times 10^{16} H^+ / cm^2$ and slowly go to lower and lower implantation doses. Later doses could be $1-9 \times 10^{15} H^+ / cm^2$. Going to lower implantation doses, at some point the defect structures, which are formed should change from extended defect complexes (platelets) to line defect complexes or directly to agglomerations of point defect complexes. High resolution TEM and electron diffraction investigations should be performed on all these samples. Some additional parameters have to taken into account before the investigation is started: 1) substrate material: it would be interesting to investigate the difference of the formed defect complexes in oxygen/carbon rich Cz/m:Cz silicon or Fz silicon because of the big differences in the oxygen and carbon concentration. 2) Annealing parameters: During a post implantation annealing process defect complexes can diffuse, heal out or vanish. Nevertheless the most interesting defect complexes might be the hydrogen related donor complexes (HTDs) activated due to a the annealing process at temperatures ranging from 350-500 °C. When only the region around the implantation depth is investigated the silicon samples don't have to be annealed too long: an anneal at around 400 °C for one hour seems reasonable.

To perform EDMR measurements of H^+ -implanted silicon samples various test diodes have been designed and produced. These samples have been implanted with implantation doses from $10^{14} - 10^{15} H^+ cm^{-2}$ and with implantation energies from 400-600 keV to vary the position of the *pn*-junction in the diode. Until now only a few diodes with few different annealing parameters have been investigated. Previous results showed that a difference in the EDMR measurement signal could be seen between: a) not implanted and not annealed, b) implanted and not annealed, c) implanted and annealed samples. These diodes were formed on *n*-type Fz silicon. It should be tried to correlate TEM and electron diffraction measurement results of H^+ implanted Fz silicon samples with the EDMR results of samples annealed with analogous annealing temperatures and durations.

As shown by SRP measurements, H^+ implantations into Cz/m:Cz and Fz silicon, subsequently annealed after the implantation, lead to different charge carrier concentration profiles. The most obvious difference is the extra peak beyond the projected implantation depth formed in Cz/m:Cz. It is marked as area III in figure 2.17. To investigate the donors formed in this peak, spatially resolved DLTS investigations should be performed on the cross section on H^+ implanted silicon. Here a significant difference between two differently formed donor complex families could be found. The sample can be contacted on the cross section with metal needles or on a bevel, what might simplify contacting and improve the spacial resolution of the mea-

surement.

An extensive number of SRP investigations of variously H^+ implanted (energies: 400-4000 keV, doses: $1-1000 \times 10^{13} H^+ / cm^2$) and annealed (25-1000 °C, for durations from 5 minutes to 300 hours) silicon wafers have been performed during this thesis. Using Schottky EBIC measurements, changes of the doping type were determined. So the formation of donor and acceptor complexes at different annealing temperatures was investigated as is visualized in figure 5.1.

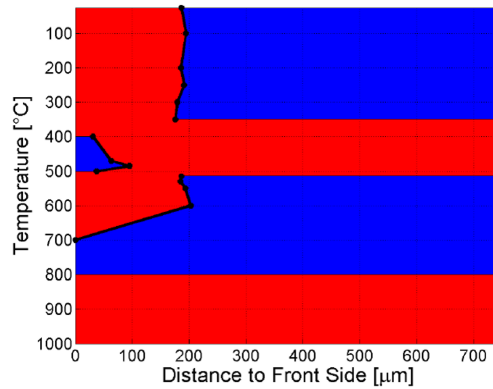


Figure 5.1: Visualization of the change of the doping type as a function of the annealing temperature and the distance to the front side of a H^+ implanted m:Cz silicon wafer (4 MeV, $1 \times 10^{14} H^+ cm^{-2}$). *n*-type regions are coloured red, *p*-type regions are coloured blue. Image taken from M. Faccinelli [124]

Also diffusion coefficients (for different annealing temperatures) and the activation energies of the hydrogen decorated defect complexes in m:Cz and Fz silicon have been determined. These studies pointed out the different activation and diffusion parameters of hydrogen related donor complexes occurring due to the major difference in the oxygen and carbon concentration in the silicon samples. Another study was started where the influence of the implantation dose was investigated: five m:Cz and five Fz silicon samples were implanted with protons (2.5 MeV) with doses ranging from 1×10^{14} to $1 \times 10^{16} H^+ / cm^2$. The idea behind this experiment was, that due to the high energy implants, different defect complexes are formed that might be less mobile during annealing processes. To extract reliable values for the diffusivity at least 3 (optimally: 4-10) anneals have to be performed for every temperature. To determine the activation energy for every sample at least 3 (optimally: 4-6) different diffusivities (one for every annealing temperature and implantation dose) need to be collected.

Another tool that can be used for a better understanding of the implantation process are SRIM/TRIM simulations. As shown in figure 5.2 the depth of the hydrogen implanted into silicon can be simulated accurately and matches approximately to TEM investigation results. Obviously only the stopping mechanism can be taken into account so it provides no information about the formed defect complexes and charge carrier concentration profile.

The SRIM/TRIM simulation package performs all simulations for the fixed temperature of zero Kelvin. Most of the ion implantations in semiconductor manufacturing industry are

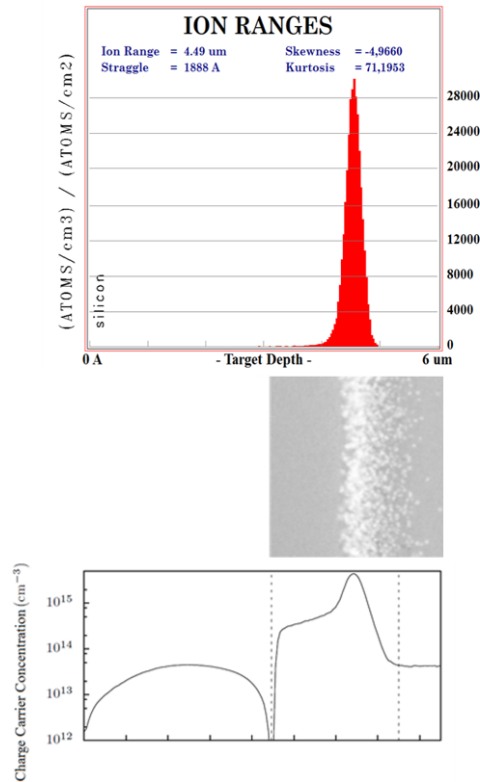


Figure 5.2: SRIM Simulation of H^+ implanted into Fz silicon with an energy of 400 keV and implantation dose of $1 \times 10^{16} H^+ cm^{-2}$ (top) compared to a TEM image of the area (middle) and the representative schematic charge carrier concentration profile (bottom)

performed at room temperature. This discrepancy results in much thinner implantation profile distribution in the simulation. At room temperature the implanted ions diffuse away slightly from the implantation depth. During the implantation of high energetic ions in the crystal lattice energy is dissipated where the electrons are decelerated (electr. or nucl. influences). So in the implanted area the temperatures can reach up to 150 °C (especially at the implantation depth where most of the energy of the ions is dissipated), depending on the implantation current that is used. Locally these temperatures can result in the formation of defect complexes of low formation/activation energy. The radiation damage concentration differs from zero Kelvin conditions and some fraction of it will heal out already at room temperature.

In the last years a few groups worked on the improvement of EBIC measurement techniques. One very promising approach was performed by the group of M. Troyon mounting a tilted AFM (atomic force microscope) in a SEM. The AFM tip was used to contact the semiconductor specimen. The electron beam was coming in from the side to let high energy electrons penetrate through the surface close to the contact point of the AFM needle. They called this approach nano-EBIC or near field EBIC [169]. Due to the combination of the very precise probing

mechanism of AFM (with a cantilever) and the electron beam the resolution of EBIC measurements can be improved significantly. Using a modern field emission gun (FEG) electron microscope and a nano EBIC setup makes it possible to monitor defect complexes and investigate electrical properties in a far better resolution than regular EBIC. Of course the electron beam interaction volume is still a limiting factor reach even better resolutions.

Just recently Electron Channeling Contrast Imaging (ECCI), has become more prominent in the world of semiconductor analysis. This method could be used to monitor defect complexes, closely positioned to the surface (until 200 nm depth) without any specimen preparation necessary. Defect densities of platelet and extended defect complexes can be visualized with this technique. Like EBIC, it can be another useful indirect technique, providing additional information that might help to adjust sample geometries, implantation doses for methods that can provide more direct information about point defect complexes.

5.3 Summary

In the next short paragraphs the most important discoveries and investigations of this thesis should be pointed out in a very short form once again.

- Isothermal annealing experiments of H⁺ implanted silicon were performed to determine the diffusion coefficient of hydrogen and the activation energy of hydrogen related thermal donors. For the manufacturing of semiconductor devices it is important to know the diffusion coefficients for the relevant temperatures for a controlled use of proton implantation as a method for semiconductor doping. The activation energy of the hydrogen related defect complexes can be a valuable input parameter for future simulations of the defect structure.
- A series of isochronal anneals (one hour) of H⁺ implanted silicon in the temperature range from room temperature to 1000 °C was performed. This enabled a better understanding of the thermal double donor and hydrogen related donor formation process and indicated the existence of high temperature thermal donors. Additionally, initial *n*-type doping in the irradiated region was detected in oxygen rich silicon.
- The formation of the charge carrier concentration profile in m:Cz silicon was investigated extensively. Especially the shoulder formation process beyond the projected implantation depth was investigated. It was found that after the H⁺-implantation and before any annealing step only a peak at the position of the later shoulder (deeper than the implantation depth) is present. After low temperature anneals, between 150 and 200 °C for less than an hour, the implantation peak forms and the deeper peak becomes a shoulder. This effect was not detected in Fz silicon. It is assumed that oxygen or carbon related thermal donor complexes form with the thermal budget incorporated during the H⁺-implantation at room temperature. This effect was seen during SRP and EBIC investigations.
- Due to the further development of the measurement method Electron Beam Induced Current (EBIC), the local determination of the doping type and the diffusion length was possible by the formation of small Schottky contacts. This makes EBIC to a very useful reverse engineering tool. The determination of the doping type can be performed at very low doping levels (down to $5 \cdot 10^{12}$ charge carriers/cm³) which makes it an important tool for the investigation of power semiconductor devices, where very low doped semiconductor materials are necessary.
- The visualization of the depletion process of a reverse biased diode was demonstrated using pulsed EBIC measurements in combination with a Lock-In amplifier. From the exact visualisation of the depletion process, the charge carrier concentration profile of the diode was determined like in a CV measurement. Combining the pulsed EBIC measurements with semiconductor device simulations it was possible to calibrate the measurement method for the specific surface preparation and surface charges. The resulting charge carrier concentration profiles show to be comparable with results from SRP or CV measurements. Additionally EBIC is a visualizing technique that makes it possible

to monitor the depletion process at any time during the measurement in case any problem occurs, that can be a big advantage.

- The accurate detection of *pn*-junctions was demonstrated for multiple H⁺ implanted silicon wafers. In other measurement methods (such as SRP) the position of the junction can not be determined in the same reliable and accurate way.
- Developing biased EBIC measurements, it was possible to visualize the depletion process of semiconductor device structures. From the expansion of the depletion region through the device with increasing reverse bias, the charge carrier concentration profile was obtained (like in CV measurements). But in comparison to CV measurements EBIC is an image giving method where the depletion process can be seen in situ.
- A depth profile of the minority charge carrier diffusion length of H⁺ implanted silicon was generated. The minimum diffusion length was determined at the prospected implantation depth, so at the position of the maximum damage in the profile.
- During TEM measurements it was found out that the implantation of H⁺ into silicon results in a change in the crystal lattice distances in the projected implantation depth.

Chapter 6

Appendix

6.1 Analytical analysis of SRP measurements

In 1904 J. C. Maxwell was the first to investigate the electrical properties of point contacts [162]. He considered a material with a resistivity ρ , divided it into two parts, separated by an insulating membrane with a hole in it. The hole has a radius of a . If a voltage is applied between the two parts of the material the charge carriers were flowing through the hole in the membrane. From Maxwell's calculations the resistance of that contact is $R = \rho/2a$. A big fraction of the voltage drops close to the hole where the current density is high. Away from the hole the current density becomes nearly zero, and so does the electric field as it is directly proportional to the current density. The electrostatic potential is the integral of the electric field and therefore constant far away from the hole. A derivation of J. C. Maxwell's result [162] made by Prof. P. Hadley [163] is shown below. With the help of M. Faccinelli the derivation to calculate the resistance for different measurement geometries was modified. To determine the potential Φ , the Laplace equation has to be solved for the relevant geometry:

$$\nabla^2 \phi = 0. \quad (6.1)$$

It is more convenient to solve this problem in oblate spheroidal coordinates (μ, ν, θ) which are defined as

$$x = a \cosh \mu \cos \nu \cos \theta, \quad (6.2)$$

$$y = a \cosh \mu \cos \nu \sin \theta, \quad (6.3)$$

and

$$z = a \sinh \mu \sin \nu. \quad (6.4)$$

with the restrictions $0 < \mu < \infty$, $-\pi/2 < \nu < \pi/2$ and $0 < \theta < 2\pi$ (see figure 6.1).

In oblate spheroidal coordinates, the potential Φ is only a function of μ . The Laplace equation in these coordinates then is

$$0 = \frac{1}{a^2 (\sinh^2 \mu + \sin^2 \nu)} \left[\frac{1}{\cosh \mu} \frac{\partial}{\partial \mu} \left(\cosh \mu \frac{\partial \phi}{\partial \mu} \right) + \frac{1}{\cos \nu} \frac{\partial}{\partial \nu} \left(\cos \nu \frac{\partial \phi}{\partial \nu} \right) \right] + \frac{1}{a^2 (\cosh^2 \mu + \cos^2 \nu)} \frac{\partial^2 \phi}{\partial \theta^2}. \quad (6.5)$$

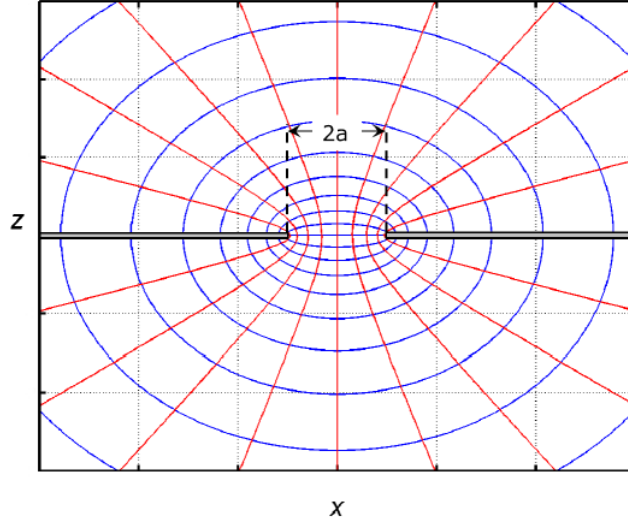


Figure 6.1: Current flowing through a round hole with the diameter a . Visualization of the electric field (red lines) and equipotential (blue lines) distribution. The electric field lines are calculated for a constant μ , and the equipotential lines are calculated for a constant v . The charge carrier current flows parallel to the electric field lines. Figure was taken from reference [163].

differentiating the equation results in

$$\frac{\partial}{\partial \mu} \left(\cosh \mu \frac{\partial \phi}{\partial \mu} \right) = 0. \quad (6.6)$$

This yields,

$$\cosh \mu \frac{d^2 \phi}{d\mu^2} = -\sinh \mu \frac{d\phi}{d\mu}. \quad (6.7)$$

When $y = \frac{d\phi}{d\mu}$

$$\frac{dy}{d\mu} = -\tanh \mu y. \quad (6.8)$$

Using the separation of variables this equation can be solved

$$\frac{dy}{y} = -\tanh \mu d\mu, \quad (6.9)$$

via integration

$$\ln y = -\ln(\cosh \mu) + c_1. \quad (6.10)$$

Where c_1 is the integration constant. The result is exponentiated

$$y = \frac{d\phi}{d\mu} = \frac{\exp(c_1)}{\cosh \mu}, \quad (6.11)$$

and integrated again

$$\phi = 2 \exp(c_1) \tan^{-1} \left(\tanh \frac{\mu}{2} \right) + c_2. \quad (6.12)$$

c_2 is another integration constant. It is possible to add a constant to a potential, so c_2 can be set to zero. The function $\tan^{-1}(\tanh \frac{\mu}{2})$ approaches $\frac{\pi}{4}$ for large μ as shown in figure 6.2. When a

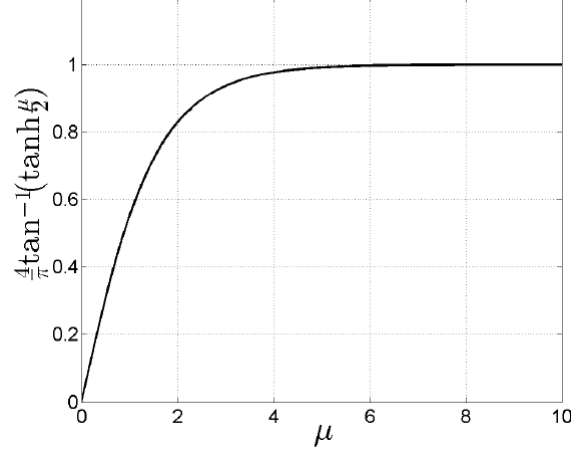


Figure 6.2: Plot of the function $\tan^{-1}(\tanh \frac{\mu}{2})$ over μ . Figure was taken from reference [163].

voltage $V/2$ is applied on one side and $-V/2$ is applied on the other side, for very large values of μ the potential that satisfies this boundary conditions is

$$\phi = \frac{2V}{\pi} \tan^{-1} \left(\tanh \frac{\mu}{2} \right). \quad (6.13)$$

The electric field is minus the gradient of the electrostatic potential,

$$\vec{E} = -\nabla\phi = -\frac{V \operatorname{sech}\mu}{\pi a \sqrt{\sinh^2\mu + \sin^2\nu}} \hat{\mu}. \quad (6.14)$$

The current density can be calculated from its direct proportionality to the electric field

$$\vec{j} = -\frac{\vec{E}}{\rho} = \frac{V \operatorname{sech}\mu}{\pi a \rho \sqrt{\sinh^2\mu + \sin^2\nu}} \hat{\mu}. \quad (6.15)$$

for $z = 0$ and $\mu = 0$ the current density results in

$$\vec{j}(z = 0) = -\frac{V}{\pi a \rho \sin\nu} \hat{z}. \quad (6.16)$$

The total current flowing is the integral of the current density over the hole. The current density does not depend on θ as it is cylindrically symmetric around the z -axis. It only depends on the distance from the z -axis and results in the current

$$I = \int_0^a 2\pi j(s) s ds. \quad (6.17)$$

Due to the cylindrical symmetry the integration can be done in the x direction

$$I = -2\pi \int_0^a \frac{V}{\pi a \rho \sin \nu} x dx. \quad (6.18)$$

at $z = 0$, $x = a \cos \nu$ and $dx = -a \sin \nu d\nu$

$$I = 2\pi \int_{\pi/2}^0 \frac{V a \cos \nu}{\pi \rho} d\nu = \frac{2aV}{\rho}. \quad (6.19)$$

then the values for the spreading resistance result from the quotient of the voltage and the current

$$R = \frac{\rho}{2a}. \quad (6.20)$$

From this point the expressions for the current density, electric field and potential can be rewritten with the total current I

$$\phi = \frac{\rho I}{\pi a} \tan^{-1} \left(\tanh \frac{\mu}{2} \right). \quad (6.21)$$

$$\vec{E} = - \frac{\rho I \operatorname{sech} \mu}{2\pi a^2 \sqrt{\sinh^2 \mu + \sin^2 \nu}} \hat{\mu}. \quad (6.22)$$

$$\vec{j} = \frac{I \operatorname{sech} \mu}{2\pi a^2 \sqrt{\sinh^2 \mu + \sin^2 \nu}} \hat{\mu}. \quad (6.23)$$

As can be seen there is no dependency of the current density on the resistivity. Thus when two different materials (ρ_1 and ρ_2) are present on the two sides of the membrane, the potentials can be calculated separately. This results in a spreading resistance of

$$R = \frac{\rho_1 + \rho_2}{4a}. \quad (6.24)$$

When the difference in the resistivity of the two materials on both sides of the membrane is very big ($\rho_1 \ll \rho_2$)

$$R = \frac{\rho_2}{4a}. \quad (6.25)$$

This is the formula that is used to determine the resistivity of semiconductor materials when round metal contacts are made on the surface of a semiconducting material as is shown in fig. 6.3 in a two-dimensional cut orthogonal to the surface:

It is implied by the use of Ohm's law $\rho \vec{j} = \vec{E}$ that the transport is assumed to be in the diffusive limit. To fulfil this, a has to be larger than the electron mean free path l . If this is not true and a is in the range of l , several modifications of this result (mentioned in references [170] and [171]) have to be taken into account.

During a Spreading Resistance Measurement, two metal tips are placed on a semiconductor so two metal contacts with the radii a_1 and a_2 are formed. The positions of the metal contacts are $x = -d/2$ and $x = d/2$. To calculate the overall potential the individual potentials of the two metal contacts are summed.

$$\phi = \frac{\rho I}{\pi} \left(\frac{1}{a_1} \tan^{-1} \left(\tanh \frac{\mu_1}{2} \right) - \frac{1}{a_2} \tan^{-1} \left(\tanh \frac{\mu_2}{2} \right) \right). \quad (6.26)$$

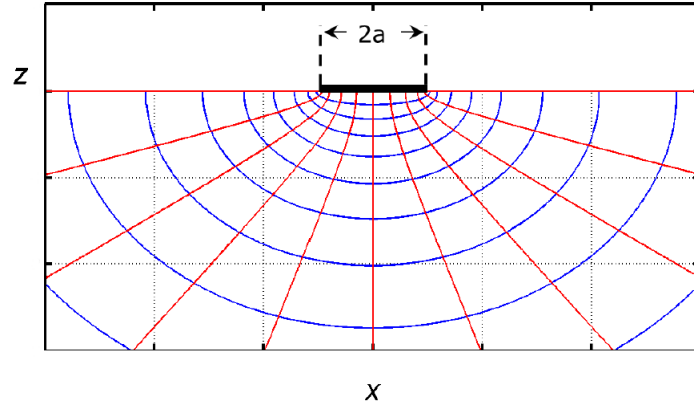


Figure 6.3: Equipotential lines (blue) and electric field (red) distribution for a current flowing from a round metal pad/metal contact. The current is again flowing from the pad parallel to the electric field lines. This figure was taken from reference [163].

for the $y = 0$ plane

$$\mu_1 = \cosh^{-1} \left(\frac{\sqrt{(x + \frac{d}{2} + a_1)^2 + z^2} + \sqrt{(x + \frac{d}{2} - a_1)^2 + z^2}}{2a_1} \right) \quad (6.27)$$

and

$$\mu_2 = \cosh^{-1} \left(\frac{\sqrt{(x - \frac{d}{2} + a_2)^2 + z^2} + \sqrt{(x - \frac{d}{2} - a_2)^2 + z^2}}{2a_2} \right). \quad (6.28)$$

In figure 6.4 the equipotential line distribution during an SRP measurement when the current is flowing from one contact to the other is shown.

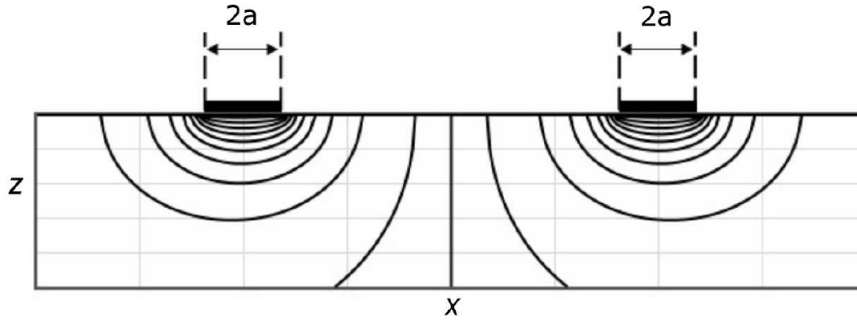


Figure 6.4: The equipotential line distribution during an SRP measurement when the current is flowing from one contact to the other. Figure was taken from reference [163]

It can be seen that most of the voltage drops close to the metal contact pads. The potential at the surface, where $y = 0$ and $z = 0$, is used to calculate the voltage between the two contacts.

At the surface

$$\mu_1 = \cosh^{-1} \left(\frac{|x + \frac{d}{2}|}{a_1} \right) \quad (6.29)$$

and

$$\mu_2 = \cosh^{-1} \left(\frac{|x - \frac{d}{2}|}{a_2} \right). \quad (6.30)$$

the voltage between the contacts is

$$V = \frac{\rho I}{\pi} \left(\frac{1}{a_1} \tan^{-1} \left(\tanh \left(\frac{1}{2} \cosh^{-1} \frac{d - a_2}{a_1} \right) \right) + \frac{1}{a_2} \tan^{-1} \left(\tanh \left(\frac{1}{2} \cosh^{-1} \frac{d - a_1}{a_2} \right) \right) \right), \quad (6.31)$$

and the resistance is

$$R_{\text{SRP}} = \frac{V}{I} = \frac{\rho}{\pi} \left(\frac{1}{a_1} \tan^{-1} \left(\tanh \left(\frac{1}{2} \cosh^{-1} \frac{d - a_2}{a_1} \right) \right) + \frac{1}{a_2} \tan^{-1} \left(\tanh \left(\frac{1}{2} \cosh^{-1} \frac{d - a_1}{a_2} \right) \right) \right) \quad (6.32)$$

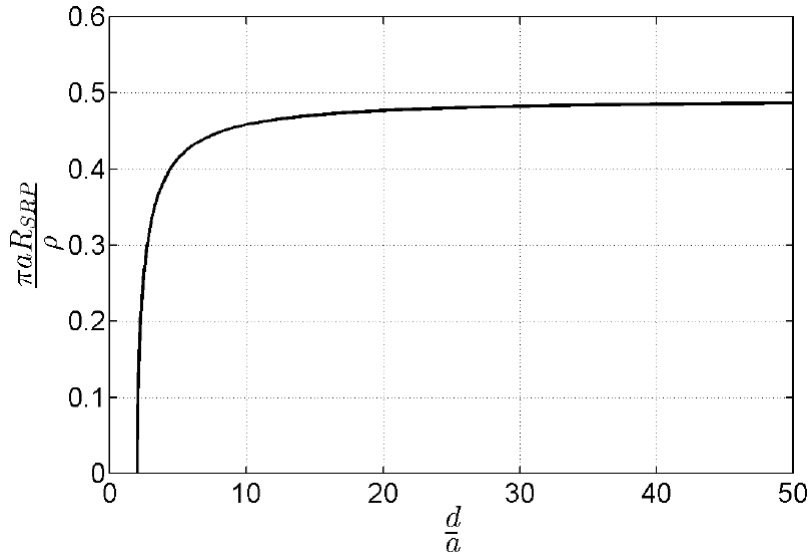


Figure 6.5: Calculated spreading resistance over the distance between the tips for $a=a_1=a_2$. Figure was taken from reference [163]

In figure 6.5 the spreading resistance as a function of the distance between the tips ($a=a_1=a_2$) is plotted. As can be seen from this plot, the measured resistance during the measurement is only weakly influenced by the distance between the metal pads as long as it is a few times the size of the radius of the contact itself. In the extreme case where $d < 2a$ the contacts overlap and the resistance is zero.

6.2 Measurement equipment and materials

In this section the measurements equipment and materials used in this thesis are listed.

6.2.1 Measurement equipment

SEM, EBIC and electrical probing equipment

Scanning electron microscope	JEOL JSM 6490LV
Backscatter detector	semiconductor (<i>pn</i> -junction) detector
Secondary electron detector	E.T. detector (collector, scintillator, light guide and photo multiplier tube)
Current amplifier	Stanford Research Systems Model SR570 Low-Noise Current Preamplifier
AD-converter	AdWin Pro II
Lock-in-amplifier	Stanford Research Systems Model SR830 DSP Lock-In Amplifier
Micromanipulators	Kleindiek Nano Control NC30
Micromanipulator tips	Various Tips from Picoprobe, Nauga Needles and Micromanipulator
Sourcemeeter	Keithly 2636A System Sourcemeeter
Grinding machine	Struers Knuth-Rotor
Grinding papers	Struers SiC Grinding Paper 500, 800, 1000 and 4000 grains per square inch
Silver paint	Electrolube Silver Conductive Paint

SRP, TEM and XRD equipment

SRP measurement tool	SSM2000
SRP analysis software	NANOSRP Analysis
Transmission electron microscope	FEI Tecnai F20 and FEI Titan
TEM sample preparation	
Sawing	Well diamond saw
Grinding	Gatan disc grinder
Polishing	Struers Tegramin 25
Dimpling	Gatan Dimple Grinder Model 656
Ion milling tool	Gatan Precession Ion Polishing System (PIPS) Model 691 Argon ions (4 kV)
X-ray diffractometer	Bruker XRD Discover D8

Proton implanter and heating stages/oven

Proton implanter	high voltage engineering (HVE) tandetron tandem accelerator
boron/phosphorus implanter	commercial batch implanter
Heating stage	Anton Paar DHS 900 and DHS 1100
Full Wafer Oven	commercial vertical furnace

6.2.2 Specimen materials

In this short section an overview about the specimen materials used during the proton implantation experiments should be given. The material parameters are taken from the material data sheets from the suppliers.

specimen material	P570	P600	C550	P743	P529	P720	P116	C235
Fz/Cz/m:Cz	m:Cz	Cz	Cz	Fz	Fz	Fz	Fz	Fz
resistivity [Ωcm]	1000	1000	8	118	1250	65	500	1200
dopant	B	P	B	P	B	P	B	P
oxygen [$1 \cdot 10^{17} cm^{-3}$]	3	2.2	7.3					0.1
supplier	SEH	MEMC	SEH	Siltronic	Siltronic	Siltronic	KEM	Siltronic
min. carrier lifetime [μs]		500		500		500		500
crystal orientation	(100)	(100)	(100)	(100)	(100)	(100)	(100)	(100)
carbon [$1 \cdot 10^{16} cm^{-3}$]			2	2		2	2	

PERSONAL INFORMATION



Stefan Kirnstötter

📍 Gartengasse 27, 8010 Graz, Austria

📞 0043 664 133596

✉ stefan_kirnstoetter@gmx.at

Sex M | Date of birth 10/07/1985 | Nationality Austrian

RESEARCH EXPERIENCE

Mar. 2011 – present

PhD Thesis

in the field of semiconductor material characterization, defects in semiconductors and power semiconductor devices at the Institute of Solid State Physics, Graz University of Technology under the supervision of Prof. Peter Hadley and in cooperation with Infineon Technologies AG

- Title: *Electron Beam Induced Current investigations of H⁺ implanted silicon and power semiconductor devices*

Nov. 2009 – Dec. 2010

Master Thesis

in the field of organic electronics and photo reactive interfacial layers in organic devices (OTFTs) at the Institute of Solid State Physics, Graz University of Technology under the supervision of Prof. Egbert Zojer

- Title: *Investigation of photo reactive interfacial layers and application of TIPS-pentacene as active layer material*

Oct. 2008 – Feb. 2009

Bachelor Thesis

in the field of nano particle physics at the Institute of Material Physics, Graz University of Technology under the supervision of Prof. Roland Würschum.

- Title: *Studie von Struktur und Kinetik an magnetischen Nanopartikeln*. In engl: *Research Study about the structure and kinetics on magnetic nano particles*

EDUCATION

Mar. 2011 – present

Doctoral programme in engineering science – Technical Physics

at Graz University of Technology

Feb. 2009 - Feb. 2011

Master's programme – Technical Physics

at Graz University of Technology (graduated with honours)

Oct. 2005 - Feb. 2009

Bachelor programme – Technical Physics

at Graz University of Technology

WORK EXPERIENCE

Feb. 2009 – Jul. 2009

Student tutor

Assistant of Prof. Gernot Pottlacher during experimental physics lab courses. Explaining experiments to students and assisting during the correction of lab protocols and exams.

Jul.- Aug. 2008 and 2009

Intern Wacker Chemie AG and Siltronic AG

Construction and calibration of silicon wafer thickness measurement setup

Jul.- Aug. 2007

Intern Borealis AG

Analytical chemistry laboratory assistant

PERSONAL SKILLS

Mother tongue German

Other languages

	UNDERSTANDING		SPEAKING		WRITING
	Listening	Reading	Spoken interaction	Spoken production	
English	C2	C2	C2	C2	C2
Spanish	A1	A1	A1	A1	A1

Levels: A1/2: Basic user - B1/2: Independent user - C1/2 Proficient user Common European Framework of Reference for Languages

Communication skills

- Good communication skills gained through my experiences with cooperation partners from industry and universities
- Participation in seminars/workshops on conflict management, communication style, discussion techniques and rhetoric
- Gained experience as a supervisor of bachelor students in our research group

Organisational / managerial skills

- Organisation talent (organisation of minor research projects, coordination of specimen production and coordination of small sports events)
- Good time management (as can be seen due to the fast progress in bachelor and master studies)
- High level of commitment/dedication to research projects
- Team worker

Scientific and Technical skills

- Experienced with various analytical measurement methods used in material characterization (SEM, TEM, XRD, IR/UV/VIS-spectroscopy), especially the characterization of semiconductor materials by EBIC, SRP, CV and DLTS.
- Broad knowledge about the electrical properties of inorganic and organic semiconductors, semiconductor devices and processing
- Very good technical understanding and analytical way of thinking
- Competent and safe working in a laboratory and in a workshop

Computer skills

- Good programming skills in C/C++, Matlab, Java, LabView and capable microcontroller programming
- Good command of Microsoft Office tools and LaTeX

Other skills/hobbies

- Sports (football, tennis, swimming, running), playing my guitar, photography, video cutting

ADDITIONAL INFORMATION

Honours and awards

- Scholarship for International Exchange Austrian physical society (ÖPG)
- Scholarship for International Exchange Graz University of Technology
- Performance Scholarship TU-Graz

References

- Prof. Peter Hadley (Graz University of Technology)
- J. G. Laven Ph.D. and W. Schustereder Ph.D. (Infineon Technologies AG)
- Prof. Egbert Zojer (Graz University of Technology)
- Prof. Reinhart Job (Münster University of Applied Sciences)

ANNEXES

- Reference letters
- List of publications and presentations at conferences
- Transcript of records

DATE and SIGNATURE

2014/4/7



List of Figures

2.1	Scheme of the Czochralsky method to pull single crystalline silicon from melted poly-Si.	6
2.2	Scheme of the zone melting method. Here a molten region moves from one side of the rod to the other by slowly pulling the heater ring.	7
2.3	(left) Silicon crystallizes in diamond crystal cell. (right) Tetrahedral structure of silicon atoms with four covalent bonds to neighbours. Taken from references [16] and [17]	9
2.4	Schematic illustration of the band diagrams of metals, semiconductors and isolators.	10
2.5	Simulated dispersion relationship (left and middle figure) and density of states (right) of silicon. The energy levels of the bands are plotted over the reciprocal space vector k . Taken from reference [21] with permission.	12
2.6	Doping concentration dependency of charge carrier mobility. According to Bart Van Zeghbroeck [24].	16
2.7	Illustration of the most important point defects in solids (vacancy, interstitial, substitutional, Frenkel pair).	18
2.8	Electron Band diagram visualizing deep and shallow traps for electrons and holes. Some prominent acceptor, donor and amphoteric defects in silicon are shown with their levels in the band gap. Figure was generated according to reference [29].	20
2.9	Schematic structure of a tandetron proton implanter. Showing all the important components from the ionization, acceleration and implantation. Drawn according to references [33] and [34].	22
2.10	Schematic energetic process of migration, defect formation and dissociation. According to reference [11].	24
2.11	a) Projection of silicon lattice on the (110) plane b) O_3 core complex of a thermal donor c) Stable and electrically inactive state of a O_3 complex obtained from atomic rearrangements. According to reference [60]	29
2.12	Promising candidates for the structures of the TDD1, TDD2 and TDD3 defect according to reference [62]. The red spheres symbolize oxygen atoms and the grey ones silicon lattice atoms.	30
2.13	Various possible reaction paths for a vacancy with other vacancies (left), oxygen (right) and hydrogen (top) atoms. The figure was generated according to J. G. Laven [32], all references for the activation energies of the reaction paths can be found there.	35

2.14	Typical Charge Carrier Concentration Profile resulting from a 2.5 MeV H-implantation with 4×10^{14} H ⁺ /cm ² annealed at 350 °C for five hours. Figure generated according to reference [32]	38
2.15	Schematic illustration of H-related donor (HD) formation mechanism. Taken and modified from reference [32]	39
2.16	Simulation of the H-distribution after implantation and several anneals at 400 °C for 1-30 hours (dotted lines). Simulation of the concentration of acceptors and potentially hydrogen related donors (solid lines with big dots). Taken from reference [122].	40
2.17	Typical Charge Carrier Concentration Profile resulting from a 2.5 MeV H ⁺ -implantation into Cz or m:Cz silicon	41
2.18	Schematic visualization of a <i>pn</i> -junction. The resulting charge carrier concentration, electric field and band diagram and log. charge carrier concentration are plotted	43
2.19	(Upper part) Schematic visualization of the formation of a Schottky junction and band bending between a metal and an <i>n</i> -type semiconductor. (Lower part) Schottky contact formation process visualized with charged states of donors and the resulting electric field distribution. Figure taken from [124]	44
3.1	Most important components of a Scanning Electron Microscope (SEM). The electron beam path and reduction of the beam diameter is visualized. The figure was taken from [125]	47
3.2	Visualisation of the interaction volume and the scattering mechanisms appearing when high energetic electrons penetrate into a semiconductor. Figure taken from [124]	47
3.3	Casino Simulations of the penetration paths of 20 keV (left) electrons into silicon. The right image shows the energy dissipation of the electrons in the specimen material. The box size in both figures is about five by five microns.	48
3.4	Electron mirror image of the Secondary Electron Detector inside the SEM.	49
3.5	(top) Electron mirror image of the backscattered electron detector inside the SEM. The detector around the electron cone is the part of the BSE detector used to image compositional and topological information. The off-axis oriented flat detector area to the right is the BSE shadow detector. It yields a combination of topological and compositional information, while, in contrast to the topological-mode of the detector, the image appears to be illuminated from the side and not from the top. The semicircular metal rod between the detector and the stage, where the electron mirror is positioned on, is a simple safety mechanism that avoids a collision of the stage and the detector. The wires are the contacts of the detector. (bottom) This image was made using the the backscattered electron detector. In this case only the detector itself appears bright.	51
3.6	Schematic visualization of the quasi fermi levels of electrons and holes in the space charge region of a <i>pn</i> -junction in the low injection regime. According to [135]	53
3.7	EBIC line scan measurement routine over a <i>pn</i> -junction. The direction of the EBIC measurement, over the SCR of the <i>pn</i> -junction, is shown by the dotted line. Figure taken from [124]	55
3.8	Secondary electron image (top left), EBIC linescan signal (bottom left) combined to one plot (right)	55

3.9	EBIC scan over the area shown in the SE image (top left). In the grey scale plot (top right) the bright areas indicate the maximum EBIC signal and the dark areas, regions where no or a low EBIC signal is detected. In the contour plot (bottom left) small changes can be detected more easily. In a three dimensional plot (bottom right) the increase of the signal is demonstrated more clearly, but it is not handy to get an overview over the whole region.	57
3.10	Measurement principle of the Schottky-EBIC measurement method to investigate the doping type of a semiconductor and it's local minority charge carrier diffusion length. Figure taken from [138]	58
3.11	Schematic measurement principle of the EBIC Chopping method to investigate reverse biased devices. Figure taken from [139]	59
3.12	Specimen holder for cross sectional (left) and planar (right) EBIC measurements. Figure taken from [124]	60
3.13	(left) Secondary electron image of the measurement geometry used for biased Schottky EBIC experiments. One ohmic contact on the left side of the semiconductor sample and two tungsten tips used as electrical contacts are shown. The left tip (shown in higher resolution in the right image) detects the EBIC signal. (right) Here the chosen region for biased Schottky EBIC measurements is shown.	61
3.14	A series of biased Schottky EBIC measurements with various electric fields applied. In the upper left edge of every single figure the applied electric field can be seen.	62
3.15	EBIC Linescans of Schottky EBIC measurements with various electric fields applied. In the inset top left the electron beam scan direction during the EBIC line scan measurement is indicated.	63
3.16	Calculated excess minority charge carrier distribution in a specimen for an electric field of 0 V/cm (left), 50 V/cm (middle) and 200 V/cm (right) applied. The generation of the minority charge carriers is assumed as a delta function and localized at the position zero. These simulations were programmed by Peter Hadley	64
3.17	Biased Schottky EBIC measurement signals with various electric fields applied (solid lines) compared with simulation results (solid lines + markers)	64
3.18	(left) SE image of GaN bevel with two tungsten tips pressed on either side of the AlGaIn/GaN hetero-junction. (right) Electron beam induced current measurement, the red region marks the highest EBIC signal and highest built-in electric field.	65
3.19	SEI (left) and EBIC (right) images of the AlGaIn/GaN heterojunction. In a) an overview shows all regions of the junction. Scan b) shows the region left of the metallurgical junction. c) is oriented directly on the junction. d) shows the region right from the junction.	66
3.20	(left) SE image and (right) EBIC measurement of AlGaIn/GaN hetero junction. The black points in the GaN region to the right of the junction might be due to an increased concentration of crystal defects (e.g. dislocations) in this layer. . . .	67
3.21	(left) SE image of FIB cut region. (middle) EBIC measurement showing the position of the junction in the AlGaInInP device. (right) Logarithm of the EBIC signal provides some more structural informations about the device and shows the position of the junction.	67
3.22	(top left) Secondary electron image of a planar sensor teststructure. (top right) EBIC and (bottom left) EBIC measurement signal and (bottom right) logarithm of the measured EBIC signal of the planar test structure. EBIC measurements were performed by Georg Spanring	68

3.23	TEM overview image of proton implanted ($400 \text{ keV } 1 \times 10^{16} \text{ H}^+ / \text{cm}^2$) Fz silicon focused in the end of range implantation region.	70
3.24	High resolution TEM image of a platelet defect complex formed in Fz silicon due to high dose proton implantation (energy: 400 keV , dose: $1 \times 10^{16} \text{ H}^+ / \text{cm}^2$).	70
3.25	(left) High resolution TEM images showing a platelet defect in proton implanted silicon.(right) A dislocation is indicated when the width of the defect complex changes from three to two atom rows.	71
3.26	(left) TEM image and (right) FFT image of the TEM image of the same area of a perfect silicon sample.	72
3.27	(left) TEM image of a hydrogen implanted silicon sample at the implantation depth (implantation energy: 4 MeV , implantation dose: $4 \cdot 10^{14} \text{ H}^+ / \text{cm}^2$) annealed at $500 \text{ }^\circ\text{C}$ for 1 hour (right) FFT image of the same area as the TEM image of this hydrogen implanted silicon sample.	72
3.28	(left) Simulation of an electron diffraction pattern of a perfect silicon lattice. (right) Simulation of an electron diffraction pattern of a silicon lattice with additional vacancies in the lattice positioned in periodic patterns in the lattice.	73
3.29	TEM overview image of proton implanted damage layer in approx. $4.5 \text{ } \mu\text{m}$ depth (energy: 400 keV , dose: $1 \cdot 10^{16} \text{ H}^+ / \text{cm}^2$). The specimen surface is located underneath the shown area in this image.	74
3.30	(left) TEM image of proton implantation induced defect layer in m:Cz silicon, (middle) electron diffraction measurement map (right) electron diffraction images of prominent positions on the cross section of the silicon wafer (shallower, directly on and deeper than the implantation depth).	75
3.31	(left) TEM image (middle) TEM and electron diffraction map calculated from (right) electron diffraction images of three different regions of interest.	76
3.32	(top) Electron diffraction image, (middle) electron diffraction intensity depending on position on damaged layer, (bottom) digitalized TEM images with indicated positions.	77
3.33	(left) TEM image of proton implanted silicon (middle top) Computed TEM and electron diffraction image (right) electron diffraction images of different region around the damaged region formed due to the hydrogen implantation. The red arrows indicate the positions of the electron diffractions.	78
3.34	(left) TEM image of proton implanted silicon sample, (bottom right) electron diffraction measurements used to calculate the real space structures shown top right	79
3.35	(top) TEM image (bottom middle) electron diffraction images (bottom outside) calculated defect complexes in the silicon lattice	80
3.36	a) Measurement principle of Spreading Resistance Profiling (SRP). Two metal tips are pressed against the surface of a semiconductor specimen and the resistance between the tips is measured. b) Representative circuit diagram of the measurement method. Figure has been taken from reference [32]	82
3.37	SSRM measurement of a test-diode implanted with hydrogen three times with different energies. In figure a) the two dimensional SSRM plot is shown. The bright regions represent higher dopant concentration than the dark regions. In comparison to that in figure b) the one dimensional scan is plotted. This shows the same resolution like all other SRP scans shown in this thesis. SSRM measurements were performed at Infineon Dresden.	83
3.38	Scheme of a four-point resistivity measurement	85

3.39	Thin film sample investigated with four point measurements. Taken from reference [165] with permission.	86
3.40	The figure on the left shows the implantation with all the trajectories of the penetrating 4 MeV H^+ ions into the silicon lattice. The figure to the right shows the implantation profile distribution(H in Si) for our parameters.	87
3.41	Three dimensional 4 MeV H-ion implantation into silicon distribution simulated with SRIM/TRIM	88
3.42	The implantation damage (displacements and vacancies) after the implantation of 4 MeV H^+ ions into the silicon lattice	88
3.43	(Proton implantations into silicon simulated by SRIM at zero Kelvin. The solid line represents the concentration of hydrogen and the dashed line the vacancy and interstitial concentration of the radiation damage. The H^+ -implantations were performed with 2.5 and 1 MeV and a dose of $1 \times 10^{14} H^+ cm^{-2}$ [139]	89
5.1	Visualization of the change of the doping type as a function of the annealing temperature and the distance to the front side of a H^+ implanted m:Cz silicon wafer ($4 MeV, 1 \times 10^{14} H^+ cm^{-2}$). <i>n</i> -type regions are coloured red, <i>p</i> -type regions are coloured blue. Image taken from M. Faccinelli [124]	142
5.2	SRIM Simulation of H^+ implanted into Fz silicon with an energy of 400 keV and implantation dose of $1 \times 10^{16} H^+ cm^{-2}$ (top) compared to a TEM image of the area (middle) and the representative schematic charge carrier concentration profile (bottom)	143
6.1	Distribution of the electric field for a current flowing through a round hole . . .	149
6.2	$\tan^{-1}(\tanh \frac{\mu}{2})$ vs. μ	150
6.3	Distribution of the electric field for a current flowing from a round metal contact to a semiconductor	152
6.4	Distribution of the equipotential lines in an SRP measurement	152
6.5	Spreading resistance as a function of the distance between the tips	153

List of Tables

1	Abbreviations	xx
2	Variables	xxi
2.1	List of the band gap energies and different effective masses of silicon compared to germanium	12
2.2	List of thermal double donor complexes listed in literature. The defect complex symmetry, local vibrational modes, energy levels in bandgap and potential structures are given.	31

Bibliography

- [1] L. P. Hunt. *Silicon precursors: Their manufacture and properties. Handbook of semiconductor silicon technology*. William Andrew Publishing/Noyes, 1990.
- [2] B. Ceccaroli. *Solar Grade Silicon Feedstock Handbook of Photovoltaic Science and Engineering*. J. Wiley, 2003.
- [3] Antonio et. al. Luque. *Handbook of Photovoltaic Science and Engineering (2nd edition)*. Wiley, 2011.
- [4] W. von Ammon and H. Herzer. The production and availability of high resistivity silicon for detector applications. *Nuclear Instruments and Methods in Physics Research*, 226:94–102, 1984.
- [5] Arjan Ciftja, Thorvald Abel Engh, and Merete Tangstad. Refining and recycling of silicon: A review. Trondheim, February 2008. NORWEGIAN UNIVERSITY OF SCIENCE AND TECHNOLOGY Faculty of Natural Science and Technology Department of Materials Science and Engineering.
- [6] Werner Zulehner. Historical overview of silicon crystal pulling development. *Materials Science and Engineering: B*, 73(1–3):7 – 15, 2000.
- [7] J. Czochralski. Ein neues verfahren zur messung der kristallisationsgeschwindigkeit der metalle. *Z. Phys. Chem.*, 92:219, 1918.
- [8] C.P. Ewels. *Density functional modeling of Point Defects in Semiconductors*. PhD thesis, University of Exeter, 1997.
- [9] Z. Li, H.W. Kraner, E. Verbitskaya, V. Eremin, A. Ivanov, M. Rattaggi, P.G. Rancoita, and F.A. Rubinelli. Investigation of the oxygen-vacancy (a-center) defect complex profile in neutron irradiated high resistivity silicon junction particle detectors. *IEEE Transactions on Nuclear Science*, 39 (6):1730, 1992.
- [10] G. Lindström. Radiation hard silicon detectors—developments by the rd48 (rose) collaboration. *Nuclear Instruments and Methods in Physics Research Section A: Accelerators, Spectrometers, Detectors and Associated Equipment*, 446(2):308, 2001.
- [11] Michael Moll. *Radiation Damage in Silicon Particle Detectors*. PhD thesis, Universität Hamburg, 1999.
- [12] H.C. Theuerer, 1962.
- [13] S. M. Sze. *Semiconductor Devices Physics and Technology*. John Wiley and Sons, 1985.
- [14] Karen A. Reinhardt and Werner Kern. *Handbook of Silicon Wafer Cleaning Technology (2nd ed.)*. Noyes Publications, 2008.

- [15] C. Kittel. *Introduction to Solid State Physics*. Oldenburg, 1953.
- [16] Wikipedia. <http://en.wikipedia.org/wiki/File:Silicon-unit-cell-3D-balls.png>.
- [17] Wikipedia. <http://de.wikipedia.org/wiki/Datei:Tetrahedral-3D-balls.png>.
- [18] E. Fermi. On the quantization of the monoatomic ideal gas. *Xiv:cond-mat/9912229*, 145:9, 1926.
- [19] P. A. M. Dirac. On the theory of quantum mechanics. *Proceedings of the Royal Society, Series A* 112(726):661–77, 1926.
- [20] P. Blaha, K. Schwarz, G. Madsen, D. Kvasnicka, and J. Luitz. Wien2k, June 2013.
- [21] Katrin Unger. Bandstructure calculation of silicon with wien2k.
- [22] Albert Einstein. Zur theorie der brownischen bewegung. *Ann. Physik*, 19:371, 1906.
- [23] Albert Einstein. Investigations on the theory of the brownian movement. *Methuen & Co. Ltd., London*, (English translation):1, 1926.
- [24] Bart Van Zeghbroec, 1998.
- [25] J. W. Corbett, G. D. Watkins, R. M. Chrenko, and R. S. McDonald. Defects in irradiated silicon. infrared absorption of the si-a center. *Phys. Rev.*, 121:1015–1022, Feb 1961.
- [26] G. D. Watkins and J. W. Corbett. Defects in irradiated silicon. i. electron spin resonance of the si-a center. *Phys. Rev.*, 121:1001–1014, Feb 1961.
- [27] G. D. Watkins and J. W. Corbett. Defects in irradiated silicon: Electron paramagnetic resonance and electron-nuclear double resonance of the si-e center. *Phys. Rev.*, 134:A1359–A1377, Jun 1964.
- [28] L.C. Kimerling, H.M. DeAngelis, and J.W. Diebold. On the role of defect charge state in the stability of point defects in silicon. *Solid State Communications*, 16(1):171 – 174, 1975.
- [29] Alexandra Junkes. *Influence of radiation induced defect clusters on silicon particle detectors*. PhD thesis, Universität Hamburg, 2011.
- [30] P. Wagner and J. Hage. Thermal double donors in silicon. *Applied Physics A*, 49(2):123–138, 1989.
- [31] R. Jones, J. Coutinho, S. Öberg, and P. R. Briddon. Thermal double donors in si and ge. *Physica B: Condensed Matter*, 308–310(0):8 – 12, 2001. International Conference on Defects in Semiconductors.
- [32] J. G. Laven. *Untersuchung und Modellierung von Dotierungsprofilen in Silicium erzeugt durch hochenergetische Protonenimplantationen*. PhD thesis, Technische Fakultät der Universität Erlangen-Nürnberg, 2013.
- [33] Spirecorp.
- [34] Andreas Schriefl. Defect studies using positron annihilation on proton-doped silicon. Master’s thesis, Graz University of Technology, 2009.
- [35] C. S. Fuller, J. A. Ditzenberger, N. B. Hannay, and E Buehler. Resistivity changes in silicon single crystals induced by heat treatment. *Acta Metallurgica*, 3 (1):97–99, 01/1955.
- [36] W. Kaiser, P. H. Keck, and C. F. Lange. Infrared absorption and oxygen content in silicon and germanium. *Phys. Rev.*, 101:1264–1268, Feb 1956.
- [37] W. Kaiser, H. L. Frisch, and H. Reiss. Mechanism of the formation of donor states in heat-treated silicon. *Phys. Rev.*, 112:1546–1554, Dec 1958.

- [38] J. P. Suchert. Chemical physics of semiconductors. *J. Chim. Phys. Phys. Chim. Biol.*, 58:455, 1961.
- [39] V. N. Mordkovich. The influence of oxygen on the conductivity of silicon. *Sov. Phys. Solid State*, 6:654, 1964.
- [40] D. Helmreich and F. Sirtl. Semiconductor silicon 1977. *Electrochemical Society Princeton NJ*, 1:626, 1977.
- [41] P. Gaworzewski and K. Schmalz. On the electrical activity of oxygen in silicon. *physica status solidi (a)*, 55(2):699–707, 1979.
- [42] D. Wruck and P. Gaworzewski. Electrical and infrared spectroscopic investigations of oxygen-related donors in silicon. *physica status solidi (a)*, 56(2):557–564, 1979.
- [43] L. C. Kimerling and J. L. Benton. Oxygen related donor states in silicon. *Applied Physics Letters*, 39(5):410–412, 1981.
- [44] J. Reichel. The distinction of several different kinds of oxygen donors in silicon. *physica status solidi (a)*, 66(1):277–282, 1981.
- [45] K. Schmalz and P. Gaworzewski. On the donor activity of oxygen in silicon at temperatures from 500 to 800 degree celsius. *physica status solidi (a)*, 64(1):151–158, 1981.
- [46] U. Gösele and T.Y. Tan. Oxygen diffusion and thermal donor formation in silicon. *Applied Physics A*, 28(2):79–92, 1982.
- [47] W. Zulehner. Aggregation phenomena of point defects in silicon. *Proc. Stall. Symp. to ESSDERC 82 Munich*, 1:89, 1983.
- [48] R. Oeder. P. wagner in: Defects in semiconductors ii, edited by s. mahajan and jw corbett, 1983.
- [49] M. Suezawa and K. Sumino. Nature of thermal donors in silicon crystals. *phys. Stat. sol. (a)*, 82:235, 1984.
- [50] A. Ourmazd, W. Schröter, and A. Bourret. Oxygen related thermal donors in silicon: A new structural and kinetic model. *J. Appl. Phys.*, 56:1670, 1984.
- [51] D.A. Van Wezep, T. Gregorkiewicz, H.H.P.Th. Bekman, and C.A.J. Ammerlaan. Oxygen endor of thermal donors in silicon. *Materials Science Forum*, 10-12:1009–1014, 1986.
- [52] M Reiche and O Breitenstein. The role of silicon self-interstitials in the formation of thermally induced rod-like defects in cz silicon. *physica status solidi (a)*, 101(2):K97–K99, 1987.
- [53] M. Reiche and O. Breitenstein. Precipitation processes in silicon at 465 degrees c. *Semiconductor Science and Technology*, 3(6):529, 1988.
- [54] M. Reiche, J. Reichel, and W. Nitzsche. Correlations between thermal donor formation, rod-like defect formation, and oxygen reduction during low-temperature annealing of cz-grown silicon. *physica status solidi (a)*, 107(2):851–865, 1988.
- [55] S. Gupta, S. Messoloras, J. R. Schneider, R. J. Stewart, and W Zulehner. Oxygen precipitation in carbon-doped silicon. *Semiconductor Science and Technology*, 7(1):6, 1992.
- [56] Yoichi Kamiura, Fumio Hashimoto, and Minoru Yoneta. Strong correlation between new donors and rodlike defects formed at 650c in phosphorus doped, carbon lean czochralski silicon preannealed at 450c. *Journal of Applied Physics*, 68(3):1358–1361, 1990.
- [57] D. J. Chadi. Oxygen-oxygen complexes and thermal donors in silicon. *Phys. Rev. B*, 41:10595–10603, May 1990.

- [58] R. C. Newman and R. Jones. Diffusion of oxygen in silicon. *Semiconductors and Semimetals*, 42:289–352, 1994.
- [59] S.A. McQuaid, R.C. Newman, and Elias Muñoz Merino. Models of oxygen loss and thermal donor formation in silicon by the clustering of rapidly diffusing oxygen dimers. *Materials Science Forum*, 196-201:1309–1314, 1995.
- [60] D. J. Chadi. Core structure of thermal donors in silicon. *PhysRevLett.*, 77 Issue 5:861, 1996.
- [61] M. Pesola, Young Joo Lee, J. von Boehm, M. Kaukonen, and R. M. Nieminen. Structures of thermal double donors in silicon. *Physical Review Letters*, 84:23, 2000.
- [62] S. Singh, R. Singh, and B. C. Yadav. An insight in the formation of thermal double donors in cz-silicon. *Optoelectronics and Advanced Materials*, 5:No. 11, 2011.
- [63] H. Navarro, J. Griffin, J. Weber, and L. Genzel. New oxygen related shallow thermal donor centres in czochralski-grown silicon. *Solid State Communications*, 58(3):151 – 155, 1986.
- [64] Young Joo Lee, J. von Boehm, M. Pesola, and R. M. Nieminen. First-principles study of migration, restructuring, and dissociation energies of oxygen complexes in silicon. *Phys. Rev. B*, 65:085205, Feb 2002.
- [65] B. Surma, C. A. Londos, V. V. Emtsev, A. Misiuk, A. Bukowski, and M. S. Potsidi. Infrared studies of oxygen-related defect formation in neutron-irradiated cz-silicon after annealing at $t=450\text{--}650\text{c}$ under hydrostatic pressure. *Materials Science and Engineering: B*, 102(1–3):339 – 343, 2003. E-MRS 2002 Symposium E: Advanced Characterisation of Semiconductors.
- [66] W. Goetz, G. Pensl, and W. Zulehner. Observation of five additional thermal donor species td12 to td16 and of regrowth of thermal donors at initial stages of the new oxygen donor formation in czochralski-grown silicon. *Phys. Rev. B*, 46:4312–4315, Aug 1992.
- [67] Michio Tajima and Silizuka T. Kanamori, Akihiro. -. *Japanese Journal of Applied Physics*, 19(7):L755, 1980.
- [68] Michio Tajima, Akihiro Kanamori, and Takashi Iizuka. Photoluminescence spectra of thermal donors in silicon. *Japanese Journal of Applied Physics*, 18(7):1401–1402, 1979.
- [69] A. R. Salmanov, A. N. Shchelokov, and A. E. Zemko. Donor states of oxygen in silicon. *Inorg. Mater.(Engl. Transl.):(United States)*, 21(11):–, 1986.
- [70] V. Cazcarra and P. Zunino. -. *Journal of Applied Physics*, 51:4206, 1980.
- [71] K. Hoelzlein, G. Pensl, M. Schulz, and N. M. Johnson. Hydrogenation of the “new oxygen donor” traps in silicon. *Applied Physics Letters*, 48(14):916–918, 1986.
- [72] Yoichi Kamiura, Fumio Hashimoto, and Minoru Yoneta. A new family of thermal donors generated around 450c in phosphorus doped czochralski silicon. *Journal of Applied Physics*, 65(2):600–605, 1989.
- [73] J. J. Qian, Z. G. Wang, S. K. Wan, and L. Y. Lin. A novel model of “new donors” in czochralski grown silicon. *Journal of Applied Physics*, 68(3):954–957, 1990.
- [74] K. Tempelhoff, F. Spiegelberg, R. Gleichmann, and D. Wruck. Precipitation of oxygen in dislocation-free silicon. *physica status solidi (a)*, 56(1):213–223, 1979.
- [75] K. Tempelhoff, R. Gleichmann, and B. Hahn. Oxygen precipitation in silicon between 600-degrees-c and 800 degrees-c . In *Journal of electrochemical society*, volume 128, pages C94–C94, 1981.

- [76] Yu. M. Babitskii, N.I. Gorbacheva, P.M. Grinshtein, and M.G. Milvidskii. The generation of thermal donors in silicon doped with germanium. *Fizika i Tekhnika Poluprovodnikov*, 24:1129–1132, 1984.
- [77] W. A. Tiller, S. Hahn, and F. A. Ponce. Thermodynamic and kinetic considerations on the equilibrium shape for thermally induced microdefects in czochralski silicon. *Journal of Applied Physics*, 59(9):3255–3266, 1986.
- [78] K. Hoelzlein, G. Pensl, and M. Schulz. Trap spectrum of the “new oxygen donor” in silicon. *Applied Physics A*, 34(3):155–161, 1984.
- [79] W. Batavin and E. Kochina. Mechanism of formation of thermal donors in silicon containing oxygen. *Sov. Phys. Semicond.*, 19(4):426–428, 1985.
- [80] G. H. Schwuttke, K. Brack, E. F. Gorey, A. Kahan, and L. F. Lowe. Resistivity and annealing properties of implanted si:h. *Rad. E6*, Nr. 1:103–106, 1970.
- [81] Y. Zohta, Y. Ohmura, and M. Kanazawa. Shallow donor state produced by proton bombardment of silicon. *Jpn. J. Appl. Phys.*, 10 Nr. 4:532–533, 1971.
- [82] Yu. V. Gorelkinski, V. O. Sigle, and Zh. S. Takibaev. Epr of conduction electrons produced in silicon by hydrogen ion implantation. *Phys. Status Solidi A*, 22:K55–K57, 1974.
- [83] Y. Ohmura, Y. Zohta, and M. Kanazawa. Shallow donor formation in si produced by proton bombardment. *Phys. Status Solidi A*, 15 Nr. 1:93–98, 1973.
- [84] X.-T. Meng, J.-W. Xiong, G.-G. Qin, and Y.-C. Du. New si-h infrared absorption peak corresponding to the hydrogen-defect shallow donors in silicon. *Phys. Scr.* 52, Nr. 1:108–112, 1995.
- [85] J. Hartung, J. Weber, and L. Genzel. Photothermal ionization studies of effective mass-like hydrogen-related donors in silicon. *Mater. Sci. Forum*, 65-66:157–162, 1990.
- [86] J. Hartung and J. Weber. Defects created by hydrogen implantation into silicon. *Mater. Sci. Eng. B* 4, Nr. 1-4:47–50, 1989.
- [87] J. Hartung and J. Weber. Shallow hydrogen-related donors in silicon. *Phys. Rev. B* 48, 19:14161–14166, 1993.
- [88] J. Hartung and J. Weber. Detection of residual defects in silicon doped by neutron transmutation. *J. Appl. Phys.*, 77 Nr. 1:118–121, 1995.
- [89] S. Z. Tokmoldin, A. T. Issova, Kh. A. Abdullin, and B. N. Mukashev. Shallow bistable non-effective-mass-like donors in hydrogenimplanted silicon. *Physica B*, 376-377:185–188, 2006.
- [90] Joachim Hartung. *Infrarot-Untersuchungen an Wasserstoff-induzierten Defekten in Silizium*. PhD thesis, Stuttgart, Max-Planck Institut fuer Festkoerperforschung, 1991.
- [91] A. T. Isova, V. V. Klimenov, I. S. Nevmerzhitsky, M. A. Zakharov, M. A. Yeleuov, and S. Z. Tokmoldin. Isotope study of far ir absorption of bistable centers in hydrogen-implanted silicon. *Physica B*, 23-24:5089–5092, 2009.
- [92] B. N. Mukashev, M. F. Tamendarov, S. Z. Tokmoldin, and V. V. Frolov. Hydrogen implantation into silicon. infra-red absorption spectra and electrical properties. *Phys. Status Solidi A*, 91:509–522, 1985.
- [93] H.J. Stein and S. Hahn. Hydrogen introduction and hydrogen enhanced thermal donor formation in silicon. *Appl. Phys. Lett.*, 75:3477, 1994.

- [94] L. Tsetseris, S. Wang, and S. T. Pantelides. Thermal donor formation in silicon and the catalytic role of hydrogen. *Appl. Phys. Lett.*, 88:051916, 2006.
- [95] E. Simoen, Y. L. Huang, Y. Ma J. Lauwaert, P. Clauws, J.M. Rafi, A. Ulyashin, and C. Claeys. What do we know about hydrogen-induced thermal donors in silicon? *J. Electrochemical Soc.*, 156 (6):H434–H442, 2009.
- [96] A. J. Morris, C.J. Pickard, and R. J. Needs. Hydrogen/nitrogen/oxygen defect complexes in silicon from computational searches. *Physical Review B*, 80:144112, 2009.
- [97] S. Dannefaer, V. Avalos, D. Kerr, R. Poirier, V. Shmarovoz, and S. H. Zhang. Annealing of electron-, proton-, and ion-produced vacancies in si. *Phys. Rev. B*, 73:115202–1–14, 2006.
- [98] J. Chevallier and B. Pajot. Interaction of hydrogen with impurities and defects in semiconductors. *Solid State Phenom*, 85-86:203–284, 2002.
- [99] J. Coutinho, R. Jones, S. Oberg, and P. R. Briddon. The formation, dissociation and electrical activity of divacancy-oxygen complexes in si. *Physica B*, 340-342:523–527, 2003.
- [100] M. Mikelsen, J. H. Bleka, J. S. Christensen, E. V. Monakhov, B. G. Svensson, J. Harkonen, and B. S. Avset. Annealing of the divacancy-oxygen and vacancy-oxygen complexes in silicon. *Phys. Rev. B*, 75 Nr. 15:155202–1–8, 2007.
- [101] B. G. Svensson and J. L. Lindstrom. Kinetic study of the 830 and 889 cm⁻¹ infrared bands during annealing of irradiated silicon. *Phys. Rev. B*, 34 Nr. 12:8709–8717, 1986.
- [102] P. Pellegrino, P. Leveque, J. Lalita, A. Hallen, C. Jagadish, and B. G. Svensson. Annealing kinetics of vacancy-related defects in low-dose mev self-ion-implanted n-type silicon. *Phys. Rev. B*, 64 Nr. 19:195211–1–10, 2001.
- [103] P. Johannesen, J. R. Byberg, B. Bech Nielsen, P. Stallinga, and K. Bonde Nielsen. Identification of vh in silicon by epr. *Mater. Sci. Forum* 258, 263:515–520, 1997.
- [104] E. V. Lavrov, J. Weber, L. Huang, and B. Bech Nielsen. Vacancy hydrogen defects in silicon studied by raman spectroscopy. *Phys. Rev. B*, 64, Nr. 3:035204–1–5, 2001.
- [105] K. Sixtus and W. Gerlach, 1966.
- [106] J. Bartko and K. H. Westinghouse Electric Corporation Sun. Reducing the switching time of semiconductor devices by nuclear irradiation, 1977.
- [107] B. J. Baliga and E. Sun. Comparison of gold, platinum, and electron irradiation for controlling lifetime in power rectifiers. *In: IEEE Trans. Electron. Dev.*, 6:685–688, 1977.
- [108] Yu. V. Bulgakov, T. I. Kolomenskaya, N. V. Kuznetsov, V. I. Shulga, and V. A.. Zaritskaya. The nature and distribution of radiation-induced defects in silicon along the range of protons and alpha particles. *Rad. Effects*, 54:129–134, 1981.
- [109] N. Q. Khanh, Cs. Kovacsics, T. Mohacsy, M. Adam, and J. Gyulai. Measuring the generation lifetime profile modived by mev h+ ion implantation in silicon. *Nucl. Instr. and Meth. in Phys. Res. B*, 147:111–115, 1999.
- [110] W. Wondrak and D. Silber. Buried recombination layers with enhanced n-type conductivity for silicon power devices. *Physica B*, 129:322–326, 1985.
- [111] Wolfgang Wondrak. *Erzeugung von Strahlenschäden in Silizium durch hochenergetische Elektronen und Protonen*. PhD thesis, Frankfurt am Main, Johann-Wolfgang-Goethe-Universität, 1985.
- [112] W. Wondrak and A. Boos. Helium implantation for lifetime control in silicon power devices. *Proc. ESSDERC*, 1:649–652, 1987.

- [113] M. Buzzo, M. Ciappa, M. Rub, and W. Fichtner. Characterization of 2d dopant profiles for the design of proton implanted high-voltage superjunction. *Proceedings of the 12th IPFA IEEE*, 1:285–289, 2005.
- [114] D. Barake, A. Ulyashin, I. Perichaud, and Martinuzzi S. n-p junction formation in p-type silicon by hydrogen ion implantation. *Solar Energy Materials & Solar Cells*, 72:285–290, 2002.
- [115] D. Barakel and S. Martinuzzi. Donor behaviour of implanted hydrogen ions in silicon wafers. *Mater. Res. Soc. Symp. Proc.*, 813:S. H7.3, 2004.
- [116] S. Romani and J. H. Evans. Platelet defects in hydrogen implanted silicon. *Nucl. Instr. and Meth. in Phys. Res. B* 44, 3:313–317, 1990.
- [117] B. Aspar, M. Bruel, H. Moriceau, C. Maleville, T. Poumeyrol, A. M. Papon, and A. Claverie. Basic mechanisms involved in the smart-cut® process. *Microelectron. Eng.* 36, Nr. 1-4:233–240, 1997.
- [118] W. K. Chu, R. H. Kastl, R. F. Lever, S. Mader, and B. J. Masters. Distribution of irradiation damage in silicon bombarded with hydrogen. *Phys. Rev. B* 16, 9:3851–3859, 1977.
- [119] M. Bruel. Process for the production of thin semiconductor material lms, 1993.
- [120] Michel Bruel, B. Aspar, and Andre-Jacques Auberton-Herve. Smart-cut: a new silicon on insulator material technology based on hydrogen implantation and wafer bonding. *Japanese journal of applied physics*, 36(part 1):1636–1641, 1997.
- [121] A. Agarwal, T. E. Haynes, V. C. Venezia, O. W. Holland, and D. J. Eaglesham. Efficient production of silicon-on-insulator films by co-implantation of he^+ with h^+ . *Appl. Phys. Lett.*, 72:1086–1088, 1998.
- [122] S. Kirnstoetter, M. Faccinelli, W. Schustereder, J. G. Laven, H.-J. Schulze, and P. Hadley. Hydrogen decoration of radiation damage induced defect structures. *AIP conference proceedings*, 1583:–, 2014.
- [123] J. F. Ziegler. *The Stopping and Range of Ions in Matter*. Pergamon Press, 1977-1985.
- [124] M. Faccinelli. Spatially resolved measurements of charge carrier properties in proton doped silicon. Master’s thesis, University of Technology Graz, 2013.
- [125] Wikipedia.org. Diagram of a scanning electron microscope with english captions.
- [126] A. E. Grün. Lumineszenz-photometrische messungen der energieabsorption im strahlungsfeld von elektronenquellen: Eindimensionaler fall in luft. *Zeitschrift für Naturforschung*, 12a(2):89–95, 1956.
- [127] W. Ehrenberg and B. E. N. King. The penetration of electrons into luminescent materials. *Proc. Phys. Soc. (London)*, 81:751–766, 1963.
- [128] A. Cohn and G. Caledonia. Spatial distribution of the fluorescent radiation emission caused by an electron beam. *J. Appl. Phys.*, 41(9):3767–3775, 1970.
- [129] H. J. Leamy. Charge collection scanning electron microscopy. *J. Appl. Phys.*, 53(6):R51–R77, 1982.
- [130] D. B. Holt. The conductive mode in sem microcharacterisation of semiconductors. *Academic Press Limited*, 1:241–338, 1989.
- [131] J. J. Friel. *X-Ray and Image Analysis in Electron Microscopy*. Princenton Gamma-Tech Inc., Princenton NJ/USA, 1995.

- [132] P. J. Potts. A handbook of silicate rock analysis. *Chapman and Hall*, 1:336–337., 1987.
- [133] Hendrix Demers, Nicolas Poirier-Demers, Alexandre Réal Couture, Dany Joly, Marc Guilmain, Niels de Jonge, and Dominique Drouin. Three-dimensional electron microscopy simulation with the casino monte carlo software. *Scanning*, 33(3):135–146, 2011.
- [134] T. E. Everhart, K. C. A. Smith, O. C. Wells, and C. W. Oatley. Recent developments in scanning electron microscopy. *Proceedings of the Fourth International Conference on Electron Microscopy Physics*, 1:269–273, 1958.
- [135] Juan Rechid. *Elektrische Mikrocharakterisierung von elektrochemisch hergestellten CIS-Solarzellen mittels EBIC*. PhD thesis, Universität Oldenburg, 2000.
- [136] Synopsis.com.
- [137] C. Donolato. An alternative proof of the generalized reciprocity theorem for charge collection. *J. Appl. Phys.*, 66 (9):4524–4525, 1989.
- [138] S. Kirnstoetter, M. Faccinelli, P. Hadley, R. Job, W. Schustereder, J. G. Laven, and H.-J. Schulze. Investigation of doping type conversion and diffusion length extraction of proton implanted silicon by ebic. *ECS transactions*, 50 (5):145–160, 2013.
- [139] S. Kirnstoetter, M. Faccinelli, M. Jelinek, J. G. Laven, W. Schustereder, H.-J. Schulze, and P. Hadley. Multiple proton implantations into silicon: A combined ebic and srp study. *Solid State Phenomena*, 205-206:311–316, 2014.
- [140] F. Berz and K. Kuiken. Theory of life time measurements with the scanning electron microscope: steady state. *Solid-State Electronics*, 19:437–445, 1976.
- [141] V. K. S. Ong, J. C. H. Phang, and D. S. H. Chan. A direct and accurate method for the extraction of diffusion length and surface recombination velocity from an ebic line scan. *Solid-State Electronics*, 37 (1):1–7, 1994.
- [142] A. Boudjani, G. Bassou, T. Benbakhti, M. Beghdad, and M. Belmekki. Direct measurement of minority carrier diffusion length in planar devices. *Solid-State Electronics*, 38:471–475, 1995.
- [143] D. S. H. Chan, V. K. S. Ong, and J. C. H. Phang. A direct method for the extraction of diffusion length and surface recombination velocity from an ebic line scan: planar junction configuration. *IEEE Transactions on Electron Devices*, 42:963–968, 1995.
- [144] D. E. Ioannou and S. M. Davidson. Diffusion length evaluation of boron-implanted silicon using the sem-ebic/schottky diode technique. *Journal of Physics D: Applied Physics*, 12 (8):1339–1344, 1979.
- [145] D. E. Ioannou and C. A. Dimitriadis. A sem-ebic minority-carrier diffusion-length measurement technique. *IEEE Transactions on Electron Devices*, 29:445–450, 1982.
- [146] L. Chernyak, A. Osinsky, H. Temkin, J. W. Yang, Q. Chen, and M. Asif Khan. Electron beam induced current measurements of minority carrier diffusion length in gallium nitride. *Applied Physics Letters*, 69 (17):2531–2533, 1996.
- [147] V. K. S. Ong. A direct method of extracting surface recombination velocity from an electron beam induced current line scan. *Review of Scientific Instruments*, 69 (4):1814–1816, 1998.
- [148] O. Kurniawan and V. S. Ong. An analysis of the factors affecting the alpha parameter used for extracting surface recombination velocity in ebic measurements. *Solid-State Electronics*, 50:345–354, 2006.

- [149] Th. Flohr and R. Helbig. Determination of minority carrier lifetime and surface recombination velocity by optical beam induced current measurements at different light wavelengths. *Journal of Applied Physics*, 66(7):3060–3065, 1989.
- [150] Edward I Cole Jr, Paiboon Tangyunyong, Charles F Hawkins, Michael R Bruce, Victoria J Bruce, and Rosalinda M Ring. Apparatus and method for analyzing functional failures in integrated circuits, April 15 2003. US Patent 6,549,022.
- [151] R. G. Mazur and D. H. Dickey. A spreading resistance technique for resistivity measurements on silicon. *J. Electrochem. Soc.*, 113 (3):255–259, 1966.
- [152] E. F. Gorey, C. P. Schneider, and M. R. Poponiak. Preparation and evaluation of spreading resistance probe tip. *J. Electrochem. Soc.*, 117 (5):721–725, 1970.
- [153] W. R. Thurber, R. L. Mattis, Y. M. Liu, and J. J. Filliben. Resistivity-dopant density relationship for phosphorus-doped silicon. *J. Electrochem. Soc.*, 127 (8):1807–1812, 1980.
- [154] W. R. Thurber, R. L. Mattis, Y. M. Liu, and J. J. Filliben. Resistivity-dopant density relationship for boron-doped silicon. *J. Electrochem. Soc.*, 127 (10):2291–2294, 1980.
- [155] S. M. Hu. Between carrier distributions and dopant atomic distribution in beveled silicon substrates. *Journal of Applied Physics*, 53:1499–1510, 1982.
- [156] A. Casel and H. Jorke. Comparison of carrier profiles from spreading resistance analysis and from model calculations for abrupt doping structures. *Applied Physics Letters*, 50:989–991, 1987.
- [157] P. A. Schumann and E. E. Gardner. Spreading resistance correction factors. *Solid-State Electronics*, 12:371–375, 1969.
- [158] S. C. Choo, M. S. Leong, and J. H. Sim. An efficient numerical scheme for spreading resistance calculations based on the variational method. *Solid-State Electronics*, 26 (8):723–730, 1983.
- [159] A. F. Yaremchuk. Analysis of the correction factor in the spreading resistance technique for monitoring epitaxial silicon. *Applied Physics (a)*, 76.3:405–411, 2003.
- [160] J. van Linschoten, J. Snijder, and M. W. Hillen. Preprocessing of data from spreading resistance measurements. *Solid State and Electron Devices*, 127 (2):100–104, 1980.
- [161] T. Clarysse and W. Vandervorst. An efficient smoothing algorithm for spreading resistance calculations. *Solid-State Electronics*, 31 (1):53–63, 1988.
- [162] J. C. Maxwell and J. J. Thompson. A treatise on electricity and magnetism. Oxford Calendron, 1904.
- [163] Peter Hadley.
- [164] L. B. Valdes. Resistivity measurements on germanium for transistors. *Proceedings of the IRE*, 42:420–427, 1954.
- [165] <http://lamp.tu-graz.ac.at/hadley/sem/4pt/4pt.php>. Four point resistivity measurements.
- [166] J. F. Ziegler and J. P. Biersack. Srim - the stopping and range of ions in solids, 1985.
- [167] J. P. Biersack and L. Haggmark. A monte carlo computer program for the transport of energetic ions in amorphous targets. *Nucl. Instr. and Meth*, 174:257, 1980.
- [168] C. Herring, N. M. Johnson, and Chris G. Van de Walle. Energy levels of isolated interstitial hydrogen in silicon. *PHYSICAL REVIEW B*, 64:125209, 2001.

- [169] K. Smaali, J. Fauré, A. El Hdiy, and M. Troyon. High-resolution scanning near-field (EBIC) microscopy: Application to the characterisation of a shallow ion implanted p+-n silicon junction. *Ultramicroscopy*, 108(6):605 – 612, 2008.
- [170] Y. V. Sharvin. A possible method for studying fermi surfaces. *Soviet Physics JETP*, 21:655–656, 1965.
- [171] G. Wexler. The size effect and the non-local boltzmann transport equation in orifice and disk geometry. *Proceedings of the Physical Society*, 89 (4):927–941, 1966.